Fakultäts-Graduiertenzentrum Maschinenwesen

TECHNISCHE UNIVERSITÄT MÜNCHEN

Roughness-Induced Transition in a Hypersonic Capsule Boundary Layer under Wind-Tunnel and Reentry Conditions

Antonio Di Giovanni

Vollständiger Abdruck der Fakultät für Maschinenwesen der Technischen Universität München zur Erlangung des akademischen Grades eines

Doktor-Ingenieurs

genehmigten Dissertation.

Vorsitzender:		Prof. Dr.-Ing. Manfred Hajek
Prüfende/-r der Dissertation:	1.	apl. Prof. Dr.-Ing. habil. Christian Stemmer
	2.	Prof. Dr.-Ing. Wolfgang Schröder

Typesetting LaTeX

Abstract

Direct Numerical Simulations (DNS) are used to investigate roughness-induced instability mechanisms on a capsule-like hemispherical configuration. Numerical investigations are first performed for the cold wind-tunnel conditions ($M = 5.9$) of the Hypersonic Ludwieg Tube in Braunschweig (HLB). The development of unsteady disturbances downstream of two different roughness geometries is analyzed and quantified. In the case of a spanwise periodic roughness element, two main unstable modes are found in the roughness wake, corresponding to the symmetric and antisymmetric modes already known for isolated roughness elements. In the case of a patch of (pseudo-)randomly distributed roughness, a new type of roughness-induced crossflow-type instability is observed for the blunt-capsule configuration. The growth of primary and secondary instabilities in the wake of the distributed roughness is analyzed in both the linear and non-linear stages up to the laminar-turbulent breakdown. Successively, boundary-layer transition on the hemispherical geometry with distributed roughness is numerically investigated for a typical reentry scenario at $M = 20$. For the considered conditions, molecular dissociation and non-equilibrium effects significantly change the temperature profiles of the capsule boundary layer and have a noticeable influence on the stability properties of the roughness wake. The influence of the various non-equilibrium effects on the steady base flow and on the (non-)linear growth of unsteady disturbances are compared by performing simulations with different gas models of increasing complexity. Furthermore, the influence of the gas modeling on the transition location is analyzed, showing the importance of considering the effects of non-equilibrium to correctly predict the transition location and the values of the augmentation of the wall heating induced by the laminar-turbulent breakdown. Finally, numerical simulations are performed for the cold wind-tunnel conditions of the HLB to investigate the evolution of unsteady perturbations on the capsule boundary layer in the presence of a micron-sized roughness. No evidence of disturbance growth in the roughness wake is found by DNS. The investigations presented in this work provide an in-depth insight into various roughness-induced instability mechanisms for the capsule boundary layer and lay the groundwork for future studies aimed at developing improved, physics-based methods for the prediction of roughness-induced transition on blunt capsules at altitudes where high-temperature gas effects cannot be neglected.

Zusammenfassung

Die vorliegende Arbeit untersucht die Instabilitätsmechanismen des laminar-turbulenten Umschlags an einer Kapselgeometrie mit einer rauen Wand durch Direkte Numerische Simulationen (DNS). Zunächst werden Simulationen unter den kalten Windkanalbedingungen vom Hypersonic Ludwieg Tube in Braunschweig (HLB) durchgeführt. Die Entwicklung von instationären Störungen wird im Nachlauf von zwei verschiedenen Rauigkeitsgeometrien analysiert und quantifiziert. Im Fall von spannweitig periodischen sinusförmigen Einzelrauigkeiten sind zwei Hauptmoden im Rauigkeitsnachlauf zu finden, die den symmetrischen und antisymmetrischen Moden im Nachlauf von einzelnen Rauigkeitselementen entsprechen. Bei einem stochastisch verteilten Rauigkeitsfeld entsteht auch ohne eine Querströmungskomponente der Grundströmung ein langlebiger Querströmungswirbel. Die primären sowie sekundären Instabilitäten im Rauigkeitsnachlauf werden sowohl im linearen als auch im nicht-linearen Bereich einschließlich des laminar-turbulenten Strömungsumschlags analysiert. Danach werden die Ergebnisse für die stochastisch verteilte Rauigkeit auf ein Wiedereintrittsszenario mit realistischen Bedingungen ($M = 20$) übertragen. Dabei steht der Einfluß der Heißgaseffekte (nämlich Dissoziation und Nichtgleichgewichtseffekte) auf die Stabilitätseigenschaften des Rauigkeitsnachlaufs im Mittelpunkt der Untersuchung. Um die Heißgaseffekte zu beurteilen, werden die Simulationen im Wiedereintrittsfall mit verschiedenen Gasmodellen wachsender Komplexität durchgeführt. Darüber hinaus wird der Einfluß der Gasmodellierung auf die Lage des Strömungsumschlags sowie auf die darauffolgende Zunahme des Wärmestroms an der Wand untersucht. Schließlich werden numerische Simulationen für die Kapselgeometrie unter den HLB-Bedingungen durchgeführt, um die Entwicklung instationärer Störungen in der Kapselgrenzschicht in Anwesenheit von kleinen quaderförmigen Rauigkeitselementen zu untersuchen. Die DNS weisen in Übereinstimmung mit vorherigen Untersuchungen, die auf der Linearen Stabilitätstheorie sowie auf der Theorie des optimalen transienten Wachstums basieren, auf kein Störungswachstum im Rauigkeitsnachlauf hin. Die vorliegende Arbeit stellt eine ausführliche Beschreibung verschiedener rauigkeitsinduzierter Instabilitätsmechanismen für die Kapselgeometrie dar und legt die Basis für die Entwicklung von zuverlässigen physikbasierten Methoden zur Vorhersage des Strömungsumschlags an der Kapsel unter Berücksichtigung von Heißgaseffekten.

Acknowledgments

Contents

Contents

Nomenclature

2D	Two-Dimensional
3D	Three-Dimensional
AUSM+	Advection Upstream Splitting Method
CEV	Crew Exploration Vehicle
DFG	Deutsche Forschungsgemeinschaft
DLR	German Aerospace Center
DNS	Direct Numerical Simulations
HLB	Hypersonic Ludwieg tube Braunschweig
LaRC	NASA Langley Research Center
LST	Linear Stability Theory
MPI	Message-Passing Interface
NSMB	Navier Stokes Multi Block
PSE	Parabolized Stability Equations
SSOR	Symmetric Successive Over Relaxation
TPS	Thermal Protection System
TUM	Technical University of Munich

Contents

List of Symbols

A	disturbance amplitude
c	species concentration
Da	Damköhler number
e^{rot}, e^{tr}, e^{vib}	rotational, translational and vibrational energy [J/kg]
h^0	zero-point energy [J/kg]
k	roughness height [m]
$\overline{k}$	mean roughness height [m]
M	Mach number
M	molar mass [Kg/mol]
N	N-factor
p	pressure [N/m²]
Q^{chem}	heat transfer due to chemical reactions [J/(kg·s)]
$Q^{\mathrm{t-v}}$	translational-vibrational heat transfer [J/(kg·s)]
q^{vib}	heat-conduction term based on the vibrational temperature [J/(kg·s)]
R	radius of the hemisphere [m]
$R_{\circ}$	universal gas constant [J/(mol·K)]
Re_{kk}	roughness Reynolds number, $\frac{\rho_k u_k k}{\mu_k}$
Re_{∞}	unit Reynolds number [1/m]
T	temperature [K]
T^{vib}	vibrational temperature [K]
u, v, w	velocities in x, y and z directions [m/s]

$\mathbf{u}^D$ diffusion velocity [m/s]

x, y, z coordinates in streamwise, wall-normal and spanwise directions [m]

Greek

δ boundary-layer thickness [m]

μ dynamic viscosity [kg/(m·s)]

ρ density [kg/m^3]

σ growth rate [1/m]

τ_f, τ_c convection timescale and timescale of the chemical reactions [s]

$\dot{\omega}_s$ species chemical production rate [kg/(m$^3 \cdot$ s)]

Subscripts

0   location of the initial disturbance

k value taken at the height of the roughness

m molecular species

s species

w   value taken at the wall

∞ freestream conditions

1 Introduction

This work investigates different instability mechanisms in the hypersonic boundary layer of a blunt-capsule configuration with a rough wall. Direct Numerical Simulations are undertaken to analyze the origin and the (non-)linear development of unstable modes in the wake of different roughness geometries. Analyses are performed for both cold wind-tunnel conditions and high-enthalpy reentry conditions, including high-temperature gas effects. The primary goal of the present study is to identify potential roughness-induced instabilities for the blunt-capsule configuration. In addition, the influence of chemical and thermal non-equilibrium on the amplification of unsteady disturbances in the roughness wake is assessed.

The thesis is structured as follows. Chapter 1 provides an introduction to the problem of roughness-induced transition on capsule geometries as well as an overview of the state-of-the-art in the literature for laminar-turbulent transition under consideration of high-temperature gas effects. The chapter ends with a summary of the thesis objectives. In Chapter 2, the set-up of the investigated geometry and the numerical procedure are presented. Chapter 3 summarizes the main accomplishments with reference to the relevant publications produced within this work. Chapter 4 provides a discussion across the dissertation topics including a review of the relevant literature. A full list of the produced publications is given in Appendix A. The main peer-reviewed journal publications can be found in full text in Appendix B.

The present work is part of a joint project in collaboration with other German research institutes (DLR Göttingen, Technische Universität Braunschweig and RWTH Aachen) with the goal of investigating hypersonic transition on capsule geometries and was financially supported by the German Research Foundation (Deutsche Forschungsgemeinschaft - DFG) under contract STE 1454/8-2.

1.1 Motivation

After the tragic accident of the Space Shuttle Columbia in 2003, new attention has been given to the space capsule as return-vehicle configuration. The capsule geometry was selected by several countries for the first human spaceflight programs, including the American project MERCURY, which was further developed in the suc-

cessive APOLLO program. Because of the immediately available technology and the well-established historical safety, the space capsule has been newly selected in the current ORION program. However, in spite of the multi-decennial experience gained through intensive investigations on hypersonic flows, the previous programs have left several questions unanswered. Among the topics without satisfactory understanding, the characterization of the laminar-turbulent transition on hypersonic capsule configurations assumes central importance, as the flow is nominally stable to modal instability.

Laminar-turbulent transition strongly affects the heat transfer on the capsule wall. Specifically, for fully turbulent boundary layers, the heat-transfer rate at the wall can be up to one order of magnitude larger than in the laminar case. At transition, the wall heating can even exceed the turbulent levels. As a protection against the extreme heat load experienced during reentry, capsules are equipped with an ablative Thermal Protection System (TPS). A precise evaluation of the heat load on the TPS is important in order to minimize weight and costs of the TPS and to ensure a safe reentry of the crew. However, due to the lack of a precise transition-prediction criterion for capsule boundary layers, the current design of the TPS includes extra margins of safety and is based on a fully turbulent heating profile, leading to an oversize of the heat shield and a penalization of the vehicle payload (Bertin and Cummings, 2006; Berry and Horvath, 2008).

A large number of experimental investigations have been conducted on capsule-like models for flight-relevant conditions. However, high speeds and temperatures typical of hypersonic flows make measurements difficult to realize compared to cold low-speed flows. Many transition experiments conducted over the past 50 years in conventional hypersonic ground test facilities are affected by high level of noise radiating from the turbulent boundary layer normally present on the wind-tunnel walls, causing an earlier transition compared to the case of free flight (Schneider, 2006). Furthermore, at the moment there exists no ground test facility that can simultaneously reproduce all the relevant features and parameters of free flight at high altitudes, including Mach number, surface temperature, finite-rate chemistry and thermal non-equilibrium effects.

With the advent of modern high-fidelity computational methods, numerical simulations have become a valuable and often indispensable investigation tool in the analysis of the transition process. Compared to experiments, numerical simulations allow for a more detailed description of the physical phenomena underlying laminar-turbulent transition. In addition, finite-rate chemistry and thermal non-equilibrium can be included in the computations and the stability analysis of hypersonic flows can be performed for realistic free-flight conditions at high altitudes. Numerical methods for stability analysis include, among others, Linear Stability Theory (LST), (non-)linear Parabolized Stability Equations (PSE) and Direct Numerical Simulations (DNS). Compared to LST and PSE, Direct Numerical Simulations allow for investigations on more complex geometries and provide a more complete insight into

non-linear mechanisms, including the laminar-turbulent breakdown. Since the development of mechanism-based prediction methods for capsule transition is subject to the understanding of the physics behind the transition process, numerical simulations should be carried out alongside ground-test experiments to develop models that can be extrapolated to flight.

1.2 Instability mechanisms in high-speed compressible boundary layers

The amplification of unstable modes in laminar boundary layers is one of the basic mechanisms which can lead to laminar-turbulent transition. Instability waves, with a small amplitude relative to the mean flow component, travel in the boundary layer with a certain frequency. If these waves are unstable, their amplitude grows and can eventually trigger boundary-layer transition. In compressible boundary layers, multiple modes of instability can be found (Mack, 1987). The first-mode instability (also known as Tollmien-Schlichting wave) is a vorticity-type disturbance, dominant in subsonic boundary layers as well as in supersonic boundary layers at low Mach numbers ($M < 4$). The first mode is the most unstable when a generalized inflection point is present in the velocity profile of the boundary layer, whereas the presence of a favorable pressure gradient has a stabilizing effect. The second mode (Mack mode) and higher modes are acoustic disturbances and set in at Mach numbers typical of hypersonic flows, usually presenting larger growth rates than the first mode for $M > 4$. As shown by Hudson et al. (1996), chemical dissociation and thermochemical non-equilibrium have a noticeable influence on the growth rate of both first and second modes.

In three-dimensional boundary layers, the presence of a spanwise component of the velocity in the base flow can give birth to a crossflow instability. This type of instability manifests itself as steady co-rotating vortices aligned with the inviscid flow streamlines and has mainly been investigated for three-dimensional subsonic boundary layers, such as in the case of swept wings (see, e.g., Malik et al., 1999). These vortices strongly deform the boundary layer and form potentially unstable shear layers where the linear growth of small disturbances can be observed.

Assuming that the initial unsteady disturbances are small relative to the mean flow component, the growth of unstable modes can be described by Linear Stability Theory. In this framework, the amplitude of a disturbance with a constant frequency grows exponentially, leading to the e^N boundary-layer transition criterion,

$$\mathrm{e}^N = \frac{A}{A_0} = \exp \int_{x_0}^{x} -\sigma \mathrm{d}x, \tag{1.1}$$

where x is the streamwise coordinate, A_0 and x_0 are the amplitude and the location

of the initial disturbance, A is the integrated disturbance amplitude and $-\sigma$ is the disturbance growth rate. Experimentally, it has been shown that, for different vehicles and flows, transition is expected for values of N in the order of 10, depending on the tunnel conditions and the background disturbance levels.

1.3 Boundary-layer stability of blunt capsules

Laminar-turbulent transition of the boundary layer of blunt capsules has been puzzling the scientific community for decades. As reported by Morkovin (1984), already in the 1950s, experiments showed clear evidence of transition on blunt noses, although all theories at that time said that the accelerated boundary layer on blunt bodies should be stable. In capsule geometries with a spherical-section forebody, like the Apollo capsule or the Orion Crew Exploration Vehicle (CEV), the presence of a strongly favorable pressure gradient with the boundary-layer edge velocity rapidly increasing from the stagnation point to the capsule shoulder highly stabilizes the flow against first-mode instabilities. Furthermore, due to the presence of a strong bow shock ahead of the capsule, the boundary layer on the forepart of the capsule remains in the subsonic to transonic range and the presence of second-mode instabilities in the capsule boundary layer can also be excluded. In addition, the lateral curvature of the boundary-layer streamlines on the smooth-wall capsule is weak and the spanwise component of the velocity can be neglected. Hence, crossflow-mode instabilities are not relevant either. The presence of Görtler-type instabilities is also prevented by the convex surface curvature. The phenomenon of laminar-turbulent transition on blunt bodies without modal disturbance growth is known in the literature as "blunt-body paradox" (Morkovin, 1984; Reshotko and Tumin, 2000). In the absence of a known instability mechanism for the blunt-body configuration with a smooth wall, roughness seems to be the most likely cause of transition of the capsule boundary layer.

Roughnesses are present on the TPS as both localized non-uniformities (single roughness elements) and distributed roughness. Single roughness elements comprehend TPS joints, compression pads and gap fillers between heat-shield tiles and are usually integral parts of the heat shield. Instead, the presence of distributed roughness is mainly due to ablation of the TPS. The TPS is a low-density heat shield resistant to high temperatures and with low-conductivity properties. In ablative TPS, thermal energy is reduced through endothermic chemical reactions and taken away from the capsule surface by sacrifice of the surface material. Charring ablators, like the one used for the Apollo capsule, are initially composed of a fibrous material filled with injected resin that pyrolyzes at high temperature (Graves and Witte, 1996). The remaining pyrolyzed material, the char, is characterized by low heat conductivity, providing insulation of the underlying structure, and high emissivity, which allows for a partial re-radiation of the incident heat. As the heat flux

increases, the ablation of the surface char begins and further mass is removed from the surface. Due to these phenomena of oxidation and surface recession, extended regions of distributed roughness appear on the surface of the TPS (see Figure 1.1). Laminar ablation generates roughnesses with a height usually of the order of the boundary-layer thickness or smaller. Larger roughness elements can apparently be generated only after transition occurs (Grabow and White, 1975).

Figure 1.1: Photo of the Apollo 12 Command Module (left) and enlargement of the burnt TPS (right), taken at Virginia Air & Space Center, USA.

1.4 Effects of roughness on boundary-layer transition

To date, there is no general mechanism-based criterion to predict roughness-induced transition. However, the ratio roughness-height to boundary-layer thickness k/δ and the roughness Reynolds number,

$$Re_{kk} = \frac{\rho_k u_k k}{\mu_k}, \tag{1.2}$$

defined with the flow properties at the roughness height for the corresponding smooth configuration, are regarded as the parameters of greatest relevance. Depending on the values of the roughness height and of the roughness Reynolds number for a given configuration, the presence of roughness can trigger various instability mechanisms. Note that the roughness Reynolds number is not a mechanism-based parameter and the correlations between Re_{kk} and the stability properties of the boundary layer as found in the literature are purely empirical.

Small roughness elements ($Re_{kk} < 10$) can initiate Görtler-vortex instabilities along highly concave walls. Crossflow-vortex instabilities can be triggered in the

presence of a spanwise component of the velocity in the base flow. In the case of blunt bodies with small surface roughness, transient growth has been proposed as a possible instability mechanism in the situations where the boundary layer does not support modal instabilities (Reshotko and Tumin, 2004). Transient growth refers to the transitory amplification of the linear superposition of decaying modes and derives from the non-orthogonality of the individual modes described by LST. Even though this topic is still subject of ongoing research (see, e.g., Paredes et al., 2017; Leidy et al., 2018; Hein et al., 2019), the overall non-modal growth described by transient-growth theory strongly depends on the shape of the initial disturbance, with disregard of the physical realizability of the initial disturbance and, thus, raising questions about the limits of applicability of the optimal transient-growth approach. For larger roughness elements, the roughness generates a wake with a potentially unstable shear layer where modal growth of small disturbances takes place. For example, Choudhari et al. (2010) showed that, in the presence of isolated diamond trips of $Re_{kk} = 547$ in a flat-plate boundary layer at Mach $M = 3.5$, the roughness wake is characterized by the presence of two main unstable modes of symmetric (varicose) and antisymmetric (sinuous) nature.

At given freestream conditions, the smallest roughness height for which transition is influenced by the presence of the roughness is called critical roughness size. Once the critical roughness size for transition is reached, an increase of the roughness height leads to an earlier onset of the laminar-turbulent breakdown, with the transition location moving upstream towards the roughness position. For very large values of the roughness height (typically in the order of the boundary-layer thickness) and, hence, of Re_{kk}, the roughness becomes effective, in the sense that transition is triggered as close as possible to the roughness location (Reda, 2002; Schneider, 2008a). Once the roughness has become effective, a further increase of the roughness height and of the roughness Reynolds number does not have any influence on the transition location and absolute instabilities dominate the transition process.

Attempts have been made to find a correlation between the roughness Reynolds number and laminar-turbulent transition. For blunt geometries, these correlations were investigated, among others, by Reda (Reda, 2002; Reda et al., 2008). In the case of distributed roughness, Reda et al. (2008) correlated laminar-turbulent transition to a roughness Reynolds number built with the arithmetic average of the measured roughness heights. Transition was observed for Re_{kk} in the range of $250 \pm 20\%$. Further experiments on blunt-body geometries with rough walls were carried out by Wilder et al. (2015) in both a CO_2 and an air-dominated atmosphere. The critical value for transition was $Re_{kk} = 259$ for tests conducted in air and $Re_{kk} = 223$ for tests conducted in CO_2. Experiments on sphere-cone and hemisphere geometries with sand-grain roughness were conducted at NASA Langley Research Center (LaRC) and are summarized in Hollis (2014). A roughness Reynolds number based on the friction velocity was used, $Re_{k+} = \rho_w u_\tau k / \mu_k$. Transitional flow was found

for $\sim 10 < Re_{k+} < \sim 70$. Further available experimental data on roughness-induced transition on hypersonic blunt bodies are provided by Schneider (2008b).

Even though the parameter Re_{kk} provides a first good estimation for the roughness effects on the stability of the boundary layer, other parameters have a significant influence on the stability properties of the roughness wake. In the case of flat-plate boundary layers, it has been shown that the edge Mach number affects the value of the effective roughness Reynolds number. For example, in the numerical simulations of a flat-plate boundary layer at $M = 4.8$ performed by Groskopf and Kloker (2016), no absolute instability was observed for skewed roughness elements with roughness Reynolds numbers in the range of $72 - 990$. Instead, a global instability for roughness configurations with $Re_{kk} \sim 600$ was observed by Kurz and Kloker (2016) in the numerical investigations of a flat-plate boundary layer at $M < 1$. Furthermore, the shape of the roughness itself greatly influences the stability properties of the roughness wake. In the numerical investigations on a flat plate at $M = 6$ conducted by Van den Eynde and Sandham (2016), it was shown that the aft section of the roughness influences the properties of the roughness recirculation zone, greatly affecting the amplification of disturbances in the roughness wake. In the numerical investigations conducted by Groskopf and Kloker (2016) for a supersonic ($M = 4.8$) flat-plate boundary layer in the presence of elongated roughness elements, a larger disturbance amplification was found for roughnesses with a skew angle to the flow direction compared to roughnesses with a symmetric profile. These results show that the critical value of Re_{kk} for transition is affected by the shape of the roughness. Therefore, a direct comparison between the observed critical values of Re_{kk} for different roughness geometries is not always possible.

Additional roughness parameters, such as spatial distribution and spatial gradients of the roughness elements, should be taken into account in the formulation of improved transition-prediction methods beyond the Re_{kk}-based criteria. In the case of a non-effective roughness, a systematic investigation of different geometries is needed to identify those parameters that can influence the growth of unstable modes in the roughness wake. Within the context of modal growth as predicted by Linear Stability Theory, numerical investigations are needed to quantify the dependence of the total disturbance amplification on different roughness features in terms of N-factors. The role of non-parallel effects, originating in the rapid streamwise variation of the flow topology in the roughness wake, is also of significant importance.

1.5 Influence of high-temperature gas effects on the stability of hypersonic boundary layers

At hypersonic speeds, the temperature strongly increases downstream of the bow shock ahead of the blunt body. For moderate temperature and pressure (e.g.,

$T < 800$ K at 1 atm), air can be considered as a calorically and thermally perfect gas (in the research community called "ideal gas" for brevity), with constant specific heat capacities. As the temperature starts to increase, the vibrational energy of the molecules is excited and variable specific heats must be considered in the gas modeling. When the temperature exceeds 2500 K, molecular oxygen begins to dissociate at considerable levels, while at about 4000 K dissociation of molecular nitrogen takes place. At temperatures as large as 9000 K significant ionization is present.

Depending on the altitude and the velocity of the vehicle, the air in the post-shock flow ahead of the blunt body undergoes different chemical and thermal processes due to varying temperature and pressure. In particular, at moderate altitudes and velocities for a hypersonic vehicle, the reacting air is in chemical equilibrium. In chemical equilibrium, reactions take place at a much faster rate than any local change of the flow and the gas properties immediately adapt to any temperature changes. The Damköhler number is a dimensionless quantity defined as the ratio between the convection timescale of the flow τ_f and the timescale of the chemical reactions τ_c,

$$Da = \frac{\tau_f}{\tau_c}, \tag{1.3}$$

and quantifies the degree of non-equilibrium in the flow. For a gas in chemical equilibrium, it holds $Da \to \infty$. When the velocity and the altitude of the vehicle increase and, consequently, the temperature increases and the pressure decreases, the timescale of the chemical dissociation and the convection timescale are of the same order of magnitude and the effects of finite-rate chemistry need to be accounted for (chemical non-equilibrium). In the limit $Da \to 0$, the flow is said to be in frozen conditions. At higher altitudes and velocities, the convection timescale can become even smaller than the timescale of the changes in vibrational energy τ_v (thermal non-equilibrium) and the relaxation process of translational, rotational and vibrational energy must be taken into account.

For reentry altitudes where transition is expected, high-temperature gas effects are non-negligible (Malik and Anderson, 1991). However, experiments on ground facilities matching all relevant dimensionless parameters, including the Damköhler number, cannot be realized and stability analyses of flows at high-altitude reentry conditions have been performed mainly based on numerical simulations.

Molecular dissociation and non-equilibrium can have counteracting effects on the stability of the boundary layer. On the one hand, a gas with low dissociation energy, such as O_2 in air, exhibits a higher absorption of energy fluctuations compared to a gas with higher dissociation energy, such as N_2, and can thus diminish the disturbance amplification rates (Germain and Hornung, 1997; Johnson et al., 1998). On the other hand, chemical reactions alter velocity and temperature profiles of the boundary layer and, compared to the case of ideal gas, can lead to a destabilization of the base flow.

First stability investigations, including high-temperature gas effects, were performed by means of LST for the flat-plate boundary layer. Malik and Anderson (1991) studied the modal instability mechanisms of a two-dimensional boundary layer at $M = 10$ and $M = 15$ under the assumption of reacting flow in equilibrium. Compared to the case of ideal gas, the incorporation of chemical dissociation stabilizes the first-mode instability, whereas it destabilizes the second-mode instability. In this regard, chemical reactions have broadly similar effects as cooling at the wall in supersonic boundary layers. Stuckert and Reed (1994) extended the LST analysis by including the effects of chemical non-equilibrium, while Hudson et al. (1996) also included both chemical and thermal non-equilibrium effects. Compared to the case of equilibrium gas, chemical non-equilibrium destabilized the second mode, whereas thermal non-equilibrium was slightly stabilizing. With regard to the first mode, chemical equilibrium was the most unstable among the reacting-gas cases. The trends found in the LST analyses were later confirmed by PSE-based analyses by Chang et al. (1997) and Johnson and Candler (1999), who included chemistry and non-equilibrium in the Parabolized Stability Equations. DNS were undertaken by Marxen et al. (2014) to investigate both linear and non-linear instability mechanisms in a finite-rate chemically reacting boundary layer at $M = 10$. It was observed that finite-rate reactions increase the instability of the linear modes, while not directly affecting the growth-rate of secondary instabilities. Stemmer et al. (2017a,b) used DNS to investigate the development of unsteady linear disturbances in the wake of a cuboid roughness element in the three-dimensional reacting boundary layer of the HyBoLT geometry ($M = 8.5$). The same symmetric and antisymmetric modes were found in the wake of the cuboid as in the case of isolated roughness elements in cold-flow boundary layers (see, e.g., De Tullio et al., 2013). A larger disturbance amplification rate was observed in the case of chemical non-equilibrium compared to chemical equilibrium.

In the case of a two-dimensional Apollo-capsule configuration with a smooth wall, the influence of high-temperature gas effects on the profiles of the laminar boundary layer under reentry conditions was analyzed by Stemmer and Fehn (2014). It was found that the inclusion of chemical dissociation in the gas modeling significantly reduces the boundary-layer edge velocity and increases the boundary-layer thickness compared to the case of simulations conducted under the assumption of ideal gas. The velocity profiles of the boundary layer were not significantly affected by the inclusion of chemical or thermal non-equilibrium. Instead, non-equilibrium had a notable effect on the temperature profiles. In particular, the inclusion of thermal non-equilibrium resulted in an increase in the temperature gradient at the wall compared to the case of chemical non-equilibrium only. These results were confirmed by the steady numerical simulations performed by Di Giovanni and Stemmer (2017) for a three-dimensional Apollo-capsule geometry with an angle of attack at identical freestream conditions. In addition to the case of a smooth-wall geometry, the case of a capsule wall equipped with a patch of randomly distributed roughness was

considered. Several regions of high streamwise vorticity developed and interacted downstream of the different protuberances in the roughness patch. As a result, high and low-speed streaks formed in the streamwise direction. Since the boundary-layer thickness was much thinner in the case of ideal gas than in the case of reacting gases, the steady disturbance induced by the roughness was the largest for the ideal gas. Among the reacting gases, chemical equilibrium generated the largest steady disturbance in the roughness wake, followed by the case of gas in chemical non-equilibrium and, finally, by the gas in both thermal and chemical non-equilibrium.

Experimentally, the reacting high-enthalpy flow on an Apollo-capsule model of 178 mm diameter was investigated by Marineau et al. (2010) at the T5 Hypersonic Shock Tunnel at GALCIT. Natural transition was observed on the model with a smooth wall for $Re_\infty = 0.9 \cdot 10^6$ m^{-1} and a stagnation enthalpy of 10 MJ/kg. Further experiments on an Apollo-capsule model of 150 mm diameter were undertaken at the free-piston shock tunnel HIEST (Tanno et al., 2010, 2014) for Mach numbers in the range of $6 - 8$ and unit Reynolds numbers between 10^5 and $5 \cdot 10^6$ m^{-1}. At these conditions, no hint of transition was found for the smooth geometry. However, a heat-flux augmentation at the stagnation point was measured in the experiments at high-enthalpy conditions. The origin of this increased heat flux, also observed in other facilities (see, e.g., Olejniczak et al., 2005), remained unclear and remarks the difficulty of realizing accurate and reliable ground experiments at relevant high-enthalpy conditions.

1.6 Investigations at the Hypersonic Ludwieg Tube in Braunschweig

The recent experimental campaign conducted at the Hypersonic Ludwieg Tube in Braunschweig (HLB) represents a reference for the numerical investigations of the present work. At the HLB, extensive experimental investigations have been conducted for an Apollo-capsule model with a diameter of 170 mm and an angle of attack of 24°. A Mach number of 5.9 and unit Reynolds numbers in the range of $Re_\infty = 6 - 20 \cdot 10^6$ m^{-1} were considered. As documented in Ali et al. (2014) and Theiss et al. (2014), an infrared thermography coating with a root-mean-square roughness of $\bar{k} = 10$ μm was applied to the capsule model in order to monitor laminar-turbulent transition heating. For a unit Reynolds number of $Re_\infty = 18 \cdot 10^6$ m^{-1}, an increase in the surface heating compared to the laminar case was observed. Experiments for a highly polished surface ($\bar{k} = 0.5$ μm) at the same unit Reynolds number did not show any evidence of transition. The absence of modal instability mechanisms on the boundary layer of the capsule model was confirmed by numerical simulations and linear stability analyses for the equivalent smooth-wall capsule geometry (Theiss et al., 2014). In particular, it was shown that

the capsule boundary layer remains stable against first-mode and crossflow instabilities even at values of the Reynolds number significantly higher (one or more orders of magnitude) than the ones that could be realized in the experiments.

Further numerical analyses on the HLB capsule were conducted by Theiss et al. (2016, 2017), who investigated the instability mechanisms of the steady wake developing downstream of various isolated roughness elements on the windward side of the capsule. Roughness Reynolds numbers in the range of $124-336$ were considered. Stability analyses based on two-dimensional Linear Stability Theory (LST-2D) and three-dimensional Parabolized Stability Equations (PSE-3D) revealed the presence of two main unstable modes in the wake of the isolated roughness elements. These unstable modes had the same symmetric and antisymmetric character as the modes already known in the case of isolated roughness elements on a flat plate (Choudhari et al., 2010). The symmetric mode provided the largest overall disturbance amplification in all considered cases with N-factors up to 8, although for $Re_{kk} = 336$ the antisymmetric mode was amplified over a longer downstream extent in the wake of the roughness.

The presence of transitional flow on the HLB capsule was further addressed in Hein et al. (2019) on the base of optimal transient-growth theory. It was shown that the amplification predicted by optimal transient-growth theory on the capsule geometry with low values of the surface roughness ($Re_{kk} \leq 25$) is too small to explain experimentally observed transition. In recent experiments at the HLB, Radespiel et al. (2019) showed that transition data for the capsule model with an increased roughness height ($Re_{kk} > 150$) well correlates with estimations based on the transient-growth theory proposed by Reshotko and Tumin (2004). However, for roughness elements of the considered height, modal growth in the roughness wake was expected to be the dominant instability mechanism (Theiss et al., 2016). Therefore, further numerical studies for the rough-wall capsule model at increased roughness heights should be conducted to understand the effects of distributed roughnesses on the mean flow as well as on the induced (non-)modal disturbance growth.

1.7 Objectives

In the present work, Direct Numerical Simulations are undertaken to investigate the stability properties of the boundary layer on a capsule-like forebody with a rough wall. Roughness Reynolds numbers up to 421 are considered, with roughness heights smaller than 0.35 boundary-layer thicknesses. For these parameters, the roughness is non-effective and immediate transition to turbulence can be excluded. Instead, steady longitudinal vortices develop in the roughness wake. The growth of various unstable modes in the roughness wake is expected in the presence of incoming disturbances within a certain range of frequencies. The effects of the roughness on the boundary layer are analyzed and quantified in terms of the distortion of the

steady base flow and the evolution of unsteady disturbances forced in the roughness wake. Both the linear and non-linear evolution of the disturbances, including laminar-turbulent transition, are considered.

Two different scenarios are investigated. In the first part of the thesis, freestream conditions are chosen to match the cold wind-tunnel conditions of the HLB at $M = 5.9$ and $Re_\infty = 18 \cdot 10^6$ m^{-1}. The base flow is computed for a capsule-like hemispherical geometry with a radius of $R = 203$ mm, corresponding to the base flow obtained on the symmetry plane of the Apollo-capsule model with an angle of attack used in the HLB experiments. The main objectives of the analysis are summarized as follows.

- As a starting point, the numerical approach used to simulate the base flow is validated with experimental results obtained for a capsule model with a smooth wall. Beside the validation against the experiments at the HLB, a further validation is achieved with the experimental data obtained at the JAXA's shock tunnel HIEST (Tanno et al., 2010). In comparison to the HLB, HIEST operates at higher freestream temperatures and, thus, chemical dissociation and non-equilibrium effects are included in the corresponding simulations.

- Steady simulations are performed for the capsule boundary layer in the presence of a patch of randomly distributed roughness. The influence of the roughness patch on the steady base flow is analyzed and compared to the case of a periodic roughness element.

- Unsteady pressure disturbances are forced in the domain upstream of the roughness patch. The interaction of the disturbances with the roughness patch and the development of the disturbances in the roughness wake are studied by means of Direct Numerical Simulations in order to reveal the modes of instability induced by the roughness. In the non-linear range of disturbance growth, the mechanisms leading to laminar-turbulent transition are analyzed. A parameter study is also conducted for different roughness heights.

In the second part of the work, the investigations are extended to the case of a reentry scenario at $M = 20$ at an altitude of about 57.7 km. The capsule geometry corresponds to the one used for the investigations under wind-tunnel conditions, scaled by a factor of about 30 in order to match the size of a realistic reentry capsule (e.g., CEV). At the considered conditions, the temperature downstream of the bow shock ahead of the capsule reaches up to 6000 K and the flow is characterized by chemical reactions and non-equilibrium effects. In order to highlight the different high-temperature gas effects, simulations are performed with three different gas models. Starting with the model of equilibrium air, chemical non-equilibrium and thermal non-equilibrium are gradually included in the simulations. The main objectives in the case of reentry conditions are summarized as follows.

- The effects of both chemical and thermal non-equilibrium on the steady base flow are analyzed. Emphasis is given to the influence of the gas modeling on the roughness parameters, such as the ratio of roughness-height to boundary-layer thickness and the roughness Reynolds number. The different effects of the high temperatures on the topology of the flow are analyzed for both the smooth-wall capsule and the rough-wall capsule.

- The effects of the gas modeling on the growth of linear disturbances forced in the wake of the roughness are evaluated. The growth rates of different unstable modes are analyzed in a range of relevant frequencies.

- The effects of non-equilibrium on the growth of unsteady disturbances in the non-linear range are investigated in a scenario of roughness-induced laminar-turbulent transition. The analysis is aimed at quantifying the influence of high-temperature gas effects both on the transition location, identified by a sudden augmentation of the heat transfer at the wall, and on the level of wall heating in the transitional boundary layer.

In the third part of the thesis, the instability mechanisms on the capsule-like hemisphere under HLB conditions are investigated for a patch of squared, micron-sized roughness elements. This roughness patch features the pattern of surface roughness used in recent experiments at the HLB by Radespiel et al. (2019). The results shown here are part of a joint investigation on hypersonic roughness-induced transition conducted by several international institutes within the task group NATO STO AVT-240. Within the framework of the present thesis, DNS are undertaken with the following objectives.

- The flow on the HLB capsule is compared to the flow on a hemispherical geometry. The hemispherical geometry is used as an approximation of the capsule geometry with an angle of attack. Both the case of a smooth wall and a rough wall are considered.

- Unsteady simulations are performed to detect potential modal and non-modal instability mechanisms in the wake of the roughness patch.

The results of DNS are discussed and compared with the results based on optimal transient-growth theory obtained by the partner institutes in the attempt to find an explanation for the laminar-turbulent transition observed in the corresponding experiments.

1. Introduction

2 Numerical Approach

The following chapter provides a brief overview of the governing equations and the numerical method used to simulate the capsule boundary layer both on a smooth wall and in the presence of a rough wall. The validation of the proposed numerical approach in the case of the smooth-wall geometry is achieved based on experimental data from two different wind tunnels (i.e., HLB, Theiss et al., 2014, and HIEST, Tanno et al., 2010) and is discussed in Di Giovanni and Stemmer (2017). Details on the accuracy of the numerical approach for the rough-wall simulations can be found in Di Giovanni and Stemmer (2018), see also in Appendix B.1.

2.1 Gas modeling and governing equations

For the simulations conducted under the cold-flow wind-tunnel conditions of the HLB, the temperature downstream of the bow shock does not exceed 500 K. Hence, the model of a calorically and thermally perfect gas, with constant specific heat capacities, can be used. Instead, for the computations under reentry conditions, the temperature downstream of the bow shock reaches up to 6000 K and chemical reactions must be included in the simulations. Furthermore, for the reentry conditions considered here, the combination of low density and high speed results in convection timescales of the same order as the timescales of chemical and energy-transfer processes, i.e. the hypotheses of thermal and chemical equilibrium do not hold any longer. Ionization phenomena can be neglected.

In the case of reacting gas, a Park's two-temperature model for air consisting of five species (O_2, N_2, O, N, NO) is applied (Park, 1989). The concentration of the species s is defined as $c_s = \rho_s/\rho$, where ρ_s is the partial density of the single species s. For the densities and temperatures found in hypersonic flows, the intermolecular forces can be neglected and each gas present in the mixture can be treated as a perfect gas. Assuming that the ideal-gas equation holds for each gas component, the equation of state of the gas mixture is given by

$$p = \rho R_\circ T \sum_s \frac{c_s}{M_s}, \qquad (2.1)$$

where p and ρ are the pressure and density of the gas mixture, T the equilibrium temperature, $R_\circ$ the universal gas constant and M_s the molar mass of the species s.

In a mixture, the internal energy is a function of the concentration of the single species, $e = \sum c_s e_s$, with e_s being the internal energy relative to each chemical species. The internal energy of each species is in turn obtained as a sum of different energy contributions,

$$e_s = e_s^{\text{tr}} + e_s^{\text{rot}} + e_s^{\text{vib}} + h_s^0, \tag{2.2}$$

where the various forms of energy summed up in the previous equation are, in order, the translational, the rotational, the vibrational and the zero-point energy per unit mass of the species s and are all known functions of the temperature.

Contrary to the non-reacting case, Equation (2.1) does not close the Navier-Stokes equations. In the case of air in chemical equilibrium (CEQ), three algebraic equations are solved for the dissociation of molecular species (law of mass action) and two algebraic equations are solved for the conservation of the elements O and N. In the case of air in chemical non-equilibrium (CNEQ), a continuity equation should be solved for each one of the five species to determine the values of the species concentrations,

$$\rho \frac{\mathrm{D}c_s}{\mathrm{D}t} + \nabla \cdot (\rho_s \mathbf{u}_s^D) = \dot{\omega}_s, \tag{2.3}$$

where $\dot{\omega}_s$ are the chemical production terms, which depend on an Arrhenius-type relation. The diffusion velocity $\mathbf{u}_s^D$ is described by Fick's law under the assumption of a constant Schmidt number with the diffusion coefficients independent of the species concentration. For a gas in thermochemical non-equilibrium (CTNEQ), both the hypotheses of chemical and thermal equilibrium do not hold and an additional equation for the vibrational energy e^{vib} must be included for each molecular species m,

$$\frac{D}{Dt}(c_m e_m^{\text{vib}}) + \frac{1}{\rho}\nabla \cdot (\rho_m \mathbf{u}_m^D e_m^{\text{vib}}) = -q_m^{\text{vib}} + Q_m^{\text{t-v}} + Q_m^{\text{chem}}, \tag{2.4}$$

where q_m^{vib} describes the heat-conduction term, $Q_m^{\text{t-v}}$ the translational-vibrational energy transfer rate and Q_m^{chem} the source term due to reactions of the species m. Once e_m^{vib} is solved from the system in Eq. (2.4), three vibrational temperatures T_m^{vib} can be derived for the three molecular species, assuming

$$e_m^{\text{vib}} = \frac{\Theta_m}{e^{\Theta_m/T_m^{\text{vib}}} - 1}\frac{R_\circ}{M_m}, \tag{2.5}$$

where Θ_m is a constant depending on the molecular species m. Further details on the governing equations for viscous high-temperature flows can be found in Anderson Jr. (2006).

In the present study, the species' viscosities are calculated according to Blottner et al. (1971), the species' thermal conductivities are calculated according to Hirschfelder et al. (1964) and the properties of the gas mixture are computed with

16

Case	M	p_∞ [Pa]	T_∞ [K]	T_w [K]	Re_∞ [m^{-1}]	R [m]
HLB	5.9	1377	59	295	$18 \cdot 10^6$	0.203
Reentry	20	29.9	253.3	1800	$1.97 \cdot 10^6$	5.98

Table 2.1: Freestream conditions and parameters for the present simulations.

Wilke's mixing rules (Wilke, 1950). For further details on the governing equations and on the modeling of the physical and thermal coefficients as applied in this work, see Stemmer et al. (2017b) and Di Giovanni and Stemmer (2019b).

2.2 Geometrical set-up

The considered geometry is a capsule-like hemispherical forebody. The radius R of the hemisphere depends on the analyzed scenario and its value is shown in Table 2.1 together with the conditions of the freestream flow (M, p_∞, T_∞ and Re_∞) and the capsule-wall temperature (T_w) for both the wind-tunnel case and the reentry case.

Since unsteady three-dimensional DNS of the entire hemisphere with a rough wall would be extremely expensive in terms of computational costs, simulations are sequentially performed on two different geometries, zooming in on the roughness position. First, a full two-dimensional hemispherical smooth-wall domain is considered. Second, the results on the full domain are used to generate the boundary conditions for a restricted three-dimensional domain with a highly resolved rough wall.

The full domain consists of a spherical segment with an angular extension of 90.8° (Figure 2.1). The domain ends in a shoulder which resembles the one of a generic Apollo capsule. The shoulder provides a strong natural damping region due to the strong acceleration of the flow and, therefore, the computational domain can be truncated after the shoulder without influencing the boundary layer upstream of the shoulder on the spherical part of the domain. The angular extension of the domain and the shape of the shoulder are chosen to generate a flow that approximates the one on a blunt-capsule geometry. In particular, in the case of simulations under HLB conditions, the radius of the hemisphere is equal to 203 mm and the flow on the hemisphere well represents the flow on the Apollo-capsule model with an angle of attack used in the HLB experiments, as shown by the author in Hein et al. (2019). Compared to the three-dimensional capsule model with an angle of attack, the hemisphere geometry is azimuthal periodic and allows for a substantial reduction of the computational domain. In the case of simulations under reentry conditions, the radius of the hemisphere is equal to 5.98 m, providing a size similar to the one of a realistic capsule geometry, such as the CEV.
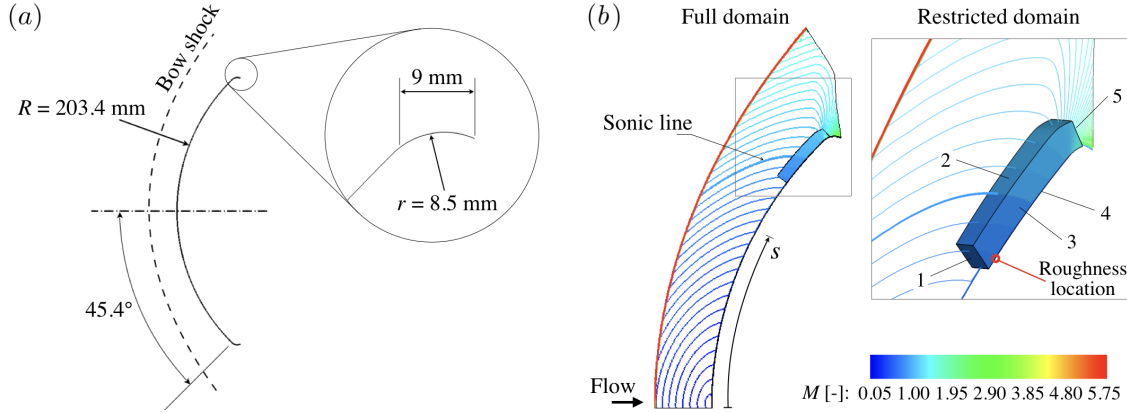
Figure 2.1: (*a*) Scheme of the investigated hemisphere geometry and (*b*) full and restricted domains with Mach number color coded for the case of HLB conditions (from Di Giovanni and Stemmer, 2018).

The grid of the full domain consists of about 80,000 points clustered at the shock location and inside the boundary layer. The grid has the same resolution properties as the grids already used and tested in previous works (Di Giovanni and Stemmer, 2017). The shock is represented through a shock-fitting procedure, accounting for the change in the shock stand-off distance according to freestream conditions and gas model. Non-reflective characteristic boundary conditions are used for freestream and far-field boundaries. The wall is modeled as non-catalytic and isothermal with a constant temperature of 295 K in the case of HLB conditions and 1800 K in the case of reentry conditions, as estimated from available flight data (see, e.g., Park, 2004).

The results on the full two-dimensional domain are used to generate the inflow conditions for a restricted three-dimensional domain, as shown in Figure 2.1*b* for the case of simulations at wind-tunnel conditions. The wall of the restricted domain (face 4 in Figure 2.1*b*) is equipped with a roughness patch that destabilizes the boundary layer. The restricted domain is located in the region of the sonic line and close to the shoulder of the capsule, where the local values of the Reynolds number are large enough for the roughness wake to exhibit modal instabilities for roughness heights significantly smaller than the boundary-layer thickness. Conditions at the inflow boundaries (faces 1 and 2) are derived from the two-dimensional domain, azimuthal periodicity of the domain is imposed in spanwise direction (faces 3) and Riemann invariants are used at the outflow (face 5). The bow shock is excluded from the computations of the rough wall and a higher grid resolution compared to the full domain is used to resolve the boundary layer at the roughness location and in the roughness wake. A total number of grid points between 35 million and 100 million is used depending on the considered roughness geometry and flow conditions.

In the streamwise direction, the concentration of grid points is high at the roughness location and reduces as the outflow boundary is reached. In the wall-normal direction, a large number of points (~ 120) are used to resolve the boundary layer. In the spanwise direction the grid points are equally spaced. The smallest wavelength present in the roughness geometry is resolved with at least 80 points in the spanwise direction. Downstream of the roughness, the grid properties are carefully chosen to fully resolve the wavelength of the high-frequency disturbances considered in the analysis as well as the vortical structures developing in the nonlinear range of disturbance growth until the point of laminar-turbulent breakdown.

The solutions in the full domain and in the restricted domain have been carefully analyzed to check the absence of potential errors rising because of the different computational schemes and grid resolutions used in the two different domains. The boundary-layer profiles on the full and restricted domains have been compared for the smooth-wall configuration at different positions. No appreciable differences are present between the results for the two domains. Therefore, a negligible error is made when passing from the full domain to the restricted domain. The accuracy of the steady simulations as well as the absence of numerically produced unsteady disturbances are further guaranteed by achieving very good convergence of the residuals.

Particular attention has been paid to ensuring that the presence of the roughness patch does not induce disturbances outside the boundary layer, influencing the results through interaction with the upper boundary or the inflow boundary of the integration domain. In particular, the height of the domain has been chosen to guarantee that any potential residual reflection at the upper boundary exits in the domain at the outflow boundary without impinging on the boundary layer, and therefore without affecting the stability properties of the roughness wake. Note that the Mach number rapidly increases in the streamwise direction and any disturbance induced by the roughness in the inviscid flow is very small and is highly deflected in the flow direction. Details on the grid resolution as well as several grid-convergence studies for the different scenarios analyzed in this work are documented in Di Giovanni and Stemmer (2018, 2019b).

To investigate various potential instability mechanisms induced by the rough wall, different roughness geometries are considered. The main focus is on the instability mechanisms induced by a patch of randomly distributed roughness, which is obtained by superposing different sinusoidal waves with (pseudo-)random amplitudes and phases. The computational grid close to the patch of randomly distributed roughness is shown in Figure 2.2 for the case of wind-tunnel conditions. The coordinates x, y and z represent the streamwise, wall-normal and spanwise coordinates, respectively. Details on the shape and on the parameters defining the different roughness geometries analyzed here can be found in the corresponding works (Di Giovanni and Stemmer, 2018, 2019b,a; Hein et al., 2019), see also Appendix B.

For every roughness geometry, the height of the largest protuberance in the patch

is referred to as the height of the roughness patch. Roughness heights up to 0.1 mm are considered for the simulations under wind-tunnel conditions, corresponding to roughness Reynolds numbers up to 421. In the reentry case, the roughness height is set to $k = 4.6$ mm and corresponds to about one fifth of the thickness of the reacting boundary layer. Roughness Reynolds numbers in the range of $221 - 244$ are obtained depending on the gas model.
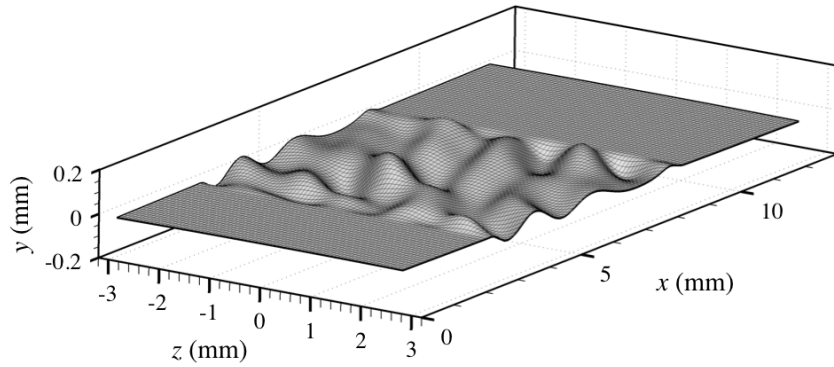

Figure 2.2: Computational grid close to the patch of randomly distributed roughness in the case of HLB conditions (from Di Giovanni and Stemmer, 2018).

The roughness wake is characterized by regions of local streamwise-vorticity maxima. These streamwise vortices are unstable to various modes, potentially interacting with each other. Therefore, in order to comprehensively evaluate the stability properties of the entire roughness wake, the entire spanwise extent of the domain downstream of the roughness is analyzed by means of Direct Numerical Simulations.

Unstable modes in the roughness wake are excited by forcing unsteady disturbances within a certain range of relevant frequencies at the inflow boundary. In the case of wind-tunnel conditions, the values of the investigated disturbance frequencies fall into the range of relevant frequencies measured in the experiments with transitional flow conducted at HLB for the rough-wall capsule geometry (Theiss et al., 2014). In the case of reentry conditions, the experimental values have been scaled with boundary-layer thicknesses and velocities for the corresponding simulations.

Since the boundary layer of the smooth-wall configuration is stable against modal growth, the profiles of the unsteady disturbances cannot be deduced by Linear Stability Theory. Therefore, only the pressure is perturbed at the inflow boundary, while velocity, temperature and density disturbances are induced by the pressure fluctuations within the first few cells downstream of the inflow boundary. In all cases, the amplitude of the pressure disturbances at the inflow is very small compared to the boundary-layer values and linear growth of unstable modes is expected in the

near field downstream of the roughness patch. To allow the transient effects to vanish, simulations are performed over a long time interval, corresponding to many periods of the forced disturbance with the lowest frequency. The convergence of the spectrum has been verified in the simulation domain in the regions of linear and, when applicable, nonlinear growth, including the region of laminar-turbulent breakdown. Since the main focus of the investigation is the (non-)linear growth of instabilities and the onset of laminar breakdown to turbulence, the pseudoturbulent flow is not analyzed quantitatively and has to be considered as not fully resolved. Details on the frequencies and amplitudes of the forced disturbances in the various investigations are provided in the corresponding works (Di Giovanni and Stemmer, 2018, 2019b,a; Hein et al., 2019).

2.3 Flow solver and numerical schemes

Parallel Direct Numerical Simulations are performed with the Navier Stokes Multi Block (NSMB) solver (Vos et al., 1999; Hoarau et al., 2016). NSMB is a semi-commercial, finite-volume code for parallel computations based on a message-passing interface (MPI) environment. In the field of hypersonic flows, NSMB has been validated and successfully applied in numerous works (Goebel et al., 2012; Stemmer and Fehn, 2014; Stemmer et al., 2017a; Di Giovanni and Stemmer, 2017; Hein et al., 2019; Di Giovanni and Stemmer, 2018).

A variety of numerical schemes can be used. In the presence of a bow shock in the computational domain, steady simulations are performed starting with an advection upstream splitting method (AUSM+) upwind scheme of first-order accuracy and an implicit Euler time integration based on a Symmetric Successive Over Relaxation (SSOR). Once the shock has been established, better accuracy of the solution is reached by continuing the computation with a central discretization scheme of second-order accuracy and an explicit five-stage Runge-Kutta time-integration scheme. The shock is captured with a shock fitting mesh and explicit second- and fourth-order artificial-dissipation terms are locally added to the numerical scheme to suppress spurious oscillations. In the computational domain without bow shock, a fourth-order central scheme is used for the spatial discretization and a Runge-Kutta fourth-order method is used for the time integration for both steady and unsteady simulations.

3 Summary of Publications

This chapter summarizes the main contributions of this thesis. A detailed description of the results can be found in selected publications in Appendix B.

3.1 Roughness-induced crossflow-type transition at Mach 5.9

A. Di Giovanni and C. Stemmer (2018)
Cross-flow-type breakdown induced by distributed roughness in the boundary layer of a hypersonic capsule configuration
Journal of Fluid Mechanics, 856:470−503.

Summary
As discussed in Section 1.4, the topology of the flow in the roughness wake significantly depends not only on the roughness height but also on the shape and spatial distribution of the roughness itself. Accordingly, different transition mechanisms are expected. In the literature, several numerical studies have been conducted for blunt geometries with isolated roughness elements (Chang et al., 2011; Theiss et al., 2016; Hein et al., 2019). However, for reentry capsules with an ablative TPS, distributed roughness is likely to be the normality rather than the exception.

This work presents an in-depth description of the instabilities induced by both a singular and a distributed roughness in the boundary layer of a capsule-like hemispherical forebody. Direct Numerical Simulations are conducted for the cold-flow wind-tunnel conditions of the HLB at $M = 5.9$. Two different types of roughness are considered: a spanwise periodic roughness element and a patch of randomly distributed roughness. For both geometries, the maximum roughness height is $k = 0.1$ mm, corresponding to 0.35 boundary-layer thicknesses. Unsteady disturbances are forced at the inflow boundary and their evolution in the roughness wake is analyzed by means of Fast Fourier Transform. Results from DNS are validated with those from PSE-3D and excellent agreement is achieved.

A pair of counter-rotating vortices form downstream of the spanwise periodic roughness element. The two main unstable modes in the roughness wake exhibit a symmetric and antisymmetric character. For the unsteady disturbance forced at the inflow, the boundary layer remains laminar. In the case of randomly distributed roughness, different roughness protuberances are present in the roughness patch. The only appreciable disturbance amplification is found in the wake of the highest protuberance of the patch ($Re_{kk} = 406$). Here, the skewness of the roughness introduces a spanwise component of the velocity that is not present in the base flow on the smooth wall. The roughness-induced spanwise velocity gives birth to a new crossflow-type vortex for the blunt-capsule configuration. This crossflow-type vortex greatly amplifies the forced unsteady disturbances and turns out to be more persistent than the counter-rotating vortices generated by the spanwise periodic roughness element, in spite of similar values of Re_{kk} and k/δ. Accordingly,

a larger amplification is found for the same inflow disturbance and boundary-layer transition is observed. A parameter study conducted for different roughness heights reveals that for $k/\delta \leq 0.263$ and $Re_{kk} \leq 261$ the roughness is too small to generate a crossflow-type vortex and the disturbance amplification is limited to the region close to the roughness.

This work shows the necessity to account for the roughness shape in the formulation of improved transition-prediction methods beyond the Re_{kk}-based criteria. It is shown that roughness shapes with a skew profile can induce crossflow-type vortices in the absence of a spanwise velocity in the base flow. The breakdown of these crossflow-type vortices provides a new possible explanation of laminar-turbulent transition on the capsule configuration with distributed roughness in the absence of modal instabilities and insufficient transient-growth rates.

Individual contributions of the candidate

My main contribution to this work was the development of a realistic distributed roughness geometry for the capsule configuration and the in-depth investigation of the roughness-induced crossflow-type vortices. I conducted the numerical simulations including grid generation, performed the analysis of the simulation data and wrote the paper.

3.2 Roughness-induced crossflow-type instabilities at Mach 20

Summary
Free-flight experiments at relevant altitudes and speeds are extremely expensive. On the other hand, wind-tunnel experiments at realistic reentry conditions matching all relevant dimensionless parameters, including the Damköhler number, cannot be realized. Therefore, numerical simulations represent an important and often indispensable investigation tool used in the extrapolation of the results of roughness-induced transition from wind-tunnel to reentry conditions.

In this work, Direct Numerical Simulations are performed to study the stability properties of the wake of a patch of randomly distributed roughness in the boundary layer of a capsule-like hemisphere in a realistic high-altitude reentry scenario at $M = 20$. The considered geometry corresponds to the one used in Di Giovanni and Stemmer (2018) for the investigations under wind-tunnel conditions and is rescaled by a factor of about 30 in order to obtain the size of a realistic reentry capsule. Different high-temperature gas effects have been investigated by gradually including chemical non-equilibrium and thermal non-equilibrium in the simulations of the chemically reacting boundary layer. The maximum height of the roughness patch is set to 4.6 mm, corresponding to a roughness Reynolds number in the range of $221 - 244$ depending on the gas model.

As already observed in Di Giovanni and Stemmer (2018), vortical structures resembling crossflow-type vortices originate at the roughness peaks with a skew profile relative to the streamwise flow. The linear growth of unsteady disturbances in the roughness wake is investigated by introducing pressure disturbances in a range of relevant frequencies downstream of the roughness. Among the several unstable regions identified in the roughness wake, the main crossflow-type vortex originating at the highest peak of the roughness patch presents the largest overall disturbance amplification for all gas models and at all considered frequencies. Two different instability modes are found for the crossflow-type vortex. These modes are of z- and y-type, as already known from crossflow vortices in three-dimensional subsonic boundary layers (see Malik et al., 1999). The gas in chemical non-equilibrium presents the largest amplification, whereas thermochemical non-equilibrium slightly destabilizes the roughness wake compared to the equilibrium case.

The crossflow-type vortex induced by distributed roughness provides a possible explanation for laminar-turbulent transition of the capsule boundary layer at altitudes where high-temperature gas effects are non-negligible. This work shows that non-equilibrium effects can significantly stabilize or destabilize the roughness wake depending on the features of the roughness itself, such as shape and height. For sufficiently high roughness protuberances, chemical non-equilibrium is found to be destabilizing at all considered frequencies. These results highlight the importance of including non-equilibrium effects in the stability analysis of high-enthalpy boundary layers on rough walls and the consideration of the skewness of the roughness in detail.

Individual contributions of the candidate

As the main contribution to the present work, I defined both the roughness and the simulation parameters and highlighted the presence of the two roughness-induced crossflow-vortex instabilities for the capsule geometry. I conducted the numerical simulations including grid generation, post-processed the simulation data and wrote the paper.

Roughness-Induced Boundary-Layer Transition on a Hypersonic Capsule-Like Forebody Including Nonequilibrium

Summary

In this work, the analysis conducted in Di Giovanni and Stemmer (2019b) for the case of linear instabilities is extended to the case of laminar-turbulent transition. In order to trigger transition, the amplitude of the forced inflow disturbances is chosen such that linear growth is expected close to the inflow boundary downstream of the roughness, whereas large non-linear disturbances are found further downstream, eventually leading to laminar-turbulent breakdown.

The roughness-induced transition in these simulations is qualitatively similar to the transition observed in the simulations at wind-tunnel conditions in Di Giovanni and Stemmer (2018), with the laminar-turbulent breakdown caused by the amplification of unstable modes developing in the crossflow-type vortex in the roughness wake. However, it is found that roughness elements with the same ratio roughness-height to boundary-layer thickness exhibit larger values of Re_{kk} in the case of reentry conditions than in cold wind-tunnel conditions, leading to more persistent and, thus, potentially more unstable roughness wakes.

In the case of unsteady simulations, the onset of higher modes, which originate through non-linear interaction of the disturbed modes, is identified by a first significant increase of the heat flux at the wall in the unsteady flow compared to the steady laminar flow. The onset of higher modes is first reached by the gas in chemical non-equilibrium, which produced the largest roughness Reynolds number. Analogously, the transition onset location is identified by a second noticeable increase of the wall heat flux. Laminar-turbulent breakdown is first reached by the gas in chemical equilibrium, followed by the gas in thermochemical non-equilibrium and, finally, by the gas in chemical non-equilibrium. Thermal non-equilibrium lowers the level of wall heat flux of the transitional flow.

For the first time, the non-linear instability mechanisms up to laminar-turbulent breakdown in a roughness-induced crossflow-type vortex have been numerically studied in the case of a high-enthalpy capsule boundary layer including non-equilibrium. This work suggests that the inclusion of high-temperature gas effects has a substantial influence on the development of roughness-induced instabilities in both the linear and non-linear range. Both chemical and thermal non-equilibrium turn out to be important in order to correctly predict the location and the values of heat augmentation induced by the laminar-turbulent breakdown.

Individual contributions of the candidate

I tuned the simulation parameters based on the analysis previously conducted in Di

Giovanni and Stemmer (2019b) in order to trigger the laminar-turbulent breakdown. I conducted the numerical simulations, post-processed the simulation data and wrote the paper.

3.3 Spherical capsule with micron-sized roughness

S. Hein, A. Theiss, A. Di Giovanni, C. Stemmer, T. Schilden, W. Schröder, P. Paredes, M. M. Choudhari, F. Li and E. Reshotko (2019)

Summary
In this paper, different roughness-induced mechanisms have been numerically investigated in order to assess the role of roughness in the laminar-turbulent transition for the capsule model used in the HLB (see also Section 1.6). To study roughness-induced instabilities on the capsule boundary layer, a specifically designed roughness patch with squared micron-sized roughness elements was applied on the capsule model used in the HLB experiments (Radespiel et al., 2019). The height of the roughness elements was 20 μm and was comparable to the roughness height of the thermography coating used in the previous experiments (Theiss et al., 2014). Contrary to the rough wall in the case of a thermography coating, the patch of micron-sized elements is well-defined and, hence, easily reproducible in numerical studies.

Within the framework of the present thesis, Direct Numerical Simulations have been performed for the patch of micron-sized roughness elements used at the HLB. The contribution to the presented investigations is twofold. First, the flow on a hemispherical geometry is compared to the flow on the Apollo-capsule model with an angle of attack used in the HLB experiments. The case of the steady flow on a smooth-wall geometry is presented in Section III.D, whereas Section V.D.1 presents the case of the steady flow in the presence of a patch of squared micron-sized roughness elements with values of Re_{kk} up to 25. Second, Direct Numerical Simulations are undertaken to detect potential modal and non-modal instability mechanisms in the roughness wake. The results of the DNS-based stability analysis are presented in Section V.D.2.

Numerical data for the Apollo-capsule geometry with a smooth wall are retrieved from previous computations (Di Giovanni and Stemmer, 2017), whereas numerical data for the Apollo-capsule geometry with the roughness patch are provided by the project partners of RWTH Aachen University. For both the smooth and the rough-wall geometry, the flow on the hemisphere well approximates the flow on the capsule with an angle of attack in the vicinity of the symmetry plane. A good match of velocity and temperature profiles is observed. Since azimuthal-periodic boundary conditions can be used in spanwise direction for the hemispherical geometry, the

domain can be limited in spanwise direction to one single roughness periodicity. Therefore, a significant reduction of the domain size and of the computational cost is achieved in the case of the hemisphere compared to the capsule geometry with an angle of attack. Next, unsteady pressure disturbances with frequencies in the range of $167-333$ kHz are introduced at the inflow boundary of the hemispherical geometry. This frequency range is chosen based on experimental data for transitional flow obtained in the HLB (Radespiel et al., 2019). It is shown that the roughness elements are too small to interact with the incoming unsteady disturbances and neither modal nor non-modal amplification of the disturbances is revealed by DNS.

This work shows that the boundary-layer transition observed in the HLB experiments cannot be explained by either transient growth nor modal instability mechanisms in the wake of the squared micron-sized roughness elements. A plausible explanation for the observed transition onset on the capsule model with micron-sized roughness remains to be found.

Individual contributions of the candidate
My contributions to the present work are found in Sections III.D, V.D.1 and V.D.2. I developed the idea of approximating the three-dimensional Apollo capsule with an angle of attack through a hemispherical geometry and validated the approximation. I conducted the Direct Numerical Simulations for the hemispherical geometry with and without roughness, post-processed the simulation data and wrote Sections III.D, V.D.1 and V.D.2.

4 Discussion and Conclusions

Laminar-turbulent transition on blunt capsules is observed in experiments at both free-flight and wind-tunnel conditions, although the accelerated boundary layer of the blunt body with a smooth wall is stable against known instability mechanisms. In this context, the present work aims to assess the role of different types of roughness in the amplification of unsteady disturbances in the capsule boundary layer. Direct Numerical Simulations have been performed to simulate the flow on a capsule-like hemispherical geometry in the presence of a roughness patch. The roughness height is smaller than the boundary-layer thickness and similar to the height of roughnesses that can be found on the Thermal Protection System of reentry capsules due to both manufacturing uncertainties and laminar ablation. Roughness Reynolds numbers up to 421 have been considered. These roughnesses are non-effective and immediate transition to turbulence at the roughness location can be excluded. Instead, longitudinal vortices develop in the roughness wake. These longitudinal vortices are potentially unstable and the growth of instability modes in the presence of incoming disturbances can be observed.

In the first part of this work, Direct Numerical Simulations of roughness-induced transition of the capsule boundary layer have been conducted under the assumption of ideal gas for the wind-tunnel conditions at the HLB ($M = 5.9$). In the literature, numerical investigations of roughness-induced transition have been conducted on flat-plate and blunt-body configurations mainly for the case of isolated roughness elements (Van den Eynde and Sandham, 2016; Groskopf and Kloker, 2016, see also Section 1.4). With regard to surfaces with distributed roughness, few numerical investigations have been performed for the flat-plate geometry. Drews et al. (2011) investigated the case of a Blasius incompressible boundary layer altered by randomly distributed roughness. Depending on the shape of the protuberances in the roughness patch and their alignment with the freestream, both counter-rotating vortex pairs and single vortex cores were generated. Distributed, sinusoidal roughness elements on a flat plate were numerically investigated by Muppidi and Mahesh (2012) for a supersonic boundary layer ($M = 2.9$). It was observed that the roughness surface provides an upward impulse to the near-wall fluid, resulting in paired streamwise vortices in the roughness wake. As evidenced by these studies, the topology of the

flow on a rough surface can significantly differ depending not only on the roughness height but also on the shape and spatial distribution of the roughness itself. Hence, investigations of different roughness distributions and geometries are necessary for a deep understanding of the different roughness-induced transition mechanisms.

Given the lack of numerical studies on blunt geometries with distributed roughness, a first set of simulations has been conducted in Section 3.1 (see Di Giovanni and Stemmer, 2018) with the aim to compare the instability mechanisms induced by both a singular and a distributed roughness on a capsule-like configuration. It was shown that, in the presence of a patch of randomly distributed roughness, certain roughness protuberances with a skew profile with respect to the flow direction can induce crossflow-type vortices similar to the ones known from three-dimensional subsonic boundary layers. In three-dimensional boundary layers, crossflow vortices are the result of an instability mechanism induced by the presence of a spanwise velocity component in the base flow. Instead, in the case analyzed here, the roughness acts as a local source of spanwise velocity. The downstream evolution of the roughness-induced crossflow-type vortices shows minimal decay, but the vortex strength is still large to exhibit instability towards artificial disturbances. The properties of the wake of the distributed roughness have been compared to the properties of the wake of a spanwise periodic (symmetric) roughness element. As one of the main observations in this study, the roughness-induced crossflow-type vortex turned out to be more persistent than the counter-rotating vortex pair developing in the wake of the spanwise periodic roughness element, in spite of similar values of roughness height and roughness Reynolds number. Accordingly, the disturbances forced at the inflow boundary of the domain undergo a larger overall amplification in the wake of the distributed roughness than in the case of the spanwise periodic roughness element. This result suggests that the consideration of the roughness shape is a key issue in the prediction of roughness-induced transition on capsule boundary layers, where a significant decay of both steady and unsteady disturbances can be observed due to the presence of a strong favorable pressure gradient. The breakdown of roughness-induced crossflow-type vortices presented in this study provides a new possible explanation of laminar-turbulent transition on the capsule geometry with a rough wall in the absence of modal instabilities and insufficient transient-growth rates.

In the second part of this work, the investigations on the roughness-induced crossflow-type instabilities presented in Di Giovanni and Stemmer (2018) have been extended to the case of a high-altitude reentry scenario at $M = 20$. For these flight conditions transition is expected and chemical reactions and non-equilibrium effects are non-negligible. As discussed in Section 1.5, numerous numerical investigations have been performed to analyze the influence of high-temperature gas effects on the modal instability mechanisms present on hypersonic flat plates with a smooth surface (Malik and Anderson, 1991; Hudson et al., 1996) as well as on cone configurations

(Johnson et al., 1998; Malik, 2003; Johnson and Candler, 2005; Mortensen and Zhong, 2016). In the case of an Apollo-capsule geometry under reentry conditions ($M = 20$), the influence of gas modeling on the boundary-layer profiles on both a smooth and a rough wall have been studied in Stemmer and Fehn (2014) and Di Giovanni and Stemmer (2017). These studies evidenced that the inclusion of chemistry and non-equilibrium into the computations of hypersonic boundary layers can significantly change velocity and temperature profiles of the base flow. As a result, the presence of high-temperature gas effects can considerably affect the transition location and the peak values of the heating overshoot at transition.

In the extrapolation of the results of roughness-induced transition from wind-tunnel to reentry conditions, it is important to quantify the effects of chemistry and non-equilibrium both on the steady base flow and on the development of unsteady disturbances growing in the roughness wake. In this context, in Section 3.2 (see also Di Giovanni and Stemmer, 2019a,b) the effects of both chemical and thermal non-equilibrium on the stability of the capsule boundary layer with a rough wall have been investigated. In Di Giovanni and Stemmer (2019b), only linear modes developing in the roughness wake are considered. In Di Giovanni and Stemmer (2019a), the analysis includes the non-linear growth of disturbances in the roughness wake up to laminar-turbulent breakdown. Direct Numerical Simulations have been performed on the base of an enlarged hemispherical geometry with the size of a realistic reentry capsule. Different high-temperature gas effects have been highlighted by gradually including chemical and thermal non-equilibrium in the simulations. Roughness Reynolds numbers spanned in the range of $221 - 244$ depending on the gas models, with roughness heights of about one fifth of the boundary-layer thickness. In the case of unsteady disturbances with an amplitude in the linear range, two main modes of instability have been found in the considered frequency range, featuring the y- and z-modes already known from the case of crossflow vortices in three-dimensional subsonic boundary layers. It was found that chemical non-equilibrium significantly destabilizes both the y- and z-modes at all considered frequencies. In particular, the largest linear disturbance amplification was observed in the case of gas in chemical non-equilibrium. Accordingly, in the non-linear range, the onset of higher modes, identified by a first significant increase of the heat-transfer rate at the wall, is first reached by the gas in chemical non-equilibrium. The results of the stability investigations on the present reentry configuration are in accordance with the finding that the roughness Reynolds number for chemical non-equilibrium becomes larger than the one in case of equilibrium for sufficiently high roughness elements. In particular, the stabilizing or destabilizing effect of non-equilibrium on the roughness wake significantly depends on the features of the roughness, such as shape and height. Moreover, it was observed that thermal non-equilibrium lowers the level of wall heat flux of the transitional flow. In this regard, both chemical and thermal non-equilibrium turn out to be important in the prediction of the location and of the peak values of the wall-heating increase induced by the laminar-turbulent

breakdown.

Finally, in Section 3.3, the instability mechanisms on the capsule-like hemisphere under HLB conditions have been investigated for a patch of squared, micron-sized roughness elements. These investigations aimed to find a possible explanation for the transitional flow observed in the HLB experiments for a capsule model with a low surface roughness (Ali et al., 2014; Theiss et al., 2014; Radespiel et al., 2019, see also Section 1.6). In order to assess the role of roughness in the laminar-turbulent transition for the capsule model used in the HLB, different roughness-induced mechanisms have been numerically investigated. The results of these numerical analyses are presented in Hein et al. (2019).

Transient growth has been proposed as a possible mechanism for disturbance growth in the presence of small roughnesses in those cases where modal disturbance amplification is weak (Reshotko and Tumin, 2004). In the investigations presented in Hein et al. (2019), optimal transient-growth theory was used in the numerical investigations performed by the German Aerospace Center (DLR). The transient-growth results obtained for the HLB capsule were compared with the data obtained by transient-growth analysis for the model of the Orion CEV geometry studied in the Mach 6 ACE wind tunnel at the Texas A&M University (TAMU) (see also Paredes et al., 2018). In both cases of HLB and TAMU conditions, the magnitude of transient growth was rather small. For the HLB conditions, N-factors less than 3 were obtained.

Within the framework of the present thesis, the contribution to the work reported in Hein et al. (2019) is summarized in Section 3.3. Unsteady disturbances in a broad range of frequencies have been introduced upstream of the roughness patch by means of Direct Numerical Simulations. It has been found that the roughness elements are too small to interact with the incoming unsteady disturbances. Neither modal nor non-modal instabilities could be detected. A plausible explanation for the observed transition onset on the capsule model with micron-sized roughness remains to be found.

The numerical investigations in this thesis provide insight into new potential instabilities of the boundary layer of blunt capsules with a rough wall. In particular, this study remarks the importance of including non-equilibrium effects in the stability analysis of high-enthalpy boundary layers in the presence of roughness and the consideration of the shape of the roughness in detail. For the first time, roughness-induced crossflow-type instabilities in both the linear and the non-linear range, up to laminar-turbulent transition, have been numerically studied in the case of a high-enthalpy boundary layer including non-equilibrium. The presence of roughness-induced crossflow-type vortices on reentry capsules provides a possible explanation for laminar-turbulent transition of the capsule boundary layer at altitudes where chemical reactions and non-equilibrium effects are important. The present in-

depth analyses of the observed roughness-induced instabilities provide a foundation for future studies with the aim of developing improved, physics-based methods for the prediction of roughness-induced transition on blunt capsules at altitudes where high-temperature gas effects cannot be neglected.

4. Discussion and Conclusions

A   List of Publications

A.1   Peer-reviewed publications

- **Di Giovanni, A.**, and Stemmer, C. (2019). Roughness-Induced Boundary-Layer Transition on a Hypersonic Capsule-Like Forebody Including Nonequilibrium. *Journal of Spacecraft and Rockets*, 56(6):1795−1808.
  doi:10.2514/1.A34488.

- **Di Giovanni, A.**, and Stemmer, C. (2019). Roughness-Induced Crossflow-Type Instabilities in a Hypersonic Capsule Boundary Layer Including Nonequilibrium. *Journal of Spacecraft and Rockets*, 56(5):1409−1423.
  doi:10.2514/1.A34404.

- Hein, S., Theiss, A., **Di Giovanni, A.**, Stemmer, C., Schilden, T., Schröder, W., Paredes, P., Choudhari, M. M., Li, F., and Reshotko, E. (2019). Numerical Investigation of Roughness Effects on Transition on Spherical Capsules. *Journal of Spacecraft and Rockets*, 56(2):388−404. doi:10.2514/1.A34247.

- **Di Giovanni, A.**, and Stemmer, C. (2018). Cross-flow-type breakdown induced by distributed roughness in the boundary layer of a hypersonic capsule configuration. *Journal of Fluid Mechanics*, 856:470−503.
  doi:10.1017/jfm.2018.706.

- **Di Giovanni, A.**, and Stemmer, C. (2017). Numerical Simulations of the High-Enthalpy Boundary Layer on a Generic Capsule Geometry with Roughness. In *New Results in Numerical and Experimental Fluid Mechanics XI, Contributions to the 20th STAB/DGLR Symposium*, pages 189−198. Dillmann, A. et al. (eds). Springer, Cham. doi:10.1007/978-3-319-64519-3_17.

A.2 Conferences

- **Di Giovanni, A**., and Stemmer, C. (2018). Direct Numerical Simulations of roughness-induced transition in the boundary layer of a hypersonic spherical forebody under consideration of high-temperature gas effects. *AIAA-Paper 2018-4046*, 2018 AIAA Fluid Dynamics Conference, Atlanta, Georgia, USA. doi:10.2514/6.2018-4046.

- Hein, S., Theiss, A., **Di Giovanni, A.**, Stemmer, C., Schilden, T., Schröder, W., Paredes, P., Choudhari, M., Li, F., and Reshotko, E. (2018). Numerical Investigation of Roughness Effects on Transition on Spherical Capsules. *AIAA-Paper 2018-0058*, 2018 AIAA Aerospace Sciences Meeting, Kissimmee, Florida, USA. doi:10.2514/6.2018-0058.

- Stemmer, C., and **Di Giovanni, A.** (2018). Roughness-induced instabilities leading to transition in a capsule boundary-layer under re-entry conditions. HISST (International Conference on High-Speed Vehicle Science Technology), Moscow, Russia.

- Theiss, A., Hein, S., **Di Giovanni, A.**, and Stemmer, C. (2018). Optimal transient growth behind distributed roughness elements on a spherical re-entry capsule. 7th European Conference on Computational Fluid Dynamics, Glasgow, Schottland.

- **Di Giovanni, A.**, and Stemmer, C. (2016). Boundary-layer stability of a generic reentry capsule. 11th EFCM (European Fluid Mechanics Conference), Sevilla, Spain.

- **Di Giovanni, A.**, and Stemmer, C. (2016). Boundary-layer stability of a generic reentry capsule with real-gas effects. 24th ICTAM (International Congress of Theoretical and Applied Mechanics), Montreal, Quebec, Canada.

- **Di Giovanni, A.**, and Stemmer, C. (2015). High-temperature gas effects on the high-enthalpy flow on the wind-ward side boundary-layer of a generic capsule geometry. 8th ESA Symposium on Aerothermodynamics for Space Vehicles, Lisbon, Portugal.

B   Selected Publications

B.1 Cross-flow-type breakdown induced by distributed roughness in the boundary layer of a hypersonic capsule configuration

This Agreement between Lehrstuhl fuer Aerodynamik und Stroemungsmechanik Technische Universitaet Muenchen -- Antonio DiGiovanni ("You") and Cambridge University Press ("Cambridge University Press") consists of your license details and the terms and conditions provided by Cambridge University Press and Copyright Clearance Center.

License Number	4612410558666
License date	Jun 19, 2019
Licensed Content Publisher	Cambridge University Press
Licensed Content Publication	The Journal of Fluid Mechanics
Licensed Content Title	Cross-flow-type breakdown induced by distributed roughness in the boundary layer of a hypersonic capsule configuration
Licensed Content Author	Antonio Di Giovanni, Christian Stemmer
Licensed Content Date	Oct 5, 2018
Licensed Content Volume	856
Licensed Content Issue	undefined
Start page	470
End page	503
Type of Use	Dissertation/Thesis
Requestor type	Author
Portion	Full article
Author of this Cambridge University Press article	Yes
Author / editor of the new work	Yes
Order reference number	
Territory for reuse	World
Title of your thesis / dissertation	Roughness-Induced Transition in a Hypersonic Capsule Boundary Layer under Wind-Tunnel and Reentry Conditions
Expected completion date	Jul 2019
Estimated size(pages)	130
Requestor Location	Lehrstuhl fuer Aerodynamik und Stroemungsmechanik Technische Universitaet Muenchen Lehrstuhl fuer Aerodynamik und Stroemungsmechanik Boltzmannstrasse 15 Technische Universitaet Muenchen Garching B. Munich, other 85748 Germany Attn: Lehrstuhl fuer Aerodynamik und Stroemungsmechanik Technische Universitaet Muenchen
Publisher Tax ID	GB823847609
Total	0.00 EUR
Terms and Conditions	

TERMS & CONDITIONS

Cambridge University Press grants the Licensee permission on a non-exclusive non-transferable basis to reproduce, make available or otherwise use the Licensed content 'Content' in the named territory 'Territory' for the purpose listed 'the Use' on Page 1 of this Agreement subject to the following terms and conditions.

1. The License is limited to the permission granted and the Content detailed herein and does not extend to any other permission or content.
2. Cambridge gives no warranty or indemnity in respect of any third-party copyright material included in the Content, for which the Licensee should seek separate permission clearance.
3. The integrity of the Content must be ensured.
4. The License does extend to any edition published specifically for the use of handicapped or reading-impaired individuals.
5. The Licensee shall provide a prominent acknowledgement in the following format: author/s, title of article, name of journal, volume number, issue number, page references, , reproduced with permission.

Other terms and conditions:
v1.0

Questions? customercare@copyright.com or +1-855-239-3415 (toll free in the US) or +1-978-646-2777.

Cross-flow-type breakdown induced by distributed roughness in the boundary layer of a hypersonic capsule configuration

Antonio Di Giovanni[1] and Christian Stemmer[1],†

[1]Chair for Aerodynamics and Fluid Mechanics, Boltzmannstr. 15, Technical University of Munich, 85748 Garching, Germany

Direct numerical simulations are undertaken to investigate the nature of instability mechanisms induced by singular and distributed roughnesses on a blunt-capsule configuration. On the base of a capsule-like hemispherical forebody at wind-tunnel conditions ($M = 5.9$), we analyse the development of unsteady disturbances behind a patch of two different roughness geometries. First, spanwise periodic roughness elements are considered and cross-validation with other methods of the stability analysis is achieved. Two main unstable modes are found in the roughness wake, corresponding to the symmetric and antisymmetric modes already known for single roughness elements. Second, the case of a patch of (pseudo-)randomly distributed roughness is presented. A new type of roughness-induced cross-flow-like instability is observed for the blunt-capsule configuration. The rapid growth of primary and secondary instabilities in the cross-flow-type vortex is analysed and quantified in both the linear and nonlinear stages up to the laminar–turbulent breakdown. Spatio-temporal Fourier analysis is performed to track the onset of secondary instabilities, whereas laminar–turbulent transition is identified by the steep increase of the wall heat flux.

Key words: boundary layer stability, high-speed flow, transition to turbulence

1. Introduction

Laminar–turbulent boundary-layer transition on blunt bodies is a critical issue in the design of hypersonic vehicles such as re-entry capsules. For fully turbulent boundary layers, the heat-transfer rate at the wall is significantly higher than in the laminar case. Uncertainties in transition prediction result in additional weight of the thermal protection system (TPS) and manufacturing costs aimed at guaranteeing the integrity of the vehicle. However, despite long-running investigations, transition on re-entry capsules still the defies full understanding. Already in the 1950s, experiments showed that early transition occurred on many spherical geometries, contrary to what was predicted by classical stability theory (Morkovin 1984). In fact, the strongly favourable pressure gradient and the small values of the cross-flow velocity component typical of blunt bodies ensure that the boundary layer on smooth walls remains stable against

† Email address for correspondence: christian.stemmer@aer.mw.tum.de

both Tollmien–Schlichting (TS) waves and cross-flow instabilities even at very large Reynolds numbers. Furthermore, the presence of Görtler-type instabilities is prevented by the convex surface curvature. Transient growth has been suggested as a possible transition mechanism for blunt-body geometries by Reshotko & Tumin (2000, 2004) and the topic is still the subject of ongoing research (Paredes, Choudhari & Li 2017; Hein *et al.* 2018; Leidy *et al.* 2018). However, Hein *et al.* (2018) showed that the N-factors obtained through optimal transient-growth analysis on a blunt-capsule geometry are too small ($N \leqslant 3$) to explain experimentally observed transition. In this context, wall roughness seems to be the most likely factor to influence blunt-body transition.

In the case of re-entry capsules, roughnesses are present on the thermal protection system as both localised non-uniformities and distributed roughness. Isolated roughness elements comprehend TPS joints, compression pads and gaps between heat-shield tiles, while the presence of distributed roughness is mainly associated with the ablation of the TPS. For laminar ablation, the roughness height is usually of the order of the boundary-layer thickness or smaller and larger roughness elements can apparently be generated only after transition occurs (Grabow & White 1974). Even though to date there is no general mechanism-based criterion to predict roughness-induced transition, the ratio of roughness height to boundary-layer thickness k/δ and the roughness Reynolds number $Re_{kk} = \rho_k u_k k / \mu_k$, defined with the flow properties at the roughness height for the corresponding smooth configuration, are regarded as the relevant parameters. A detailed review of experimental data on the effects of the roughness height and Reynolds numbers on transition location is presented by Schneider (2008*a*).

Initially, due to the complexity of the problem and to the lack of advanced computing resources, the phenomenon of roughness-induced transition on blunt bodies was studied experimentally. A review of available experimental data on the effects of roughness on hypersonic blunt-body transition is provided by Schneider (2008*b*).

The possible correlation between Re_{kk} and transition on blunt geometries was investigated, among others, by Reda (2002). His analysis showed that three-dimensional, distributed roughness patterns promote earlier transition compared to single roughness elements with the same height and shape. In particular, in the case of distributed roughness elements, the critical Re_{kk} can be 4–10 times smaller than the critical value of the corresponding case of isolated elements. Further analyses for blunt-body geometries with distributed sand-grain roughness were conducted by Reda *et al.* (2008). The critical value for transition of Re_{kk}, built with the arithmetic average of the measured roughness heights and fluid viscosity at the wall temperature, was found to be $250 \pm 20\%$ in those investigations. Additional tests on blunt-body geometries were performed in a CO_2 and an air-dominated atmosphere by Wilder, Reda & Prabhu (2015). The critical value for transition was $Re_{kk,tr} = 259$ for tests conducted in air and $Re_{kk,tr} = 223$ for tests conducted in CO_2, with an uncertainty of 25 %.

Experimental measurements made at NASA Langley Research Center (LaRC) on scaled models of the Crew Exploration Vehicle (CEV) for Mach 6 and 10 are presented by Berger (2009). Laminar–turbulent transition was obtained with boundary-layer trips of 0.3–0.8 boundary-layer thicknesses in height. Further results from an experimental campaign conducted at LaRC for sphere–cone and hemisphere geometries with distributed roughness are summarised in Hollis (2014). Sand-grain-type roughnesses as well as patterned roughnesses were considered. The

free-stream Reynolds number was in the range of $Re_\infty = 9.84$–27.23×10^6 m^{-1} and the roughness Reynolds number Re_{k+} was defined with the friction velocity, $Re_{k+} = \rho_w u_\tau k / \mu_w$. Transitional flow was found for $\sim 10 < Re_{k+} < \sim 70$.

On the base of a blunt Apollo-like capsule at $M = 5.9$, numerical and experimental investigations have been conducted for wind-tunnel conditions at the Hypersonic Ludwieg Tube in Braunschweig (HLB) (Ali, Radespiel & Theiss 2014; Theiss *et al.* 2014; Radespiel *et al.* 2018). Using a standard infrared coating with a root-mean-square roughness of $\bar{k} \approx 10$ µm, a surface-heating increase compared to the laminar case was observed for $Re_\infty \approx 18 \times 10^6$ m^{-1}. Experiments at the same Reynolds number for the highly polished surface did not show any evidence of transition. Numerical simulations and linear stability analyses for the equivalent smooth geometry revealed that the boundary layer is stable against TS-waves and cross-flow instabilities even at values of the Reynolds number much higher than the ones that could be investigated experimentally.

Numerically, the problem of roughness-induced transition has been investigated mainly for the case of isolated roughness elements, both at flat-plate and blunt configurations, whereas simulations of distributed roughnesses have mainly been performed on the basis of flat-plate geometries only. By means of direct numerical simulations (DNS), BiGlobal stability analysis and three-dimensional parallelised stability equations (PSE-3D), De Tullio *et al.* (2013) investigated the transition mechanisms behind a quadrilateral isolated roughness element on a flat plate at $M = 2.5$. For $Re_{kk} = 170$ and $k/\delta = 0.22$, no acceleration of the laminar–turbulent transition process was observed. On the contrary, for $Re_{kk} = 791$ and $k/\delta = 0.44$ the roughness wake became very unstable. The two most dominant unstable modes have a symmetric (varicose) and an antisymmetric (sinuous) character, with the symmetric mode growing faster than the antisymmetric one. In the numerical investigations of Van den Eynde & Sandham (2016), a variety of roughness shapes have been investigated on a flat plate at $M = 6$. The results highlighted that the growth of instabilities in the wake of the isolated roughness elements strongly depends on the shape of the roughness. In particular, an important factor is represented by the aft section of the roughness element and, hence, by the properties of the recirculation zone. The author suggested that the roughness profile is an important characteristic currently neglected in the commonly used engineering correlations. Further investigations on the influence of the roughness shape on the transition mechanisms have been presented by Groskopf & Kloker (2016), who performed DNS to analyse the nonlinear disturbance evolution in a laminar, supersonic ($M = 4.8$) flat-plate boundary layer in the presence of a skewed roughness element. Similar dominant unstable modes were found as in the case of symmetric elements, with the shape of sinuous and varicose modes being tilted.

In the case of re-entry capsule geometries, Chang *et al.* (2011) performed numerical simulations on a CEV geometry at $M = 6$ with both isolated surface protuberances and cavities. They showed that a protuberance with a $Re_{kk} = 800$ and $k/\delta = 0.73$ produces a strong wake instability and spontaneous vortex shedding and the flow is more unstable than in the case of a cavity of identical geometry. For the case of a generic three-dimensional (3-D) Apollo-capsule geometry with an angle of attack, Theiss *et al.* (2016, 2017) investigated the modal instability mechanisms of the steady wake developing downstream of isolated roughness elements positioned on the windward side of the capsule. Computation of the laminar, steady base flow was conducted at the $M = 5.9$ free-stream conditions of the HLB and values of Re_{kk} in the range of 124–336 were considered. Stability analyses were conducted with the

help of two-dimensional linear stability theory (LST-2D) and PSE-3D. It was found that the most unstable modes have the same symmetric and antisymmetric features as the modes found in the wake of isolated roughness elements in the case of the flat plate. An *N*-factor of almost 8 was found for the case of symmetric mode for a cylindrical roughness element with $Re_{kk} = 336$.

With regard to surfaces with distributed roughness, some numerical investigations have been performed in the case of a flat plate. Brehm *et al.* (2011) analysed the effects of two-dimensional, sinusoidal and rectangular roughness elements on the stability of the incompressible boundary layer. They found that the growth of small disturbances is larger for sinusoidal roughness elements than for rectangular ones. It was suggested that the increased amplification might be related to the extended region of separated flow induced by the sinusoidal shape. Furthermore, the effects of pressure gradient on the disturbance growth in the case of a rough wall seems to be less pronounced than in the case of a smooth wall. The three-dimensional case of distributed, sinusoidal roughness elements on a flat plate was numerically investigated by Muppidi & Mahesh (2012) for a supersonic boundary layer ($M = 2.9$). In this case, paired streamwise vortices resulted from an upward impulse provided by the roughness surface to the near-wall fluid.

Steady numerical simulations of the Blasius incompressible boundary layer altered by randomly distributed roughness were conducted by Drews *et al.* (2011). In this case, the main vorticity cores in the roughness wake are associated with the highest peaks of the roughness patch. Both counter-rotating vortex pairs and single vortex cores are generated according to the shape of the roughness and its alignment with the free stream. The steady base flow in the wake of the roughness patch was compared with the corresponding experimental results (Downs, White & Denissen 2008). Steady numerical simulations were undertaken by Di Giovanni & Stemmer (2017) to investigate the boundary layer of a 3-D capsule geometry with a patch of randomly distributed roughness under re-entry conditions ($M = 20$). The analysis mainly focused on the development and interaction of the steady high-vorticity regions in the roughness wake and on the influence of chemical reactions and non-equilibrium effects.

In this work we study the instability modes, in both the linear and nonlinear stages until laminar breakdown, developing in the boundary layer of a hemisphere geometry with a rough wall. The growth of unsteady disturbances forced in the inflow is analysed and quantified with DNS. Two different roughness geometries are considered: an array of spanwise periodic roughness elements and a more realistic random distributed roughness. Here, the term random is used to indicate the superposition of different sinusoidal waves with pseudo-random amplitudes and phases. In the present work, the prefix 'pseudo-' will be omitted for brevity for the remaining part of the paper. Free-stream conditions have been chosen to match the wind-tunnel conditions at HLB at $M = 5.9$.

In §2 the considered geometries as well as the numerical set-up are presented. The methods of the analysis are illustrated in §2.5. In §3 the flow in the case of spanwise periodic roughness elements is studied. Features of the base flow and stability properties of the main instability modes in the wake of the roughness are presented and compared. Results from linear stability analysis and from PSE analysis are also shown for cross-validation. In §4 the flow in the presence of randomly distributed roughness is investigated. The development of disturbance modes is described and quantified in the linear and nonlinear stages of the transition process. A discussion of the comparison between the two roughness geometries is also included. Summary and conclusions are presented in §5.

2. Configurations and numerical set-up

2.1. *DNS-solver*

Parallel DNS are conducted with the semi-commercial solver Navier–Stokes Multi Block (NSMB). The NSMB code is documented in Vos, Duquesne & Lee (1999) and Hoarau *et al.* (2016) and it has been successfully applied in numerous studies of hypersonic flows (von Kaenel *et al.* 2009; Goebel, Vos & Mundt 2012; Stemmer & Fehn 2014; Di Giovanni & Stemmer 2017; Stemmer, Birrer & Adams 2017*a*,*b*; Hein *et al.* 2018). The code is finite-volume based and it works with structured grids divided in multiple blocks using the message-passing interface (MPI) environment.

A variety of numerical schemes can be used. In the presence of a bow shock in the computational domain, steady simulations are performed starting with an advection upstream splitting method (AUSM+) upwind scheme of first-order accuracy and an implicit Euler time integration based on a lower–upper symmetric Gauss–Seidel method. Once the shock has been established, better accuracy of the solution is reached by continuing the computation with a central discretisation scheme of second-order accuracy and an explicit five-stage Runge–Kutta time-integration scheme. The shock is captured with a shock fitting mesh and explicit second- and fourth-order artificial-dissipation terms are locally added to the numerical scheme to suppress spurious oscillations. In the computational domain without bow shock, DNS are performed with a more accurate central discretisation scheme of fourth-order accuracy and a five-stage Runge–Kutta time-integration scheme.

2.2. *Computational domain and boundary conditions*

Details of geometry and size of the hemisphere are given in figure 1. The hemisphere has an angular extension of approximately 90° and it ends in a shoulder closely resembling that of a generic Apollo capsule geometry. The shoulder acts as a natural damping region through the strong flow acceleration and prevents undesired reflection of unsteady disturbances at the numerical outflow boundary.

The flow over the considered hemisphere geometry has already been shown to be almost identical to the flow over the Apollo capsule model at an angle of attack of 24° used in the experiments at HLB (Hein *et al.* 2018). In comparison to the capsule geometry with an angle of attack, the hemisphere geometry allows for a significant reduction of the computational domain and effort due to azimuthal periodicity of the domain. In the experiments at HLB, a Plexiglas capsule model with a Nextel Velvet coating was used for optical measurements of the surface temperature. The coating was sanded to provide a distributed roughness with a root-mean-square value of $\bar{k} = 10$ μm. As the simulation of the entire rough-wall capsule would have been extremely expensive, only a small roughness patch on the hemisphere's wall is considered in the present work. Besides, as the boundary layer observed in the experiments at HLB was never fully turbulent for the investigated roughness, a larger roughness height corresponding to a mean roughness of $\bar{k} \approx 22$ μm is used in the present numerical simulations (for more details of the roughness geometry see § 2.3).

To ease the computational effort in the case of unsteady simulations on the rough-wall configuration, a two-stage simulation is performed on two different simulation domains, as shown in figure 1. In the first simulation step, the flow over the entire hemisphere (full domain) is considered. This domain extends from the stagnation point to the shoulder and includes the bow shock ahead of the blunt body. The steady base flow is computed on a smooth-wall, two-dimensional, axisymmetric grid consisting of approximately 76 000 points clustered around the
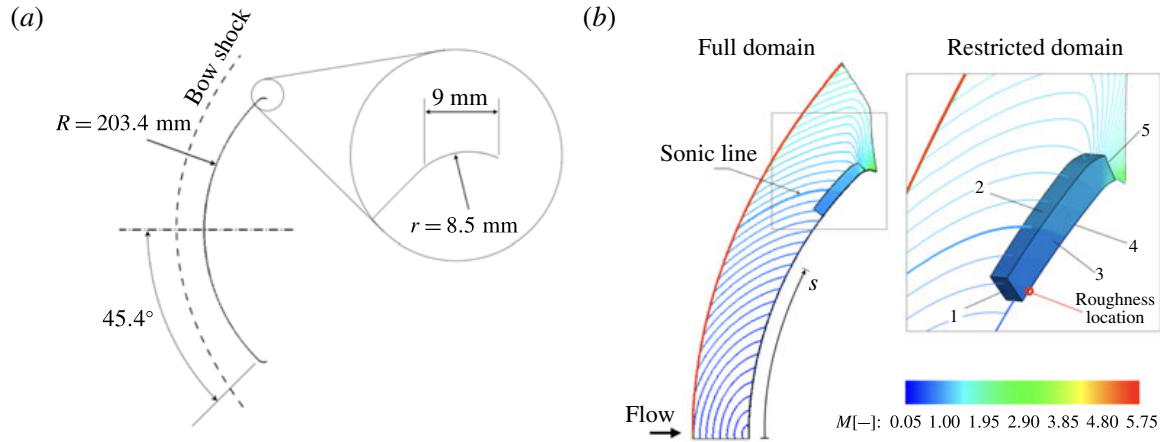
FIGURE 1. (*a*) Scheme of the investigated hemisphere geometry. (*b*) Full and restricted domains with the Mach number colour coded.
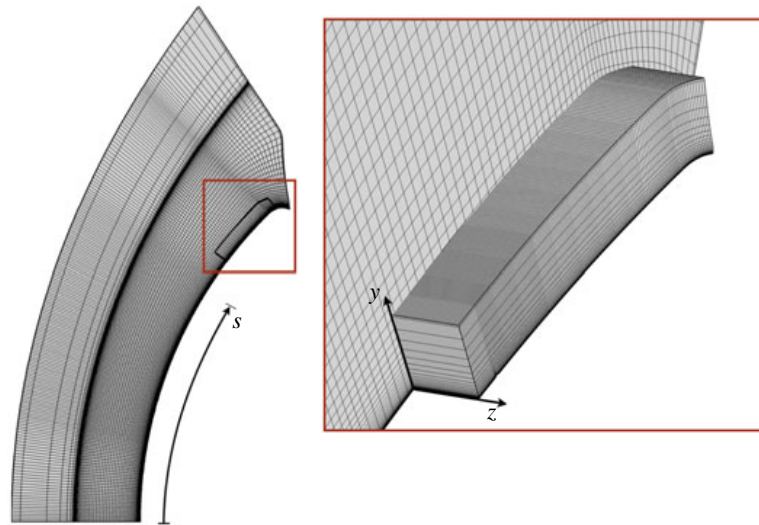

FIGURE 2. Computational grid of the full domain (every second point shown) and close-up of the computational grid of the restricted domain (every sixth point shown).

shock location and inside the boundary layer (figure 2). Previous simulations with the same grid resolution have been successfully compared with experimental results as well as with results from other numerical simulations including a grid study (Stemmer & Fehn 2014; Di Giovanni & Stemmer 2017). For free-stream and far-field boundaries, characteristic variables are used. The wall is modelled as isothermal with a constant temperature of $T_w = 295$ K, as measured in the corresponding experiments. Free-stream conditions match the wind-tunnel conditions at HLB and are listed in table 1. In particular, with a free-stream temperature of 59 K, the air temperature after the bow shock does not exceed 500 K and the model of a calorically and thermally perfect gas can be applied in the simulations.

The results for the full domain are used to generate the boundary conditions for a second restricted domain. Since the shock is excluded from the restricted domain, a fourth-order central discretisation scheme is used. Moreover, the grid resolution is

Medium	M	p_∞ (Pa)	T_∞ (K)	T_0 (K)	T_w (K)	Re_∞ (m^{-1})	R (m)
Air	5.9	1377	59	470	295	18×10^6	0.2034

TABLE 1. Free-stream conditions for the present simulations.

increased to resolve the boundary layer in the presence of the rough wall. A grid-convergence study for the restricted domain is presented in § 2.3.

The curvilinear coordinate s has its origin set on the stagnation point and it extends parallel to the wall until the end of the shoulder. With reference to s, the restricted domain is extracted for $s \in [125.3, 164.0]$ mm. In this region, the boundary layer is transonic to supersonic.

Computations are performed on a Cartesian coordinate system. For clarity purposes, results hereafter are represented on a spherical coordinate system, with x, y and z being the streamwise, wall-normal and spanwise direction, respectively. In particular, $x = 0$ is set to $s = 125.3$ mm and the domain is centred on the plane $z = 0$. In the spherical part of the domain, excluding the shoulder, the coordinates x, y and z are given by

$$\left. \begin{aligned} x &= R\theta_1 - 0.1253, \\ y &= r - R, \\ z &= R\theta_2 \sin\theta_1, \end{aligned} \right\} \tag{2.1}$$

where r is the distance from the centre of the hemisphere, θ_1 the elevation angle with reference to the stagnation point and θ_2 the azimuth angle measured clockwise on the rotation axis of the two-dimensional domain. With reference to this coordinate system, the extension of the restricted domain in the wall-normal direction is approximately $y = 7$ mm, corresponding to almost 20 boundary-layer thicknesses at the roughness location. The angular extension of the restricted domain in the spanwise direction depends on the considered roughness geometry and is discussed in more detail in § 2.3. Dirichlet boundary conditions are applied at the inflow boundaries (faces 1 and 2 in figure 1), azimuthal–periodic boundary conditions are used in the spanwise direction (face 3) and Riemann invariants are used at the outflow (face 5). Finally, face 4 is the no-slip isothermal wall.

2.3. *Characterisation of the roughness patch and grid studies*

Two different types of roughness geometries are investigated. First, we consider an array of spanwise periodic roughness elements, where the projection of the roughness profile in the y–z plane is a simple sine function. Second, a more realistic randomly distributed roughness is considered. The patch of distributed roughness is obtained from the superposition of different sinusoidal functions with different wavelengths and random amplitudes and phases. In both cases, the roughness patch is modelled using a body-fitted grid. Body-fitted grids have been successfully applied to model roughness elements in the works of Muppidi & Mahesh (2012), Groskopf & Kloker (2016) and Van den Eynde & Sandham (2016). A detailed description of each roughness geometry and corresponding grid is given hereafter. The location of the roughness patch on the capsule was chosen at a position where the local boundary-layer edge velocity is sufficiently large to provide values of the roughness Reynolds number in the range of 400 for roughness heights significantly smaller than the boundary-layer thickness.
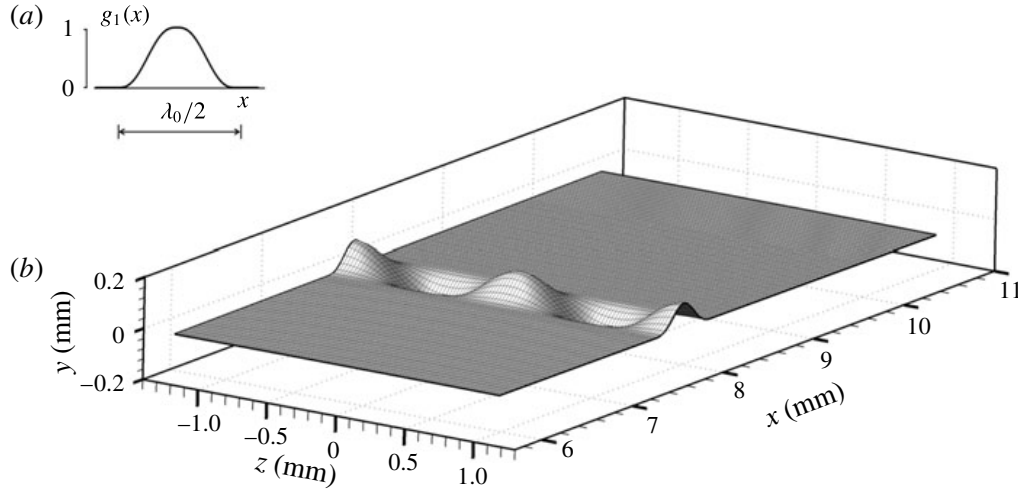
FIGURE 3. Envelope function $g_1(x)$ (a) and grid close to the array of spanwise periodic roughness elements (b). For clarity, only every second point is shown.

2.3.1. *Spanwise periodic roughness elements*

The computational grid at the roughness surface for the roughness type with spanwise periodic elements is shown in figure 3. The roughness patch starts at $x = 7.75$ mm. As the domain is represented in a spherical coordinate system, the value of the wavelength λ_0 is expressed in terms of the elevation angle θ_1 and is given by

$$\lambda_0 = \frac{2\pi}{N_\theta} R \sin \theta_1, \qquad (2.2)$$

with N_θ an integer number. In order to detect the presence of possible subharmonic modes in the analysis of the unsteady flow, the computational domain in the spanwise direction contains two times the wavelength λ_0, i.e. the spanwise extension of the domain is $(4\pi/N_\theta)R \sin \theta_1$.

The spanwise extension of the roughness is $\lambda_{0,r}$, where the subscript r indicates the value taken at the elevation corresponding to the roughness position. In the streamwise direction, the length of the roughness patch is $\lambda_{0,r}/2$. The surface height with respect to the smooth configuration is given by

$$h(x, z) = k g_1(x) \cos \left(\frac{2\pi}{\lambda_0} (x + z) \right), \qquad (2.3)$$

where k is the roughness height and $g_1(x)$ a piecewise defined function which ensures continuity with the smooth wall. In particular, $g_1(x)$ consists of two fifth-order polynomials in the range from zero to 1 within a length of $\Delta x = \lambda_{0,r}/4$, yielding a continuous and smooth flattening of the roughness boundaries, and is zero outside the roughness patch. The roughness height is $k = 0.1$ mm. The roughness height is the same as that of the isolated roughness elements investigated in Theiss *et al.* (2016).

In the case of spanwise periodic roughness elements, the roughness patch is centred at $\theta_{0,r} = 37.6°$ and $N_\theta = 650$, which yields $\lambda_{0,r} = 1.2$ mm. This value is of the same order of magnitude as the boundary-layer thickness. The values chosen for k and $\lambda_{0,r}$ guarantee a low skewness for all grid cells at the wall, while also providing a roughness profile in good approximation resembling a realistic
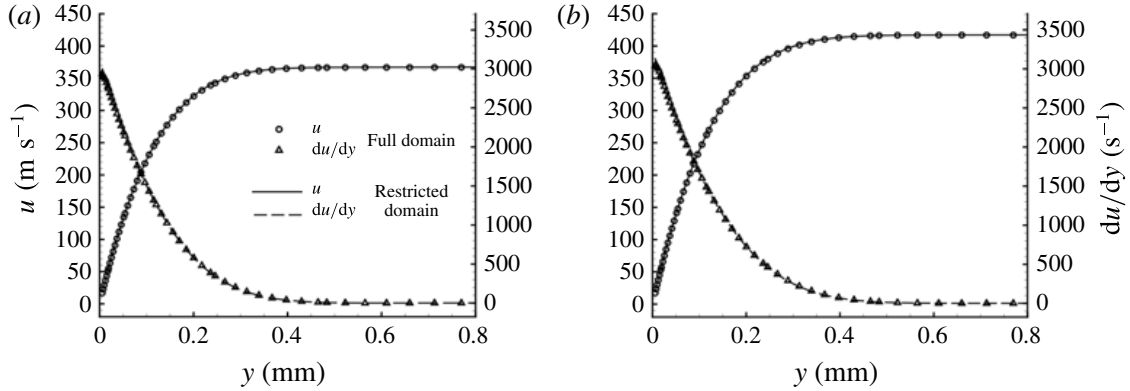
FIGURE 4. Profiles of the velocity and derivative of the velocity in the wall-normal direction at $x = 10$ mm (a) and $x = 30$ mm (b).

Roughness type	k (mm)	$\bar{k}$ (mm)	k/δ	$\bar{k}/\delta$	Re_{kk}	Re_k	$Re_{\bar{k}\bar{k}}$
Spanwise periodic elements	0.100	—	0.350	—	421	480	—
Distributed	0.100	0.022	0.350	0.079	406	458	42.5

TABLE 2. Roughness variables for the two roughness types investigated in this work.

sand-grain roughened wall (see e.g. Hollis 2017). The ratio of the roughness height to the boundary-layer thickness is $k/\delta = 0.35$ and the roughness Reynolds number is $Re_{kk} = 421$. For these values of the roughness variables, modal growth in the roughness wake is expected. Values of further roughness-related variables are listed in table 2 for both grid geometries analysed in this work. These variables are the mean roughness height $\bar{k}$ computed as the root-mean-square with reference to $y = 0$ over the roughness patch, the mean roughness height to boundary-layer thickness ratio $\bar{k}/\delta$, the roughness Reynolds number $Re_k = \rho(k)u(k)k/\mu_w$ using the density and velocity at $y = k$ and the viscosity at wall temperature and the roughness Reynolds number $Re_{\bar{k}\bar{k}} = \rho(\bar{k})u(\bar{k})\bar{k}/\mu(\bar{k})$ using flow properties at $y = \bar{k}$. The boundary-layer thickness δ is the wall-normal distance where the flow reaches 99 % of the total free-stream enthalpy.

2.3.2. *Size of the computational domain and grid convergence*

Careful analysis of the solutions in the full domain and in the restricted domain has been carried out to check the absence of errors which may rise because of the different computational schemes and grid resolutions used in the two different domains. The boundary-layer profiles on the full and restricted domains have been compared for the smooth-wall configuration at different positions. Profiles of the velocity and derivative of the velocity in the wall-normal direction are shown in figure 4 for $x = 10$ mm and $x = 30$ mm. No appreciable differences are present between the results for the two domains. Therefore, a negligible error is made when passing from the full domain to the restricted domain. The accuracy of the steady simulations as well as the absence of numerically produced unsteady disturbances are further guaranteed by achieving very good convergence of the residuals.

Particular attention has been paid to ensuring that the presence of the roughness patch does not induce disturbances outside the boundary layer, influencing the
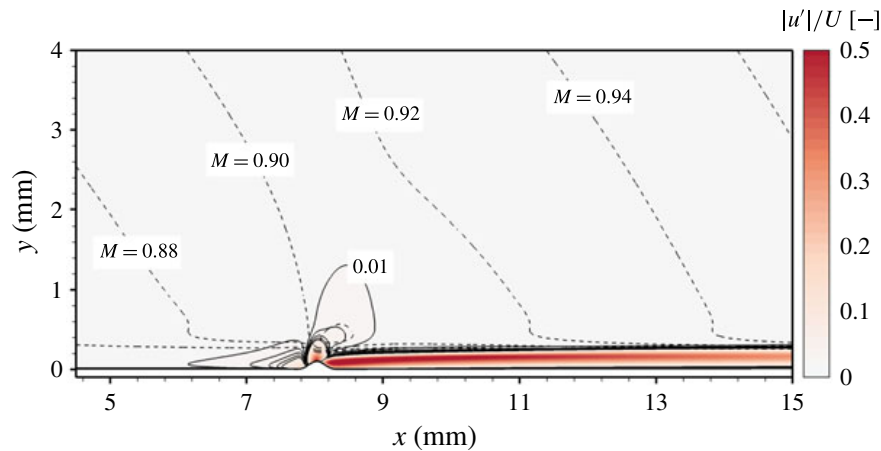
FIGURE 5. Absolute values of the roughness-induced steady disturbances of velocity (colour coded) and Mach number (dashed lines). The disturbances are normalised with the boundary-layer edge velocity and five isolines between 0.01 and 0.05 are represented with solid lines.

results through interaction with the upper boundary or the inflow boundary of the integration domain. The roughness height is significantly smaller than the boundary-layer thickness and the Mach number at the roughness height in the smooth-wall configuration is 0.6. In the wall-normal direction, the computational domain extends to almost $y = 7$ mm, corresponding to almost 20 boundary-layer thicknesses.

Due to the strong acceleration of the flow, the boundary layer grows slowly and the boundary-layer thickness increases by approximately 14 % between $x = 0$ mm and $x = 30$ mm. Note that the ratio of the domain height to boundary-layer thickness in the present work is larger than the values found in other numerical works on roughness-induced transition of high-speed boundary layers with comparable roughness features, such as in De Tullio *et al.* (2013), Groskopf & Kloker (2016) and Muppidi & Mahesh (2012). Further extension of the domain size did not result in any noticeable variation of the flow solution. In addition, the height of the upper boundary (face 2) guarantees that, for the unsteady simulations, any potential residual reflections at the upper boundary exit the domain at the outflow boundary without impinging on the boundary layer and, hence, without affecting the stability properties of the roughness wake.

The effect of the roughness on the steady base flow is limited to the viscous boundary-layer region downstream of the roughness location. This aspect is evidenced in figure 5, which shows the steady disturbances of the velocity obtained as absolute value of the difference between smooth-wall and rough-wall simulations. The values are normalised with the boundary-layer edge values of the streamwise velocity and isolines of the disturbance corresponding to 1 % of the edge values are labelled with 0.01. Isolines of the Mach number are also shown. Values are shown for the z-plane intersecting the roughness peak where the maximum disturbance is found. For clarity purposes, the restricted domain is represented up to $y = 4$ mm only. The effects of the roughness remain limited to the boundary-layer region and do not induce any inviscid effects outside the boundary layer.

A grid-convergence study has been conducted with the numerical grids listed in table 3. The different grids are identified by G_i, where the index i is the grid number.
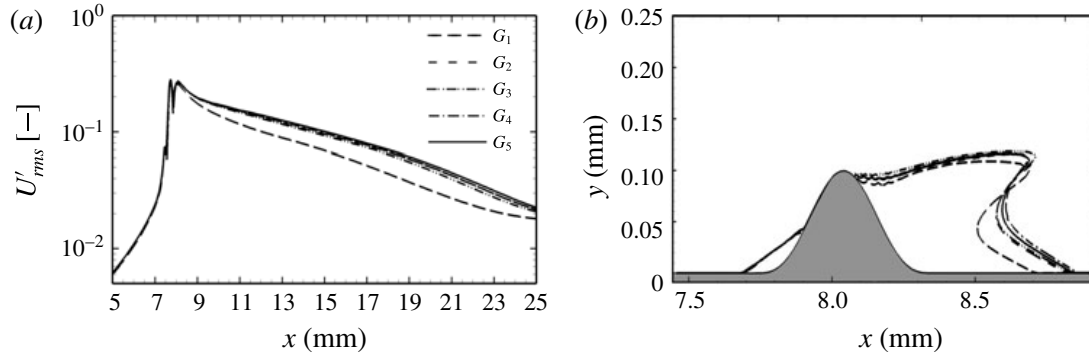
FIGURE 6. Results of the grid-convergence analysis: U'_{rms} along x (a) and recirculation zone as the zero-velocity line at $z = 0$ (b).

Case	N_x	N_y (n_y^δ)	N_z (n_z^λ)	N_{tot}
G_1	840	120 (65)	60 (30)	6×10^6
G_2	1120	160 (90)	120 (60)	21.5×10^6
G_3	1680	240 (132)	120 (60)	48.4×10^6
G_4	1120	160 (90)	160 (80)	28.7×10^6
G_5	1120	160 (90)	200 (100)	35.8×10^6

TABLE 3. Computational grids used in the grid-convergence study.

N_x, N_y and N_z are the number of points in the streamwise, wall-normal and spanwise directions, respectively, while N_{tot} is the total number of grid points, n_y^δ is the number of points in the wall-normal direction inside the boundary layer and n_z^λ the number of points used to resolve one roughness wavelength in the spanwise direction.

The relevant parameter in the grid-convergence study is the amplitude of the root-mean-square of the disturbance velocity,

$$U'_{rms} = \max_y \left(\frac{1}{\lambda_0} \int_0^{\lambda_0} u(x, y, z) - u_b(x, y, z) \, dz \right), \qquad (2.4)$$

where $u(x, y, z)$ is the streamwise velocity in the case of a rough wall and $u_b(x, y, z)$ is the streamwise velocity for the smooth configuration. The values of U'_{rms} over x are shown in figure 6(a) normalised with the boundary-edge velocity at the roughness position.

A grid with a medium resolution (G_2) already provides good results. By further increasing the number of grid points in both the x- and y-direction (G_3) or in the z-direction (G_4 and G_5), no significant improvement of the solution is observed. For completeness, figure 6(b) shows the recirculation zone downstream of the roughness for different grid resolutions. We found that 80 grid points per wavelength λ_0 are sufficient (G_4). Simulations for the case of spanwise periodic roughness elements are performed on the grid G_5, which corresponds to a medium resolution in the x- and y-direction and a fine resolution in the z-direction.

2.3.3. *Randomly distributed roughness*

The computational grid at the roughness surface for the randomly distributed roughness type is shown in figure 7. The patch shape is obtained by superposing
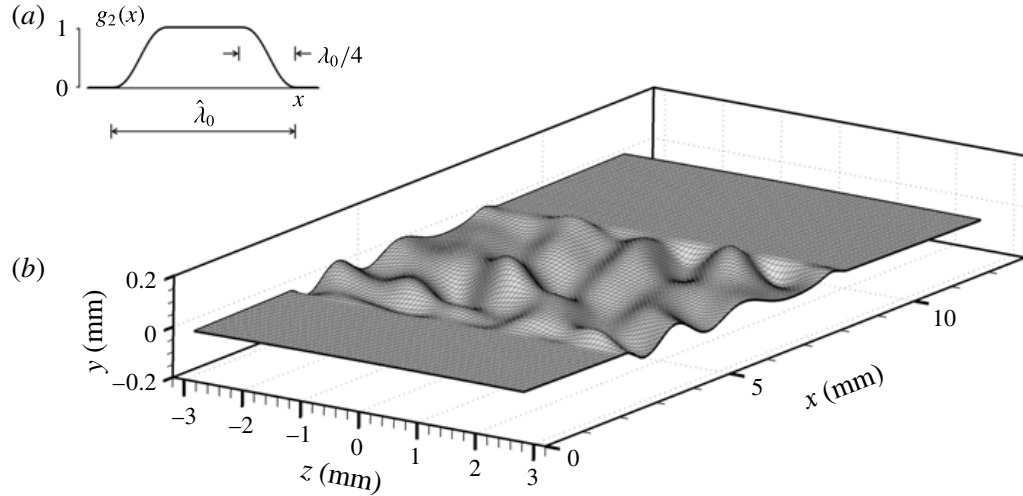
FIGURE 7. Envelope function $g_2(x)$ (*a*) and computational grid close to the randomly distributed roughness patch (*b*). For clarity, only every fifth point is shown.

different sinusoidal waves with pseudo-random amplitudes and phases. According to the definition of distributed roughness also presented in Downs *et al.* (2008), the surface height with respect to the smooth configuration is given by

$$ h(x, z) = k g_2(x) \sum_{m,n=1}^{5} A_{m,n} \cos\left(\frac{2\pi m}{5\lambda_0}x + \frac{2\pi n}{5\lambda_0}z + \phi_{m,n}\right), \qquad (2.5) $$

with $\phi_{m,n} \in [0, 2\pi]$. Values of $A_{m,n}$ and $\phi_{m,n}$ have been randomly extracted from a uniform distribution and are listed in table 4. Values of $A_{m,n}$ are normalised with the maximum of the absolute value of the summation term in (2.5). Therefore, the maximum height of the roughness is k and equal to 0.1 mm, as in the case of spanwise periodic roughness elements. The largest roughness wavelength is equal to five times $\lambda_{0,r}$. Values of $A_{m,n}$ with $n^2 + m^2 > 5^2 + 1$ are set to zero in order to ensure a minimum roughness wavelength of $\lambda_{0,r}$ in all directions.

The roughness patch starts at $x = 2.5$ mm and its length in the x-direction is $5\lambda_{0,r}$. As shown by the analysis in §3.2, subharmonic modes are found to be negligible in this set-up. Hence, in order to limit the size of the simulation, the angular extension of the domain in the spanwise direction is $(2\pi/130)R\sin\theta_1$ and is designed to contain the fundamental wavelength $5\lambda_0$.

The highest peak in the distributed roughness is found at $x_k = 4.80$ mm. Since this position does not correspond to that of the roughness peak in the case of spanwise periodic roughness elements, a slightly different roughness Reynolds number is found ($Re_{kk} = 406$). Nevertheless, as the boundary layer grows very slowly, the ratio of roughness height to boundary-layer thickness remains nearly unchanged and is equal to $h/\delta = 0.35$.

The smallest wavelength in the roughness patch is $\lambda_{0,r}$ and, as shown in the case of spanwise periodic roughness elements, a resolution of 80 grid points per λ_0 provides good grid-convergence properties. Therefore, a grid with the same resolution properties as grid G_4 in table 3 is chosen. The grid for the randomly distributed roughness patch consists of 1120 grid points in the streamwise direction, 160 in the wall-normal direction and 400 in the spanwise direction.

$A_{m,n}$	$A_{m,1}$	$A_{m,2}$	$A_{m,3}$	$A_{m,4}$	$A_{m,5}$	$\phi_{m,n}$	$\phi_{m,1}$	$\phi_{m,2}$	$\phi_{m,3}$	$\phi_{m,4}$	$\phi_{m,5}$
$A_{1,n}$	0.008	0.079	0.008	0.139	0.113	$\phi_{1,n}$	5.328	5.212	4.393	1.753	1.637
$A_{2,n}$	0.119	0.103	0.092	0.076	0	$\phi_{2,n}$	4.931	5.166	5.003	4.244	—
$A_{3,n}$	0.077	0.140	0.116	0.140	0	$\phi_{3,n}$	1.702	3.586	2.775	5.678	—
$A_{4,n}$	0.102	0.065	0.101	0	0	$\phi_{4,n}$	1.431	3.593	2.804	—	—
$A_{5,n}$	0.031	0	0	0	0	$\phi_{5,n}$	2.017	—	—	—	—

TABLE 4. Amplitude coefficients (left) and phases (right) used in (2.5).

2.4. *Disturbance generation*

The boundary layer for the smooth-wall configuration is stable against modal growth throughout the entire domain. Thus, profiles of the disturbance for the unsteady simulations could not be deduced by linear stability theory. Only pressure disturbances are introduced at the inflow of the restricted domain (face 1). In a short region downstream of the inflow boundary upstream of the roughness patch, velocity disturbances generated by the pressure disturbances appear at a very low amplitude and are attenuated exponentially. The variation of this region moving the location of the inflow boundary further upstream with the fixed roughness location had no effect on the results as shown.

The disturbance is a zero-mean, time-varying function characterised by a single frequency f_1,

$$p'(y, z, t) = c(y)\hat{p}_0(z) \sin(2\pi f_1 t), \tag{2.6}$$

where the function $c(y) = e^{-(y/\delta)^3}$ guarantees that the perturbation vanishes outside the boundary layer and $\hat{p}_0(z)$ describes the amplitude of the pressure disturbance at the inflow. For the analysis of symmetric instability modes, $\hat{p}_0(z)$ is a constant value (i.e. $\hat{p}_0(z) = P_0$) and the disturbance is a two-dimensional wave constant in the spanwise direction. For the analysis of antisymmetric instability modes, $\hat{p}_0(z)$ is a sine function odd with respect to $z = 0$ given by $\hat{p}_0(z) = P_0 \sin(2\pi z/\lambda_0)$, with λ_0 the spanwise period of the roughness patch. The unsteady inflow condition $p(0, y, z, t)$ is obtained by adding the function $p'(y, z, t)$ to the value of the pressure prescribed at the boundary for the steady flow,

$$p(0, y, z, t) = p_0(0, y, z) + p'(y, z, t). \tag{2.7}$$

In order to study linear growth of the introduced unsteady disturbances, the constant P_0 is kept several orders of magnitude smaller than the value of the boundary-layer pressure at the inflow position. In particular, the ratio of the inflow disturbance and the inflow value of the steady flow is $P_0/p_0(0, 0, z) \approx 6 \times 10^{-6}$.

A single disturbance frequency equal to 250 kHz is investigated. This value has been chosen based on numerical LST-2D investigations of the base flow with a rough wall. The value of the disturbance frequency falls into the range of relevant frequencies measured in the experiments with transitional flow conducted at HLB for the rough-wall capsule geometry (Theiss *et al.* 2014, 2016).

2.5. *Stability analyses*

2.5.1. *LST-2D and PSE-3D analyses*

The flow variable q is split into a steady primary state $\bar{q}$ and an unsteady perturbation part $\tilde{q}$. The LST-2D analysis is based on the assumption of a locally

parallel base flow, i.e. $\bar{q}$ is assumed to be two-dimensional with the velocity component normal to the wall assumed to be zero. Streamwise gradients of the base flow are neglected. The unsteady perturbation $\tilde{q}$ is three-dimensional and periodic in x at each instant in time. The spatial framework is used, with real frequency ω and complex wavenumber α. The real part of α defines the wavenumber of $\tilde{q}$ in the x-direction, whereas the imaginary part defines the growth rate, $\sigma = -\text{Im}(\alpha)$.

The linear PSE-3D solver is formulated in primitive variables and is based on the non-dimensional Navier–Stokes equations. The steady primary state $\bar{q}$ and the unsteady perturbation part $\tilde{q}$ are assumed to be three-dimensional and slowly varying in the streamwise direction. The disturbance growth of the wake modes is measured in terms of the total disturbance kinetic energy E,

$$E = \int_{-\infty}^{-\infty} \int_{-\infty}^{-\infty} |\bar{\rho}|(|\hat{u}|^2 + |\hat{v}|^2 + |\hat{w}|^2) \, \mathrm{d}y \, \mathrm{d}z, \tag{2.8}$$

with $|\hat{u}|$, $|\hat{v}|$ and $|\hat{w}|$ the amplitude of the velocity disturbances. The growth rate is defined by

$$\sigma = -\text{Im}(\alpha) + \frac{\partial}{\partial x} \ln(\sqrt{E}). \tag{2.9}$$

The full description and verification of both PSE-3D and LST-2D solvers are presented in the work of Theiss *et al.* (2016). PSE-3D as well as LST-2D analyses are used here for comparison and cross-validation only.

2.5.2. *Two-dimensional Fourier analysis of the unsteady disturbances*

Spatio-temporal analysis of the DNS is performed by means of two-dimensional fast Fourier transform. The generic flow variable $q(x, y, z, t)$ is decomposed into a spanwise wavenumber–frequency spectrum,

$$Q_{m,n}(x, y) = \sum_{j=0}^{J-1} \sum_{l=0}^{L-1} q(x, y, z_j, t_l) \mathrm{e}^{-\mathrm{i}2\pi(nj/J + ml/L)}, \tag{2.10}$$

where L and J are the number of time and space samples, respectively. The spatio-temporal modes are indicated by (m, n), where m identifies multiples of the fundamental frequency and n multiples of the fundamental spanwise wavenumber. In particular, $(1, 1)$ is a three-dimensional wave with frequency f_1 and wavelength equal to the spanwise extension of the computational domain. The amplitude of the mode (m, n) for the variable q is defined at each position x as the local maximum in the wall-normal direction:

$$A_{m,n}^q(x) = \max_{y \geqslant 0} |Q_{m,n}(x, y)|. \tag{2.11}$$

In addition, the growth rate of the disturbance associated with each frequency is computed with reference to the disturbance energy as in De Tullio *et al.* (2013). Mack's disturbance energy norm (Mack 1969) is expressed as

$$\mathcal{E}_m(x) = \int_0^\delta \hat{\rho}_0 [\hat{U}_m^2 + \hat{V}_m^2 + \hat{W}_m^2] + \frac{\hat{\rho}_m^2 \hat{T}_0}{\gamma \hat{\rho}_0 M^2} + \frac{\hat{T}_m^2 \hat{\rho}_0}{\gamma(\gamma - 1)\hat{T}_0 M^2} \, \mathrm{d}y, \tag{2.12}$$

with the disturbance amplitude associated with each frequency computed as

$$\hat{Q}_m(x, y) = \sum_{n=0}^{N} |Q_{m,n}(x, y)|. \tag{2.13}$$

The growth rate is computed as

$$\sigma_{\mathcal{E}} = \frac{1}{2}\frac{\mathrm{d}}{\mathrm{d}x} \ln(\mathcal{E}_m(x)). \tag{2.14}$$

In the investigated domain, the terms relative to the inner energy in the definition of the disturbance energy norm remain very small and can be neglected. The growth rate based on the kinetic energy is computed as

$$\sigma_{\mathcal{K}} = \frac{1}{2}\frac{\mathrm{d}}{\mathrm{d}x} \ln\left(\int_0^{\delta} \hat{\rho}_0 [\hat{U}_m^2 + \hat{V}_m^2 + \hat{W}_m^2]\,\mathrm{d}y\right), \tag{2.15}$$

and similar results are found for the two analyses ($\sigma_{\mathcal{E}} \approx \sigma_{\mathcal{K}}$).

3. Results for the spanwise periodic roughness elements

3.1. *Laminar base flow*

The roughness patch is characterised by three regions of separated flow, shown in figure 8 as dashed green lines. Two separation regions are located immediately upstream and downstream of the roughness protuberance. A third separation region is associated with the roughness cavities and is highlighted by the recirculating streamlines.

Figure 8 also shows isosurfaces of the streamwise vorticity. The roughness wake is mainly influenced by the protuberances rather than by the cavities. In particular, a pair of counter-rotating vortices originate at the sides of the roughness protuberance and the roughness wake resembles the one already observed in the case of isolated roughness elements. Through the lift-up mechanisms described by Landahl (1980), these vortices induce movement of low-momentum fluid from the near-wall region upwards immediately behind the roughness protuberance. As a consequence, a low-speed streak originates along the protuberance centreline, as shown in figure 9. The rotation of the fluid around the vortex cores is visualised in figure 8 by the helicoidal shape of the streamlines in the near region of the roughness wake. Further downstream, as the vortices weaken, the flow pattern evolves into a mushroom-shaped geometry, as is known from the case of an isolated roughness element (Stemmer *et al.* 2017*b*). Compared to the case of the smooth-wall geometry, the presence of the low-speed streaks is associated with a strong deformation of the flow and, hence, with regions of high shear stress, resulting in a potentially unstable wake.

Note that the flow variables and the shape of the wake rapidly change in the streamwise direction because of the strong acceleration of the base flow due to the hemispherical shape of the blunt body. Especially close to the roughness in the region of the separated flow, the boundary-layer properties change fast in the flow direction and parallel-flow assumptions in the stability analysis might not be valid.
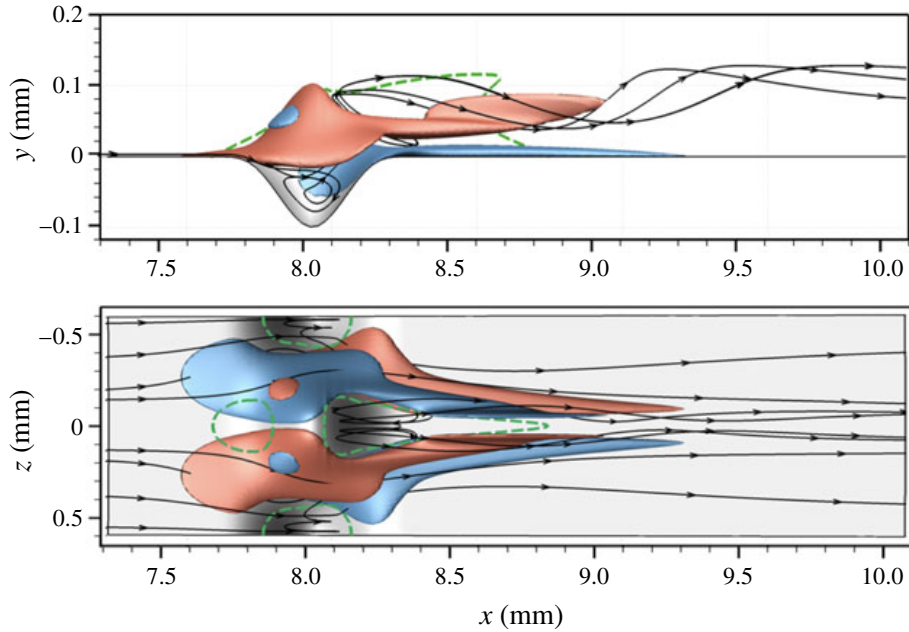
FIGURE 8. Isosurfaces of streamwise vorticity (red, $\omega_x = +10^6$ s^{-1}; blue, $\omega_x = -10^6$ s^{-1}) near the roughness patch. The flow-separation regions in the plane $z = 0$ and on the wall are marked with the dashed green line.
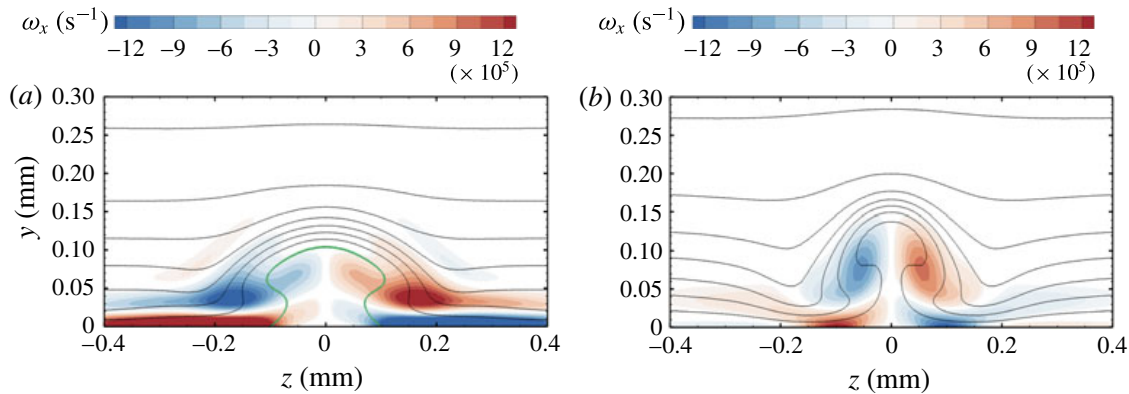
FIGURE 9. Contours of the streamwise vorticity and streamwise velocity levels at $x = 8.4$ mm (a) and $x = 9.2$ mm (b). Values of the streamwise vorticity with an absolute value below 10 % of the absolute maximum value are blanked out. Velocity levels are shown every 50 m s^{-1}. The zero-velocity line in (a) is marked in green.

3.2. Stability properties

The presence of unstable modes in the wake of the spanwise periodic roughness elements has been investigated with the help of LST-2D, PSE-3D and DNS. The results obtained with the different methods are compared for cross-validation. In the case of DNS, unsteady pressure perturbations with a frequency $f_1 = 250$ kHz are introduced at the inflow, as described in § 2.2. As the boundary layer for the smooth-wall geometry is stable at the roughness location, the value of the disturbance frequency has been chosen based on numerical investigations of the base flow with a rough wall through LST-2D analysis.
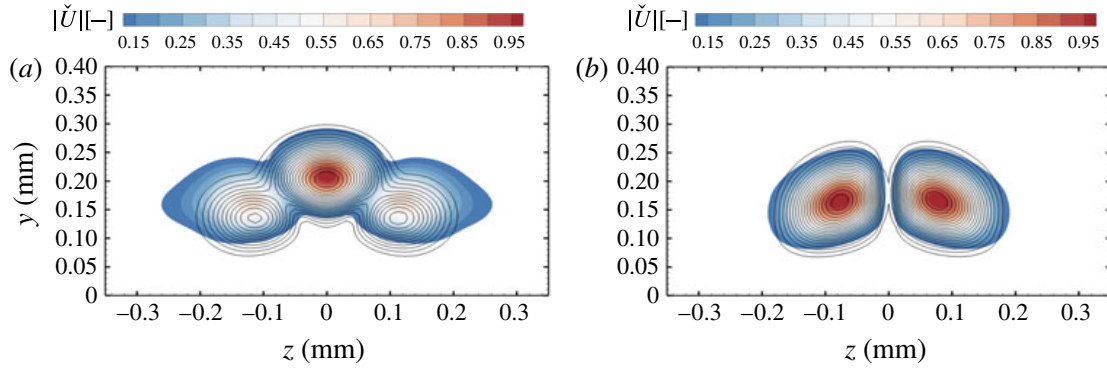
FIGURE 10. Mode shape from DNS (black contour lines) and LST-2D (coloured contours). Results are shown for the S-mode (*a*) and the A-mode (*b*) at $x = 18.5$ mm. Values are normalised to unity and absolute values below 10 % of the absolute maximum value are blanked out.

For the investigated frequency, the stability analysis evidenced the presence of two main unstable modes. As in the case of an isolated roughness element, a symmetric (S) and an antisymmetric (A) mode are present. The mode shapes for A- and S-modes of the streamwise velocity compared to DNS results are shown in figure 10. Modes from the DNS are obtained as absolute value of the temporal Fourier analysis.

The value of the growth rate $\sigma_{\mathcal{K}}$, computed with different numerical methods, is shown in figure 11. Analyses based on LST-2D and PSE-3D are limited to the flow downstream of the roughness only and do not include the recirculation region. Excellent agreement is observed for the results of DNS and PSE-3D in the S-mode case. In the A-mode case, a small difference between DNS and PSE-3D is observed close to the roughness patch downstream of the recirculation zone. We attribute this discrepancy to the difficulties of obtaining a mode in the roughness wake which is perfectly antisymmetric. In fact, the growth rates in the recirculation zone are much stronger for the S-mode than for the A-mode and a relatively small symmetric component was always present even in case of a pure antisymmetric inflow disturbance. Instead, an almost perfect match is reached further downstream. There is a small deviation between the curves of LST-2D and of PSE-3D. This discrepancy indicates that gradients in the flow direction of base flow and disturbance play a small but non-negligible role in the investigated region.

Even though larger values of the growth rate are reached for the S-mode, the A-mode remains amplified over a longer distance downstream of the roughness location. In particular, the zero growth rate is found at $x = 14.2$ mm for the S-mode and at $x = 17.9$ mm for the A-mode. This behaviour is better illustrated in figure 12, which shows a two-dimensional representation of the *N*-factor as calculated from DNS results. The *N*-factor is computed as

$$N = \int_{x_0}^{x_1} \sigma_{\mathcal{K}} \, \mathrm{d}x \qquad (3.1)$$

and is a function of both the start location x_0 and the end location x_1. The largest value of the *N*-factor for the S-mode is 9.6 and is obtained for $x_0 = 7.7$ mm and $x_1 = 14.2$ mm, whereas for the A-mode the largest value of the *N*-factor is 7.3 and it is obtained for $x_0 = 7.7$ mm and $x_1 = 17.9$ mm. Note that for both the A- and
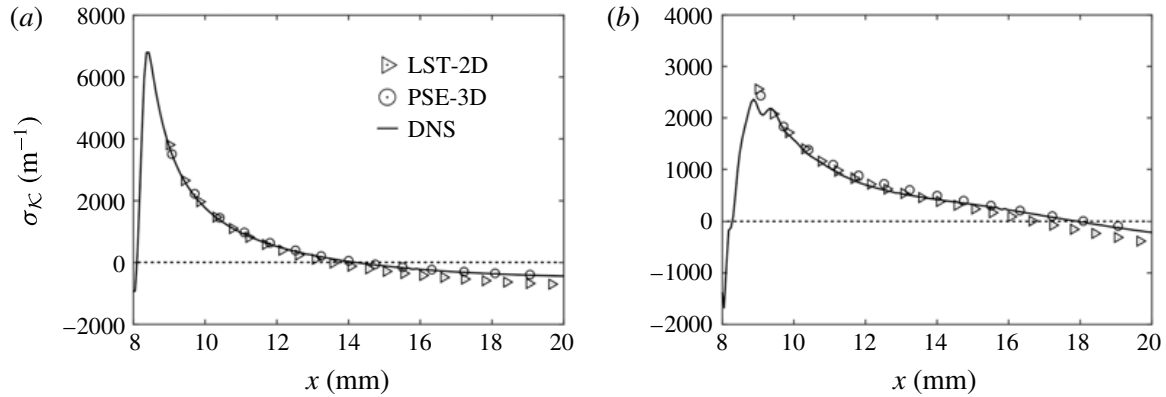
FIGURE 11. Growth rate of the S-mode (*a*) and A-mode (*b*) in the wake of spanwise periodic roughness elements.
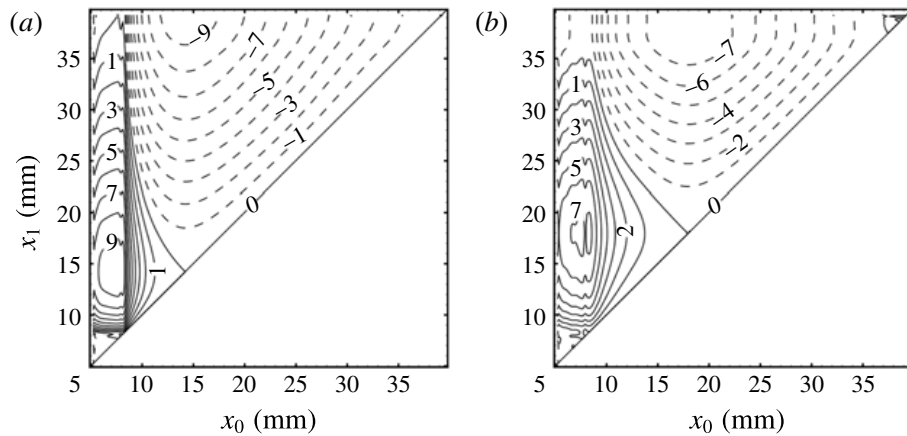
FIGURE 12. Two-dimensional representation of the N-factor as a function of both the initial and end positions (x_0, x_1) for the symmetric (*a*) and antisymmetric (*b*) mode. N-factor isolines (solid for $N \geqslant 0$ and dashed for $N < 0$) are shown every 0.5.

S-modes, the value of x_0 for the maximum N-factor turns out to be the same and it corresponds to a position just upstream of the roughness element, which starts at $x = 7.75$ mm. In this respect, the possibility of easily incorporating the flow over the roughness patch and the recirculation zone in the stability analysis can be regarded as one of the advantages of DNS.

The amplitude development of the disturbance modes is shown in figure 13. The amplitudes are normalised by $U = 359$ m s^{-1}, which is the boundary-layer edge velocity at $x = 8$ mm. At the inflow, only one particular perturbation mode is introduced. Specifically, (1, 0) is perturbed to generate the S-mode and (1, 2) is perturbed to generate the A-mode. At the roughness position, further modes with the same frequency, (1, :), are generated. For both the S-mode and the A-mode, (1, 2) and (1, 4) are the most amplified spatio-temporal modes. Since (1, 2) corresponds to a wave with a spanwise wavelength equal to the roughness wavelength λ_0, the mode (1, 1) represents a subharmonic of (1, 2). Note that values of (1, 1) remain several orders of magnitude lower than the most relevant modes over the entire range. Additional modes with multiple frequencies (2, :) are generated through superposition of the modes (1, :) due to nonlinear interactions.
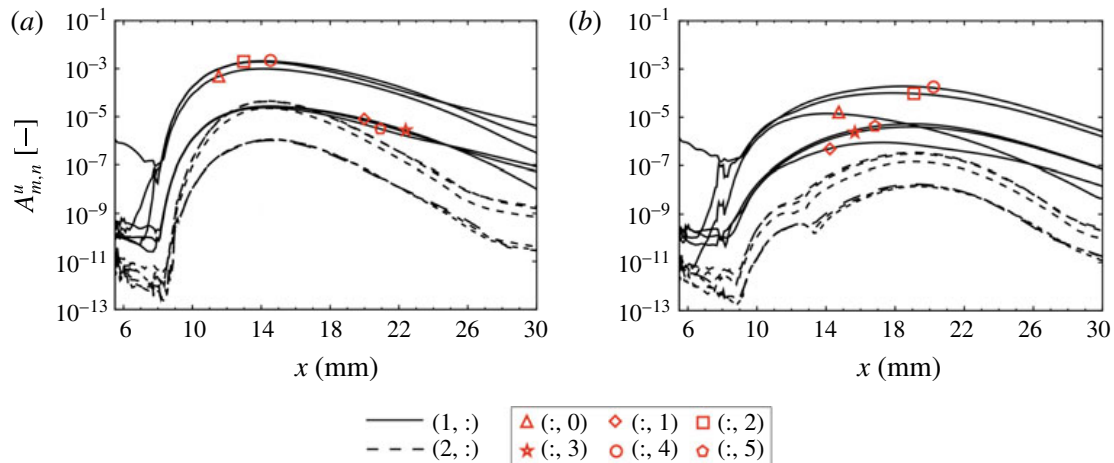
FIGURE 13. (Colour online) Amplitude of disturbance Fourier modes of the streamwise velocity for the symmetric (*a*) and antisymmetric (*b*) unstable modes.

4. Results for the randomly distributed roughness

4.1. *Laminar base flow with a cross-flow-type vortex*

In the case of a patch of randomly distributed roughness (figure 7), the concurrent effect of protuberances and cavities of different size, shape and streamwise profile can be investigated. Figure 14 shows a representation of the rough wall with elevation isocontours seen from the top. The eight main roughness peaks are marked with numbers 1–8 and their properties (e.g. height, position on the wall, height to boundary-layer thickness ratio and local Re_{kk}) are summarised in table 5. The highest roughness peak has an elevation of $k = 0.1$ mm and the relative roughness Reynolds number is $Re_{kk} = 406$. The other peaks marked in the figure have an elevation of between 0.039 mm and 0.062 mm and roughness Reynolds numbers between 87 and 191. To give an insight into the flow topology, sample streamlines and flow recirculation regions are shown. The presence of recirculation regions seems to be related both to the height of the roughness and to its shape as well as to its alignment with the flow. In particular, the shape of both peaks 2 and 4 is elongated in the flow direction and the flow remains attached as it passes over these protuberances. Instead, the smaller protuberances 6, 7 and 8 are mainly elongated in the cross-flow direction and are followed by cavities that promote the formation of recirculation regions.

As in the case of the spanwise periodic roughness elements, the roughness peaks produce streamwise vortices. Figure 15 shows four streamlines passing over the roughness and centred on the main vortex cores downstream of the patch. At the vortex core, vorticity and velocity tend to align and, therefore, the vortex lines are to a good approximation identical to the streamlines (Levy, Degani & Seginer 1990). The streamlines allow us to track the evolution of the flow in the upstream direction back to positions upstream of the roughness. The streamlines are coloured by the value of the streamwise vorticity. The interaction of the flow with subsequent peaks and valleys is evidenced by the alternation of high- and low-vorticity values along the same streamline. As the streamlines are deflected at the protuberance, the magnitude of the streamwise vorticity strongly increases. As expected, the main vortex developing downstream of the roughness originates from the highest protuberance (peak 1, streamline *b*). Streamlines *a*, *c* and *d* exhibit a high vorticity
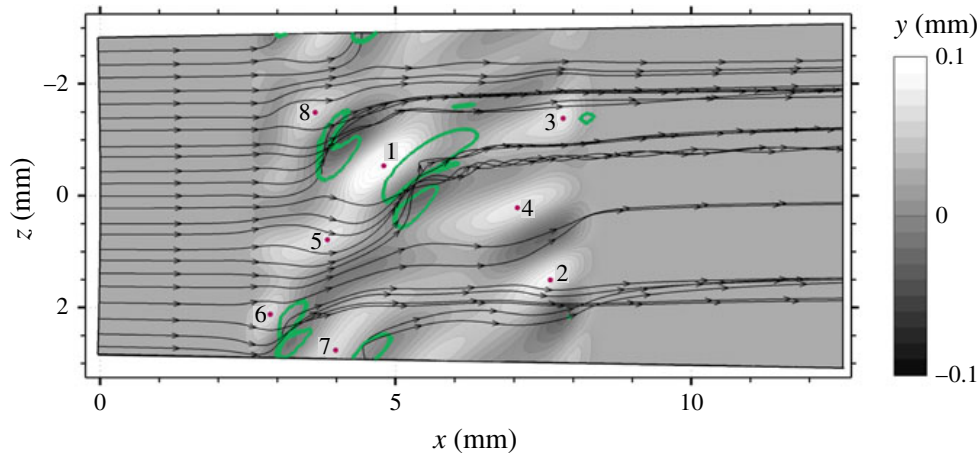
FIGURE 14. Representation of the rough wall with streamlines. Separation regions on the wall are marked in green.
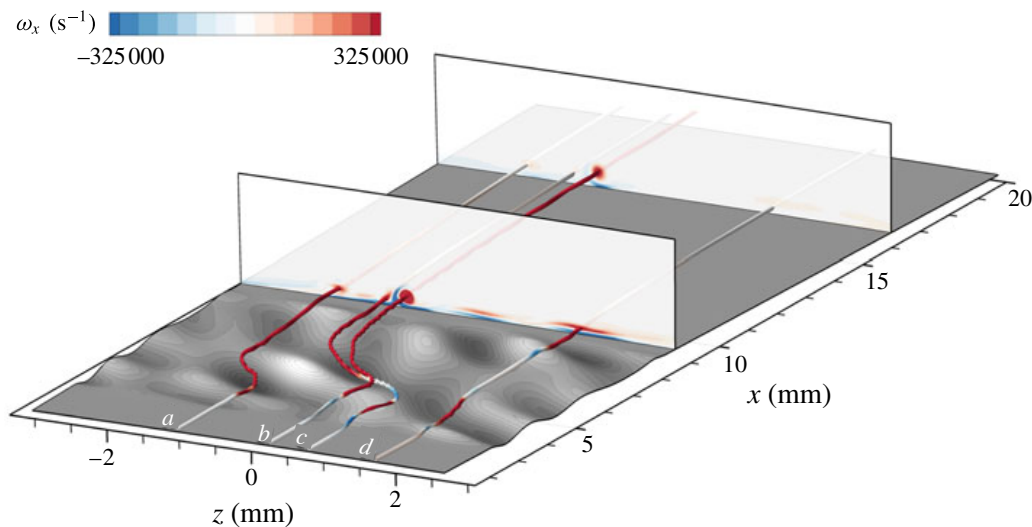
FIGURE 15. Three-dimensional representation of the flow field over the distributed roughness patch. Downstream slices at $x = 8.6$ mm and $x = 15.9$ mm and sample streamlines (*a–d*) are coloured by streamwise vorticity.

at the roughness position. This vorticity rapidly vanishes further downstream, as evidenced by the grey colour of the streamlines for $x > 12$ mm.

The vorticity distributions at three different positions in the same y–z plane downstream of the roughness patch ($x = 8.6$ mm) are shown in figure 16. The distortion of the velocity flow field is evidenced by the rolling up of the isolines of streamwise velocity. The presence of a high-shear layer induced in the surroundings of the vortex is shown in figure 17, with isolines of the y- and z-components of the gradient of the streamwise velocity, $\partial u/\partial y$ and $\partial u/\partial z$.

Of particular interest is the steady cross-flow-type vortex which develops in the wake of peak 1 (figure 16*b*). The skewness of the roughness relative to the streamwise flow induces velocity and vorticity distributions known from cross-flow vortices in three-dimensional boundary layers (streamline *b*). The cavity downstream of peak 1 contributes to the vortex generation with a further increase of the local wall-normal
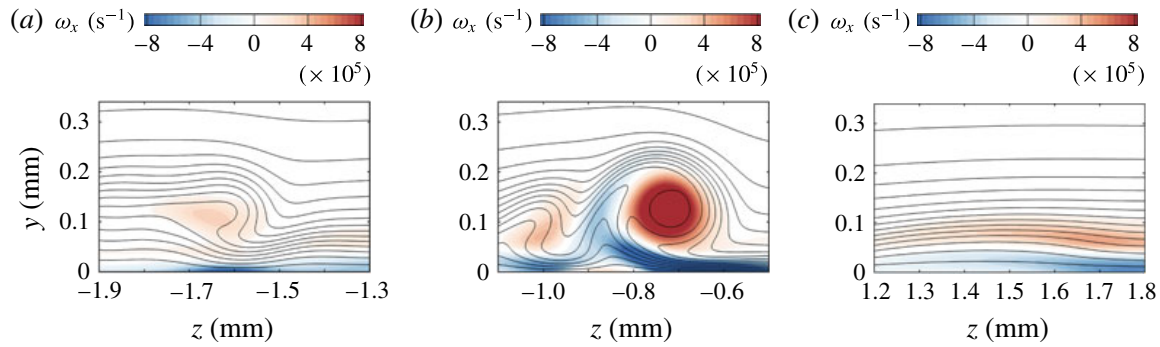
FIGURE 16. Colour contours of the streamwise vorticity and streamwise velocity isolines at $x = 8.6$ mm; values of the streamwise vorticity with an absolute value below 10 % of the absolute maximum value on the same plane are blanked out and velocity levels are shown every 25 m s^{-1}.

Peak	(x, z) (mm)	k (mm)	k/δ	Re_{kk}	Re_k
1	$(4.805, -0.555)$	0.100	0.350	406	458
2	$(7.612, 1.476)$	0.062	0.217	191	207
3	$(7.844, -1.378)$	0.057	0.199	166	180
4	$(7.015, 0.231)$	0.055	0.192	156	169
5	$(3.906, 0.739)$	0.049	0.171	130	139
6	$(2.880, 0.128)$	0.045	0.157	112	120
7	$(3.892, 2.885)$	0.043	0.150	103	110
8	$(3.656, -1.506)$	0.039	0.136	87	93

TABLE 5. Position (x, z) and local roughness variables with reference to the main roughness peaks marked in figure 14.

component of the velocity. High values of both $\partial u / \partial y$ and $\partial u / \partial z$ are found around this vortex structure (figure 17*b,e*). The presence of this high-shear layer is associated with highly unstable modes. Cross-flow vortices in three-dimensional boundary layers have been extensively studied in the past and detailed numerical studies of cross-flow instabilities are presented, among others, in Malik, Li & Chang (1994), Malik *et al.* (1999) and Wassermann & Kloker (2002). However, in the case of cross-flow vortices in three-dimensional boundary layers, a spanwise velocity is present in the base flow. Instead, the flow in the present configuration without roughness is two-dimensional and the spanwise component of the velocity typical of cross-flow vortices is directly induced by the roughness itself. In the works of Kegerise *et al.* (2014) and Choudhari *et al.* (2015), similar roughness-induced cross-flow-type vortices have been observed for the case of a supersonic, flat-plate boundary layer in the presence of an isolated roughness element with a triangle shape. Contrary to the case of a flat plate, the hemisphere configuration with a smooth wall does not support modal instabilities and the roughness can be regarded as the only cause of significant disturbance growth.

On the left side of the cross-flow-type vortex, there is a minor vortex centred at $z \approx -1.0$ mm, corresponding to the streamline *c*. A third vorticity region is shown in figure 16(*a*). This vortex originates at peak 8 and streamline *a* evolves from this peak. A sudden increase of the streamwise vorticity occurs downstream of the protuberance. Here, an additional wall-normal component of the velocity is introduced by the presence of the cavity between peaks 1 and 8.
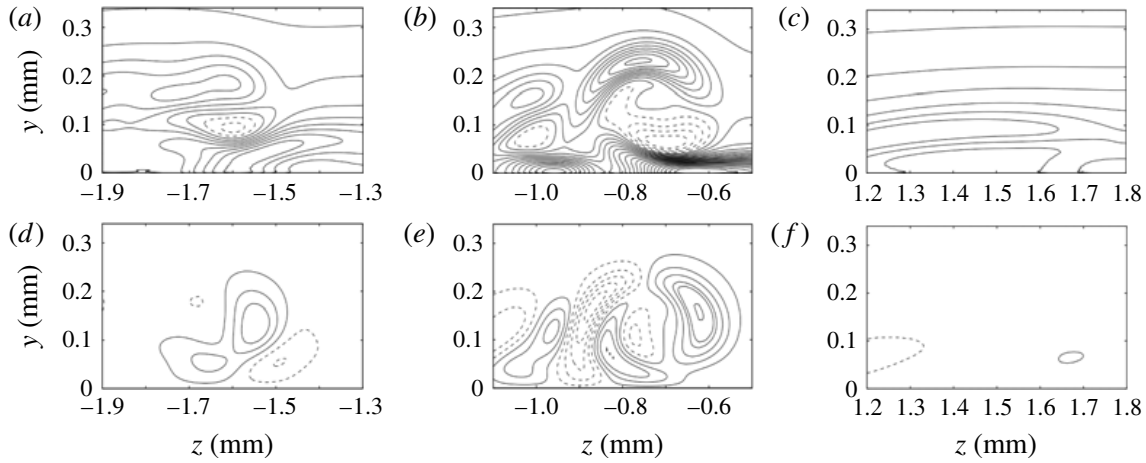
FIGURE 17. Isolines of $\partial u/\partial y$ (*a–c*) and $\partial u/\partial z$ (*d–f*) at $x = 8.6$ mm. Lines are shown every 400 s^{-1} and dashed lines represent negative values.

Finally, streamline *d* shows the subsequent effects of peaks 6 and 2 on the flow. After a slight increase immediately downstream of peak 6, the value of the streamwise vorticity rapidly falls. A second increase of the vorticity is found at peak 2 at the end of the roughness patch. Although this roughness protuberance has a non-symmetric profile alignment similar to that of peak 1, its height is too small to give birth to a significant vortex (figure 16*c*).

The downstream evolution of the streamwise vorticity ω_x along these streamlines is shown in figure 18. The streamwise vorticity reaches its maximum at the roughness position with values in the range 1.0 and 1.7×10^6 m^{-1} and it diminishes rapidly downstream of the roughness. With the only exception being the cross-flow-type vortex, the other streamwise vortices vanish within a few millimetres downstream of the roughness patch. The cross-flow-type vortex remains at a considerable amplitude in the computational domain until the outflow boundary is reached. The persistence of the cross-flow-type vortex is mainly related to its specific shape rather than to the height of the roughness peak 1. The development of ω_x in the case of the spanwise periodic roughness elements is also shown for comparison. In this case, the two streamlines located in the cores of a counter-rotating vortex pair, as shown in figure 9, have been identified. The streamwise vorticity difference was computed as $\omega_x = 1/2(\omega_x^+ - \omega_x^-)$, where ω_x^+ and ω_x^- refer to the maximum positive and negative vorticity. Although the maximum roughness height is the same as in the case of the distributed roughness, the vortices in the wake of the spanwise periodic roughness elements decay fast and are extinguished within a distance of approximately 10 mm downstream of the roughness position.

4.2. *Instability modes and breakdown scenario*

The wake of the randomly distributed roughness is more complex than that of periodic roughness elements and is characterised by several vorticity regions with different modes of instability possibly interacting with each other. Analyses based on LST-2D and PSE-3D are impossible to conduct as the flow is locally non-periodic in the spanwise direction for the various isolated vortices in the roughness wake. The evolution of small perturbations over the patch of distributed roughness and in the roughness wake is investigated with DNS only. Compared to LST-2D and
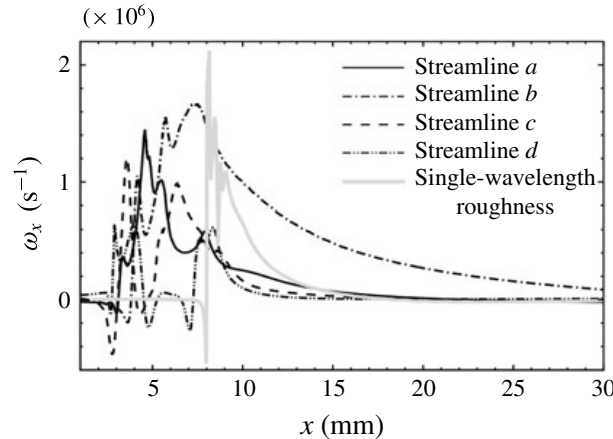
FIGURE 18. Values of the streamwise vorticity along the streamlines *a–d* as shown in figure 15.

PSE-3D, the use of DNS allows for a more detailed analysis of the flow in the entire simulation domain, including the roughness patch. Moreover, the formation and evolution of secondary instabilities and the onset of laminar breakdown to turbulence can be investigated.

A two-dimensional pressure disturbance wave is forced at the inflow boundary. Free-stream conditions and roughness variables (roughness height, roughness Reynolds number and shortest roughness wavelength in the patch) are the same as in the case of spanwise periodic roughness elements. Therefore, the analysis is conducted with the same frequency $f_1 = 250$ kHz as in §3.

We accurately analysed the disturbance evolution downstream of each protuberance and cavity of the roughness patch and found that the only appreciable disturbance amplification is associated with the steady cross-flow-type vortex presented in §4.1. This vortex is responsible for a prolonged and strong disturbance amplification which, eventually, leads to transition. On the contrary, as the wakes of the other roughness peaks rapidly vanish in the strongly accelerated boundary layer, no significant amplification is observed in these wakes at the investigated frequency.

The downstream development of the Fourier amplitudes is presented in figure 19. The mode $(1, 0)$ corresponds to the inflow disturbance. Modes with the same frequency but different wavenumbers are generated at the roughness location. Modes $(1, :)$ rapidly grow in the roughness wake, whereas higher harmonic frequency modes $(m > 1, :)$ are generated due to nonlinear interactions. Eventually, a growth saturation of the base modes $(1, :)$ is reached for $x > 17$ mm, followed by a saturation of the higher frequency modes around $x \approx 18$ mm. Downstream of this location, nonlinear interactions dominate the flow, leading to breakdown to turbulence. Subharmonic frequency modes $(0.5, :)$, i.e. modes with 125 kHz, remain negligible in amplitude over the entire domain. Furthermore, we note that, although disturbance growth is present at the roughness location, the onset of secondary instabilities occurs in the roughness wake downstream of the patch. Since linear as well as nonlinear growth of the disturbances to transition is the focus of our analysis, investigation of the pseudo-turbulent flow is not presented here and the flow for $x > 25$ mm has to be considered as not fully resolved.

The instability of the boundary layer originates in the high-shear layer in the vicinity of the vortex and in the corresponding inflection points. In particular, the
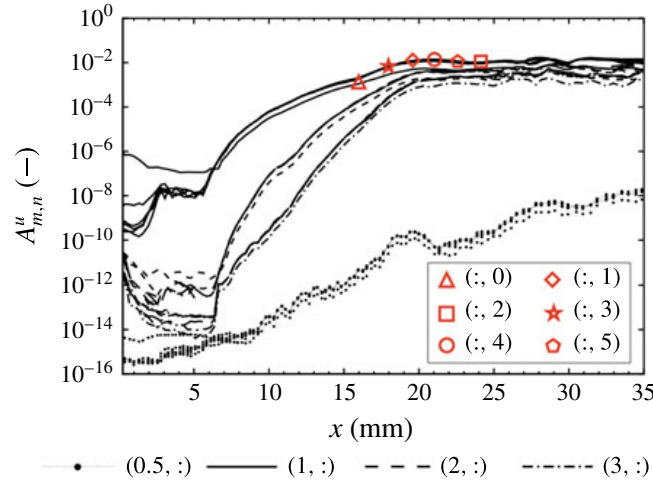
FIGURE 19. (Colour online) Amplitude of spatio-temporal Fourier modes of the streamwise velocity in the case of distributed roughness. Values are normalised with the velocity at the boundary-layer edge $U = 359$ m s^{-1}.

increase of disturbance kinetic energy associated with the growth of unstable modes is mainly due to energy transfer through wall-normal and spanwise velocity gradients. To investigate whether instabilities in the present case originate from wall-normal or spanwise gradients similar to the y- and z-modes in three-dimensional boundary layers (Wassermann & Kloker 2002), we analyse the two main production terms P_y and P_z in the disturbance kinetic energy,

$$P_y = -\overline{u'v'}\frac{\partial \overline{u}}{\partial y}, \quad P_z = -\overline{u'w'}\frac{\partial \overline{u}}{\partial z}, \qquad (4.1a,b)$$

where the overbar denotes the time average and the prime a fluctuating quantity. Local values of P_y and P_z at consecutive x positions in the roughness wake are shown in figure 20. For clarity purposes, values of P_y and P_z at each x position are normalised with the maximum value of the total production term $P = P_y + P_z$ in the y–z plane. Also shown are the disturbance modes of the streamwise velocity, computed from DNS for the frequency f_1.

In the near-field region (figure 20a,b), the disturbance mode of the streamwise velocity appears as a single, elongated and curved shape wrapped around the cross-flow-type vortex. As this mode evolves downstream, two main instability regions of elliptical shape become evident. The evolution of the disturbance mode in the streamwise direction correlates well with the main regions of disturbance-energy production (colour isocontours). In particular, P_y identifies three regions of high disturbance production which resemble a distorted version of the S-mode analysed in §3.2. Furthermore, P_y seems to be related to the formation of the instability region visible in the upper-left corner of figure 20(c,d). The effects of P_z are confined mainly to the descending (right) side of the vortex.

The integrals of the production terms, obtained from the local P_y and P_z over the y–z plane, are shown in figure 21. Before transition occurs, the value of P_z is slightly larger than the value of P_y, indicating a major role of the lateral shear layer to the disturbance growth. However, the values of both terms remain of the same order of magnitude over the entire domain and neither y-modes nor z-modes can be regarded as dominant.
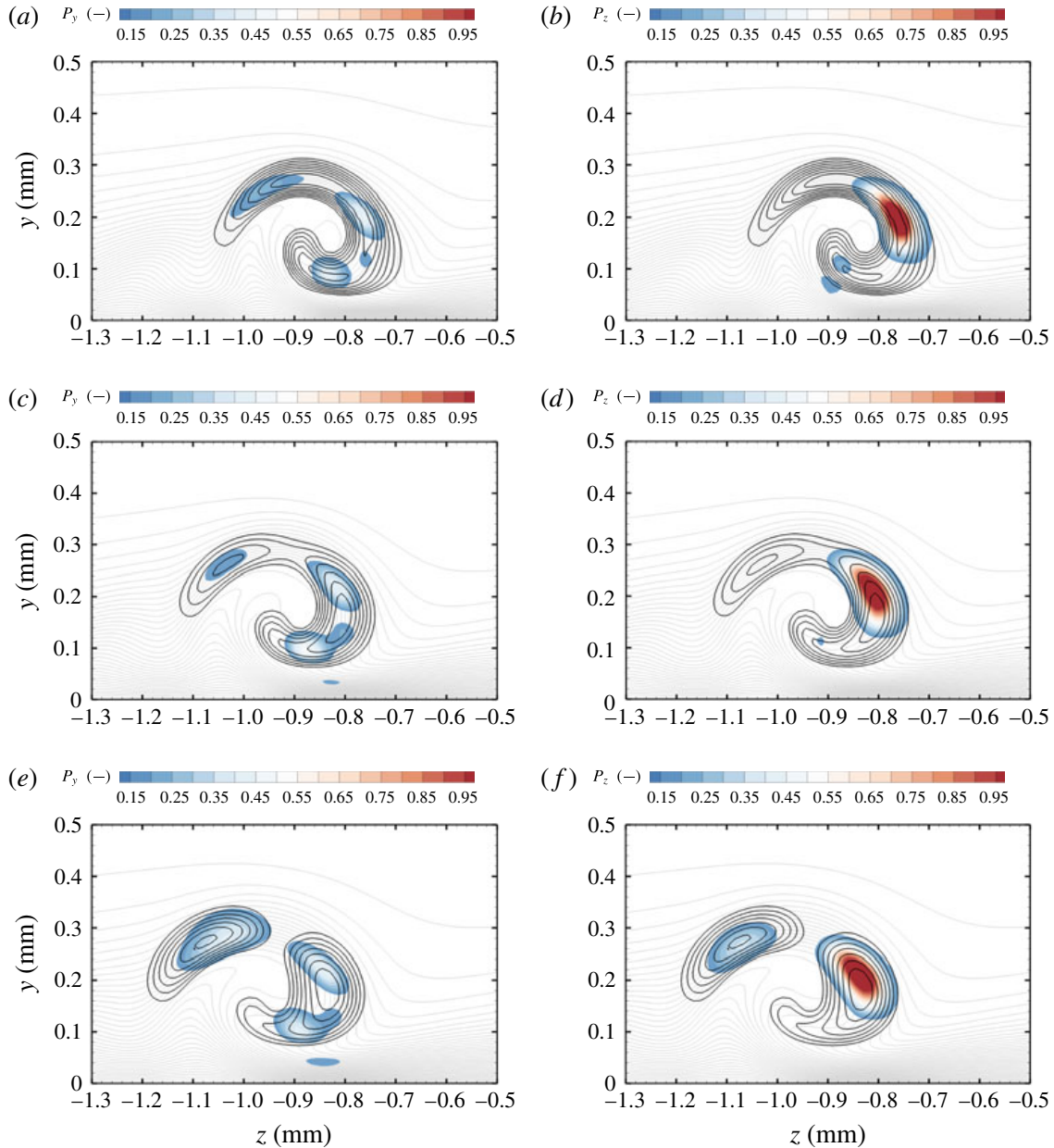
FIGURE 20. Unstable disturbance modes of the streamwise velocity (black contour lines every 0.1 for values $\geqslant 0.3$), local values of P_y (a,c,e) and P_z (b,d,f) (coloured isocontours) and streamwise velocity levels (grey background isolines for every 10 m s^{-1}) at $x = 12.0$ mm (a,b), $x = 14.7$ mm (c,d) and $x = 16.8$ mm (e,f).

For the cross-flow-vortex breakdown, as analysed by Wassermann & Kloker (2002), it was observed that the interaction between the steady vortex and the unsteady incoming disturbances gives birth to finger-like vortices wrapping around the ascending side of the steady vortex. Similar finger-like structures on the ascending (left) part of the vortex can be identified in the present simulation as well and are visualised by means of the Q-isosurfaces shown in figure 22. The first appearance of these structures becomes visible at $x \approx 17$ mm with a downstream wavelength of 1 mm, twining around the left side of the vortex centreline. However, another finger-like structure on the descending side of the steady vortex can also be seen.
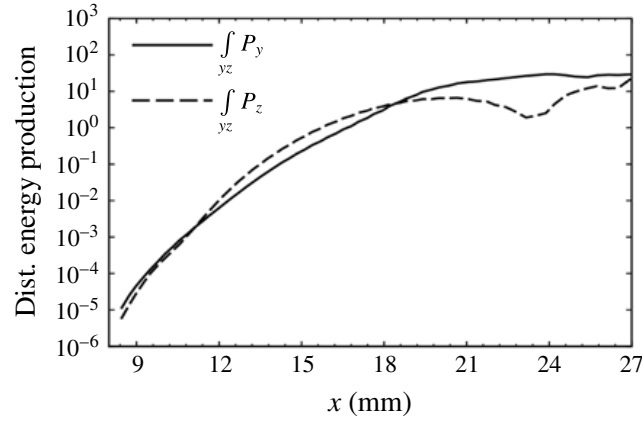
FIGURE 21. Integral values of P_y and P_z along the x-direction.
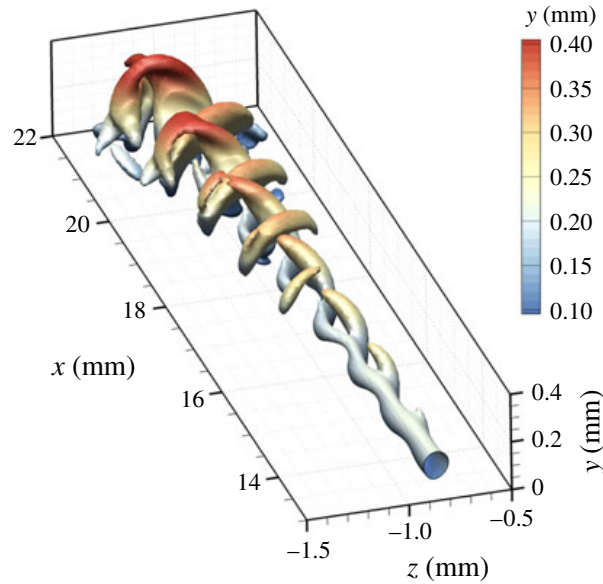
FIGURE 22. Isosurfaces of $Q = 3 \times 10^{10}$ coloured by distance from the wall downstream of the roughness.

This structure, which occurs alternating with the one on the ascending side, gradually evolves into horseshoe vortices during the transition process. This mode of instability was not present in the work of Wassermann & Kloker (2002) and, in our case, is obviously related to the region of large P_z on the descending side of the vortex. In fact, $\partial u / \partial z$ presents a significant peak on the descending side of the vortex (figure 17e, for -0.7 mm $< z < -0.5$ mm), which was not found in Wassermann & Kloker (2002).

Figure 23(a) shows the instantaneous value of the disturbance pressure p' at the wall, obtained as the difference between the unsteady and the steady simulations. The dominant streamwise wavelength of the disturbance can be retrieved by measuring the distance between two consecutive peak values of p' in the fishbone-like pattern. At the end of the roughness patch, the wavenumber of the disturbance is $\alpha = 6310$ m^{-1}. With reference to f_1, this wavenumber corresponds to a phase velocity of $c_{ph} = 0.68U$, where U is the edge velocity of the boundary layer at the same position. No significant
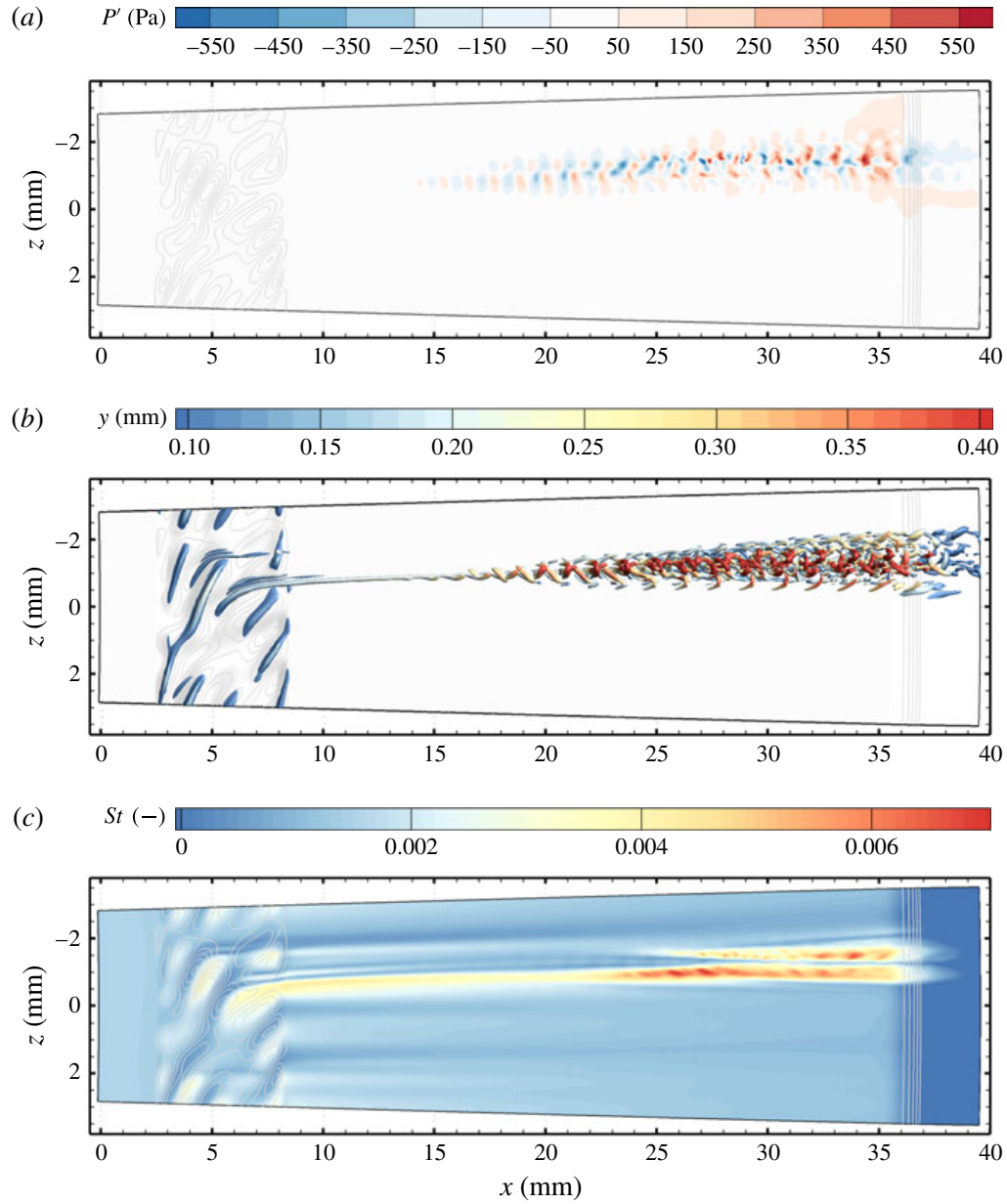
FIGURE 23. Representation of instantaneous disturbance pressure at the wall (*a*), vortical structures visualised with isosurfaces of $Q = 3 \times 10^{10}$ coloured by the distance from the wall (*b*) and instantaneous Stanton number (*c*).

variation of the absolute value of c_{ph} was found in the distance between the roughness and the onset of the secondary instabilities.

The transition location is also visible in the normalised heat flux at the wall (figure 23*c*). The local, instantaneous Stanton number is calculated as

$$St = \frac{\dot{q}}{\rho_\infty U_\infty (H_w - H_{tot})},$$ (4.2)

with $\dot{q}$ as the wall heat flux, U_∞ and ρ_∞ the free-stream velocity and density, H_{tot} the total enthalpy and H_w the wall enthalpy. A significant increase of the Stanton number is observed in the roughness wake due to the distortion of the flow induced by the
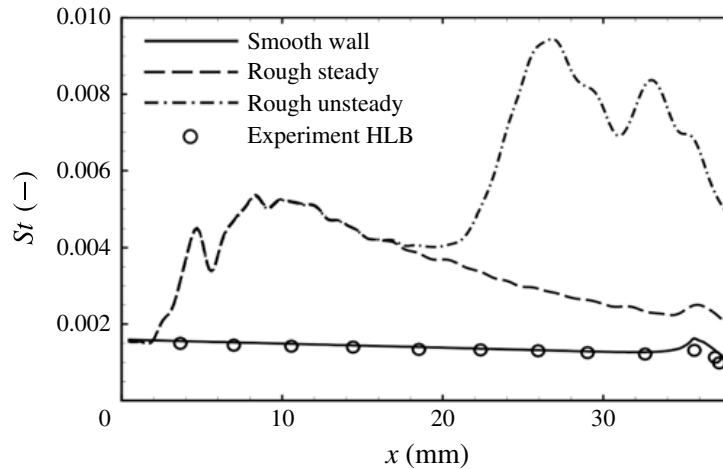
FIGURE 24. Values of the Stanton number.

steady vortices. As the cross-flow-type vortex weakens, the Stanton number decreases. A further and sudden increase is observed for $x > 21$ mm as a consequence of the ongoing laminar–turbulent transition. This behaviour is also illustrated in figure 24, which represents the maximum value in the spanwise direction of the time-averaged Stanton number found along the streamwise coordinate. The value of the Stanton number for the smooth wall configuration and for the steady simulation with a rough wall are shown for comparison. In addition, we represented the Stanton number measured in the experiments at HLB under the same free-stream conditions. These values are retrieved from Theiss *et al.* (2016) for the capsule model with highly polished surface and correspond to the Stanton number measured close to the shoulder on the lee side of the capsule. In the case of the rough wall, the Stanton number significantly increases at the roughness location to 3–4 times the smooth values. For the steady rough-wall case, the value of the Stanton number starts to decrease for $x > 10$ mm. In the case of unsteady simulation, a deviation from the steady case is observed at $x > 17$ mm, corresponding to the point where secondary modes become important (cf. figure 19). The laminar–turbulent transition occurs further downstream and can be identified by the sudden and steep increase of the Stanton number occurring at $x \approx 22$ mm. The Stanton number in the transition region rises to a threefold value compared to the steady rough case and can be significantly larger than the turbulent Stanton number.

Finally, we note that, in spite of the similar values of Re_{kk} and k/δ for both geometries investigated, the roughness wake in the case of the distributed roughness leads to larger amplification rates compared to the case of spanwise periodic roughness elements. In the case of the distributed roughness, the modes undergo a longer and larger amplification, with an observed N-factor with reference to the disturbance energy of approximately 13.2. In the case of the spanwise periodic roughness elements, the maximum amplification reached by the S-mode is smaller, with an N-factor of 9.6.

4.3. *Simulations with different roughness heights*

A parameter study with different roughness heights is carried out for the case of randomly distributed roughness. Different roughness patches are obtained by varying the value of k in (2.5). Amplitude and phase coefficients are the same as in table 4.
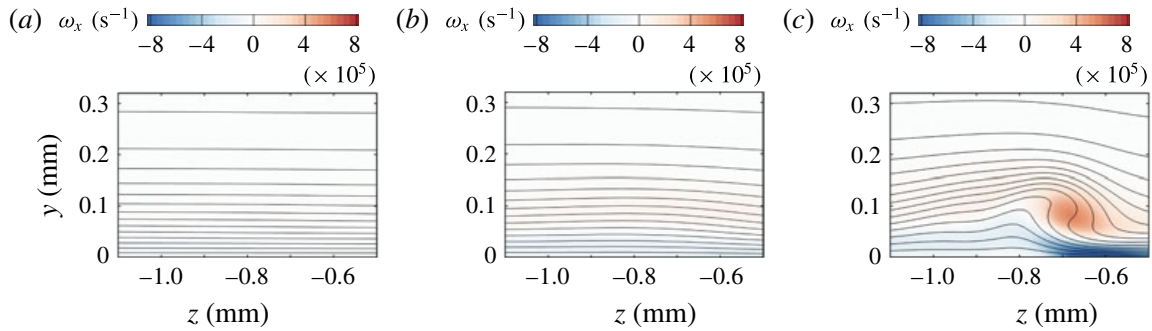
FIGURE 25. Colour contours of the streamwise vorticity and isolines of the streamwise velocity at $x = 8.6$ mm for distributed roughness with $k = 0.025$ mm (*a*), $k = 0.050$ mm (*b*) and $k = 0.075$ mm (*c*). Velocity levels are shown every 25 m s^{-1}.

k (mm)	$\bar{k}$ (mm)	k/δ	Re_{kk}
0.025	0.006	0.088	39
0.050	0.011	0.175	134
0.075	0.017	0.263	261

TABLE 6. Roughness variables for the distributed roughness investigated in the parameter study.

Three different roughness heights are additionally considered: $k = 0.025$, 0.050 and 0.750 mm. The corresponding roughness parameters are listed in table 6.

Figure 25 shows velocity and vorticity distributions in an y–z plane downstream of the roughness patch at $x = 8.6$ mm (cf. figure 16*b*). Only in the case of $k = 0.075$ mm does the roughness wake present a vortical structure which induces a significant distortion of the base flow. In the case of $k = 0.050$ mm a slight warping of the velocity isolines is visible downstream of the roughness patch, whereas almost no influence of the roughness at the considered position is visible for $k = 0.025$ mm.

The amplitude of the modes of the streamwise velocity for the perturbed frequency $f = 250$ kHz is shown in figure 26. For clarity, only the mode (1, 3) is shown (the same behaviour is observed for modes with same frequency and different wavenumber). The mode for the case of $k = 0.100$ mm is also shown for comparison. Only in the case of $k = 0.075$ mm does a significant amplification of the unsteady disturbance take place in the wake of the roughness. However, the roughness height is not large enough to generate a cross-flow-like vortex with characteristics similar to those analysed in § 4.2. As the generated vortex weakens downstream of the roughness patch, a positive growth rate of the disturbances is found in the vicinity of the roughness patch only. The observed N-factor is 8.5. For roughness heights smaller than 0.050 mm, the disturbance amplification is limited in the region of the roughness patch only. The generation of the cross-flow-type vortex is of a nonlinear nature as the roughness has to be high enough to induce enough vorticity to keep the vortex alive. In the case of small roughness heights, the structures appearing are not cross-flow-like and are attenuated too fast to be the source of an instability mechanism. Only for $k = 0.100$ mm does this mechanism kick in and cause breakdown.
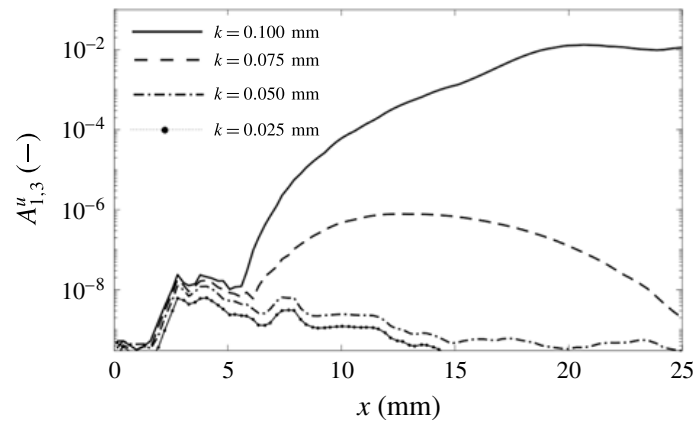
FIGURE 26. Amplitude of spatio-temporal Fourier modes (1, 3) of the streamwise velocity in the case of distributed roughness for different roughness heights. Values are normalised with the velocity at the boundary-layer edge $U = 359$ m s^{-1}.

5. Summary and conclusions

This work presents analysis and in-depth description of roughness-induced instabilities in the highly accelerated boundary layer of a capsule-like hemispherical forebody at $M = 5.9$. Direct numerical simulations have been performed to study the development of disturbances with a frequency of $f_1 = 250$ kHz introduced in the inflow boundary of the simulation domain. Previous studies showed that known instability mechanisms (such as TS-waves, Görtler-type instabilities, cross-flow instabilities and transient growth) cannot explain transition for the considered blunt-capsule configuration with a smooth wall. In this regard, the present work aimed at investigating the presence of instability mechanisms induced by roughness.

Two different types of roughness are analysed. In the first case, a spanwise periodic roughness element is modelled with a single-wavelength sinusoidal function of the surface. In the second case, the roughness patch is obtained by superposing different sinusoidal functions with pseudo-random amplitudes and phases. The maximum roughness height was $k = 0.1$ mm, with $k/\delta = 0.35$, for both geometries.

In the case of spanwise periodic roughness elements, two main unstable modes were found, corresponding to the symmetric and antisymmetric modes already known for the case of single roughness elements. The symmetric mode is more amplified than the antisymmetric mode if the recirculation zone is taken into account. An N-factor of up to 9.6 was found for the symmetric mode, whereas an N-factor of up to 7.3 was found for the antisymmetric mode. In the roughness wake, results from DNS were compared with results from PSE-3D analysis for validation and excellent agreement was achieved. Due to the strong acceleration of the flow, steady disturbances developing downstream of the roughness rapidly decay.

In the case of a randomly distributed roughness patch, the values of Re_{kk} for the local roughness peaks ranged from 87 to 406. The flow downstream of the roughness is characterised by separate vorticity regions, which originate at different peaks in the roughness. No significant amplification was observed in the wake of small roughness peaks with values of Re_{kk} up to 191. The only appreciable disturbance amplification was found in the wake of the highest protuberance of the patch. Here, the skewness of the roughness together with the subsequent depression introduce a spanwise component of the velocity, giving birth to a new roughness-induced cross-flow-like vortex for the blunt-capsule configuration. The base flow for the

smooth wall does not support modal cross-flow instabilities due to the insignificant component of the spanwise velocity. This cross-flow-type vortex greatly amplified the controlled unsteady disturbances introduced at the inflow boundary. The growth of the unsteady disturbances is characterised by the formation of finger-like vortical structures which wrap themselves alternatingly around both ascending and descending sides of the cross-flow-type vortex. Further downstream, these vortical structures evolve into horseshoe vortices and, eventually, lead to laminar–turbulent breakdown. The finger vortices on the descending side of the cross-flow-type vortex are related to high values of the spanwise velocity gradient and are not present in the cross-flow transition scenario in three-dimensional boundary layers.

Fourier modes of the forced frequency induce a nonlinear growth of higher frequency modes. The amplitude of higher modes reaches the amplitude of the forced modes at $x \approx 18$ mm, where growth saturation is observed. However, analysis of the Stanton number at the wall showed that laminar–turbulent transition takes place further downstream, for $x \approx 22$ mm, where a sudden and explosive increase can be observed.

The steady cross-flow-like vortex in the wake of the randomly distributed roughness is more persistent than the counter-rotating vortex pair in the wake of spanwise periodic roughness elements, in spite of the similar values of Re_{kk} and k/δ. The vortices generated by the spanwise periodic roughness elements decay fast and are extinguished within a few millimetres downstream of the roughness position in the strongly accelerated boundary layer. On the contrary, the main vortex generated by the randomly distributed roughness remains at a considerable amplitude in the domain up to the outflow boundary. As expected, a larger N-factor is found in the case of distributed roughness than in the case of periodic roughness elements. In fact, Re_{kk} does not take into account either the roughness shape or the presence of cavities surrounding the roughness peak. It was shown that certain roughness shapes with a skew profile with respect to the flow direction can induce vortices similar to cross-flow vortices as known from three-dimensional boundary-layer flows. Their breakdown characteristics in the flow presented here resemble those known from three-dimensional boundary layers, where cross-flow vortices are a result of the stability properties of the flow with a spanwise velocity component. In the case analysed here, the roughness acts as a local source of spanwise velocity. The downstream evolution of the cross-flow-type vortices shows minimal decay, but the vortex strength is still large enough to exhibit instability towards artificial disturbances as introduced in this study.

A parameter study conducted for different roughness heights revealed that for $k/\delta \leqslant 0.263$ and $Re_{kk} \leqslant 261$ the vortex downstream of the roughness patch does not exhibit the characteristics of the cross-flow-type vortex. Because of the rapid decay of the vortex downstream of the roughness patch, the disturbance amplification is limited to the region close to the roughness, with an N-factor of $N \leqslant 8.5$ for the investigated frequency. For re-entry vehicles, such as capsules with ablative TPS, the presence of distributed roughness is likely to be the normality rather than the exception. This work shows the necessity to account for roughness shapes on blunt bodies in the formulation of improved transition-prediction methods beyond Re_{kk}-based criteria taking into account, e.g. spanwise and downstream gradients of the roughness elements as a measure. Other factors of influence still have to be investigated and their quantitative influence on the laminar–turbulent process revealed. The breakdown of the cross-flow-type vortex as described in this paper provides a possible explanation of laminar–turbulent transition on the capsule with distributed roughness in the absence of modal instabilities and insufficient transient-growth rates.

REFERENCES

ALI, S. R., RADESPIEL, R. & THEISS, A. 2014 Transition experiment with a blunt Apollo shape like capsule in hypersonic Ludwieg tube. *63. Deutscher Luft-und Raumfahrtkongress 2014, Paper* 2014-340270.

BERGER, K. T. 2009 Aerothermodynamic testing of the crew exploration vehicle at Mach 6 and Mach 10. *J. Spacecr. Rockets* **46** (4), 758–765.

BREHM, C., DACKERMANN, T., GRYGIER, F. & FASEL, H. 2011 Numerical investigations of the influence of distributed roughness on Blasius boundary layer stability. *AIAA Paper* 2011-0563.

CHANG, C.-L., CHOUDHARI, M., VENKATACHARI, B. S. & LI, F. 2011 Effects of cavities and protuberances on transition over hypersonic vehicles. *AIAA Paper* 2011-3245.

CHOUDHARI, M., LI, F., BYNUM, M., KEGERISE, M. & KING, R. 2015 Computations of disturbance amplification behind isolated roughness elements and comparison with measurements. *AIAA Paper* 2015-2625.

DE TULLIO, N., PAREDES, P., SANDHAM, N. & THEOFILIS, V. 2013 Laminar–turbulent transition induced by a discrete roughness element in a supersonic boundary layer. *J. Fluid Mech.* **735**, 613–646.

DI GIOVANNI, A. & STEMMER, C. 2017 Numerical simulations of the high-enthalpy boundary layer on a generic capsule geometry with roughness. In *New Results in Numerical and Experimental Fluid Mechanics XI, STAB/DGLR Symposium* (ed. A. Dillmann *et al.*), pp. 189–198. Springer.

DOWNS, R. S., WHITE, E. B. & DENISSEN, N. A. 2008 Transient growth and transition induced by random distributed roughness. *AIAA J.* **46** (2), 451–462.

DREWS, S., DOWNS, R., DOOLITTLE, C., GOLDSTEIN, D. & WHITE, E. 2011 Direct numerical simulations of flow past random distributed roughness. *AIAA Paper* 2011-0564.

GOEBEL, F., VOS, J. & MUNDT, C. 2012 CFD simulation of the FIRE II flight experiment. *AIAA Paper* 2012-3350.

GRABOW, R. M. & WHITE, C. O. 1974 Surface roughness effects on nosetip ablation characteristics. In *7th Fluid and Plasma Dynamics Conference, Fluid Dynamics and Co-located Conferences*, American Institute of Aeronautics and Astronautics.

GROSKOPF, G. & KLOKER, M. J. 2016 Instability and transition mechanisms induced by skewed roughness elements in a high-speed laminar boundary layer. *J. Fluid Mech.* **805**, 262–302.

HEIN, S., THEISS, A., DI GIOVANNI, A., STEMMER, C., SCHILDEN, T., SCHRÖDER, W., PAREDES, P., CHOUDHARI, M. M., LI, F. & RESHOTKO, E. 2018 Numerical investigation of roughness effects on transition on spherical capsules. *AIAA Paper* 2018-0058.

HOARAU, Y., PENA, D., VOS, J. B., CHARBONIER, D., GEHRI, A., BRAZA, M., DELOZE, T. & LAURENDEAU, E. 2016 Recent developments of the Navier–Stokes Multi Block (NSMB) CFD solver. *AIAA Paper* 2016-2056.

HOLLIS, B. R. 2014 Distributed roughness effects on blunt-body transition and turbulent heating. *AIAA Paper* 2014-0238.

HOLLIS, B. R. 2017 Experimental investigation of roughness effects on transition onset and turbulent heating augmentation on a hemisphere at Mach 6 and Mach 10. *NASA Tech. Rep.* NASA/TM-2017-219613.

VON KAENEL, R., SANCHI, S., VOS, J., GAFFURI, M., LEYLAND, P., WALLOSCHEK, T. & BINETTI, P. 2009 IXV CFD simulations for wind tunnel rebuilding and extrapolation to flight. In *Proceedings of the 6th European Symposium on Aerothermodynamics for Space Vehicles, ESA SP-659*. ESTEC.

KEGERISE, M. A., KING, R. A., CHOUDHARI, M., LI, F. & NORRIS, A. 2014 An experimental study of roughness-induced instabilities in a supersonic boundary layer. *AIAA Paper* 2014-2501.

LANDAHL, M. T. 1980 A note on algebraic instability of inviscid parallel shear flows. Part 2. *J. Fluid Mech.* **98**, 243–251.

LEIDY, A. N., RESHOTKO, E., SIDDIQUI, F. & BOWERSOX, R. D. W. 2018 Transition due to roughness on blunt capsule: comparison with transient growth correlation. *J. Spacecr. Rockets* **55** (1), 167–180.

LEVY, Y., DEGANI, D. & SEGINER, A. 1990 Graphical visualization of vortical flows by means of helicity. *AIAA J.* **28** (8), 1347–1352.

MACK, L. M. 1969 Boundary layer stability theory. *JPL Rep.* 900-277. Jet Propulsion Laboratory, California Institute of Technology, Pasadena, CA, USA.

MALIK, M. R., LI, F. & CHANG, C.-L. 1994 Crossflow disturbances in three-dimensional boundary layers: nonlinear development, wave interaction and secondary instability. *J. Fluid Mech.* **268**, 1–36.

MALIK, M. R., LI, F., CHOUDHARI, M. M. & CHANG, C.-L. 1999 Secondary instability of crossflow vortices and swept-wing boundary-layer transition. *J. Fluid Mech.* **399**, 85–115.

MORKOVIN, M. V. 1984 Bypass transition to turbulence and research desiderata. *Transition in Turbines* **NASA CP-2386**, 161–199.

MUPPIDI, S. & MAHESH, K. 2012 Direct numerical simulations of roughness-induced transition in supersonic boundary layers. *J. Fluid Mech.* **693**, 28–56.

PAREDES, P., CHOUDHARI, M. M. & LI, F. 2017 Blunt-body paradox and transient growth on a hypersonic spherical forebody. *Phys. Rev. Fluids* **2**, 053903.

RADESPIEL, R., ALI, S. R., BOWERSOX, R. D., LEIDY, A., TANNO, H., KIRK, L. C. & RESHOTKO, E. 2018 Experimental investigations of roughness effects on transition on blunt spherical capsule shapes. *AIAA Paper* 2018-0059.

REDA, D. C. 2002 Review and synthesis of roughness-dominated transition correlations for reentry applications. *J. Spacecr. Rockets* **39** (2), 161–167.

REDA, D. C., WILDER, M. C., BOGDANOFF, D. W. & PRABHU, D. K. 2008 Transition experiments on blunt bodies with distributed roughness in hypersonic free flight. *J. Spacecr. Rockets* **45** (2), 210–215.

RESHOTKO, E. & TUMIN, A. 2000 The blunt body paradox: a case for transient growth. In *Laminar–Turbulent Transition: IUTAM Symposium* (ed. H. Fasel & W. Saric), pp. 403–408. Springer.

RESHOTKO, E. & TUMIN, A. 2004 Role of transient growth in roughness-induced transition. *AIAA J.* **42** (4), 766–770.

SCHNEIDER, S. P. 2008*a* Effects of roughness on hypersonic boundary-layer transition. *J. Spacecr. Rockets* **45** (2), 193–209.

SCHNEIDER, S. P. 2008*b* Summary of hypersonic boundary-layer transition experiments on blunt bodies with roughness. *J. Spacecr. Rockets* **45** (6), 1090–1105.

STEMMER, C., BIRRER, M. & ADAMS, N. A. 2017*a* Disturbance development in an obstacle wake in a reacting hypersonic boundary layer. *J. Spacecr. Rockets* **54** (4), 945–960.

STEMMER, C., BIRRER, M. & ADAMS, N. A. 2017*b* Hypersonic boundary-layer flow with an obstacle in thermochemical equilibrium and nonequilibrium. *J. Spacecr. Rockets* **54** (4), 899–915.

STEMMER, C. & FEHN, J. 2014 High-temperature gas effects at a capsule under re-entry and wind-tunnel conditions. *AIAA Paper* 2014-2645.

THEISS, A., ALI, S. R., HEIN, S., HEITMANN, D. & RADESPIEL, R. 2014 Numerical and experimental investigation of laminar–turbulent boundary layer transition on a blunt generic re-entry capsule. *AIAA Paper* 2014-2353.

THEISS, A., HEIN, S., ALI, S. R. C. & RADESPIEL, R. 2016 Wake flow instability studies behind discrete roughness elements on a generic re-entry capsule. *AIAA Paper* 2016-4382.

THEISS, A., LEYH, S. & HEIN, S. 2017 Pressure gradient effects on wake flow instabilities behind isolated roughness elements on re-entry capsules. In *7th European Conference for Aeronautics and Aerospace Sciences.* EUCASS.

VAN DEN EYNDE, J. P. J. P. & SANDHAM, N. D. 2016 Numerical simulations of transition due to isolated roughness elements at Mach 6. *AIAA J.* **54**, 53–65.

VOS, J., DUQUESNE, N. & LEE, H. 1999 Shock wave boundary layer interaction studies using the NSMB flow solver. In *Proceedings of the 3rd European Symposium on Aerothermodynamics for Space and Vehicles, ESA SP-426*, pp. 229–236. ESTEC.

WASSERMANN, P. & KLOKER, M. 2002 Mechanisms and passive control of crossflow-vortex-induced transition in a three-dimensional boundary layer. *J. Fluid Mech.* **456**, 49–84.

WILDER, M. C., REDA, D. & PRABHU, D. K. 2015 Transition experiments on blunt bodies with distributed roughness in hypersonic free flight in carbon dioxide. *AIAA Paper* 2015-1738.

B.2 Roughness-Induced Crossflow-Type Instabilities in a Hypersonic Capsule Boundary Layer Including Nonequilibrium

3.1 All Works and all rights therein, including copyright rights, remain the sole and exclusive property of the Rightsholder. The license created by the exchange of an Order Confirmation (and/or any invoice) and payment by User of the full amount set forth on that document includes only those rights expressly set forth in the Order Confirmation and in these terms and conditions, and conveys no other rights in the Work(s) to User. All rights not expressly granted are hereby reserved.

3.2 General Payment Terms: You may pay by credit card or through an account with us payable at the end of the month. If you and we agree that you may establish a standing account with CCC, then the following terms apply: Remit Payment to: Copyright Clearance Center, 29118 Network Place, Chicago, IL 60673-1291. Payments Due: Invoices are payable upon their delivery to you (or upon our notice to you that they are available to you for downloading). After 30 days, outstanding amounts will be subject to a service charge of 1-1/2% per month or, if less, the maximum rate allowed by applicable law. Unless otherwise specifically set forth in the Order Confirmation or in a separate written agreement signed by CCC, invoices are due and payable on "net 30" terms. While User may exercise the rights licensed immediately upon issuance of the Order Confirmation, the license is automatically revoked and is null and void, as if it had never been issued, if complete payment for the license is not received on a timely basis either from User directly or through a payment agent, such as a credit card company.

3.3 Unless otherwise provided in the Order Confirmation, any grant of rights to User (i) is "one-time" (including the editions and product family specified in the license), (ii) is non-exclusive and non-transferable and (iii) is subject to any and all limitations and restrictions (such as, but not limited to, limitations on duration of use or circulation) included in the Order Confirmation or invoice and/or in these terms and conditions. Upon completion of the licensed use, User shall either secure a new permission for further use of the Work(s) or immediately cease any new use of the Work(s) and shall render inaccessible (such as by deleting or by removing or severing links or other locators) any further copies of the Work (except for copies printed on paper in accordance with this license and still in User's stock at the end of such period).

3.4 In the event that the material for which a republication license is sought includes third party materials (such as photographs, illustrations, graphs, inserts and similar materials) which are identified in such material as having been used by permission, User is responsible for identifying, and seeking separate licenses (under this Service or otherwise) for, any of such third party materials; without a separate license, such third party materials may not be used.

3.5 Use of proper copyright notice for a Work is required as a condition of any license granted under the Service. Unless otherwise provided in the Order Confirmation, a proper copyright notice will read substantially as follows: "Republished with permission of [Rightsholder's name], from [Work's title, author, volume, edition number and year of copyright]; permission conveyed through Copyright Clearance Center, Inc. " Such notice must be provided in a reasonably legible font size and must be placed either immediately adjacent to the Work as used (for example, as part of a by-line or footnote but not as a separate electronic link) or in the place where substantially all other credits or notices for the new work containing the republished Work are located. Failure to include the required notice results in loss to the Rightsholder and CCC, and the User shall be liable to pay liquidated damages for each such failure equal to twice the use fee specified in the Order Confirmation, in addition to the use fee itself and any other fees and charges specified.

3.6 User may only make alterations to the Work if and as expressly set forth in the Order Confirmation. No Work may be used in any way that is defamatory, violates the rights of third parties (including such third parties' rights of copyright, privacy, publicity, or other tangible or intangible property), or is otherwise illegal, sexually explicit or obscene. In addition, User may not conjoin a Work with any other material that may result in damage to the reputation of the Rightsholder. User agrees to inform CCC if it becomes aware of any

infringement of any rights in a Work and to cooperate with any reasonable request of CCC or the Rightsholder in connection therewith.

4. Indemnity. User hereby indemnifies and agrees to defend the Rightsholder and CCC, and their respective employees and directors, against all claims, liability, damages, costs and expenses, including legal fees and expenses, arising out of any use of a Work beyond the scope of the rights granted herein, or any use of a Work which has been altered in any unauthorized way by User, including claims of defamation or infringement of rights of copyright, publicity, privacy or other tangible or intangible property.

5. Limitation of Liability. UNDER NO CIRCUMSTANCES WILL CCC OR THE RIGHTSHOLDER BE LIABLE FOR ANY DIRECT, INDIRECT, CONSEQUENTIAL OR INCIDENTAL DAMAGES (INCLUDING WITHOUT LIMITATION DAMAGES FOR LOSS OF BUSINESS PROFITS OR INFORMATION, OR FOR BUSINESS INTERRUPTION) ARISING OUT OF THE USE OR INABILITY TO USE A WORK, EVEN IF ONE OF THEM HAS BEEN ADVISED OF THE POSSIBILITY OF SUCH DAMAGES. In any event, the total liability of the Rightsholder and CCC (including their respective employees and directors) shall not exceed the total amount actually paid by User for this license. User assumes full liability for the actions and omissions of its principals, employees, agents, affiliates, successors and assigns.

6. Limited Warranties. THE WORK(S) AND RIGHT(S) ARE PROVIDED "AS IS". CCC HAS THE RIGHT TO GRANT TO USER THE RIGHTS GRANTED IN THE ORDER CONFIRMATION DOCUMENT. CCC AND THE RIGHTSHOLDER DISCLAIM ALL OTHER WARRANTIES RELATING TO THE WORK(S) AND RIGHT(S), EITHER EXPRESS OR IMPLIED, INCLUDING WITHOUT LIMITATION IMPLIED WARRANTIES OF MERCHANTABILITY OR FITNESS FOR A PARTICULAR PURPOSE. ADDITIONAL RIGHTS MAY BE REQUIRED TO USE ILLUSTRATIONS, GRAPHS, PHOTOGRAPHS, ABSTRACTS, INSERTS OR OTHER PORTIONS OF THE WORK (AS OPPOSED TO THE ENTIRE WORK) IN A MANNER CONTEMPLATED BY USER; USER UNDERSTANDS AND AGREES THAT NEITHER CCC NOR THE RIGHTSHOLDER MAY HAVE SUCH ADDITIONAL RIGHTS TO GRANT.

7. Effect of Breach. Any failure by User to pay any amount when due, or any use by User of a Work beyond the scope of the license set forth in the Order Confirmation and/or these terms and conditions, shall be a material breach of the license created by the Order Confirmation and these terms and conditions. Any breach not cured within 30 days of written notice thereof shall result in immediate termination of such license without further notice. Any unauthorized (but licensable) use of a Work that is terminated immediately upon notice thereof may be liquidated by payment of the Rightsholder's ordinary license price therefor; any unauthorized (and unlicensable) use that is not terminated immediately for any reason (including, for example, because materials containing the Work cannot reasonably be recalled) will be subject to all remedies available at law or in equity, but in no event to a payment of less than three times the Rightsholder's ordinary license price for the most closely analogous licensable use plus Rightsholder's and/or CCC's costs and expenses incurred in collecting such payment.

8. **Miscellaneous.**

8.1 User acknowledges that CCC may, from time to time, make changes or additions to the Service or to these terms and conditions, and CCC reserves the right to send notice to the User by electronic mail or otherwise for the purposes of notifying User of such changes or additions; provided that any such changes or additions shall not apply to permissions already secured and paid for.

8.2 Use of User-related information collected through the Service is governed by CCC's privacy policy, available online here:
http://www.copyright.com/content/cc3/en/tools/footer/privacypolicy.html.

8.3 The licensing transaction described in the Order Confirmation is personal to User. Therefore, User may not assign or transfer to any other person (whether a natural person or

an organization of any kind) the license created by the Order Confirmation and these terms and conditions or any rights granted hereunder; provided, however, that User may assign such license in its entirety on written notice to CCC in the event of a transfer of all or substantially all of User's rights in the new material which includes the Work(s) licensed under this Service.

8.4 No amendment or waiver of any terms is binding unless set forth in writing and signed by the parties. The Rightsholder and CCC hereby object to any terms contained in any writing prepared by the User or its principals, employees, agents or affiliates and purporting to govern or otherwise relate to the licensing transaction described in the Order Confirmation, which terms are in any way inconsistent with any terms set forth in the Order Confirmation and/or in these terms and conditions or CCC's standard operating procedures, whether such writing is prepared prior to, simultaneously with or subsequent to the Order Confirmation, and whether such writing appears on a copy of the Order Confirmation or in a separate instrument.

8.5 The licensing transaction described in the Order Confirmation document shall be governed by and construed under the law of the State of New York, USA, without regard to the principles thereof of conflicts of law. Any case, controversy, suit, action, or proceeding arising out of, in connection with, or related to such licensing transaction shall be brought, at CCC's sole discretion, in any federal or state court located in the County of New York, State of New York, USA, or in any federal or state court whose geographical jurisdiction covers the location of the Rightsholder set forth in the Order Confirmation. The parties expressly submit to the personal jurisdiction and venue of each such federal or state court.If you have any comments or questions about the Service or Copyright Clearance Center, please contact us at 978-750-8400 or send an e-mail to info@copyright.com.

v 1.1

Roughness-Induced Crossflow-Type Instabilities in a Hypersonic Capsule Boundary Layer Including Nonequilibrium

Antonio Di Giovanni* and Christian Stemmer†

Technical University of Munich, 85748 Garching, Germany

DOI: 10.2514/1.A34404

The current study investigates the unsteady disturbance development in a three-dimensional, high-enthalpy boundary layer on a capsule-like hemispherical geometry with pseudo-random distributed roughness. Direct Numerical Simulations are conducted for a typical reentry scenario at $M = 20$ where chemical dissociation takes place. Unsteady disturbances at various frequencies are introduced into the flow to analyze the instabilities developing in the wake of the roughness patch. The amplification of small disturbances is shown for various chemical models (i.e., chemical equilibrium, chemical nonequilibrium, and thermochemical nonequilibrium). The largest disturbance amplification is observed for a crossflow-type vortex developing in the wake of the highest skewed protuberance of the roughness patch. The modes of instability of this crossflow-type vortex are analyzed and compared for different frequencies. The influence of the different nonequilibrium effects on the steady base flow as well as on the disturbance development is quantified and compared. The study highlights the necessity to include nonequilibrium effects in transitional scenarios as the unsteady development of the instabilities are affected strongly by the chemical modeling.

Nomenclature

$A_{q,r}$	=	amplitude coefficients used in the roughness definition
$c(y)$	=	smoothing function used in the definition of the unsteady disturbance
c_s	=	species concentration
E_K	=	integral value of the disturbance kinetic energy over a y–z plane, J/m
e_k	=	local value of the disturbance kinetic energy, J/m^3
e^{vib}	=	vibrational energy, J/kg
f_{1-6}	=	frequencies of the unsteady inflow disturbances, Hz
$g(x)$	=	envelope function used in the roughness definition
h	=	surface height with respect to the smooth configuration, m
k	=	roughness height, m
M	=	Mach number
M_s	=	molar mass, kg/mol
N	=	N-factor
N_{tot}	=	total number of grid points
N_x, N_y, N_z	=	number of grid points in x, y, and z directions
n_y^δ	=	number of grid points within the boundary layer in y direction
p	=	pressure, N/m^2
Q^{chem}	=	heat transfer due to chemical reactions, J/(kg · s)
Q^{t-v}	=	translational-vibrational heat transfer, J/(kg · s)
q^{vib}	=	heat-conduction term based on the vibrational temperature, J/(kg · s)
$\dot{q}$	=	heat flux at the wall, W/m^2
R_a	=	mean roughness, m
$R_\circ$	=	universal gas constant, J/(mol · K)
Re_{kk}	=	roughness Reynolds number
Re_∞	=	unit Reynolds number, m^{-1}
$\tilde{r}$	=	distance from the center of the hemisphere, m
T	=	temperature, K
U	=	reference velocity, m/s
u, v, w	=	velocities in x, y, and z directions, m/s
$\boldsymbol{u}_s^D$	=	diffusion velocity of the species s, m/s
x, y, z	=	coordinates in streamwise, wall-normal, and spanwise directions, m
x_0	=	x coordinate at the inflow boundary
α	=	amplitude coefficients used in the definition of the unsteady disturbance
δ	=	boundary-layer thickness, m
θ_1	=	elevation angle, rad
θ_2	=	azimuth, rad
λ_0	=	fundamental roughness wavelength, m
μ	=	viscosity, kg/(m · s)
ρ	=	density, kg/m^3
σ_K	=	growth rate computed with the integral disturbance kinetic energy, m^{-1}
ϕ	=	phase
ω_x	=	streamwise vorticity, s^{-1}
$\dot{\omega}_s$	=	species chemical production rate, kg/(m^3 · s)

Subscripts

e	=	value taken at the boundary-layer edge
f	=	frequency in the Fourier analysis
i, j	=	summation indices
k	=	value taken at the height of the roughness
m	=	molecular species
max	=	maximum value
min	=	minimum value
q	=	multiples of the fundamental roughness wavenumber in x direction
r	=	multiples of the fundamental roughness wavenumber in z direction
s	=	species
st	=	condition of the steady base flow

Superscripts

$*$	=	value at the inflow boundary of the unsteady-simulation domain
$\hat{\ }$	=	temporal Fourier mode

*Ph.D. Candidate, Chair of Aerodynamics and Fluid Mechanics, Boltzmannstr. 15.

†Privatdozent, Adjunct Teaching Professor, Chair of Aerodynamics and Fluid Mechanics, Boltzmannstr. 15.

I. Introduction

RENTRY capsules are equipped with thermal protection systems (TPS) to protect instruments and crew members against the extreme aerodynamic heating experienced during the reentry phase. Because the heat-transfer rate at the capsule wall in the case of a turbulent boundary layer can be much higher than the one in the laminar case, prediction of laminar-turbulent transition of the boundary layer at hypersonic speeds is a critical issue in the design of the TPS. Several studies showed that the boundary layer of smooth-wall blunt-capsule configurations is stable against first- and second-mode instabilities as well as against crossflow and Görtler-vortex instability mechanisms [1–3]. Therefore, laminar-turbulent transition observed on such configurations under both wind-tunnel and free-flight experiments is believed to be mainly affected by surface roughness. Distributed roughness is present on the surface of reentry vehicles as a result of ablation of the TPS, thermal surface deformation, and manufacturing uncertainties.

A large number of publications on experimental investigations conducted on capsule-like models with rough wall exist for flight-relevant Reynolds numbers. However, further numerical investigations based on high-fidelity computational methods are still needed [4]. Compared with stability analyses, such as linear stability theory (LST) and parabolized stability equations (PSE), Direct Numerical Simulations (DNS) allow for investigations on more complex geometries and provide a more complete insight into nonlinear mechanisms, including laminar-turbulent breakdown. Furthermore, for the flight conditions in altitudes where transition is expected, high-temperature gas effects, such as chemical reactions and non-equilibrium effects, are nonnegligible [5]. The Damköhler number, defined as the ratio between the timescales of chemical reactions and the convection timescale, quantifies the degree of nonequilibrium in the flow. Because wind-tunnel experiments at realistic reentry conditions matching all relevant dimensionless parameters, including the Damköhler number, cannot be realized, numerical simulations represent an important and often indispensable investigation tool.

Previous experimental investigations on rough blunt bodies encompass the measurements made at NASA Langley Research Center (LaRC) both on scaled models of the Crew Exploration Vehicle (CEV) [6] and on hemisphere geometries with distributed roughnesses [7,8]. The works of Reda [9,10] highlighted the correlation existing between transition and a roughness Reynolds number $Re_{kk} = \rho_k u_k k / \mu_k$, defined with the flow properties at the roughness height for the corresponding smooth configuration. Experimental and numerical investigations for an Apollo-like capsule with a diameter of 17 cm at a Mach number of $M = 5.9$ have been conducted for the Hypersonic Ludwieg Tube in Braunschweig [2,11,12]. Different inflow Reynolds numbers were considered. Compared with the numerically computed laminar case, an increase of the surface heating was observed at the rough wall with a mean roughness value of $R_a = 10 \; \mu m$ for a unit Reynolds number of $Re_\infty = 18 \cdot 10^6 \; m^{-1}$. The flow was not regarded as fully turbulent for the Reynolds number considered. No evidence of transitional flow was observed for the highly polished smooth-surface model at the same conditions.

An experimental campaign was undertaken at the T5 Hypervelocity Shock Tunnel at GALCIT for the reacting high-enthalpy flow on a Apollo capsule model of 17.78 cm diameter, with stagnation enthalpies in the range of 7–20 MJ/kg [13]. Natural transition was observed on the smooth geometry for $Re_\infty = 0.9 \cdot 10^6 \; m^{-1}$ and a stagnation enthalpy of 10 MJ/kg. Application of trips with a height between 0.5 and 1 boundary-layer thicknesses resulted in an increase of the heat transfer at the wall downstream of the trips beyond the fully turbulent values, followed by a relaxation to the turbulent heat-transfer values. In addition, experimental results were compared with the results of turbulent nonequilibrium computations revealing the level of nonequilibrium present in the tunnel. Further experimental investigations of the surface heating for an Apollo-capsule geometry of 15 cm diameter were conducted at the free-piston shock tunnel HIEST [14,15]. Mach numbers in the range of 6–8 and Reynolds numbers between 10^5 and $5 \cdot 10^6 \; m^{-1}$ were considered.

No hint of transition was found for the smooth geometry. However, an increase in the normalized heat flux at the stagnation point was measured for the high-enthalpy conditions. The nature of this heat-flux augmentation, also observed in other facilities (see, e.g., [16]), was unclear. A detailed review of further available experimental data on roughness-induced transition on hypersonic blunt bodies is presented by Schneider [4].

Numerically, roughness-induced transition on reentry capsules under cold freestream conditions was investigated by Chang et al. [17] for the CEV geometry at $M = 6$. In correspondence of a protuberance of $Re_{kk} = 800$ and a height–to–boundary-layer thickness ratio of 0.73, a spontaneous vortex shedding is present in the roughness wake. The effects of protuberances on the instability of the boundary layer were shown to be more effective than the effects of cavities of identical geometry. Theiss et al. [18,19] investigated the modal instability of the steady wake of isolated roughness elements positioned on the windward side of an Apollo capsule model for freestream conditions matching the inflow conditions of HLB. Analyses based on LST and PSE showed that the instability mechanisms in the roughness wake are characterized by the presence of unstable modes featuring the symmetric and antisymmetric modes already known for the case of isolated roughness element on a flat plate [20].

An extensive number of stability studies of high-enthalpy boundary layers, including high-temperature gas effects, have been conducted for the flat-plate and cone configurations. Malik and Anderson [5] used LST to investigate the modal instability mechanisms for a two-dimensional flat plate at $M = 10$ and $M = 15$. It was found that, compared with boundary-layer profiles obtained with the assumption of ideal gas, the incorporation of chemistry stabilizes the first-mode instability, whereas it destabilizes the second-mode instability. Following the studies of Malik and Anderson [5], Hudson et al. [21,22] extended the analysis incorporating both thermal and chemical nonequilibrium effects. The first mode resulted to be more unstable in the thermochemical nonequilibrium case than in the chemical nonequilibrium case, with air in chemical equilibrium being the most unstable among the reacting-gas cases. With regard to the second mode, the effects of thermal nonequilibrium were found to be slightly stabilizing, whereas the effects of chemical nonequilibrium were slightly destabilizing compared with the case of equilibrium gas. These results were later numerically confirmed by the work of Chang et al. [23], who additionally addressed the effects of supersonic modes in the case of a 6-deg wedge at $M = 20$. Both chemical equilibrium and chemical nonequilibrium were considered in their PSE-based analysis. An enhanced growth of supersonic modes was found in the case of air in chemical equilibrium compared with the ideal-gas and non-equilibrium cases. The presence of a cuboid roughness element in the reacting boundary layer of the HyBoLT geometry ($M = 8.5$) was investigated by Stemmer et al. [24,25]. It was shown that a pair of longitudinal vortices originating at the roughness transport hot fluid toward the wall, resulting in elongated streaks in the roughness wake with increased wall heat transfer. The peak of wall heat-transfer augmentation in the wake of the cuboid was found to be larger for the case of equilibrium air compared with nonequilibrium air. In the far field, the wall heat-transfer for nonequilibrium air overtook the values of the wall heat-transfer for equilibrium air. Furthermore, the amplification rate of unsteady disturbances was larger for chemical nonequilibrium than for chemical equilibrium. LST-based analyses revealed that, under the assumption of ideal gas, the antisymmetric mode of instability presents larger amplification rates compared with the symmetric mode. The inverse situation was observed after incorporation of chemical reactions.

Stability analysis of the high-enthalpy flow on a sharp cone was conducted by Johnson et al. [26]. They found that the transitional Reynolds number increases with the freestream total enthalpy, with the rate of increase being greater for gases with lower dissociation energy. The change in the mean-flow profiles due to the presence of chemical dissociation was regarded as a further aspect associated to the stability properties of the boundary layer. Malik [27] conducted a numerical study of the high-temperature boundary layer of the Reentry-F experiment (5-deg cone). In this case, transition was

caused by the amplification of the second mode and the comparison with numerical simulations performed using the model of ideal gas remarked the destabilizing effect of chemical dissociation. Johnson and Candler [28] considered the same geometry from the Reentry-F experiment and extend the analysis including thermal non-equilibrium. In spite of the slightly different boundary-layer profiles deriving from the inclusion of nonequilibrium, similar N-factors were found as in the case of thermal equilibrium. The case of a 7-deg blunt cone at $M = 16$ was investigated by Mortensen and Zhong [29], who separately considered the destabilizing effects of high-temperature gas effects, the inclusion of carbon species in the medium composition as a result of the surface ablation, and the blowing at the wall.

For the Apollo-capsule geometry, the influence of gas modeling on the profiles of a steady, laminar boundary layer under realistic reentry conditions was studied by Stemmer and Fehn [30]. The inclusion of chemistry was found to significantly reduce the edge velocity while also increasing the boundary-layer thickness. The velocity profiles for the considered reacting-gas models were all very similar. Compared with the model of gas in chemical nonequilibrium, the model of gas in thermochemical nonequilibrium induced an increase of the temperature gradient at the wall. Further analyses on a similar Apollo-capsule geometry at an angle of attack and with the same freestream conditions were presented by Di Giovanni and Stemmer [31]. Both cases of smooth and rough walls were considered. In the case of ideal gas, the boundary layer was significantly smaller than in the reacting-gas case. As a result, larger steady disturbances developed in the roughness wake when the model of ideal gas was used. Furthermore, the damping rate of steady disturbances downstream of the roughness patch was found to be larger after inclusion of non-equilibrium for the studied configuration.

The stability of the boundary layer on a spherical forebody with a patch of random distributed roughness was investigated by Di Giovanni and Stemmer [32]. A hemisphere with a radius of 20 cm was considered and the freestream conditions matched the wind-tunnel conditions of the Hypersonic Ludwieg Tube in Braunschweig at $M = 5.9$. It was observed that a crossflow-type vortex develops in the wake of a roughness protuberance with a skew profile with respect to the main flow direction. This crossflow-type vortex is significantly more persistent than the pair of counter-rotating vortices originating at symmetrical roughness elements with the same height and roughness Reynolds number. Accordingly, a stronger amplification of forced disturbances was found and transition mechanisms known from the breakdown of crossflow vortices in three-dimensional subsonic boundary layers were observed.

In the present work we investigate the instability mechanisms in the high-enthalpy boundary layer of a hemisphere geometry in the presence of distributed roughness. The considered geometry corresponds to the one used in [32] for investigations under wind-tunnel conditions. The radius of the hemisphere is about 6 m and is chosen to match the size of a realistic reentry capsule. A set of simulations are conducted for freestream conditions in a typical reentry scenario at $M = 20$. DNS are undertaken to analyze and quantify the development of unsteady disturbances forced at the inflow boundary. By gradually including chemical and thermal nonequilibrium in the reacting boundary layer, the effects of the high temperatures on the stability of the boundary layer in the wake of the roughness are analyzed and compared for three gas models (i.e., chemical equilibrium, chemical nonequilibrium, and thermo-chemical nonequilibrium). First, the flow topology of the steady, laminar boundary layer downstream of the roughness patch is described. Then, the growth of small disturbances is quantified and compared for the different gas models and different frequencies.

II. Numerical Procedure

To ease off the total computational effort, the computation is sequentially performed on three geometries, starting from the full configuration and zooming in on the roughness. First, the entire two-dimensional hemispherical domain is considered. Steady laminar simulations of the smooth-wall geometry include the bow shock

ahead of the blunt body. Second, the results on the full domain are used to generate the boundary conditions for a three-dimensional restricted domain. The wall of the second domain is equipped with a patch of distributed roughness that gives birth to steady vortical structures in the boundary layer. The procedure of extracting a restricted domain from the axisymmetric computation for the unsteady simulations on a rough wall has already been successfully verified and presented in [32]. Furthermore, it was shown that the interaction between the small roughness and the incoming linear disturbances introduced upstream of the roughness is weak and the nonlinear generation of higher harmonics of the forced frequency at the roughness location can be excluded. Hence, in the present work a further restriction of the domain is performed and the roughness patch is excluded from the unsteady simulations of disturbances forced downstream of the roughness patch.

The height of the roughness is about one fifth of the boundary-layer thickness with values of the roughness Reynolds number not larger than 244. For these values, the roughness is not effective, in the sense used by Reda [9] and Schneider [33], where the term *effective* is used to describe a roughness that triggers transition as close as possible to the roughness location. Instead, for the present geometry the roughness generates a wake with a potential unstable shear layer where linear growth of small disturbances can be observed. We remark that, as observed in [32,34], the nature of the unstable modes and the growth rate of instabilities in the roughness wake depend not only on the values of Re_{kk} and k/δ, but also on other roughness features, such as the shape of the roughness in detail. The potential onset of secondary instabilities occurs further downstream in the roughness wake. A grid-convergence study is also included.

A. Governing Equations

As the temperature downstream of the bow shock reaches up to 6000 K, the model of ideal gas is not appropriate any more. Instead, the flow is characterized by chemical reactions and nonequilibrium effects. To highlight the different effects of the high temperature, simulations are performed with three different gas models. Starting with the model of gas in chemical equilibrium, we gradually include in the simulations chemical nonequilibrium and thermal non-equilibrium.

A Park's two-temperature model for air consisting of five species (N_2, O_2, N, O, NO) is used [35]. Each species is treated as an ideal gas and the equation of state of the gas mixture is given by

$$p = \rho R_\circ T \sum_s \frac{c_s}{M_s} \qquad (1)$$

where p and ρ are pressure and density of the gas mixture, T the equilibrium temperature, $R_\circ$ the universal gas constant, $c_s = \rho_s/\rho$ the concentration, and M_s the molar mass of the species s.

To compute the composition of air in chemical equilibrium (CEQ), three algebraic equations are solved for the dissociation of molecular species (laws of mass action) and two algebraic equations are solved for the conservation of the elements O and N. In the case of air in chemical nonequilibrium (CNEQ), the Navier-Stokes equations are supplemented by differential equations describing the mass balance of the chemical species involved,

$$\rho \frac{D c_s}{Dt} + \nabla \cdot (\rho_s \boldsymbol{u}_s^D) = \dot{\omega}_s \qquad (2)$$

where $\dot{\omega}_s$ are the chemical production terms and $\boldsymbol{u}_s^D$ is the diffusion velocity of the species s. The chemical production terms follow an Arrhenius-type relation, whereas the diffusion is described by Fick's law, assuming a constant Schmidt number with the diffusion coefficients independent of the species concentration.

For the gas in thermochemical nonequilibrium (CTNEQ), an additional energy-conservation equation is solved for the vibrational energy e_m^{vib} of each molecular species m,

$$\frac{D}{Dt}(c_m e_m^{\text{vib}}) + \frac{1}{\rho}\nabla\cdot(\rho_m \boldsymbol{u}_m^D e_m^{\text{vib}}) = -q_m^{\text{vib}} + Q_m^{t-v} + Q_m^{\text{chem}} \qquad (3)$$

where q_m^{vib} describes the heat-conduction term, Q_m^{t-v} the translational-vibrational energy transfer rate, and Q_m^{chem} the source term due to reactions of the species m. Once e_m^{vib} is solved from the system in Eq. (3), three vibrational temperatures T_m^{vib} can be derived for the three molecular species, assuming

$$e_m^{\text{vib}} = \frac{\Theta_m}{e^{\Theta_m/T_m^{\text{vib}}} - 1}\frac{R_\circ}{M_m} \qquad (4)$$

where Θ_m is a constant depending on the molecular species m [36].

The viscosities of the single species are calculated according to Blottner et al. [37], the species' thermal conductivities are calculated according to Hirschfelder et al. [38] and the thermodynamic properties of the gas mixture are computed with Wilke's mixing rules [39]. For further details on the governing equations and on the modeling of the physical and thermal coefficients as applied in this work, see Stemmer et al. [24].

B. Simulations of the Full Domain

The hemisphere (Fig. 1) has a radius of 5.981 m and an angular extension of 90.8° and ends in a shoulder that resembles the one of a generic Apollo capsule. The size and the shoulder shape are chosen to feature a realistic capsule geometry. The similarity between the flow on an Apollo-capsule model and the flow on the present hemispherical geometry has been already shown by Hein et al. [3]. Furthermore, the shoulder provides a natural damping region at the outflow for the unsteady disturbances. The domain is two-dimensional and axisymmetric. The grid consists of about 80,000 points clustered inside the boundary layer and at the shock location. A shock-fitting procedure is used to represent the shock. The change in the shock stand-off distance according to the gas model is considered. The grid has the same resolution properties of the grids already used and tested in previous works (see [30,31]).

The present simulations are based on freestream conditions encountered in a realistic reentry scenario at $M = 20$ at an altitude of about 57.7 km. The freestream conditions are summarized in Table 1. Nonreflective characteristic boundary conditions are used for free-stream and far-field boundaries. The wall is modeled as noncatalytic and isothermal with a constant temperature of 1800 K, as estimated from available flight data (see [40]).

C. Simulations of the Rough Wall

From the full two-dimensional domain a restricted three-dimensional domain is generated for the simulations of the boundary layer in the presence of a rough wall, as shown in Fig. 1. The restricted domain is located close to the capsule shoulder in the region of the

Table 1   Freestream conditions for the present simulations

| M	p_∞, Pa	T_∞, K	T_w, K	Re_∞, m^{-1}
20	29.9	253.3	1800	$1.97 \cdot 10^6$

sonic line. At the roughness location, the boundary layer is transonic ($M \approx 0.9$) and the edge velocity is about 1800 m/s. Here, values of the roughness Reynolds number above 200 can be found for rough-ness heights of about one fifth of the boundary-layer thickness. For these conditions, modal growth of small disturbances forced in the roughness wake is expected.

Computations are performed on a Cartesian coordinate system. For clarity, the results hereafter are represented on a spherical coordinate system with x the wall-parallel streamwise coordinate, y the wall-normal coordinate, and z the spanwise direction. The origin of the coordinate system $(x, y, z) = (0, 0, 0)$ is located on the stagnation point of the hemisphere, and the domain is centered on the plane $z = 0$. In the spherical part of the domain, excluding the shoulder, the coordinate x, y, and z are given by

$$x = R\theta_1,$$
$$y = \tilde{r} - R,$$
$$z = R\theta_2 \sin\theta_1 \qquad (5)$$

where R is the radius of the hemisphere (see Fig. 1), $\tilde{r}$ the distance from the center of the hemisphere, θ_1 the elevation angle with reference to the stagnation point, and θ_2 the azimuth angle measured clockwise on the rotation axis. With reference to this coordinate system, the restricted domain is extracted for $x \in [3.682, 4.843]$ m and has an angular extension in spanwise direction of $2\pi/130$ rad, corresponding to the spanwise periodicity of the roughness patch. In wall-normal direction, the computational domain extends to almost $y = 0.35$ m, corresponding to about 12 boundary-layer thicknesses. Note that, because of the strong acceleration of the flow in streamwise direction, the boundary layer grows slowly and the boundary-layer thickness increases by about 20% between $x = 3.7$ m and $x = 4.7$ m. A representation of the computational domain with rough wall is shown in Fig. 2a. Boundaries are labeled from 1 to 5. The solution of the full domain is used to generate the inflow boundary conditions on the faces 1 and 2, whereas azimuthal periodic boundary conditions are used in spanwise direction (face 3). Face 4 represents the wall and Riemann invariants are used at the outflow boundary (face 5).

Between $x = 3.755$ m and $x = 3.925$ m, a patch of random distri-buted roughness (Fig. 2b) is prescribed at the wall. The roughness patch is modeled using a body-fitted grid and is obtained by
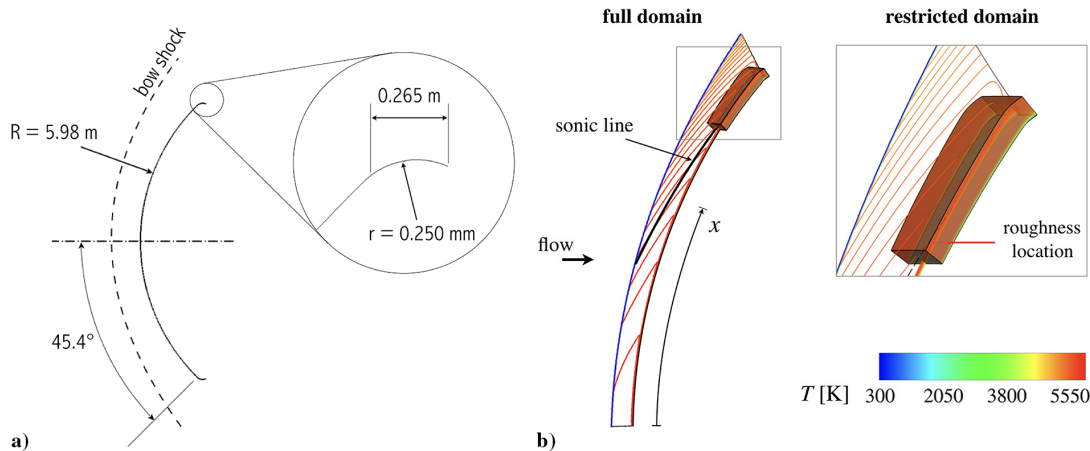
Fig. 1   Representation of a) the hemisphere geometry and b) full and restricted domains with the temperature color-coded.
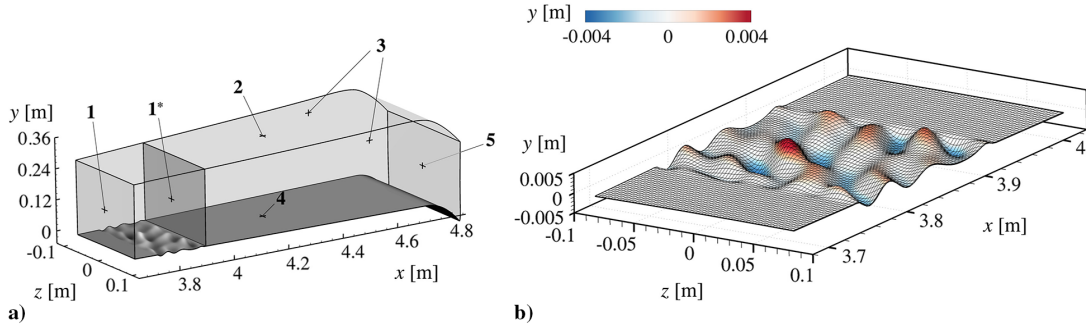
Fig. 2 Representation of a) restricted domain and b) grid close to the roughness (every sixth point shown).

superposing different sinusoidal functions with pseudo-random amplitudes and phases. For brevity, the prefix *pseudo-* is omitted. The surface height with respect to the smooth configuration is given by

$$h(x,z) = kg(x) \sum_{q,r=1}^{5} A_{q,r} \cos\left(\frac{2\pi q}{\lambda_0} x + \frac{2\pi r}{\lambda_0} z + \phi_{q,r}\right) \quad (6)$$

with $\phi_{q,r} \in [0, 2\pi]$ and $g(x)$ a piecewise defined function with two fifth-degree polynomials in the range from zero to one within a length of $\lambda_0/4$, which yield a continuous and smooth flattening of the roughness boundaries, ensuring continuity with the smooth wall. The fundamental roughness wavelength is given by $\lambda_0 = (2\pi/130)R\sin\theta_1$. Values of $A_{q,r}$ and $\phi_{q,r}$ have been randomly extracted from a uniform distribution and are listed in Table 2. Values of $A_{q,r}$ are normalized such that the maximum height of the roughness k is equal to 4.6 mm. The size of the domain in spanwise direction is chosen to contain the fundamental roughness wavelength λ_0. At the roughness location, the fundamental wavelength is $\lambda_0 = 170$ mm and the smallest roughness wavelength, $\lambda_0/5$, is comparable to the boundary-layer thickness. The size of the roughness has been chosen to resemble a realistic sand-grain roughened wall (see, e.g., [8]), where the distance between a roughness peak and the successive cavity is of the same order of magnitude of the roughness height.

Body-fitted grids have been applied to model the rough wall in several works [34,41,42]. The roughness patch is smooth without sharp edges. A comparison with stability investigations conducted for roughnesses with sharp edges (see, e.g., [18,20,25]) shows that, for the values of k/δ and Re_{kk} considered in this work, the presence of sharp edges in the roughness profile has a minor impact on the far field of the roughness wake. Qualitatively, the topology of the roughness wake in the far field and the nature of the relevant unstable modes are similar both in the case of a smooth-edge roughness and in the case of a sharp-edge roughness, given the similarity of other features such as the roughness height and the alignment of the roughness with the flow direction.

D. Unsteady Simulations of the Roughness Wake

The wake of the random distributed roughness is characterized by regions of local streamwise-vorticity maxima. These streamwise vortices are unstable to various modes, potentially interacting with each other. Therefore, in order to comprehensively evaluate the stability properties of the entire roughness wake, the entire spanwise extent of the domain downstream of the roughness is analyzed by means of Direct Numerical Simulations.

From studies on roughness-induced instabilities with roughness elements of the size considered here (see [20,32,42]), with the roughness height small compared with the boundary-layer thickness, it could be observed that the direct interaction of incoming linear disturbances with the rough wall is small. The presence of secondary instabilities as well as higher harmonics of the forced frequencies is limited to the roughness wake only. Moreover, in the case of a spherical geometry, the boundary layer for the smooth configuration is stable against modal instabilities throughout the entire domain and the only significant unstable modes are confined downstream of the roughness patch. Hence, to save on computational efforts, unsteady simulations are performed for the roughness wake only. A new computational domain is extracted from the restricted domain downstream of the roughness patch, from $x_0^* = 3.935$ m up to the shoulder (see Fig. 2). The grid properties remain unchanged.

Pressure disturbances are forced at the new inflow boundary (face 1^*). The disturbance is a time-varying function given by the superposition of five spatial modes and six different frequencies. The unsteady inflow condition for the pressure $p(x_0^*, y, z, t)$ is obtained as the sum of the pressure prescribed at the boundary for the steady flow, $p_{st}(x_0^*, y, z)$, and the function describing the unsteady disturbance as

$$p(x_0^*, y, z, t) = p_{st}(x_0^*, y, z) + c(y)\left(\sum_{i=1}^{5} \alpha_i \cos\left(\frac{2\pi i}{\lambda_0} z + \phi_i\right)\right)$$
$$\cdot \left(\sum_{j=1}^{6} \cos(2\pi f_j t + \phi_j)\right) \quad (7)$$

The function $c(y) = e^{-(y/\delta)^3}$, with δ the boundary-layer thickness, guarantees that the perturbation vanishes outside the boundary layer. The phases ϕ_i and ϕ_j are randomly chosen from $[0, 2\pi]$ to avoid peak values due to constructive interference of the cosine functions. The amplitudes α_i are also pseudo-random values and are kept very small in comparison to the boundary-layer pressure at the inflow position. Specifically, the amplitudes α_i are normalized such that $\sum |\alpha_i|/p_{st}(x_0^*, y < \delta, z) = 5 \cdot 10^{-6}$.

Note that the boundary layer on the smooth-wall configuration is stable against modal growth. Therefore, the profiles of the unsteady disturbance could not be provided by analyses of the two-dimensional flow based on the linear stability theory. At the inflow, only the pressure is perturbed and velocity disturbances induced by pressure disturbances appear at a low amplitude in a very short region downstream of the inflow boundary. In the absence of the flow distortion caused by a roughness, these disturbances are rapidly damped and vanish within a short distance from the inflow boundary corresponding to few boundary-layer thicknesses.

Table 2 Amplitude coefficients (left) and phases (right) used in Eq. (6)

$A_{q,r}$	$A_{q,1}$	$A_{q,2}$	$A_{q,3}$	$A_{q,4}$	$A_{q,5}$
$A_{1,r}$	0.008	0.079	0.008	0.139	0.113
$A_{2,r}$	0.119	0.103	0.092	0.076	0
$A_{3,r}$	0.077	0.140	0.116	0.140	0
$A_{4,r}$	0.102	0.065	0.101	0	0
$A_{5,r}$	0.031	0	0	0	0
$\phi_{q,r}$	$\phi_{q,1}$	$\phi_{q,2}$	$\phi_{q,3}$	$\phi_{q,4}$	$\phi_{q,5}$
$\phi_{1,r}$	5.328	5.212	4.393	1.753	1.637
$\phi_{2,r}$	4.931	5.166	5.003	4.244	——
$\phi_{3,r}$	1.702	3.586	2.775	5.678	——
$\phi_{4,r}$	1.431	3.593	2.804	——	——
$\phi_{5,r}$	2.017	——	——	——	——

E. Flow Solver and Numerical Schemes

Parallel DNS are conducted with the semicommercial solver Navier Stokes Multi Block (NSMB). The NSMB code is documented in [43,44] and it has been successfully applied and validated in numerous studies of hypersonic flows [3,24,25,30–32,45,46]. The code is finite-volume based on a variety of numerical schemes. NSMB works with structured grids divided in multiple blocks using the message-passing interface (MPI) environment.

For the full domain, the asymptotic solution is reached starting from freestream conditions with a second-order central discretization scheme and an implicit time integration based on a Symmetric Successive Over Relaxation (SSOR) method with two Gauss–Seidel iterations. Explicit second- and fourth-order artificial dissipation terms are locally added to suppress spurious oscillations at the shock location.

In the restricted domain the bow shock is excluded from the simulation. Thus, the order of the numerical scheme is increased. Steady simulations on the restricted domain are performed with a central discretization scheme of fourth-order accuracy and the asymptotic solution is reached with an implicit time integration. Successively, a more accurate solution is achieved switching to a hybrid Runge–Kutta time-integration scheme, where both the divergence and skew-symmetric forms are used. In the case of unsteady simulations, a central discretization scheme of fourth-order accuracy and the hybrid Runge–Kutta time-integration scheme are used.

F. Domain Size and Grid Analysis

The absence of errors that may arise because of the different computational schemes and grid resolutions used in the full and restricted domain has been carefully checked. The accuracy of the steady simulations and the absence of numerically produced unsteady disturbances are ensured by achieving very good convergence of the residuals. Furthermore, the domain size has been designed to guarantee that the presence of the roughness does not influence the inflow boundaries. In wall-normal direction, the computational domain extends for about 12 boundary-layer thicknesses. Because of the rapidly increasing Mach number in streamwise direction, the steady disturbance induced by the roughness in the inviscid flow is very small and is strongly deflected in the flow direction. Therefore, any potential residual reflection at the upper boundary (face 2) exits the domain at the outflow boundary without impinging on the boundary layer and, thus, without affecting the stability properties of the roughness wake. Further extension of the domain in wall-normal direction did not result in any notable variation of the base flow.

The grid of the restricted domain in the presence of the roughness consists of $1280 \times 200 \times 400$ points. In the streamwise direction, the concentration of grid points is high at the roughness location and reduces as the outflow boundary is reached. In the wall-normal direction, a large number of points ($\sim$120) are used to resolve the boundary layer, whereas in the spanwise direction the grid points are equally spaced. The smallest wavelength present in the roughness geometry is resolved with at least 80 points in the spanwise direction. Details on the points distribution in the three spatial directions are given in Table 3, where N_x, N_y, and N_z are the number of points in x, y, and z directions; n_y^δ the number of points within the boundary layer; $\Delta x(\min, \max)$, $\Delta y(\min, \max)$, and $\Delta z(\min, \max)$ the minimum and maximum length of the grid cells; and N_{tot} the total number of grid points.

A grid study has been conducted to ensure convergence of the results. Two grids are considered: a fine grid and a medium grid, where the total number of points has been uniformly reduced by
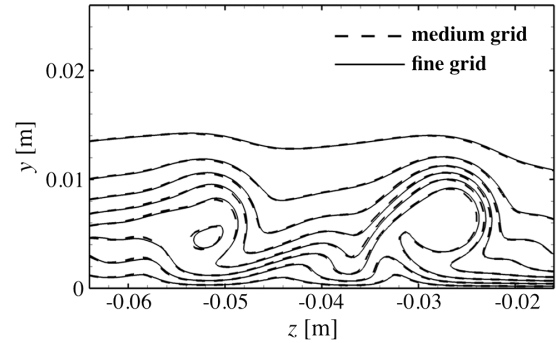
Fig. 3 Results of the grid-convergence analysis: isolines of streamwise velocity at $x = 3.958$ m every 200 m/s.

almost a factor of two with respect to the fine grid. The grid convergence is shown in Fig. 3 for the case of gas in chemical equilibrium, as in this case the gradients at the wall are the largest of all cases. Comparison of the streamwise velocity is shown for a cross plane immediately downstream of the roughness patch, where the flow topology is very sensitive to grid changes due to the rapid variation of the flow associated with the presence of the roughness. Almost no difference is present between the results on the two grids. All simulations discussed hereafter will be performed on the fine grid. Further studies on the domain size as well as on the grid convergence for the present geometry can be found in [32].

III. Results

A. Analysis of the Laminar Base Flow

The effect of the roughness patch on the stability of the boundary layer is closely related to the properties of the boundary layer at the roughness location. To better understand the influence of non-equilibrium on the base flow, Fig. 4a shows boundary-layer velocity and temperature profiles for the smooth-wall configuration for the three gas models at $x = 3.8$ m. As already noticed in previous works (see [30,31]), neither chemical nor thermal nonequilibrium significantly affect the velocity profiles. Instead, due to the energy-releasing recombination of both oxygen and nitrogen fully achieved at the wall in the case of equilibrium, a larger boundary-layer edge temperature as well as a larger temperature gradient at the wall are observed for CEQ compared with CNEQ and CTNEQ. In comparison to CNEQ, the inclusion of thermal nonequilibrium slightly increases the profile curvature and the temperature gradient at the wall.

The difference in the profiles of the thermal boundary layer as well as in the profiles of the species' concentration (not shown here) translates into different boundary-layer thicknesses and different values of the viscosity. When comparing roughnesses of the same geometry, the stability of the roughness wake is influenced, among others, by the values of the roughness Reynolds number. In the case of random distributed roughness, protuberances with different heights present different local roughness Reynolds numbers. To better understand how the use of different gas models affects the local roughness Reynolds numbers, Fig. 4b shows the profiles of the quantity $Re_{kk}/k = (u\rho)/\mu$ along the wall-normal direction. In the case of gas in CEQ, the local maximum of Re_{kk}/k is reached at about $y = 2$ mm and is about one fifth larger than the values of CNEQ and CTNEQ at the same height. This value rapidly decreases as the distance from the wall increases and, at about $y = 3.5$ mm, the value of Re_{kk}/k for CEQ becomes smaller than the one of CNEQ.

Table 3 Details of the computational grids

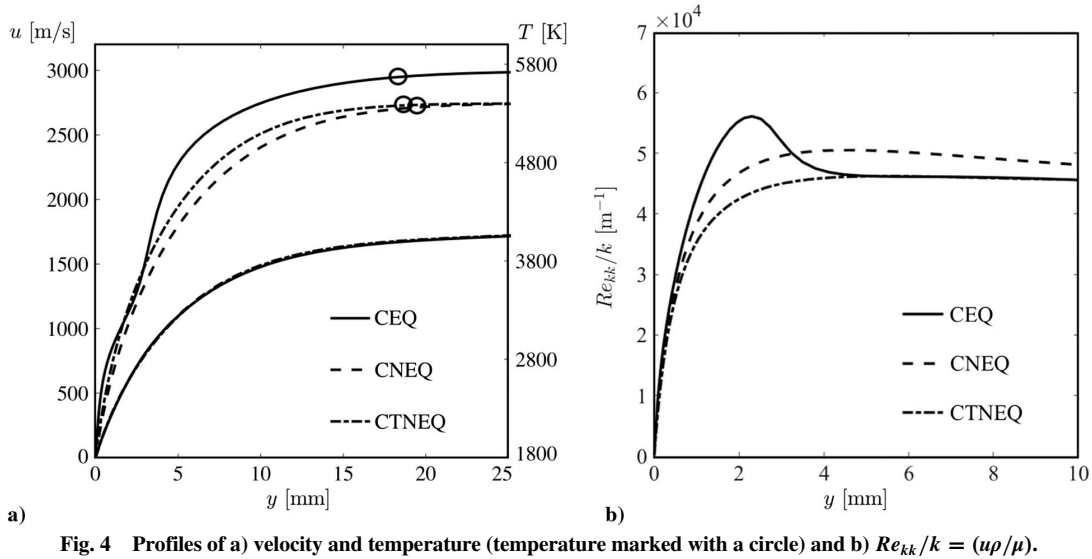| Grid	N_x	$\Delta x(\min, \max)$	N_y (n_y^δ)	$\Delta y(\min, \max)$	N_z	$\Delta z(\min, \max)$	N_{tot}
Medium	1030	0.87, 1.56 mm	160(96)	0.018, 4.294 mm	320	0.52, 0.65 mm	$52.7 \cdot 10^6$
Fine	1280	0.70, 1.28 mm	200(120)	0.014, 3.456 mm	400	0.42, 0.52 mm	$102.4 \cdot 10^6$

Fig. 4 Profiles of a) velocity and temperature (temperature marked with a circle) and b) $Re_{kk}/k = (u\rho/\mu)$.
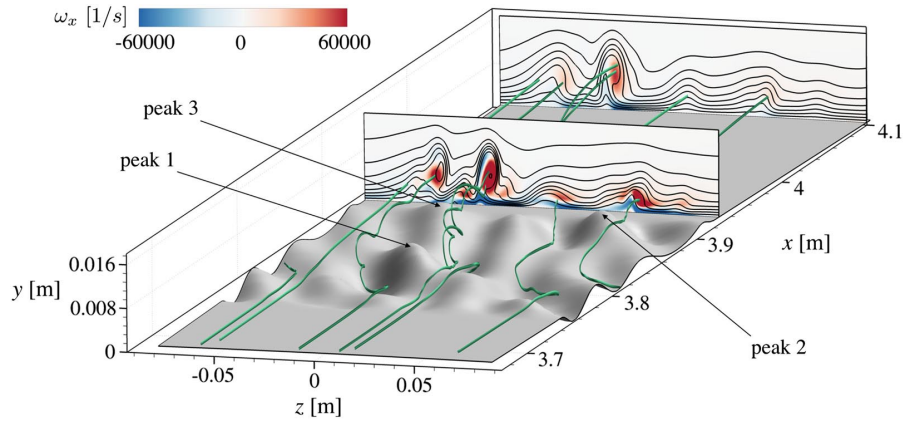

Fig. 5 Flow field with sample streamlines and slices at $x = 3.939$ m and $x = 4.105$ m colored by streamwise vorticity.

This behavior is related to the recombination of atomic oxygen and nitrogen within the boundary layer. Because the profiles computed with reference to the different gas models intersect each other, the mutual comparison of the roughness Reynolds numbers for different gas models depends on the wall distance. In particular, in the case of roughness elements smaller than $y = 3.5$ mm, the largest Reynolds number is found for CEQ, whereas for higher roughness elements, the largest Reynolds number is found for CNEQ.

The three main peaks in the roughness patch are shown in Fig. 5. The corresponding positions, roughness Reynolds numbers, and ratios of roughness-height to boundary-layer thickness are summarized in Table 4. At the roughness location, the gas in thermochemical non-equilibrium presents the smallest boundary-layer thickness, computed as the distance from the wall where 99% of the total enthalpy is reached. However, the largest value of Re_{kk} is found in the case of CNEQ ($Re_{kk} = 244$). The roughness Reynolds numbers relative to peak 1 are similar for CEQ and CTNEQ and equal to $Re_{kk} = 226$ in the case of equilibrium air and $Re_{kk} = 221$ in the case of thermochemical nonequilibrium. For peaks 2 and 3 the largest roughness Reynolds number is presented by the gas in equilibrium. All roughness

Reynolds numbers are significantly lower than effective Re_{kk} for immediate transition to turbulence at the roughness location.

The process of vortex formation in the wake of the roughness patch is shown in Fig. 5, where the paths of streamlines ending up in the vortex cores at $x = 4.105$ m are shown together with $y-z$ slices colored by streamwise vorticity and isolines of streamwise velocity (every 200 m/s). The streamlines are deflected at the different protuberances and cavities encountered in the roughness patch and a helicoidal movement is induced downstream of the roughness peaks. Several vorticity regions are found in the wake of the patch. As expected, the main vortical structure originates at the highest peak. The skewness of the roughness protuberances relative to the stream-wise flow and the subsequent cavities induce spanwise and wall-normal components of the velocity, which result in vorticity distributions as known from crossflow vortices in three-dimensional subsonic boundary-layer flows.

In Fig. 6, color contours of the streamwise vorticity together with isolines of the streamwise velocity (every 100 m/s) are shown for the cross section at the inflow boundary 1* of the restricted domain for the three chemical models considered. The main vortex originates at

Table 4 Roughness parameters for the different gas models

| Peak	(x, z), m	k, mm	k/δ			Re_{kk}		
			CEQ	CNEQ	CTNEQ	CEQ	CNEQ	CTNEQ
1	$(3.826, -0.016)$	4.60	0.183	0.198	0.227	226	244	221
2	$(3.909, 0.043)$	2.85	0.113	0.123	0.141	161	147	131
3	$(3.916, -0.041)$	2.62	0.104	0.113	0.129	150	131	124
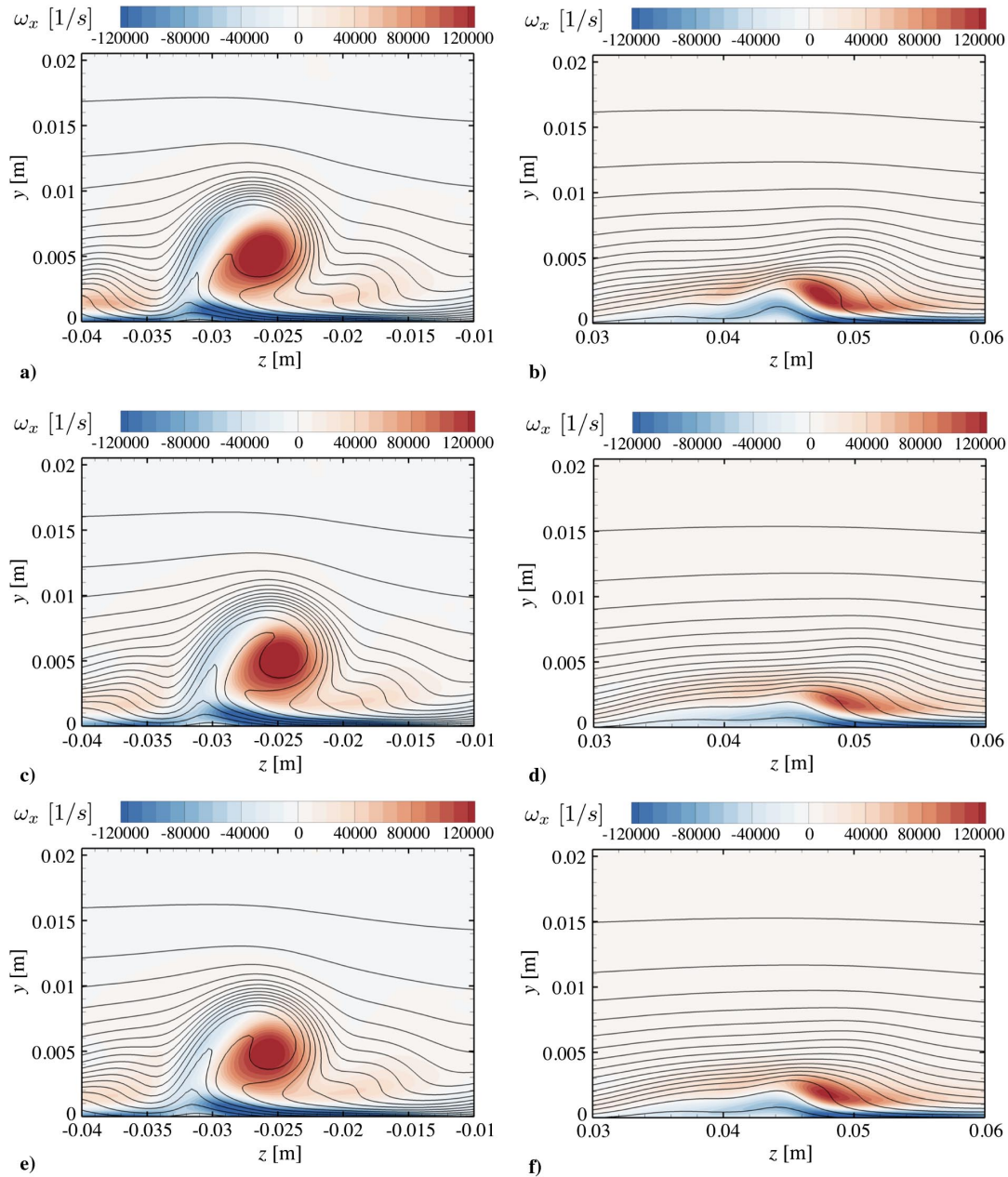
Fig. 6   Streamwise vorticity (color contours) and streamwise velocity (isolines) at $x = 3.935$ m for a,b) equilibrium air; c,d) chemical nonequilibrium; and e,f) thermochemical nonequilibrium.

the roughness peak 1 and is found at $z \approx -0.028$ m (Figs. 6a, 6c, and 6e). This vortex persists along the entire extension of the computational domain up to the outflow boundary. The rolling-up of the velocity isolines is associated with unstable high-shear layers. The maximum value of the streamwise vorticity ω_x in this section is found for the case of CEQ, with $\omega_x^{max} = 152 \cdot 10^3$ 1/s, followed by CNEQ ($\omega_x^{max} = 143 \cdot 10^3$ 1/s) and CTNEQ ($\omega_x^{max} = 136 \cdot 10^3$ 1/s). No significant difference in the damping rate of the streamwise vorticity was found for the different gas models and the streamwise vorticity reaches 90% of the maximum value at about $x = 3.947$ m and 50% at about $x = 4.052$ m. This result was expected, as the velocities are almost unaffected by the gas model used. The vortex shown in Figs. 6b, 6d, and 6f originates at peak 2 of the roughness patch. The vortex induced by peak 3 is similar to the one induced by peak 2 and is not shown here.

Figure 7 shows the color contours of the temperature for the same cross sections. The vortices bring hot fluid toward the wall in the descending part of the vortex and cold fluid from the wall region is moved upward on the ascending side. This effect is visible in the squeezing of temperature isocontours on the descending side and in

the expansion of temperature isocontours on the ascending side of the vortices, respectively. Isolines of the atomic concentration of nitrogen are also shown every 0.01. The dashed isoline represents an atomic-nitrogen concentration equal to 0.18. As the temperature wall is fixed at $T_w = 1800$ K, a full nitrogen recombination is reached close to the wall in the case of CEQ. Because of the noncatalytic wall, atomic nitrogen for CNEQ and CTNEQ is still present at the wall, whereas almost no oxygen recombination (not shown here) takes place. Note that, in the case of nonequilibrium, isolevels of the species concentration might intersect the temperature isolevels as a consequence of the finite rate of the dissociation/recombination process.

Finally, the effects of the roughness on the wall heat transfer are shown in Fig. 8, where the wall heat flux is presented for the three gas models. In the case of CEQ, the wall heat flux is higher and a different color scale is used for CNEQ and CTNEQ. In all three cases, a long streak of heating augmentation is found between $z = -0.01$ m and $z = -0.03$ m, corresponding to the downwash motion of the main crossflow-type vortex, with hot fluid transported toward the wall. The largest values of the heat flux in the roughness wake are observed for
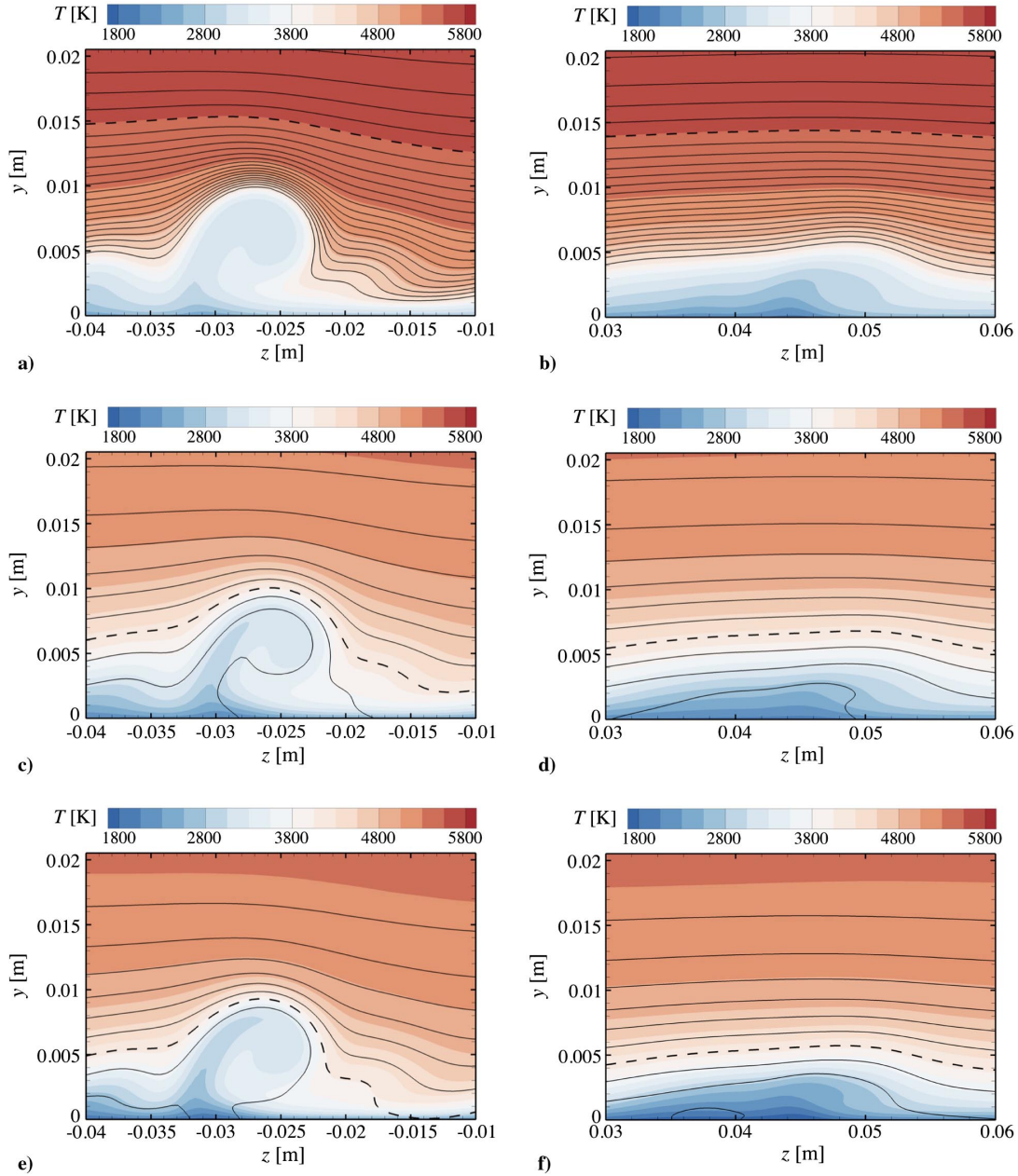
Fig. 7 Temperature (color contours) and atomic nitrogen concentration (isolines) at $x = 3.935$ m for a,b) equilibrium air; c,d) chemical nonequilibrium; and e,f) thermochemical nonequilibrium.

the case of equilibrium air. In the case of CTNEQ the temperature gradients are slightly larger than that for CNEQ (see also Fig. 4a).

B. Growth of Linear Disturbances

To analyze the linear growth of small disturbances in the wake of the distributed roughness, pressure disturbances are introduced in the restricted simulation domain downstream of the roughness patch. Six different frequencies are forced simultaneously at the inflow boundary. These frequencies are $f_1 = 8.3$ kHz, $f_2 = 16.7$ kHz, $f_3 = 25.0$ kHz, $f_4 = 33.3$ kHz, $f_5 = 41.7$ kHz, and $f_6 = 50.0$ kHz. This range of values has been deduced from the frequency spectrum of an experimental campaign conducted at HLB for similar geometries (capsule model of 17 cm diameter at $M = 5.9$; see [2,3]). In the experiments at HLB, a peak in the frequency spectrum in the range of 200–300 kHz was measured for transitional flow. The experimental values have been scaled with boundary-layer thicknesses and velocities for the present simulations. The frequencies f_3 and f_4 are centered on the considered frequency interval, whereas frequencies f_1 and f_6 represent its limits. Preliminary simulations did not reveal any relevant instabilities in frequency ranges higher than the one considered here. In particular,

as also documented in [47], the N-factor decreases for frequencies larger than 33.3 kHz, and in the case of a disturbance with a frequency of 100 kHz, no linear amplification at all was found for any of the gas models. Because the smooth-wall boundary layer is stable against modal instabilities throughout the entire domain, no frequency could be suggested by evaluating the eigenvalues of the steady base flow of the smooth configuration. The amplitude of the inflow disturbance is kept very small and the largest value reached in the roughness wake remains less than 1% of the boundary-layer edge values, ensuring that nonlinear interactions remain negligible throughout the entire domain.

A temporal Fourier analysis is performed by means of the Fast Fourier Transform. The growth rate of the disturbance associated with each frequency is computed with reference to the disturbance kinetic energy. The disturbance kinetic energy as a function of the three spatial coordinates and the frequency is expressed as

$$e_{K,f}(x, y, z) = \rho_{st}(\hat{U}_f^2 + \hat{V}_f^2 + \hat{W}_f^2) \qquad (8)$$

where $\hat{U}_f$, $\hat{V}_f$, and $\hat{W}_f$ are the Fourier transforms of the three velocity components with reference to the frequency f, and ρ_{st} is the density of
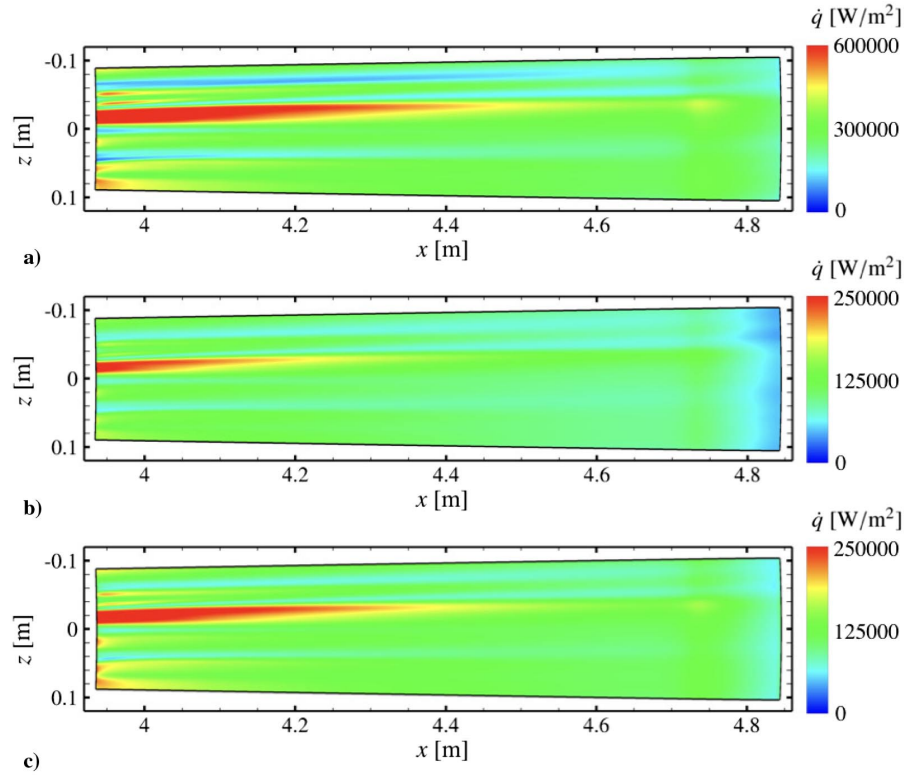
Fig. 8   Wall heat flux for a) equilibrium air, b) chemical nonequilibrium, and c) thermochemical nonequilibrium.
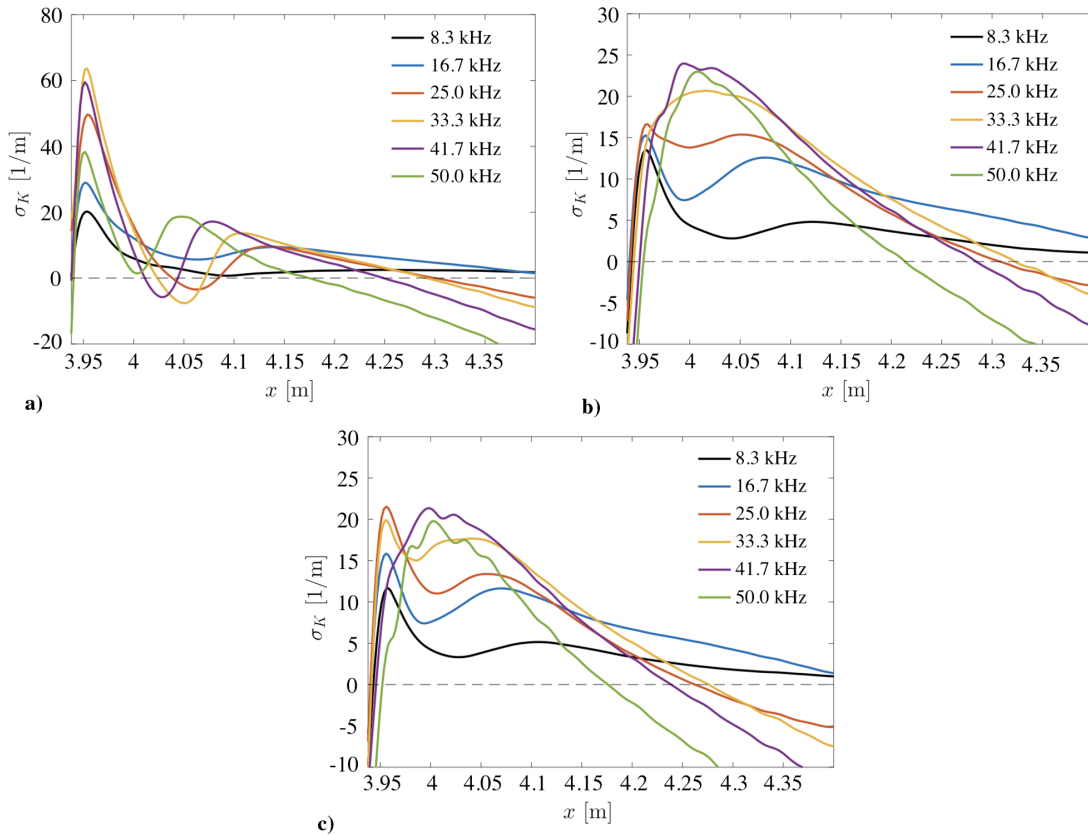

Fig. 9   Growth rate for a) equilibrium air, b) chemical nonequilibrium, and c) thermochemical nonequilibrium.

the base flow. The integral value of the disturbance kinetic energy on the plane y–z is given by

$$E_{K,f}(x) = \int_{-\lambda_0/2}^{\lambda_0/2} \int_0^{y_{max}} e_{K,f}(x, y, z)\, \mathrm{d}y\, \mathrm{d}z \qquad (9)$$

and the growth rate associated to each frequency is computed as

$$\sigma_{K,f}(x) = \frac{1}{2} \frac{\mathrm{d}}{\mathrm{d}x} \ell n\left(E_{K,f}(x)\right) \qquad (10)$$

The growth rate in the roughness wake is shown in Fig. 9 for the three gas models. The growth rate of all gas models presents two main
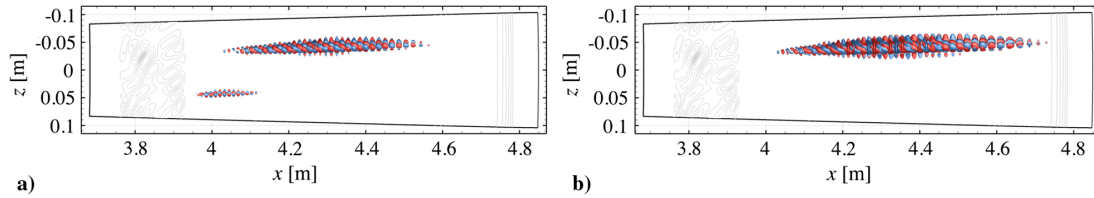
Fig. 10   Isosurfaces of the real part of the Fourier-transformed u velocity for a) equilibrium air and b) chemical nonequilibrium.

peaks, one located in the near field of the roughness wake at about $x = 3.96$ m and a second one for $y > 4.05$ m. Accurate analysis of the flow revealed that the presence of the first peak is associated with the strong growth of an instability originating in the vortical structure found at positive values of the z coordinate (see Figs. 6b, 6d, and 6f). As this vortex weakens for increasing values of the streamwise coordinate, the amplification of the disturbances due to the main crossflow-type vortex at $z \approx -0.028$ m (Figs. 6a, 6c, and 6e) takes over and dominates the growth of the disturbances in the far field of the wake. This behavior is evidenced in Fig. 10, which shows isosurfaces of the real part of the Fourier-transformed u velocity ($Re\{\hat{U}\} = \pm 2$) for the frequency f_4. In the case of CEQ, two main instability-growth regions can be identified, aligned in the streamwise direction at $z \approx -0.04$ m and $z \approx 0.05$ m, respectively. The instability at positive z corresponds to the first interval of large growth in Fig. 9a and is not visible in the case of CNEQ.

In the case of CEQ, the growth rate of the disturbance kinetic energy in the near field reaches much larger values than in the case of CNEQ and CTNEQ. The presence of two peaks at all investigated frequencies indicates that the growth of the disturbance energy in the near field is dominated by the instability at positive z values at all frequencies. In the case of CNEQ and CTNEQ, the two main peaks are visible only for frequencies up to 25.0 and 33.3 kHz, respectively. At higher frequencies, the growth of the disturbance kinetic energy is mainly driven by the instability of the crossflow-type vortex. The presence of minor oscillations in the growth-rate profile for frequencies larger or equal to 41.7 kHz is due to the kick-in of instabilities of other minor vortices in the roughness wake.

We recall that, as shown in Sec. III.A, the properties of the flow at the roughness height significantly depend on the gas model. In particular, the roughness protuberance responsible for the vortical structure at $z \approx 0.05$ m (peak 2) has a height of 2.85 mm and it exhibits the largest roughness Reynolds number in the case of CEQ. A larger amplification is expected, accordingly.

The use of the integral value of the disturbance kinetic energy over $y-z$ planes allows for a more inclusive analysis of the instabilities present in the wake of the entire roughness patch. Nevertheless, it provides incomplete information on the local growth of the disturbances. For example, the negative values of the growth rate observed immediately downstream of the roughness patch for $x < 3.95$ m refer to the overall growth of the disturbance over the entire span width. However, the disturbance is locally amplified from the very beginning of the truncated domain downstream of the roughness. Analysis of the flow revealed that the disturbance in the wake of the main crossflow-type vortex is the most amplified for all gas models and for all frequencies considered here. Specifically, the growth rate in the crossflow-type vortex remains positive for a long distance downstream of the roughness, and the total growth, computed as integral value of the growth rate over the streamwise direction, is the largest in this case.

Figure 11 shows the N-factors for the investigated range of frequencies for the different gas models,

$$N = \ell_n \left(\frac{A_{max}}{A_{in}} \right) \quad (11)$$

Here, A_{max} is the maximum of the disturbance amplitude found along x and A_{in} is the amplitude of the disturbance at the inflow. We compute the N-factor in two different ways. In the first case (black curve), the disturbance amplitudes are the values of the integral disturbance kinetic energy as in Eq. (9). In the second case
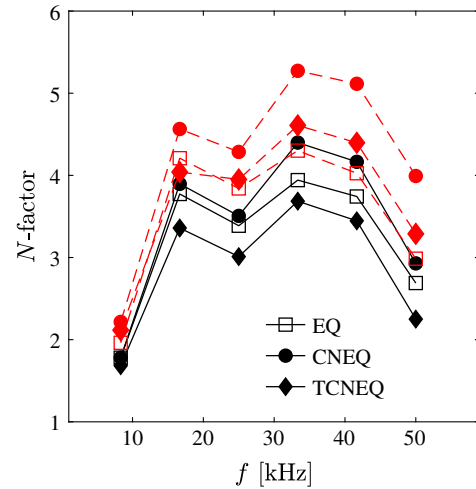

Fig. 11 N-factors computed with integral (black line) and maximum (red line) of the disturbance kinetic energy.

(red curve), the disturbance amplitudes are computed as the maximum value of the disturbance kinetic energy Eq. (8) in the $y-z$ plane. As expected, the N-factors of the disturbance kinetic energy with reference to the local maximum are larger than the ones computed with the integral of the disturbance kinetic energy.

For all gas models, the largest N-factors are found for the frequency 33.3 kHz. With regard to the N-factors computed with the maximum of the disturbance kinetic energy, the largest amplification is observed for the case of gas in chemical nonequilibrium at all frequencies, with N-factors up to 5.3, followed by the case of gas in thermochemical nonequilibrium ($N = 4.6$) and by gas in equilibrium ($N = 4.3$). Thus, the thermochemical nonequilibrium locally enhances the disturbance amplification compared with the equilibrium case. Instead, for the N-factors computed with the integral value of the disturbance kinetic energy, the gas in thermochemical nonequilibrium is the least unstable at all frequencies, suggesting that the thermochemical nonequilibrium has an overall stabilizing effect for the present configuration.

The presence of two local maxima in the N-factor curve at 16.7 and 33.3 kHz indicates that the amplification of the disturbance is dominated by two distinct phenomena. This assumption is substantiated by Fig. 12, which shows the shape of the disturbance modes for the streamwise velocity in correspondence to the main crossflow-type vortex. Streamwise velocity levels are also shown as background isolines every 150 m/s. The modes of instability are obtained as absolute values of the temporal Fourier analysis and are represented for the case of CEQ only, as the mode shapes are very similar for the three gas models. Modes are normalized to unity with the maximum value in each subfigure and values <0.25 are blanked out. At lower frequencies (8.7–16.7 kHz), the mode of instability consists of two bean-shaped regions, one on the top-ascending side of the crossflow-type vortex and the other one on the descending side. As the frequency increases (33.3–50.0 kHz), the mode of instability evolves into one main region on the top of the vortex spreading along the ascending side and a smaller region on the down side. This result shows that there are at least two modes of instability being active in two intersecting frequency ranges. At $f = 25.0$ kHz, the two modes are both present and a hybrid of the two eigenmodes can be seen.
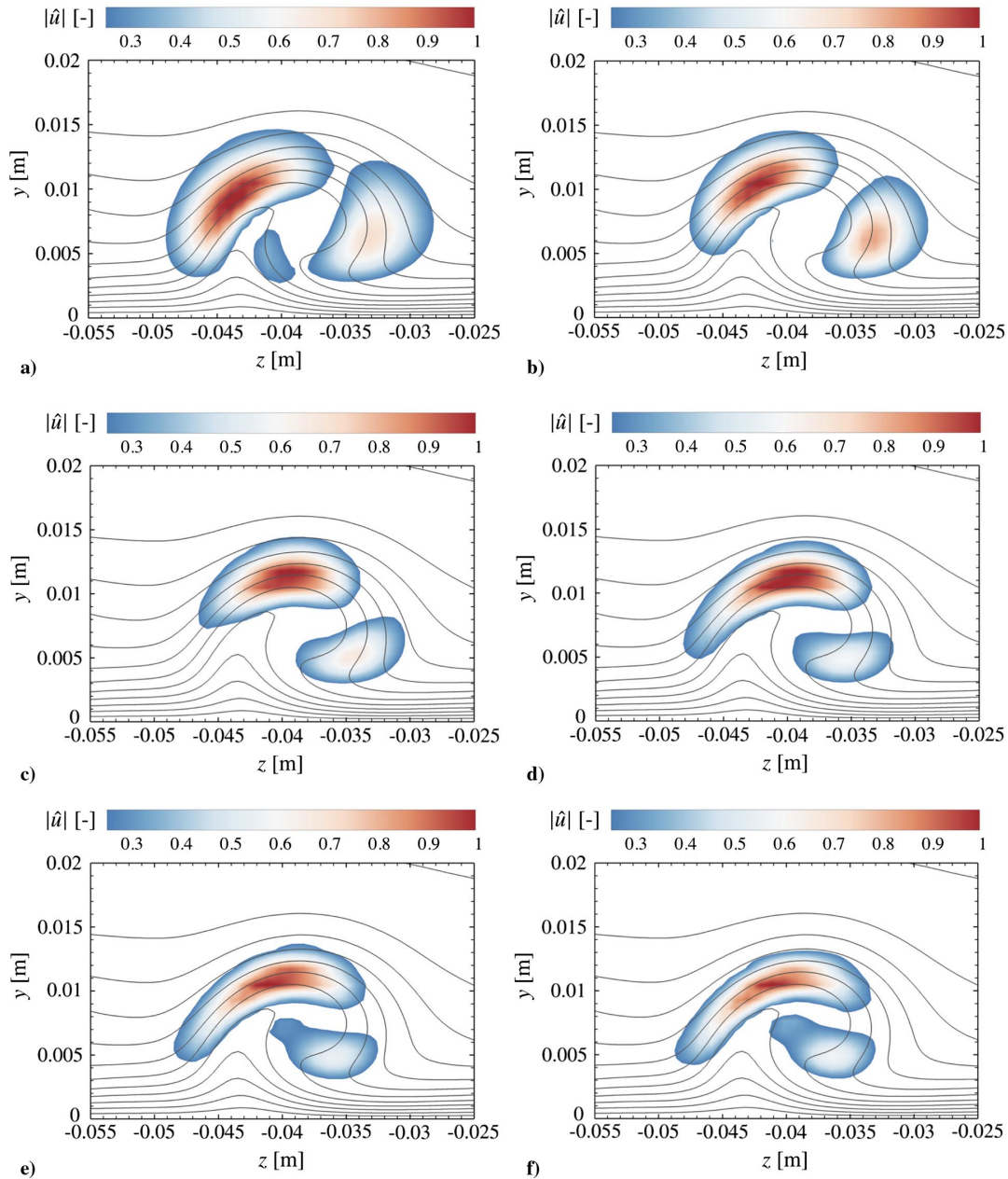
Fig. 12 Disturbance modes at $x = 4.295$ m for a) 8.3 kHz, b) 16.7 kHz, c) 25.0 kHz, d) 33.3 kHz, e) 41.7 kHz, and f) 50.0 kHz.

It is known that the main instability modes in crossflow vortices in low-speed boundary layers are induced by spanwise gradients (z modes) and wall-normal gradients (y modes) of the streamwise velocity (see, among others, [48–50]). To investigate the possible relation between the instability modes of the roughness-induced crossflow-type vortex and the velocity gradients in the roughness wake, Fig. 13 shows isocontours of the disturbance modes at 8.3 kHz with isolines of spanwise shear stress (Fig. 13a) and isocontours of the disturbance modes at 50.0 kHz with isolines of wall-normal shear stress (Fig. 13b). The dependence between shear stresses and instability modes is confirmed by the striking overlapping of the regions identified by isocontours and isolines. In particular, unstable modes at lower frequencies are of the z-mode type, whereas at higher frequencies the unstable modes are of the y-mode type.

Among the considered harmonics, the frequency of maximum amplification of the y mode (33.3 kHz) is twice the frequency of the z mode (16.7 kHz). The same relation between y and z modes was also observed in the experiments conducted by White and Saric [50] in three-dimensional, incompressible boundary layers. Two distinct peaks of disturbance amplification could be observed in the power spectra presented in [50], corresponding to the two different ranges of

disturbance amplification also visible in Fig. 11. Furthermore, in the experiments of White and Saric [50], the frequency of the z mode could be approximated by $f \approx U/(2\delta)$, where U is the boundary-layer edge velocity. With regard to the present investigation on high-enthalpy capsule boundary layers, this relation provides a value of $f \approx 38$ kHz, which is in the same range of relevant frequencies found in our computations, with a shift of a factor 2 toward lower frequencies.

Contrary to crossflow vortices in three-dimensional boundary layers, where a spanwise velocity is present in the base flow, the flow for the present configuration in the absence of roughness is two-dimensional and the spanwise component of the velocity typical of crossflow vortices is solely induced by the roughness itself. In this regard, the present case differs from most experimental and numerical works conducted so far on crossflow instabilities. Recently, Chou et al. [51] presented an experimental investigation for a Mach-3.5 flat-plate boundary layer in the presence of rectangular roughness elements with a profile skew to the flow directions. Representation of the mean mass flux behind the roughness elements showed a distortion of the flow qualitatively similar to the distortion of the flow induced by skew roughness protuberances considered in our work. Analysis of the
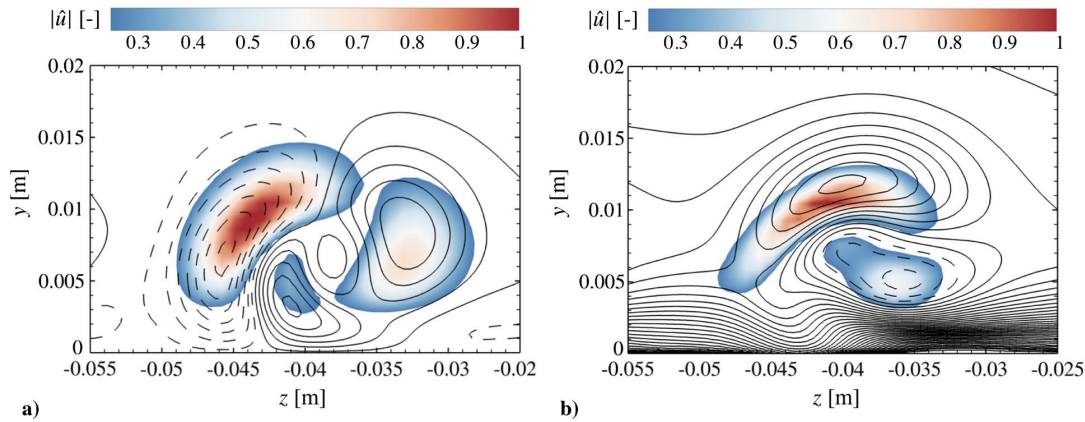
Fig. 13 Disturbance modes at a) 8.3 kHz with isolines of spanwise shear stress and b) 50.0 kHz with isolines of wall-normal shear stress.

mass-flux fluctuations revealed the presence of modes of instability with a low-frequency instability corresponding to regions of higher spanwise shear of the mass flux and a high-frequency instability corresponding to regions of higher wall-normal shear of the mass flux, featuring the modes shown in the present investigation.

IV. Conclusions

Direct Numerical Simulations have been undertaken to analyze the stability of the wake of a patch of distributed roughness in the boundary layer of a hemispherical capsule-like geometry at $M = 20$. Simulations have been performed with three different gas models for a five-species air model. Different high-temperature gas effects have been investigated by gradually including chemical nonequilibrium and thermal nonequilibrium in the simulations of the high-enthalpy, chemically reacting boundary layer. Chemical and thermal non-equilibrium significantly affects the steady boundary-layer properties, such as boundary-layer thickness, temperature profiles, and species concentration. As a result, the stability properties of the roughness wake differ according to the gas model used in the simulation. When comparing roughness protuberances with the same height, the largest roughness Reynolds number is found in the case of gas in equilibrium for a roughness height up to about 3.5 mm. For larger roughness heights, the largest roughness Reynolds number is present for the gas in chemical nonequilibrium due to the impact on the temperature profiles and, subsequently, on the viscosity.

In the case of the steady laminar boundary layer, several vortical structures are generated at the roughness peaks. In particular, vortical structures resembling crossflow-type vortices originate at the largest peaks of the patch due to the skewness of the roughness protuberances relative to the streamwise flow. The main vortex persists along the entire computational domain and exhibits unstable high-shear layers. There seems to be no direct correlation between the magnitude of the flow distortion and roughness variables such as the ratio of roughness-height to boundary-layer thickness and the roughness Reynolds number. In particular, the smallest boundary-layer thickness was present for the gas in thermochemical nonequilibrium, whereas the largest roughness Reynolds number was found for the gas in chemical nonequilibrium. However, the maximum value of the streamwise vorticity at the end of the roughness patch was found in the case of gas in chemical equilibrium, followed by gas in chemical nonequilibrium. No significant difference was found in the damping rate of the streamwise vorticity for the different gas models, as the velocities are almost unaffected by the gas model.

On the descending side of the vortices, hot fluid is transported toward the cold wall and streaks of high temperature gradients at the wall are found in the wake of the roughness. In the case of equilibrium air, the full exothermic recombination of atomic nitrogen and oxygen leads to larger values of the wall temperature gradient in comparison to the nonequilibrium cases.

The linear growth of unsteady disturbances in the roughness wake has been investigated by introducing pressure disturbances at the inflow boundary downstream of the roughness patch. Six different perturbation frequencies have been considered in the range of 8.3 and 50.0 kHz. Several unstable regions were identified in the wake of the distributed roughness. At all considered frequencies and for all gas models, the main crossflow-type vortex originating at the highest peak of the roughness patch presented the largest overall disturbance amplification. For all gas models, the largest amplification was found for modes at 33.3 kHz, followed by the modes at 16.7 kHz. The gas in chemical nonequilibrium presents the largest amplification for all considered frequencies. The thermochemical nonequilibrium model has an overall stabilizing effect compared with the equilibrium case. However, in the region of the main crossflow-type vortex, thermo-chemical nonequilibrium locally enhances the disturbance amplification compared with equilibrium. In particular, the largest N-factor, computed with the local maxima of the disturbance kinetic energy, was found for the gas in chemical nonequilibrium ($N = 5.3$), followed by the gas in thermochemical nonequilibrium ($N = 4.6$). The gas in chemical equilibrium resulted to be the least unstable, with $N = 4.3$. With reference to the integral value of the disturbance kinetic energy, the largest N-factor is presented by the gas in chemical nonequilibrium, followed by the gas in equilibrium, and, finally, the gas in thermochemical nonequilibrium.

The roughness Reynolds number provides an easy, although over-simplified, way to characterize the flow perturbed by small roughness elements in terms of stability properties. The results of the stability investigations on the present configuration are in accordance with the finding that the roughness Reynolds number in case of non-equilibrium becomes larger than the one in the case of equilibrium for sufficiently high roughness elements.

Two different instability modes have been identified associated to the crossflow-type vortex. One of the modes is mainly amplified around 16.7 kHz and is correlated to the spanwise gradients of the streamwise velocity. The other mode is amplified at around 33.3 kHz and is correlated to the wall-normal gradients of the streamwise velocity. These modes feature the z and y modes already known from crossflow vortices in three-dimensional subsonic boundary layers.

This work shows that the stabilizing or destabilizing effect of nonequilibrium on the roughness wake significantly depends on features of the roughness such as shape and height. Some roughness shapes with a skew profile with respect to the flow direction can induce crossflow-type vortices even in the absence of an underlying spanwise velocity in the smooth-wall base flow. The presence of roughness-induced crossflow-type vortices on reentry capsules provides a possible explanation for laminar-turbulent transition of the capsule boundary layer at altitudes where chemical reactions and nonequilibrium effects are important. In the presence of roughness protuberances as large as one fifth of the boundary-layer thickness (as the analyzed configuration), the chemical nonequilibrium was found to be destabilizing at all considered frequencies. This result highlights the importance of including nonequilibrium effects in the stability analysis of high-enthalpy boundary layers in the presence of roughness and the consideration of the skewness of the roughness in detail.

Acknowledgments

References

[1] Morkovin, M., "Bypass Transition to Turbulence and Research Desiderata," *Transition in Turbines*, NASA CP-2386, 1984, pp. 161–199.

[2] Theiss, A., Ali, S. R., Hein, S., Heitmann, D., and Radespiel, R., "Numerical and Experimental Investigation of Laminar-Turbulent Boundary Layer Transition on a Blunt Generic Re-Entry Capsule," AIAA Paper 2014-2353, 2014.
doi:10.2514/6.2014-2353

[3] Hein, S., Theiss, A., Di Giovanni, A., Stemmer, C., Schilden, T., Schröder, W., Paredes, P., Choudhari, M. M., Li, F., Reshotko, E., et al., "Numerical Investigation of Roughness Effects on Transition on Spherical Capsules," *Journal of Spacecraft and Rockets*, 2019.
doi:10.2514/1.A34247

[4] Schneider, S. P., "Summary of Hypersonic Boundary-Layer Transition Experiments on Blunt Bodies with Roughness," *Journal of Spacecraft and Rockets*, Vol. 45, No. 6, 2008, pp. 1090–1105.
doi:10.2514/1.37431

[5] Malik, M. R., and Anderson, E. C., "Real Gas Effects on Hypersonic Boundary Layer Stability," *Physics of Fluids*, Vol. 3, No. 5, 1991, pp. 803–821.
doi:10.1063/1.858012

[6] Berger, K. T., "Aerothermodynamic Testing of the Crew Exploration Vehicle at Mach 6 and Mach 10," *Journal of Spacecraft and Rockets*, Vol. 46, No. 4, 2009, pp. 758–765.
doi:10.2514/1.39247

[7] Hollis, B. R., "Distributed Roughness Effects on Blunt-Body Transition and Turbulent Heating," AIAA Paper 2014-0238, 2014.
doi:10.2514/6.2014-0238

[8] Hollis, B. R., "Experimental Investigation of Roughness Effects on Transition Onset and Turbulent Heating Augmentation on a Hemisphere at Mach 6 and Mach 10," NASA TM-2017-219613, 2017.

[9] Reda, D. C., "Review and Synthesis of Roughness-Dominated Transition Correlations for Reentry Applications," *Journal of Spacecraft and Rockets*, Vol. 39, No. 2, 2002, pp. 161–167.
doi:10.2514/2.3803

[10] Reda, D. C., Wilder, M. C., Bogdanoff, D. W., and Prabhu, D. K., "Transition Experiments on Blunt Bodies with Distributed Roughness in Hypersonic Free Flight," *Journal of Spacecraft and Rockets*, Vol. 45, No. 2, 2008, pp. 210–215.
doi:10.2514/1.30288

[11] Ali, S. R., Radespiel, R., and Theiss, A., "Transition Experiment with a Blunt Apollo Shape Like Capsule in Hypersonic Ludwieg Tube," *63. Deutscher Luft-und Raumfahrtkongress 2014*, Paper 2014-340270, DGLR, Bonn, 2014.

[12] Radespiel, R., Ali, S. R. C., Muoz, F., Bowersox, R., Leidy, A., Tanno, H., Kirk, L. C., and Reshotko, E., "Experimental Investigation of Roughness Effects on Transition on Blunt Spherical Capsule Shapes," *Journal of Spacecraft and Rockets*, 2018.
doi:10.2514/1.A34295

[13] Marineau, E. C., Laurence, S. J., and Hornung, H. G., "Apollo-Shaped Capsule Boundary Layer Transition at High-Enthalpy in T5," AIAA Paper 2010-0446, 2010.
doi:10.2514/6.2010-446

[14] Tanno, H., Kodera, M., Komuro, T., Sato, K., Takahashi, M., and Itoh, K., "Aeroheating Measurements on a Reentry Capsule Model in Free-Piston Shock Tunnel HIEST," AIAA Paper 2010-1181, 2010.
doi:10.2514/6.2010-1181

[15] Tanno, H., Sato, K., Komuro, T., and Itoh, K., "Free-Flight Aerodynamic Test of Reentry Vehicles in High-Temperature Real-Gas Flow," AIAA Paper 2014-3109, 2014.
doi:10.2514/6.2014-3109

[16] Olejniczak, J., Wright, M. J., Laurence, S., and Hornung, H. G., "Computational Modeling of T5 Laminar and Turbulent Heating Data on Blunt Cones, Part 1: Titan Application," AIAA Paper 2005-0176, 2005.
doi:10.2514/6.2005-176

[17] Chang, C.-L., Choudhari, M., Venkatachari, B. S., and Li, F., "Effects of Cavities and Protuberances on Transition over Hypersonic Vehicles," AIAA Paper 2011-3245, 2011.
doi:10.2514/6.2011-3245

[18] Theiss, A., Hein, S., Ali, S. R. C., and Radespiel, R., "Wake Flow Instability Studies Behind Discrete Roughness Elements on a Generic Re-Entry Capsule," AIAA Paper 2016-4382, 2016.
doi:10.2514/6.2016-4382

[19] Theiss, A., Leyh, S., and Hein, S., "Pressure Gradient Effects on Wake Flow Instabilities Behind Isolated Roughness Elements on Re-Entry Capsules," *7th European Conference for Aeronautics and Aerospace Sciences*, EUCASS, 2017.
doi:10.13009/EUCASS2017-594

[20] De Tullio, N., Paredes, P., Sandham, N., and Theofilis, V., "Laminar Turbulent Transition Induced by a Discrete Roughness Element in a Supersonic Boundary Layer," *Journal of Fluid Mechanics*, Vol. 735, 2013, pp. 613–646.
doi:10.1017/jfm.2013.520

[21] Hudson, M. L., Chokani, N., and Candler, G., "Linear Stability of Hypersonic Flow in Thermochemical Nonequilibrium," AIAA Paper 1996-0671, 1996.
doi:10.2514/2.204

[22] Hudson, M. L., "Linear Stability of Hypersonic Flow in Thermal and Chemical Nonequilibrium," Ph.D. Thesis, North Carolina State Univ., Raleigh, North Carolina, 1996.

[23] Chang, C.-L., Vinh, H., and Malik, M., "Hypersonic Boundary-Layer Stability with Chemical Reactions Using PSE," *28th Fluid Dynamics Conference, Fluid Dynamics and Co-Located Conferences*, AIAA Paper 1997-2012, 2012.
doi:10.2514/6.1997-2012

[24] Stemmer, C., Birrer, M., and Adams, N. A., "Hypersonic Boundary-Layer Flow with an Obstacle in Thermochemical Equilibrium and Nonequilibrium," *Journal of Spacecraft and Rockets*, Vol. 54, No. 4, 2017, pp. 899–915.
doi:10.2514/1.A32984

[25] Stemmer, C., Birrer, M., and Adams, N. A., "Disturbance Development in an Obstacle Wake in a Reacting Hypersonic Boundary Layer," *Journal of Spacecraft and Rockets*, Vol. 54, No. 4, 2017, pp. 945–960.
doi:10.2514/1.A33708

[26] Johnson, H. B., Seipp, T. G., and Candler, G. V., "Numerical Study of Hypersonic Reacting Boundary Layer Transition on Cones," *Physics of Fluids*, Vol. 10, No. 10, 1998, pp. 2676–2685.
doi:10.1063/1.869781

[27] Malik, M. R., "Disturbance Development in an Obstacle Wake in a Reacting Hypersonic Boundary Layer," *Journal of Spacecraft and Rockets*, Vol. 40, No. 3, 2003, pp. 332–344.
doi:10.2514/2.3968

[28] Johnson, H. B., and Candler, G. V., "Hypersonic Boundary Layer Stability Analysis Using PSE-Chem," AIAA Paper 2005-5023, 2005.
doi:10.2514/6.2005-5023

[29] Mortensen, C. H., and Zhong, X., "Real-Gas and Surface-Ablation Effects on Hypersonic Boundary-Layer Instability over a Blunt Cone," *AIAA Journal*, Vol. 54, No. 3, 2016, pp. 980–998.
doi:10.2514/1.J054404

[30] Stemmer, C., and Fehn, J., "High-Temperature Gas Effects at a Capsule Under Re-Entry and Wind-Tunnel Conditions," AIAA Paper 2014-2645, 2014.
doi:10.2514/6.2014-2645

[31] Di Giovanni, A., and Stemmer, C., "Numerical Simulations of the High-Enthalpy Boundary Layer on a Generic Capsule Geometry with Roughness," *New Results in Numerical and Experimental Fluid Mechanics XI, STAB/DGLR Symposium*, Springer, 2017, pp. 189–198.
doi:10.1007/978-3-319-64519-3_17

[32] Di Giovanni, A., and Stemmer, C., "Crossflow-Type Breakdown Induced by Distributed Roughness in the Boundary Layer of a Hypersonic Capsule Configuration," *Journal of Fluid Mechanics*, Vol. 856, 2018, pp. 470–503.
doi:10.1017/jfm.2018.706

[33] Schneider, S. P., "Effects of Roughness on Hypersonic Boundary-Layer Transition," *Journal of Spacecraft and Rockets*, Vol. 45, No. 2, 2008, pp. 193–209.
doi:10.2514/1.29713

[34] Van den Eynde, J. P. J. P., and Sandham, N. D., "Numerical Simulations of Transition due to Isolated Roughness Elements at Mach 6," *AIAA Journal*, Vol. 54, No. 1, 2016, pp. 53–65.
doi:10.2514/1.J054139

[35] Park, C., "A Review of Reaction Rates in High Temperature Air," AIAA Paper 1989-1740, 1989.
doi:10.2514/6.1989-1740

[36] Anderson, J. D., Jr., *Hypersonic and High-Temperature Gas Dynamics*, AIAA Education Series, AIAA, Reston, VA, Oct. 2006.
doi:10.2514/4.861956

[37] Blottner, F. G., Johnson, M., and Ellis, M., "Chemically Reacting Viscous Flow Program for Multi-Component Gas Mixtures," Sandia National Lab. TR SC- RR-70-754, 1971.

[38] Hirschfelder, J. O., Curtiss, C. F., and Bird, R. A., *Molecular Theory of Gases and Liquids*, Wiley, New York, 1954, p. 539.

[39] Wilke, C., "A Viscosity Equation for Gas Mixtures," *Journal of Chemical Physics*, Vol. 18, No. 4, 1950, pp. 517–519.
doi:10.1063/1.1747673

[40] Park, C., "Stagnation-Point Radiation for Apollo 4," *Journal of Thermophysics and Heat Transfer*, Vol. 18, No. 3, 2004, pp. 349–357.
doi:10.2514/1.6527

[41] Muppidi, S., and Mahesh, K., "Direct Numerical Simulations of Roughness-Induced Transition in Supersonic Boundary Layers," *Journal of Fluid Mechanics*, Vol. 693, 2012, pp. 28–56.
doi:10.1017/jfm.2011.417

[42] Groskopf, G., and Kloker, M. J., "Instability and Transition Mechanisms Induced by Skewed Roughness Elements in a High-Speed Laminar Boundary Layer," *Journal of Fluid Mechanics*, Vol. 805, 2016, pp. 262–302.
doi:10.1017/jfm.2016.563

[43] Vos, J., Duquesne, N., and Lee, H., "Shock Wave Boundary Layer Interaction Studies Using the NSMB Flow Solver," *Proceedings of the 3rd European Symposium on Aerothermodynamics for Space and Vehicles*, ESA SP-426, ESTEC, Noordwijk, The Netherlands, 1999, pp. 229–236.

[44] Hoarau, Y., Pena, D., Vos, J. B., Charbonier, D., Gehri, A., Braza, M., Deloze, T., and Laurendeau, E., "Recent Developments of the Navier Stokes Multi Block (NSMB) CFD Solver," AIAA Paper 2016-2056, 2016.
doi:10.2514/6.2016-2056

[45] Von Kaenel, R., Sanchi, S., Vos, J., Gaffuri, M., Leyland, P., Walloschek, T., and Binetti, P., "IXV CFD Simulations for Wind Tunnel Rebuilding and Extrapolation to Flight," *Proceedings of the 6th European Symposium on Aerothermodynamics for Space Vehicles*, ESA SP-659, ESTEC, Noordwijk, The Netherlands, 2009.

[46] Goebel, F., Vos, J., and Mundt, C., "CFD Simulation of the FIRE II Flight Experiment," AIAA Paper 2012-3350, 2012.
doi:10.2514/6.2012-3350

[47] Di Giovanni, A., and Stemmer, C., "Direct Numerical Simulations of Roughness-Induced Transition in the Boundary Layer of a Hypersonic Spherical Forebody Under Consideration of High-Temperature Gas Effects," AIAA Paper 2018-4046, 2018.
doi:10.2514/6.2018-4046

[48] Malik, M. R., Li, F., Choudhari, M. M., and Chang, C.-L., "Secondary Instability of Crossflow Vortices and Swept-Wing Boundary-Layer Transition," *Journal of Fluid Mechanics*, Vol. 399, 1999, pp. 85–115.
doi:10.1017/S0022112099006291

[49] Wassermann, P., and Kloker, M., "Transition Mechanisms Induced by Travelling Crossflow Vortices in a Three-Dimensional Boundary Layer," *Journal of Fluid Mechanics*, Vol. 483, 2003, pp. 67–89.
doi:10.1017/S0022112003003884

[50] White, E. B., and Saric, W. S., "Secondary Instability of Crossflow Vortices," *Journal of Fluid Mechanics*, Vol. 525, 2005, pp. 275–308.
doi:10.1017/S002211200400268X

[51] Chou, A., King, A., and Kegerise, M. A., "Transition Induced by Tandem Rectangular Roughness Elements on a Supersonic Flat Plate," AIAA Paper 2018-3531, 2018.
doi:10.2514/6.2018-3531

M. Borg
Associate Editor

B.3 Roughness-Induced Boundary-Layer Transition on a Hypersonic Capsule-Like Forebody Including Nonequilibrium

In the following language(s)	Original language of publication
With incidental promotional use	no
The lifetime unit quantity of new product	Up to 499
Title	Roughness-Induced Transition in a Hypersonic Capsule Boundary Layer under Wind-Tunnel and Reentry Conditions
Institution name	n/a
Expected presentation date	Oct 2019
Total (may include CCC user fee)	0.00 USD
Terms and Conditions	

be deemed jointly a "User" for purposes of these terms and conditions. In any event, User shall be deemed to have accepted and agreed to all such terms and conditions if User republishes the Work in any fashion.

3. Scope of License; Limitations and Obligations.

3.1 All Works and all rights therein, including copyright rights, remain the sole and exclusive property of the Rightsholder. The license created by the exchange of an Order Confirmation (and/or any invoice) and payment by User of the full amount set forth on that document includes only those rights expressly set forth in the Order Confirmation and in these terms and conditions, and conveys no other rights in the Work(s) to User. All rights not expressly granted are hereby reserved.

3.2 General Payment Terms: You may pay by credit card or through an account with us payable at the end of the month. If you and we agree that you may establish a standing account with CCC, then the following terms apply: Remit Payment to: Copyright Clearance Center, 29118 Network Place, Chicago, IL 60673-1291. Payments Due: Invoices are payable upon their delivery to you (or upon our notice to you that they are available to you for downloading). After 30 days, outstanding amounts will be subject to a service charge of 1-1/2% per month or, if less, the maximum rate allowed by applicable law. Unless otherwise specifically set forth in the Order Confirmation or in a separate written agreement signed by CCC, invoices are due and payable on "net 30" terms. While User may exercise the rights licensed immediately upon issuance of the Order Confirmation, the license is automatically revoked and is null and void, as if it had never been issued, if complete payment for the license is not received on a timely basis either from User directly or through a payment agent, such as a credit card company.

3.3 Unless otherwise provided in the Order Confirmation, any grant of rights to User (i) is "one-time" (including the editions and product family specified in the license), (ii) is non-exclusive and non-transferable and (iii) is subject to any and all limitations and restrictions (such as, but not limited to, limitations on duration of use or circulation) included in the Order Confirmation or invoice and/or in these terms and conditions. Upon completion of the licensed use, User shall either secure a new permission for further use of the Work(s) or immediately cease any new use of the Work(s) and shall render inaccessible (such as by deleting or by removing or severing links or other locators) any further copies of the Work (except for copies printed on paper in accordance with this license and still in User's stock at the end of such period).

3.4 In the event that the material for which a republication license is sought includes third party materials (such as photographs, illustrations, graphs, inserts and similar materials) which are identified in such material as having been used by permission, User is responsible for identifying, and seeking separate licenses (under this Service or otherwise) for, any of such third party materials; without a separate license, such third party materials may not be used.

3.5 Use of proper copyright notice for a Work is required as a condition of any license granted under the Service. Unless otherwise provided in the Order Confirmation, a proper copyright notice will read substantially as follows: "Republished with permission of [Rightsholder's name], from [Work's title, author, volume, edition number and year of copyright]; permission conveyed through Copyright Clearance Center, Inc. " Such notice must be provided in a reasonably legible font size and must be placed either immediately adjacent to the Work as used (for example, as part of a by-line or footnote but not as a separate electronic link) or in the place where substantially all other credits or notices for the new work containing the republished Work are located. Failure to include the required notice results in loss to the Rightsholder and CCC, and the User shall be liable to pay liquidated damages for each such failure equal to twice the use fee specified in the Order Confirmation, in addition to the use fee itself and any other fees and charges specified.

3.6 User may only make alterations to the Work if and as expressly set forth in the Order Confirmation. No Work may be used in any way that is defamatory, violates the rights of third parties (including such third parties' rights of copyright, privacy, publicity, or other tangible or intangible property), or is otherwise illegal, sexually explicit or obscene. In addition, User may not conjoin a Work with any other material that may result in damage to the reputation of the Rightsholder. User agrees to inform CCC if it becomes aware of any infringement of any rights in a Work and to cooperate with any reasonable request of CCC or the Rightsholder in connection therewith.

4. Indemnity. User hereby indemnifies and agrees to defend the Rightsholder and CCC, and their respective employees and directors, against all claims, liability, damages, costs and expenses, including legal fees and expenses, arising out of any use of a Work beyond the scope of the rights granted herein, or any use of a Work which has been altered in any unauthorized way by User, including claims of defamation or infringement of rights of copyright, publicity, privacy or other tangible or intangible property.

5. Limitation of Liability. UNDER NO CIRCUMSTANCES WILL CCC OR THE RIGHTSHOLDER BE LIABLE FOR ANY DIRECT, INDIRECT, CONSEQUENTIAL OR INCIDENTAL DAMAGES (INCLUDING WITHOUT LIMITATION DAMAGES FOR LOSS OF BUSINESS PROFITS OR INFORMATION, OR FOR BUSINESS INTERRUPTION) ARISING OUT OF THE USE OR INABILITY TO USE A WORK, EVEN IF ONE OF THEM HAS BEEN ADVISED OF THE POSSIBILITY OF SUCH DAMAGES. In any event, the total liability of the Rightsholder and CCC (including their respective employees and directors) shall not exceed the total amount actually paid by User for this license. User assumes full liability for the actions and omissions of its principals, employees, agents, affiliates, successors and assigns.

6. Limited Warranties. THE WORK(S) AND RIGHT(S) ARE PROVIDED "AS IS". CCC HAS THE RIGHT TO GRANT TO USER THE RIGHTS GRANTED IN THE ORDER CONFIRMATION DOCUMENT. CCC AND THE RIGHTSHOLDER DISCLAIM ALL OTHER WARRANTIES RELATING TO THE WORK(S) AND RIGHT(S), EITHER EXPRESS OR IMPLIED, INCLUDING WITHOUT LIMITATION IMPLIED WARRANTIES OF MERCHANTABILITY OR FITNESS FOR A PARTICULAR PURPOSE. ADDITIONAL RIGHTS MAY BE REQUIRED TO USE ILLUSTRATIONS, GRAPHS, PHOTOGRAPHS, ABSTRACTS, INSERTS OR OTHER PORTIONS OF THE WORK (AS OPPOSED TO THE ENTIRE WORK) IN A MANNER CONTEMPLATED BY USER; USER UNDERSTANDS AND AGREES THAT NEITHER CCC NOR THE RIGHTSHOLDER MAY HAVE SUCH ADDITIONAL RIGHTS TO GRANT.

7. Effect of Breach. Any failure by User to pay any amount when due, or any use by User of a Work beyond the scope of the license set forth in the Order Confirmation and/or these terms and conditions, shall be a material breach of the license created by the Order Confirmation and these terms and conditions. Any breach not cured within 30 days of written notice thereof shall result in immediate termination of such license without further notice. Any unauthorized (but licensable) use of a Work that is terminated immediately upon notice thereof may be liquidated by payment of the Rightsholder's ordinary license price therefor; any unauthorized (and unlicensable) use that is not terminated immediately for any reason (including, for example, because materials containing the Work cannot reasonably be recalled) will be subject to all remedies available at law or in equity, but in no event to a payment of less than three times the Rightsholder's ordinary license price for the most closely analogous licensable use plus Rightsholder's and/or CCC's costs and expenses incurred in collecting such payment.

8. **Miscellaneous.**

8.1 User acknowledges that CCC may, from time to time, make changes or additions to the Service or to these terms and conditions, and CCC reserves the right to send notice to the

User by electronic mail or otherwise for the purposes of notifying User of such changes or additions; provided that any such changes or additions shall not apply to permissions already secured and paid for.

8.2 Use of User-related information collected through the Service is governed by CCC's privacy policy, available online here: http://www.copyright.com/content/cc3/en/tools/footer/privacypolicy.html.

8.3 The licensing transaction described in the Order Confirmation is personal to User. Therefore, User may not assign or transfer to any other person (whether a natural person or an organization of any kind) the license created by the Order Confirmation and these terms and conditions or any rights granted hereunder; provided, however, that User may assign such license in its entirety on written notice to CCC in the event of a transfer of all or substantially all of User's rights in the new material which includes the Work(s) licensed under this Service.

8.4 No amendment or waiver of any terms is binding unless set forth in writing and signed by the parties. The Rightsholder and CCC hereby object to any terms contained in any writing prepared by the User or its principals, employees, agents or affiliates and purporting to govern or otherwise relate to the licensing transaction described in the Order Confirmation, which terms are in any way inconsistent with any terms set forth in the Order Confirmation and/or in these terms and conditions or CCC's standard operating procedures, whether such writing is prepared prior to, simultaneously with or subsequent to the Order Confirmation, and whether such writing appears on a copy of the Order Confirmation or in a separate instrument.

8.5 The licensing transaction described in the Order Confirmation document shall be governed by and construed under the law of the State of New York, USA, without regard to the principles thereof of conflicts of law. Any case, controversy, suit, action, or proceeding arising out of, in connection with, or related to such licensing transaction shall be brought, at CCC's sole discretion, in any federal or state court located in the County of New York, State of New York, USA, or in any federal or state court whose geographical jurisdiction covers the location of the Rightsholder set forth in the Order Confirmation. The parties expressly submit to the personal jurisdiction and venue of each such federal or state court.If you have any comments or questions about the Service or Copyright Clearance Center, please contact us at 978-750-8400 or send an e-mail to info@copyright.com.

v 1.1

Questions? customercare@copyright.com or +1-855-239-3415 (toll free in the US) or +1-978-646-2777.

Roughness-Induced Boundary-Layer Transition on a Hypersonic Capsule-Like Forebody Including Nonequilibrium

Antonio Di Giovanni* and Christian Stemmer[†]

Technical University of Munich, 85748 Garching, Germany

The present work investigates the influence of high-temperature gas effects on the laminar–turbulent transition induced by a patch of distributed roughness on a hemispherical capsule-like geometry. The freestream conditions correspond to a realistic reentry scenario at Mach 20. At these conditions, chemical reactions and nonequilibrium effects are present in the high-enthalpy boundary layer of the hemisphere. Parallel Direct Numerical Simulations are undertaken to analyze the instability mechanisms in the crossflow-type vortex developing in the wake of a skewed protuberance of the roughness patch. Both linear and nonlinear growth of unsteady disturbances forced in the roughness wake, including laminar–turbulent breakdown, are considered in the analysis. The primary focus of the study is how chemical and thermal nonequilibrium affect the location of the laminar–turbulent transition as well as the level of wall heating in the transitional boundary layer for the considered capsule configuration. The results highlight the necessity to include nonequilibrium effects in this problem of roughness-induced transition at high-altitude reentry conditions because the gas modeling turns out to have a notable influence on the development of instabilities, both in the linear and in the nonlinear ranges.

Nomenclature

$A_{q,r}$	=	amplitude coefficients used in the roughness definition
$c(y)$	=	smoothing function used in the definition of the unsteady disturbance
c_p	=	heat capacity, J/(kg · K)
c_s	=	species concentration
e^{vib}	=	vibrational energy, J/kg
f_{1-6}	=	frequencies of unsteady disturbances, Hz
$g(x)$	=	envelope function for the roughness definition
h	=	surface height with respect to the smooth configuration, m
k	=	roughness height, m
M	=	Mach number
N	=	N factor
N_x, N_y, N_z	=	number of grid points in x, y, and z directions
P_0	=	amplitude of the inflow disturbance, N/m^2
p	=	pressure, N/m^2
Q^{chem}	=	heat transfer due to chemical reactions, J/(kg · s)
Q^{t-v}	=	translational–vibrational heat transfer, J/(kg · s)
q	=	generic flow variable
q^{vib}	=	heat-conduction term based on the vibrational temperature, J/(kg · s)
$\dot{q}$	=	heat flux at the wall, W/m^2
R_a	=	mean roughness, m
Re_{kk}	=	roughness Reynolds number
Re_∞	=	unit Reynolds number, m^{-1}
$\tilde{r}$	=	radial distance, m
T	=	temperature, K
U	=	reference velocity, m/s
u, v, w	=	velocities in x, y, and z directions, m/s
$\boldsymbol{u}_s^D$	=	diffusion velocity of the species s, m/s
x, y, z	=	coordinates in streamwise, wall-normal, and spanwise directions, m
x_0^*	=	x coordinate at the inflow boundary of the unsteady simulation domain
δ	=	boundary-layer thickness, m
θ_1	=	elevation angle, rad
θ_2	=	azimuth, rad
λ	=	thermal conductivity, W/(m · K)
λ_0	=	fundamental roughness wavelength, m
μ	=	viscosity, kg/(m · s)
ρ	=	density, kg/m^3
ϕ	=	phase
ω_x	=	streamwise vorticity, s^{-1}
$\dot{\omega}_s$	=	species chemical production rate, kg/(m^3 · s)

Subscripts

f	=	frequency in the Fourier analysis
i, j	=	summation indices
in	=	value at the inflow boundary
k	=	value taken at the height of the roughness
m	=	molecular species
max	=	maximum value
min	=	minimum value
q, r	=	multiples of the fundamental roughness wave number
s	=	species
st	=	condition of the steady base flow
un	=	condition of the unsteady flow
w	=	value taken at the wall
∞	=	freestream conditions

Superscripts

^	=	temporal Fourier mode
⁻	=	time average

I. Introduction

ROUGHNESS-INDUCED laminar–turbulent transition at hypersonic speeds is an important, although still not fully understood, problem. The heat transfer at the wall in the case of a turbulent or transitional boundary layer is significantly larger than in the laminar case. Thus, understanding the phenomenon of transition on hypersonic vehicles, such as reentry capsules, is important in the

design of the thermal protection systems and for a safe reentry and return of the crew.

Many experiments on transition on capsule models have been carried out in the last decades for flight-relevant Reynolds numbers (for a detailed review, see the work of Schneider [1]). Modern high-fidelity computational methods can provide a deep insight into the problem of laminar–turbulent transition occurring at high-altitude reentry conditions. In particular, Direct Numerical Simulations (DNS) allow for investigations of complex geometries and provide a detailed description of nonlinear instability mechanisms, including the transition process.

At reentry conditions, molecular dissociation and nonequilibrium effects are important, including at altitudes where transition is expected [2]. Thermochemistry can significantly change velocity and temperature profiles, and hence the stability properties of the boundary layer. However, experiments on ground facilities at flight conditions encountered in realistic reentry scenarios are extremely difficult to realize, especially due to the inability of matching all relevant dimensionless parameters, including the Damköhler number. Therefore, numerical simulations are a fundamental and often indispensable investigation tool.

Chemical reactions and nonequilibrium can have counteracting effects on the stability of the boundary layers. As observed by Johnson et al. [3], gas with low dissociation energy, such as molecular oxygen in air, can diminish the disturbance amplification rates due to higher absorption of energy fluctuations as compared to gases with a higher dissociation energy, such as nitrogen (see also the experiments by Germain and Hornung [4]). On the other hand, the presence of chemical reactions can considerably alter the thermodynamic properties as well as the velocity and temperature profiles of the boundary layer as compared to the ideal-gas case, leading to a destabilization of the base flow.

The first stability investigations on high-enthalpy boundary layers, including high-temperature gas effects, were conducted by means of the linear stability theory (LST). Malik and Anderson [2] investigated modal instability mechanisms in a flat-plate boundary layer at $M = 10$ and $M = 15$ with the assumption of reacting flow in thermal and chemical equilibrium. Compared to the stability analyses conducted with the assumption of ideal gas, the incorporation of chemistry had a stabilizing effect on the first-mode instability, whereas it destabilized the second-mode instability. The effects of chemical nonequilibrium were included in the LST by Stuckert and Reed [5], whereas both chemical and thermal nonequilibrium were considered by Hudson et al. [6,7]. It was shown that chemical nonequilibrium destabilizes the second mode as compared to the case of equilibrium gas, whereas thermal nonequilibrium is slightly stabilizing. With reference to the first mode, the case of chemical equilibrium was the most unstable among the reacting-gas cases.

Parabolized stability equations (PSEs) were applied to high-enthalpy flows by Chang et al. [8], who addressed the case of a 6 deg wedge at $M = 20$ for both chemical equilibrium and chemical nonequilibrium. The extension of the PSE to boundary layers in thermochemical nonequilibrium was presented by Johnson and Candler [9]. These works confirmed the trends found both in previous LST-based analyses and in experiments.

DNS were used by Stemmer et al. [10,11] to investigate the linear instability mechanisms in the three-dimensional reacting boundary layer of the HyBoLT geometry ($M = 8.5$) in the presence of a cuboid roughness element. Both chemical and thermal nonequilibrium were progressively considered in the analysis. The wake of the cuboid was characterized by the presence of varicose and sinuous modes already known for the case of isolated roughness elements in cold-flow boundary layers (see, e.g., the work of De Tullio et al. [12]). In the wake of the cuboid, the amplification rates of unsteady disturbances were larger for chemical nonequilibrium than for chemical equilibrium.

So far, there has been limited use of DNS to investigate nonlinear stability and breakdown to turbulence in the case of flows where high-temperature gas effects are nonnegligible. DNS were undertaken by Marxen et al. [13] to analyze linear and nonlinear instability mechanisms in a finite-rate chemically reacting boundary layer at

$M = 10$. It was observed that chemical reactions mainly increase the instability of the modes in the linear range while not directly affecting the growth of secondary instabilities.

In the case of capsule geometries at hypersonic speeds, the stability of the boundary layer has been studied mostly under the assumption of ideal gas. In both wind-tunnel and free-flight conditions, transition is observed on blunt capsule geometries, although the boundary layer on smooth-wall blunt bodies is stable against first- and second-mode instabilities, as well as crossflow and Görtler-vortex instabilities (as studied, among others, by Morkovin [14] and Theiss et al. [15]). Furthermore, even though transient growth is present on blunt capsules, Hein et al. [16] showed that the N-factors obtained through optimal transient-growth analysis are too small to explain transition. Hence, laminar–turbulent transition on capsule configurations is believed to be mainly affected by wall roughness. Isolated roughness elements are present on the wall of reentry vehicles as heat-shield joints, compression pads, and gaps between tiles. Distributed roughness mainly results from thermal ablation or deformation of the thermal protection system and manufacturing uncertainties.

Experiments on transition on spherical forebodies were conducted, among others, by Hollis [17,18] and Reda et al. [19,20]. It was observed that roughness-induced transition depends on parameters such as the ratio roughness-height to boundary-layer thickness and the roughness Reynolds number $Re_{kk} = \rho_k u_k k/\mu_k$ defined with the flow properties at the roughness height for the corresponding smooth configuration. In the work of Reda et al. [20], transition on a blunt geometry with distributed sand-grain roughness was observed for values of Re_{kk} in the range of $250 \pm 20\%$. In this case, the roughness Reynolds number was built with the arithmetic average of the measured roughness heights.

In the Hypersonic Ludwieg Tube in Braunschweig (HLB), experimental and numerical investigations for an Apollo-like capsule with a diameter of 170 mm at $M = 5.9$ were documented by Theiss et al. [15,21,22], Hein et al. [16], and Radespiel et al. [23]. In experiments conducted with a unit Reynolds number of $Re_{\infty} = 18 \cdot 10^6$ m^{-1}, no evidence of transitional flow was observed for the smooth-wall model. Instead, an increased heating was measured at the wall with distributed roughness with a mean roughness value of $R_a = 10$ μm. For the same capsule geometry, Theiss et al. [21,22] numerically investigated the effects of an isolated roughness element positioned on the windward side of the capsule model. For roughness elements with values of Re_{kk} (built with height of the element) in the range of 124–336, the base flow remained steady. LST and PSE analyses of the roughness wake revealed the presence of at least two different unstable modes of varicose and sinuous types. Instead, no modal growth was revealed by the numerical investigation on the wake of small distributed roughness elements with $Re_{kk} = 25$ [16]. On the base of the same freestream conditions as in the HLB, Di Giovanni and Stemmer [24] used DNS to investigate the instability mechanisms in the wake of different roughness patches on a capsule-like hemispherical forebody with a radius of 200 mm at $M = 5.9$. Due to the skewed profile of the main protuberance found in a patch of random distributed roughness with $Re_{kk} = 406$, a crossflow-type vortex developed in the wake of the roughness. This crossflow-type vortex was shown to be more persistent than the pair of counter-rotating vortices generated by isolated roughness elements with the same height and roughness Reynolds number. Accordingly, a larger overall growth of unsteady disturbances was observed in the case of distributed roughnesses.

Chang et al. [25] performed unsteady simulations of the boundary layer on a model of the Crew Exploration Vehicle (CEV) at $M = 6$. Natural vortex shedding was observed in the presence of roughness elements of $Re_{kk} = 800$ and a height to boundary-layer thickness ratio of 0.73.

High-enthalpy experiments with reacting flows including nonequilibrium were conducted at the T5 hypervelocity shock tunnel at GALCIT on an Apollo-capsule model of 177.8 mm in diameter by Marineau et al. [26]. A fully turbulent boundary layer was observed downstream of trips with a height between 0.5 and 1m boundary-layer thicknesses. A further experimental campaign on an Apollo-capsule model of 150 mm in diameter was undertaken at the

hot free-piston shock tunnel HIEST by Tanno et al. [27,28]. The boundary layer on the smooth-wall model remained laminar for Mach numbers between six and eight and Reynolds numbers in the range of 1–$5 \cdot 10^6$ m^{-1}.

The present work extends the results from Di Giovanni and Stemmer [24] with the goal of numerically investigating the nonlinear development of instabilities in the wake of a patch of randomly distributed roughness for a high-enthalpy reacting boundary layer including nonequilibrium effects. A capsule-like hemisphere with a radius of 5.98 m is considered, and freestream conditions are chosen to match realistic reentry conditions at $M = 20$ at an altitude of 57.7 km. Linear disturbances with various frequencies are forced in the roughness wake, and their growth is investigated by means of Direct Numerical Simulations in both the linear and nonlinear ranges, including laminar–turbulent breakdown. The effects of the high temperature on the transitional flow are addressed by performing three different simulations with three different gas models of increasing complexity, i.e., equilibrium air, air in chemical nonequilibrium, and air in both chemical and thermal (thermochemical) nonequilibrium. The effects of transition on the heat flux at the wall are also quantified and compared for the three gas models.

II. Numerical Procedure

A. Freestream Conditions and Gas Models

The flow conditions for the present simulations are chosen based on a realistic reentry scenario. The Mach number is equal to 20, and values of air pressure and temperature correspond to an altitude of about 57.7 km. The unit Reynolds number is $Re_\infty = 1.97 \cdot 10^6$ m^{-1} (Table 1).

At these conditions, the temperature downstream of the strong bow shock ahead of the capsule exceeds 5000 K. As a consequence, the model of calorically and thermally perfect gas is not appropriate to describe the fluid any more, and molecular dissociations and nonequilibrium effects influence the flow. Three different cases are investigated with three different gas models, i.e., air in chemical and thermal equilibrium (CEQ), air in chemical nonequilibrium (CNEQ), and air in thermochemical nonequilibrium (CTNEQ). Starting with the model of reacting gas in equilibrium, the gradual inclusion of finite-rate chemistry and thermal nonequilibrium aims to highlight the different effects of the high temperature on the base flow, and consequently on its stability properties and the laminar–turbulent breakdown.

Full three-dimensional unsteady Navier–Stokes equations are solved for chemically reacting air. Air is modeled with Park's five-species model (N_2, O_2, N, O, and NO) [29], with each species treated as an ideal gas. The concentration of the species s is defined as $c_s = \rho_s/\rho$. The full compressible Navier–Stokes equations are solved together with additional equations to account for chemistry and nonequilibrium. Specifically, to compute the composition of air in chemical equilibrium, algebraic equations are solved for the dissociation of the molecular species N_2, O_2, and NO (laws of mass action), as well as for the conservation of the atomic species O and N. In the case of air in chemical nonequilibrium, the finite-rate chemistry is described by five differential equations for the mass balance of the chemical species involved:

$$\rho \frac{\mathrm{D}c_s}{\mathrm{D}t} + \nabla \cdot (\rho_s \boldsymbol{u}_s^D) = \dot{\omega}_s \qquad (1)$$

Table 1   Freestream conditions

Parameter	Value
M	20
p_∞, Pa	29.9
T_∞, K	253.3
T_w, K	1800
Re_∞, m^{-1}	$1.97 \cdot 10^6$
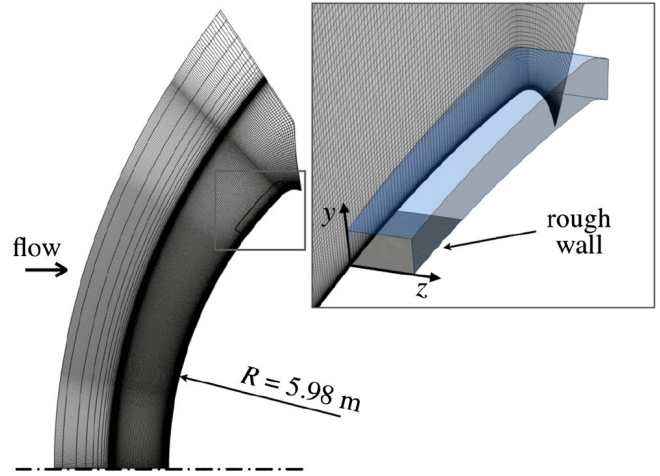
Fig. 1   Full (left) and restricted (right) computational domains.

where $\dot{\omega}_s$ is the chemical production term, and $\boldsymbol{u}_s^D$ is the diffusion velocity of the species s. The chemical production term follows an Arrhenius-type relation, whereas the diffusion is described by Fick's law, assuming a constant Schmidt number with the diffusion coefficients independent of the species concentration. If thermal nonequilibrium is included, an additional energy-conservation equation is solved for the vibrational energy e_m^{vib} of each molecular species m,

$$\frac{\mathrm{D}}{\mathrm{D}t}(c_m e_m^{\mathrm{vib}}) + \frac{1}{\rho}\nabla \cdot (\rho_m \boldsymbol{u}_m^D e_m^{\mathrm{vib}}) = -q_m^{\mathrm{vib}} + Q_m^{t-v} + Q_m^{\mathrm{chem}} \qquad (2)$$

where q_m^{vib} describes the heat-conduction term, Q_m^{t-v} is the translational–vibrational energy transfer rate, and Q_m^{chem} is the chemical production term due to reactions of the species m. The heat-conduction is described by Fourier's law, and the translational–vibrational energy transfer rate is described by the Landau–Teller theory [30] with a semiempirical method to calculate the vibrational relaxation times as proposed by Millikan and White [31].

The viscosity μ, the heat capacity c_p, and the thermal conductivity λ depend on temperature and air composition. In particular, the viscosities of the single species are calculated according to Blottner et al. [32], the species' thermal conductivities are calculated according to Hirschfelder et al. [33], and the thermodynamic properties of the gas mixture are computed with Wilke's mixing rules [34]. Further details on the constitutive equations as applied in this work were given in Refs. [10,35].

B. Geometrical Setup and Integration Domain

The considered geometry is a segment of a sphere with a radius of 5.98 m and an angular extension of 90.8 deg (see Fig. 1). This geometry has already been investigated in Refs. [16,24] for the case of cold wind-tunnel conditions ($M = 5.9$) at a reduced scale. The hemisphere ends in a shoulder resembling the one of a generic Apollo capsule geometry. Because the shoulder provides a strong natural damping region due to the strong acceleration of the flow, the computational domain can be truncated after the shoulder without influencing the boundary layer upstream of the shoulder on the spherical part of the domain. The size and the shape of the domain are chosen to feature a realistic capsule geometry. In particular, in the work of Hein et al. [16], it has been shown that the boundary layer on the present axisymmetric geometry reproduces in very good approximation the boundary layer in the symmetry plane of a generic Apollo-capsule model with an angle of attack of 24 deg. Compared to the three-dimensional capsule model with an angle of attack, the hemisphere geometry allows for a substantial reduction of the computational domain and effort due to azimuthal periodicity of the domain.

Because full unsteady three-dimensional DNS of the entire hemisphere with a rough wall would be extremely expensive in terms
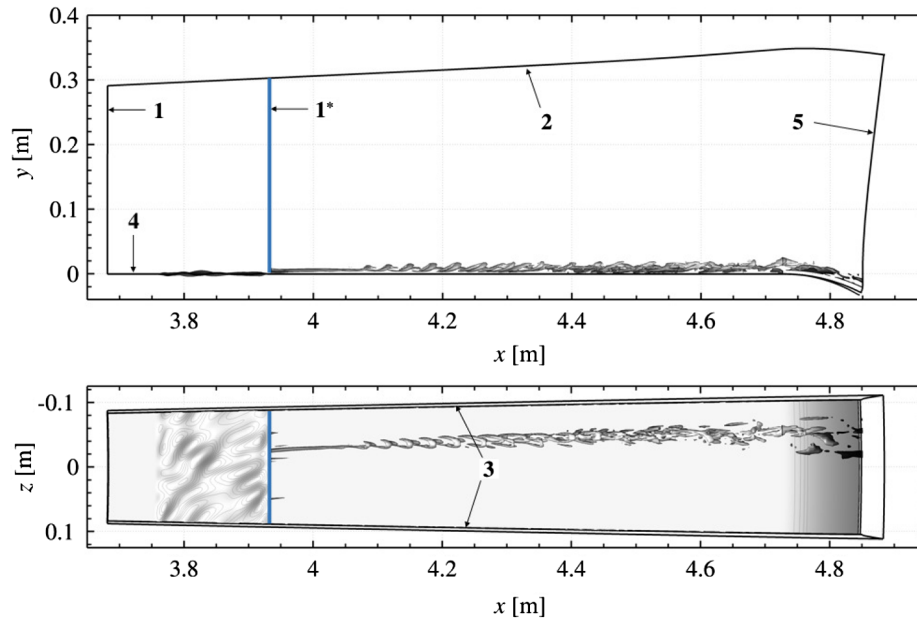
Fig. 2   Restricted computational domain with boundaries enumerated from 1 to 5.

of computational costs, the three-dimensional computations of the boundary layer are performed on a restricted domain located close to the shoulder in the transonic to supersonic region of the capsule, as represented in Fig. 1 (right). At the location of the roughness, the boundary layer is transonic, with an edge Mach number of about 0.9. Here, the local Reynolds number is large enough for the roughness wake to exhibit modal instabilities for roughness heights as small as one-fifth of the boundary-layer thickness. Computations are performed on a Cartesian coordinate system. However, results are presented in the following with reference to a curvilinear coordinate system with x as the wall-parallel streamwise coordinate, y as the wall-normal coordinate, and z as the spanwise coordinate. The origin of the coordinate system $(x, y, z) = (0, 0, 0)$ is located on the stagnation point of the hemisphere. In the spherical part of the domain, excluding the shoulder, the coordinates x, y, and z are given by

$$x = R\theta_1, \quad y = \tilde{r} - R, \quad z = R\theta_2 \sin \theta_1 \qquad (3)$$

where R is the radius of the hemisphere, $\tilde{r}$ is the distance from the center of the hemisphere, θ_1 is the elevation angle with reference to the stagnation point, and θ_2 is the azimuth angle measured clockwise on the rotation axis. The restricted domain is extracted for $x \in [3.682, 4.843]$ m and $\theta_2 \in [-2\pi/65, 2\pi/65]$ rad. The extension in the spanwise direction corresponds to the spanwise periodicity of the roughness patch, as described in Sec. II.C. The restricted domain has an extension in the wall-normal direction of 0.35 m, corresponding to about 12δ at the inflow and 10δ at the capsule shoulder.

The full domain (Fig. 1, left) is two-dimensional and axisymmetric. The grid consists of about 80,000 points clustered inside the boundary layer and at the shock location. Nonreflective characteristic boundary conditions are used for freestream and far-field boundaries. The temperature of the wall, modeled as noncatalytic and isothermal, is estimated from available flight data (see, e.g., Ref. [36]) and set to 1800 K. As the total simulated physical time is on the order of milliseconds, a change in wall temperature is neglected. In the axisymmetric computations, the shock is

represented with a shock-fitting method, accounting for the change of the shock standoff distance depending on the gas model.

A detailed representation of the restricted domain is given in Fig. 2. The Dirichlet conditions imposed at the inflow boundaries (faces 1 and 2) are derived from the simulations of the full domain. The restricted domain is periodic in the azimuthal (spanwise) direction (face 3), and the wall (face 4) is equipped with a patch of randomly distributed roughness. Riemann invariants are used at the outflow (face 5). The shock is not part of the restricted domain, and detailed computations of the boundary layer in the presence of unsteady disturbances can be performed with a low-dissipation central discretization scheme of fourth-order accuracy. The grid of the restricted domain in the presence of the roughness consists of about 100 million points, clustered inside the boundary layer, at the roughness location. Downstream of the roughness, the grid properties are carefully chosen to fully resolve the wavelength of the high-frequency disturbances considered in the present analysis as well as the vortical structures developing in the nonlinear range of disturbance growth until the point of laminar–turbulent breakdown. Further information about the computational grids used in this work (i.e., full domain, restricted domain with roughness, and restricted domain without roughness) are shown in Table 2. In particular, $(x_{\min}, x_{\max})$ and $(y_{\min}, y_{\max})$ are the coordinates defining the extension of the domain in streamwise and wall-normal directions, respectively. The angles $(\theta_{2,\min}, \theta_{2,\max})$ represent the angular extension of the domain in the spanwise direction; and N_x, N_y, and N_z are the number of points in x, y, and z directions.

The validation of the numerical procedure as well as a grid convergence study were documented in Ref. [35]. The procedure of simulation of the roughness wake on the present geometry as applied in this work, with a grid sequencing from a full two-dimensional domain to a finer three-dimensional restricted domain, is described in detail and was successfully validated in Ref. [24]. In particular, the Mach number rapidly increases in the streamwise direction and any disturbance induced by the roughness in the inviscid flow is very small and is highly deflected in the flow direction. The height of the domain has been chosen to guarantee that any potential residual

Table 2   Details of the computational grids

Domain	$(x_{\min}, x_{\max})$	$(y_{\min}, y_{\max})$	$(\theta_{2,\min}, \theta_{2,\max})$	N_x	N_y	N_z
Full	$(0.0, 4.843)$ m	$(0.0, 1.589)$ m	$(0, 0)$ rad	370	200	1
Restricted with roughness	$(3.682, 4.843)$ m	$(-0.004, 0.350)$ m	$(\frac{-2\pi}{65}, \frac{2\pi}{65})$ rad	1280	160	400
Restricted without roughness	$(3.394, 4.843)$ m	$(0.0, 0.350)$ m	$(\frac{-2\pi}{65}, \frac{2\pi}{65})$ rad	932	160	400
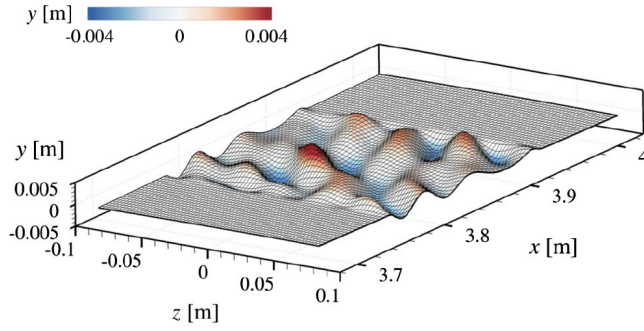
Fig. 3 Grid points at the wall in the vicinity of the roughness (every 6th point shown) from [35].

reflection at the upper boundary exits in the domain at the outflow boundary without impinging on the boundary layer, and therefore without affecting the stability properties of the roughness wake.

C. Roughness Geometry

The roughness patch (Fig. 3) is prescribed in the range from $x = 3.755$ m to $x = 3.925$ m and is represented with a body-fitting grid. The representation of a (pseudo)random distributed roughness is obtained by modulating the wall with a superposition of five sinusoidal functions with random amplitudes and phases. Following the definition of distributed roughness presented in the experiments of Downs et al. [37], the surface height with respect to the smooth configuration is given by

$$h(x, z) = k \cdot g(x) \sum_{q,r=1}^{5} A_{q,r} \cos\left(\frac{2\pi q}{\lambda_0} x + \frac{2\pi r}{\lambda_0} z + \phi_{q,r}\right) \quad (4)$$

where the values of $A_{q,r}$ and $\phi_{q,r}$ are random values listed in Tables 3 and 4, λ_0 is the fundamental roughness wavelength equal to the spanwise extension of the domain ($\lambda_0 = \pi R \sin \theta_1 / 65$), and $g(x)$ is a piecewise defined fifth-degree polynomial function that yields a continuous and smooth flattening of the roughness boundaries within a length of $\lambda_0/4$, ensuring continuity with the smooth wall at the front and back sides of the patch. The values of $A_{q,r}$ are normalized such that the maximum height of the roughness k is equal to 4.6 mm, which corresponds to the results obtained in Ref. [24] scaled with respect to the current hemispherical geometry. In the following, we refer to the maximum height of the roughness k as the roughness height. The size of the roughness is chosen to resemble a realistic sand-grain roughened wall, with the distance between a roughness peak and the successive cavity of the same order of magnitude of the roughness height. As observed in Refs. [35,37], it is expected that the instability mechanisms for the present roughness geometry are determined by the properties of the highest peak of the roughness patch. The

Table 3 Amplitude coefficients used in Eq. (4)

$A_{q,r}$	$A_{q,1}$	$A_{q,2}$	$A_{q,3}$	$A_{q,4}$	$A_{q,5}$
$A_{1,r}$	0.008	0.079	0.008	0.139	0.113
$A_{2,r}$	0.119	0.103	0.092	0.076	0
$A_{3,r}$	0.077	0.14	0.116	0.14	0
$A_{4,r}$	0.102	0.065	0.101	0	0
$A_{5,r}$	0.031	0	0	0	0

Table 4 Amplitude phases used in Eq. (4)

$\phi_{q,r}$	$\phi_{q,1}$	$\phi_{q,2}$	$\phi_{q,3}$	$\phi_{q,4}$	$\phi_{q,5}$
$\phi_{1,r}$	5.328	5.212	4.393	1.753	1.637
$\phi_{2,r}$	4.931	5.166	5.003	4.244	——
$\phi_{3,r}$	1.702	3.586	2.775	5.678	——
$\phi_{4,r}$	1.431	3.593	2.804	——	——
$\phi_{5,r}$	2.017	——	——	——	——

roughness is designed to generate a wake with unstable shear layers where modal growth of small disturbances can be observed within the boundary layer. The potential onset of secondary instabilities occurs downstream of the patch in the wake of the roughness.

D. Simulations of Unsteady Disturbances in the Roughness Wake

The wake of the roughness is characterized by the presence of longitudinal vortices. These longitudinal vortices are potentially unstable, and rapid growth of various unstable modes can be observed in the presence of incoming disturbances within a certain range of frequencies.

The unsteady simulations are conducted for the roughness wake only. A new inflow boundary is defined at $x_0^* = 3.935$ m for the restricted domain (face 1* in Fig. 2). At this face, unsteady disturbances are forced, exciting the instability modes in the roughness wake. As shown in Ref. [24], for values of Re_{kk} as low as the ones of the present simulations ($Re_{kk} = 221$–244, depending on the gas model), the emerging instabilities are of a convective nature and the direct interaction of incoming disturbances with the rough wall is small and does not affect the laminar–turbulent transition in the roughness wake. Instead, in the highly accelerated boundary layer, the only relevant instability mechanisms are limited to the region downstream of the roughness patch and laminar–turbulent transition occurs as a result of the interaction of the incoming disturbances with the steady wake of the roughness and not with the roughness itself.

Due to the absence of unstable modes in the unperturbed smooth-wall part of the domain upstream of the roughness patch, the disturbance profiles could not be provided by analyses of the two-dimensional flow based on the linear stability theory. Therefore, in the DNS, only the pressure is perturbed at the inflow boundary, whereas velocity and temperature disturbances are induced by the pressure fluctuations within the first few cells downstream of the inflow boundary. The method of perturbing the inflow pressure in order to trigger modal growth in the roughness wake has already been used on the present geometry and validated against different numerical methods (i.e., LST and PSE) in Ref. [24].

The inflow disturbance consists of five spatial spanwise modes and six frequencies, and it is superposed to the pressure already prescribed at the boundary for the steady flow: $p_{st}(x_0^*, y, z)$. The unsteady inflow pressure $p(x_0^*, y, z, t)$ is given by

$$p(x_0^*, y, z, t) = p_{st}(x_0^*, y, z) + c(y)\left(\sum_{i=1}^{5} \alpha_i \cos\left(\frac{2\pi i}{\lambda_0} z + \phi_i\right)\right)$$

$$\cdot \left(\sum_{j=1}^{6} \cos(2\pi f_j t + \phi_j)\right) \quad (5)$$

where the function $c(y) = e^{-(y/\delta)^3}$ is applied to damp the perturbation outside the boundary layer, and the phases ϕ_i and ϕ_j are randomly chosen from $[0, 2\pi]$ to avoid excessive peak values due to constructive interference of the cosine functions. The amplitudes α_i are also randomly extracted from a normal distribution and are normalized to keep the amplitude of the global disturbance at the inflow lower than a chosen value $P_0 = \sum |\alpha_i|$.

A range of relevant frequencies for the present configuration has been identified based on preliminary DNS-based stability analyses [35]. The forced frequencies are the first six harmonics of the base frequency 8.33 kHz, i.e., $f_n = n \cdot 8.33$ kHz, with $n = 1, 2, \ldots, 6$. Different modes of instabilities are present in the roughness wake for the frequencies in the range 8.3–50 kHz. The disturbance amplitude at the inflow is set equal to $P_0 = 1 \cdot 10^{-3} \cdot p_{st}(x_0^*, y < \delta, z)$, corresponding to a level of disturbance of 0.1% with reference to the values of the flow variables at the boundary-layer edge. This inflow value of the disturbance amplitude is small enough to observe linear growth in the near field downstream of the roughness and guarantees that the modal instability mechanisms relevant for this configuration are not bypassed. As shown in Sec. III.B, the unsteady disturbances enter into the nonlinear range for all gas cases before the

corresponding growth rate becomes negative in the damped region of the roughness wake.

To allow the transient effects to vanish, simulations are performed over a long time interval, corresponding to about 50 periods of the forced disturbance with the lowest frequency. The convergence of the spectrum has been verified in the simulation domain in the regions of linear and nonlinear growth, including the region of laminar–turbulent breakdown ($x \approx 4.25$ m). Because the main focus of the present investigation is the nonlinear growth of instabilities and the onset of laminar breakdown to turbulence, the pseudoturbulent flow for $x > 4.4$ m is not analyzed quantitatively here and has to be considered as not fully resolved.

E. Flow Solver and Numerical Schemes

Parallel Direct Numerical Simulations are performed with the Navier–Stokes Multi Block (NSMB) solver, which is a finite-volume code with a wide variety of numerical schemes [38,39]. Computations are parallelized using a Message Passing Interface environment. Applications and validations of the NSMB in the field of hypersonic flows can be found, among others, in Refs. [11,16,24,40–42]. Starting from freestream conditions, steady solutions for the full domain are reached with a second-order central discretization scheme and an implicit time integration based on a symmetric successive overrelaxation method with two Gauss–Seidel iterations. In the restricted domain, a fourth-order central scheme is used for spatial discretization and a five-stage Runge–Kutta time-integration method is used both in the steady simulations of the base flow in the presence of the rough wall and in the unsteady simulations of the roughness wake.

III. Results

A detailed analysis of the base flow for this configuration was given in Ref. [35]. Therefore, only a brief description of the steady flow in the roughness wake is presented in Sec. III.A. A comparison with the steady base flow on a similar geometry under cold wind-tunnel conditions is also included. The focus of the present work is on the evolution of small disturbances in the roughness wake in the linear and nonlinear ranges up to laminar–turbulent breakdown for the three gas models. Analysis and quantification of the disturbance growth in the roughness wake for the three different gas models are presented in Sec. III.B. The analysis of the wall heat flux and an evaluation of the transition location are presented in Sec. III.C.

A. Description of the Steady Flow in the Roughness Wake

The roughness wake is characterized by several longitudinal vortices induced by the distributed roughness. At the largest roughness peak, centered on $(x, z) = (3.826, -0.016)$ m, the flow is deflected such that a spanwise velocity is locally induced by the skewed shape of the roughness. As a result, a crossflow-type vortex develops downstream of the roughness. This crossflow-type vortex shows velocity distributions and stability properties similar to the ones of crossflow vortices as known from three-dimensional boundary-layer flows (see, e.g., Ref. [43]). Contrary to the case of

crossflow vortices in three-dimensional boundary layers, where a spanwise velocity is present in the base flow, the flow in the considered smooth-wall configuration is two-dimensional and the spanwise velocity typical of crossflow vortices is directly induced by the roughness itself. The evolution of this vortex is shown in Fig. 4 for CEQ only because similar results are obtained for the other gas models. The crossflow-type vortex rotates in the clockwise direction for an observer looking downstream and brings hot fluid from the boundary-layer edge toward the cold wall in the descending (right) side of the vortex. This crossflow-type vortex is very persistent in the accelerated boundary layer of this blunt-body configuration. Other vortical structures of a different nature (e.g., counter-rotating vortices, as known from symmetric isolated roughness elements, as well as single-vortex cores) are present in the roughness wake as a result of the different shapes and heights of the several protuberances of the roughness patch. The main roughness-induced crossflow-type vortex presents the largest vorticity in the far field ($x > 4.1$ m) and, accordingly, turns out to be the most unstable region in the roughness wake. Hence, the following analysis will be limited to the unsteady downstream development of the crossflow-type vortex only.

The inclusion of nonequilibrium significantly affects the boundary layer, especially in terms of thickness, temperature profiles, and chemical composition. As a result, different values of the roughness parameters are found for the different gas models. We define the boundary-layer thickness δ as the distance from the wall where 99% of the total enthalpy is reached. For all gas models, the roughness height is significantly smaller than the boundary-layer thickness. In particular, the ratio roughness height to boundary-layer thickness, computed with reference to the smooth-wall geometry at the roughness position, is the smallest for the case of CEQ ($k/\delta = 0.183$), followed by the cases of CNEQ ($k/\delta = 0.198$) and CTNEQ ($k/\delta = 0.227$), due to the variation of the boundary-layer thickness with the different gas models. The largest roughness Reynolds number Re_{kk} is present in the case of CNEQ with $Re_{kk} = 244$, followed by CEQ ($Re_{kk} = 226$), and finally by CTNEQ ($Re_{kk} = 221$). All roughness Reynolds numbers are lower than the effective Re_{kk} for immediate bypass transition to turbulence.

The base flow in the roughness wake presented in this work is qualitatively very similar to the one presented by Di Giovanni and Stemmer [24] for the case of cold wind-tunnel (HLB) conditions at $M = 5.9$, $Re_{\infty} = 18 \cdot 10^6$ m^{-1}, and $T_{\infty} = 59$ k. However, in the case of simulations at HLB conditions, for values of the ratio roughness height to boundary-layer thickness close to the ones considered here (i.e., $k/\delta = 0.175$), a roughness Reynolds number of $Re_{kk} = 134$ was found. For these values, the roughness wake at wind-tunnel conditions was attenuated too fast to sustain the presence of a crossflow-type vortex in the roughness wake, and no disturbance growth at all was observed downstream of the roughness patch. Instead, a roughness Reynolds number of 261 corresponded to a k/δ of 0.26, and the roughness-induced crossflow-type vortex in the roughness wake became unstable. This comparison suggests that, in the case of high-enthalpy reacting boundary layers at reentry conditions, roughnesses with similar values of k/δ present slightly larger Re_{kk} than in the case of wind-tunnel conditions at HLB,
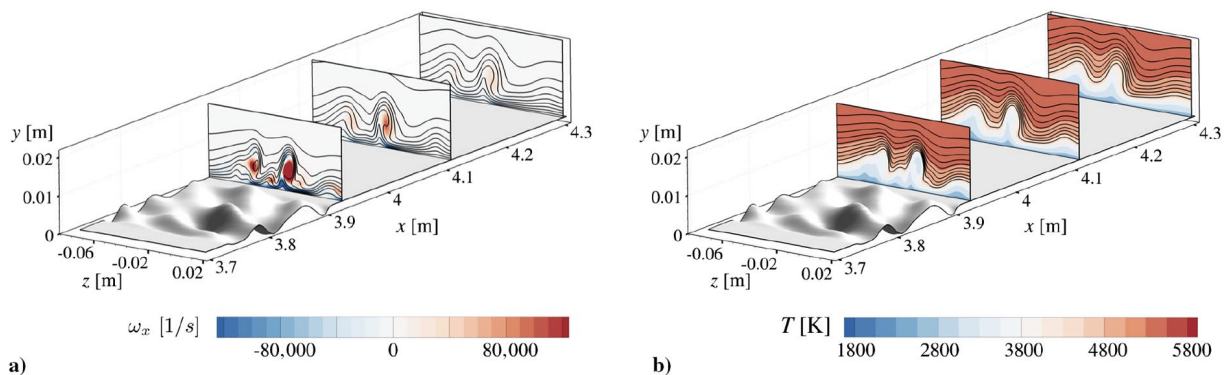

Fig. 4 Development in the base flow of a) streamwise vorticity and b) temperature in the roughness wake for equilibrium air.

Table 5 N-factors from DNS analysis of linear disturbances

	N factor					
	8.3 kHz	16.7 kHz	25.0 kHz	33.3 kHz	41.7 kHz	50.0 kHz
CEQ	2.0	4.2	3.8	4.3	4.0	3.0
CNEQ	2.2	4.6	4.3	5.3	5.1	4.0
CTNEQ	2.1	4.0	3.9	4.6	4.4	3.3

leading to more persistent and stronger roughness wakes, which can potentially sustain a larger disturbance amplification. This characteristic is more pronounced for CEQ and CNEQ than for CTNEQ. Note that the values of k/δ as well as of Re_{kk} depend on the boundary-layer properties and on the height of the roughness only. Hence, these observations can be generalized to different types of roughness geometries of the same size as the one considered here.

## B. Nonlinear Growth and Breakdown Scenario

In preliminary studies, unsteady simulations have been performed for very small inflow disturbances (with amplitudes less than 0.001%), where the amplitude of the disturbances remains in the linear range throughout the entire domain (see also Ref. [35]). It was found that all the considered frequencies in the range of 8.3–50 kHz are amplified in the roughness wake. For the investigated range of frequencies, Table 5 shows the N-factors for the three gas models, computed as $N = \ell n(A_{\max}/A_{\mathrm{in}})$, where $A_{\max}$ is the maximum amplitude reached by the disturbance along x and A_{in} is the amplitude of the disturbance at the inflow. In the present work, the level of the inflow disturbance is kept at about 0.1%. Based on the values of the N-factors, the amplitude of the inflow disturbance is such that the unsteady disturbances enter into the nonlinear range for all gas cases while also guaranteeing that linear growth still dominates the region

in the immediate vicinity of the inflow boundary downstream of the roughness patch.

The evolution of the disturbances is analyzed and quantified by means of a temporal Fourier analysis. The generic variable q is decomposed into a frequency spectrum $\hat{q}_f(x, y, z)$, and the amplitude of the temporal Fourier mode is defined at each streamwise position as the maximum of the absolute value of $\hat{q}_f$ found in the y–z plane:

$$|\hat{q}_f|_{\max}(x) = \max_{y,z}|\hat{q}_f(x, y, z)| \qquad (6)$$

The amplitudes of the temporal Fourier modes computed with reference to the streamwise velocity are shown in Fig. 5 for the three gas models. Values are normalized with the normalization velocity $U = 1800$ m/s, which corresponds to the boundary-layer edge velocity at the roughness position with reference to the smooth configuration. Disturbances with frequencies f_1 to f_6 (forced or disturbed frequencies) are linearly amplified downstream of the inflow boundary. Higher harmonics (i.e., modes with multiple frequencies of the forced ones) are present in the domain as a result of the weak nonlinear interaction between the disturbed modes. At the beginning of the simulation domain ($x < 4.05$ m), the higher modes present an amplitude several orders of magnitude smaller than the amplitudes of the disturbed modes, and their growth is nonlinearly
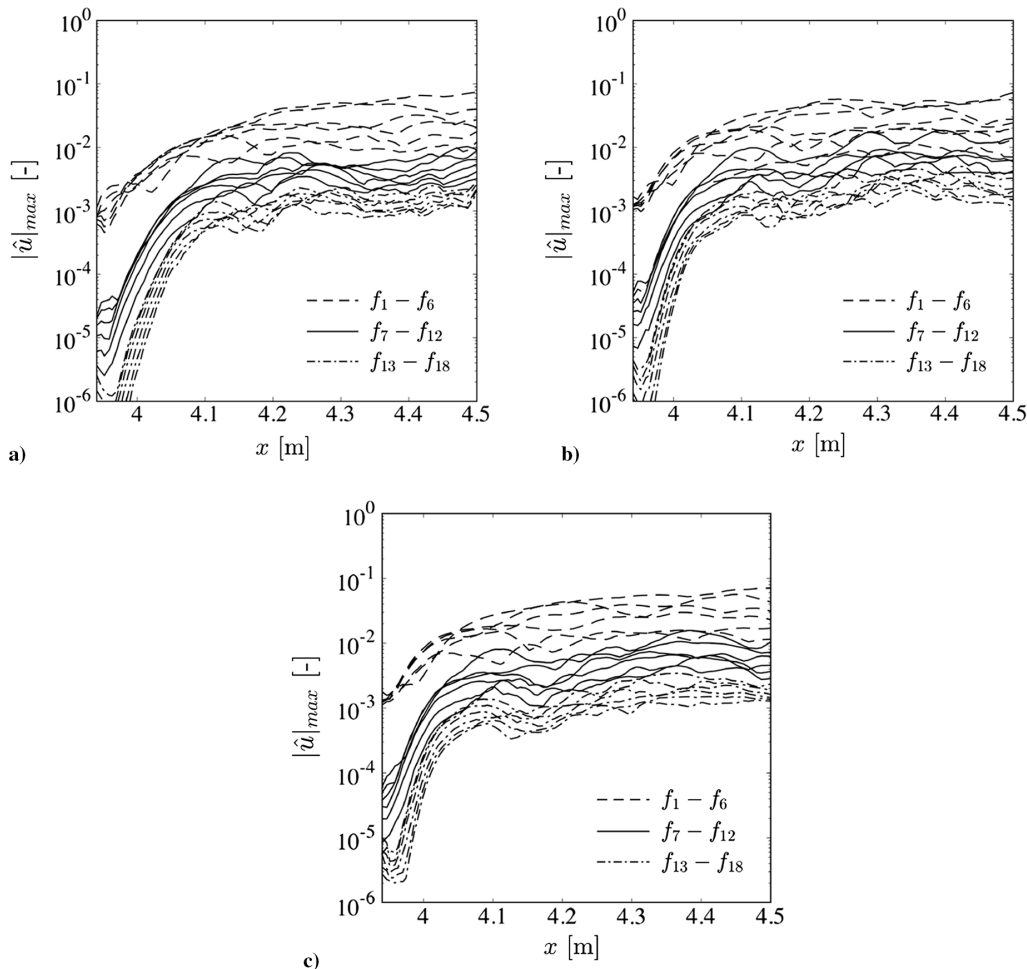
Fig. 5   Temporal Fourier modes for a) equilibrium air, b) chemical nonequilibrium, and c) thermochemical nonequilibrium.
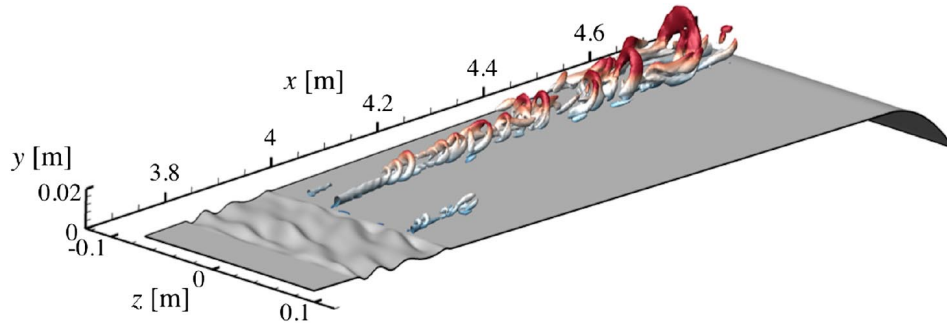
Fig. 6   Isosurfaces of $Q = 1 \cdot 10^9$ colored by the distance from the wall.

driven by the growth of the disturbed modes. The amplitudes of the disturbed modes exceed 1% between $x = 4.05$ m and $x = 4.10$ m, depending on the gas model. Both disturbed modes and higher modes tend to saturate after the onset of the nonlinear region between 4.07 and 4.11 m (cf. Sec. III.C), and significant nonlinear interaction between the different modes takes place. In the region of saturation, the amplitude of the total disturbance, obtained as a sum of the amplitudes of the different modes, becomes larger than 14%. Even though the disturbed modes are dominant throughout the entire domain, the amplitudes of both disturbed and higher modes are within one order of magnitude. In particular, in the region of saturation, the modes with frequencies in the range of $f_7 – f_{12}$ reach values up to 1%, which are well above the nonlinear level of direct generation through the disturbed modes (onset of the higher modes).

After the onset of the higher modes, the vortical structures (represented in Fig. 6 with the help of the Q-criterion) start to lose
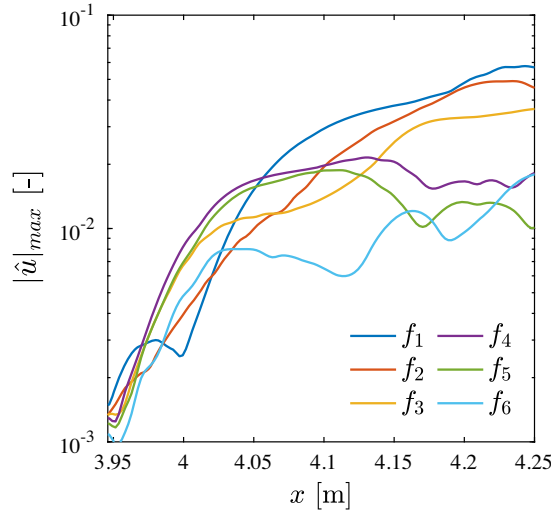
coherence and laminar–turbulent breakdown takes place for $x > 4.2$ m. Note that the main focus of the present investigation is the nonlinear growth of instabilities up to the laminar–turbulent breakdown. The (pseudo)turbulent flow is not fully resolved, and is hence not analyzed in a quantitative manner.

A more detailed and enlarged representation of the disturbed modes downstream of the roughness up to the growth saturation is presented in Fig. 7 for the case of CNEQ. The most amplified modes in the near field of the roughness wake have frequencies of $f_4 = 33.3$ kHz and $f_5 = 41.7$ kHz (cf. Table 5). The unstable modes grow linearly up to $x = 4.025$ m. Growth saturation is first reached by the modes in the high-frequency range (i.e., $f_4 - f_6$). Modes with lower frequencies (i.e., f_1 and f_3) exhibit a smaller growth rate. However, their amplitudes reach and exceed the ones of f_4 and f_5 between $x = 4.05$ m and $x = 4.10$ m. This overshoot of the low-frequency modes is driven by different factors: among others, a thickening of the roughness wake as it diffuses downstream and a strong nonlinear interaction of the disturbed modes. For $x < 4.0$ m, the local maximum of the first mode f_1, as described in Eq. (6), is found for $z = 0.04$ m. For $x > 4.0$ m, the maximum of f_1 jumps in spanwise direction to the crossflow-type vortex at $z = -0.035$ m, delivering the kink in the amplitude development.

In the far field, the instability of all modes analyzed here is primarily related to the main crossflow-type vortex generated by the largest roughness protuberance at $z = -0.016$ m. After the onset of the higher modes, the low-frequency modes ($f_1–f_3$) reach a disturbance level of about 4% and their amplitude is almost twice as large as the amplitude of the high-frequency modes ($f_4–f_6$). After growth saturation is reached, the irregular fluctuations observed in the evolution of the modes is due to the strong nonlinear interaction between the different modes.

For f_2 and f_4, Fig. 8 shows a $y–z$ section of the roughness wake at $x = 4.05$ m with the Fourier modes of the velocity. Gray contours are used to represent the modes, which are normalized to the local maximum value in each subfigure, blanking out values smaller than 0.4. For comparative purposes, we also represent with red isolines the mode shape obtained in the case of very small inflow disturbances, where the mode amplitudes remain linear in the entire domain [35].
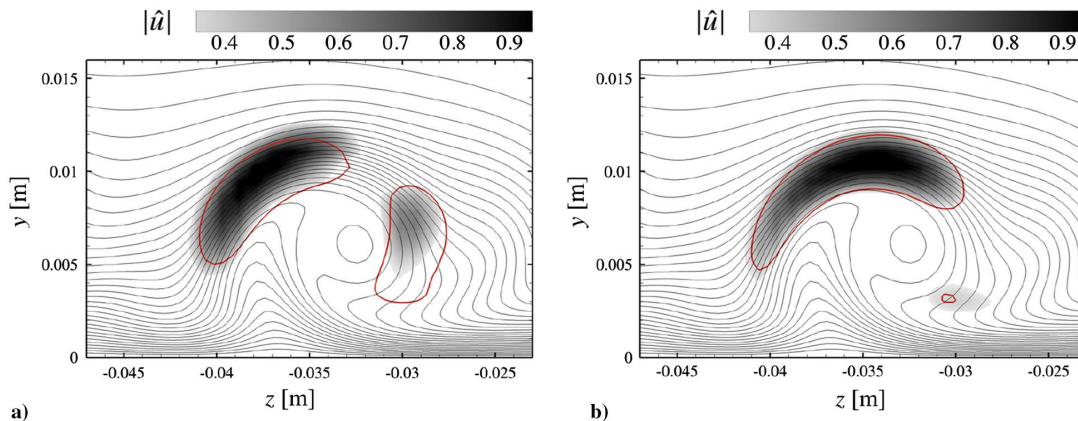

Fig. 7   Temporal Fourier modes for chemical nonequilibrium air (detailed enlargement of Fig. 5).

Fig. 8   Velocity modes from temporal Fourier analysis at a) f_2 and b) f_4 with background velocity isolines at $x = 4.05$ m.
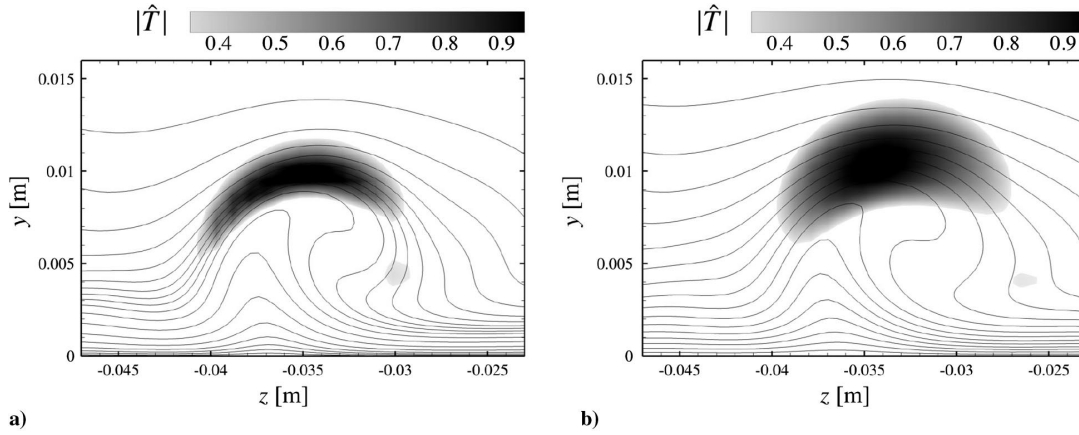
Fig. 9   Temperature modes at f_4 for a) equilibrium air and b) chemical nonequilibrium with background temperature isolines at $x = 4.05$ m.

The red isoline corresponds to a value of 0.4. The background isolines represent the streamwise velocity of the base flow every 50 m/s. The modes are shown in the case of CEQ only because the shapes of the velocity modes are very similar for the three gas models. In the case of the frequency of $f_2 = 16.7$ kHz, the velocity mode consists of two bean-shaped regions extending on the descending (right) and ascending (left) sides of the crossflow-type vortex. In the case of 33.3 kHz, the mode mainly consists of one elongated region on the top of the vortex extending toward the wall on the ascending side. The almost full overlapping of the gray contours with the red isolines indicates that the modes computed in the present simulations still resemble the linear eigenmodes. Therefore, the growth of the instability modes is still mostly linear at the considered location and the interaction between different modes at different frequencies is weak. In fact, as shown in Fig. 5a, the corresponding mode amplitudes at $x = 4.05$ m are still about 1%.

The two different mode shapes for f_2 and f_4 correspond to two different types of instability associated to the crossflow-type vortex, featuring the z and y modes already known from crossflow vortices in three-dimensional subsonic boundary layers (see, e.g., the works of Malik et al. [44], Wasserman and Kloker [45], and White and Saric [46]). The modes in the low-frequency range (f_1–f_3) are of the z type and are correlated to the spanwise gradients of the streamwise velocity of the steady base flow $\partial u/\partial z$, which is largest on the descending and ascending sides of the vortex. The modes in the high-frequency range (f_4–f_6) are of the y type and are correlated to the wall-normal gradients of the streamwise velocity $\partial u/\partial y$, which is maximum on the top of the vortex. Note that the dominant frequency of the y mode (33.3 kHz) is twice the dominant frequency of the z mode (16.7 kHz), showing a similar trend also observed in other investigations on crossflow instabilities (see the works of White and Saric [46] and Chou et al. [47]).

A comparison of the temperature modes for CEQ and CNEQ is shown in Fig. 9 at $x = 4.05$ m for the case of the frequency with the largest linear amplification: $f_4 = 33.3$ kHz. Black temperature isolines of the steady base flow are shown every $\Delta T = 200$ K. The case of gas in thermochemical nonequilibrium is very similar to the case of gas in chemical nonequilibrium and is not shown here. The temperature mode consists of one main single region on the top of the crossflow-type vortex. In the case of CEQ, the temperature mode presents a slender shape similar to the velocity mode in Fig. 8b. In the case of CNEQ, the temperature mode has a much thicker shape as compared to the case of equilibrium air. However, the maximum of the mode amplitude is found for both gas models at the same distance from the wall at $y = 0.011$ m on the top of the vortex. Therefore, no significant influence on the temperature gradient at the wall is expected from the growth of the disturbance in the linear range for any of the gas models. Once the unstable modes reach the nonlinear range and the disturbance amplitude is large enough to also significantly change the profiles of the base flow in the region close to the wall, a noticeable impact on the wall temperature gradients, and hence on the wall heat flux, is expected. An analysis of the wall heat

flux in both the linear and nonlinear ranges of the disturbance growth is given in Sec. III.C. The modes of the species concentration (not shown here) are correlated to the temperature fluctuations, and their shape differs only slightly from the shape of the temperature modes because of the nonlinear dependence between temperature and species concentrations in the gas mixture.

The evolution of the instability mode for f_4 at different x positions in the roughness wake is shown in Fig. 10. Values are normalized with the largest value found at each x location. At the inflow boundary, the temporal Fourier analysis reveals the pseudorandom shape of the inflow disturbance. For $x > 3.99$ m, the unstable mode emerges from the background disturbances, and its shape becomes more defined as the disturbance moves downstream. For $x > 4.03$ m, the region of instability widens as the interaction with other modes becomes significant. Finally, the mode loses its coherence ($x > 4.15$ m) and the laminar–turbulent breakdown follows.

Figure 11 shows instantaneous isosurfaces of the Q-criterion for the crossflow-type vortex in a close-up between $x = 3.94$ m and $x = 4.13$ m. Close to the roughness patch, finger-like structures originate and wrap around the main vortex core. As evidenced by a comparison with Fig. 10, the finger-like structures are related to the modal amplification of the incoming disturbances. These vortical structures grow in size with increasing values of x and, for $x > 4.05$ m, evolve in ring vortices, leading eventually to laminar–turbulent breakdown.

Qualitatively, the process of laminar–turbulent transition under high-enthalpy reentry conditions analyzed in the present work is very similar to the case of cold wind-tunnel conditions on a rescaled geometry at $M = 5.9$ and $Re_\infty = 18 \cdot 10^6$ m^{-1} analyzed by Di Giovanni and Stemmer [24]. In particular, the presence of chemical dissociation affects the temperature modes while leaving the shape of the velocity modes almost unaltered.
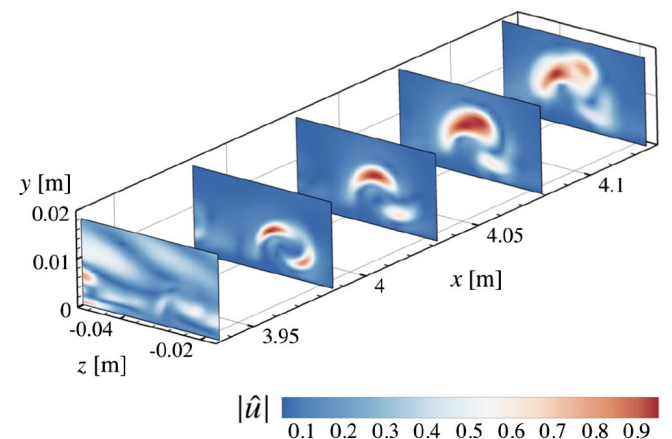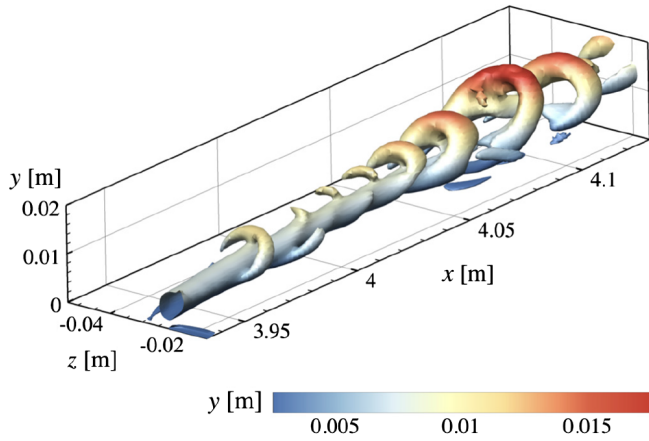

Fig. 10   Evolution of the velocity mode at f_4 for CNEQ in the roughness wake.

Fig. 11 Enlargement of isosurfaces of $Q = 1.2 \cdot 10^9$ colored by the distance from the wall.

C. Wall Heat Flux and Transition Onset Location

Finally, we analyze the effects of the roughness and of the growth of unsteady disturbances on the heat transfer at the wall. Figure 12 shows the heat flux at the wall for the gas in thermochemical nonequilibrium in the case of steady flow (Fig. 12a) and in the case of unsteady flow with transition (Fig. 12b). Long streaks of increased heating are found in the wake of the roughness. The largest wall heat transfer is found at about $z \approx -0.02$ m, in correspondence to the descending side of the main crossflow-type vortex. Here, due to the vortical motion of the flow, hot fluid is transported from the boundary-layer edge toward the cold wall. The increased heating gradually declines further downstream because the amplitude of the unsteady disturbances is still small and the wake of the roughness weakens in the accelerated boundary layer. For $x > 4.2$ m, a sudden increase of the wall heat flux can be observed at $z \approx -0.04$ m as a result of the breakdown of the vortical structures induced by the instability. A second, less pronounced streak of heating augmentation can be observed at $z \approx -0.06$ m due to the growth of instabilities in a different vortex of the roughness wake on the left side of the main crossflow-type vortex (see Fig. 4).

The small spanwise drift toward negative z values of the streaks of increased heat flux in Fig. 12 indicates that the main crossflow-type

vortex slowly moves in the spanwise direction for increasing values of x. This drift is related to the clockwise rotation of the vortex and is induced by the image vortex on the opposite side of the wall, as described by potential theory.

To quantify and compare the increase in wall heat flux for the different gas models, Fig. 13 shows the maximum value in the spanwise direction of the time-averaged wall heat flux:

$$\dot{Q}_{\max}(x) = \max_{z}(\overline{\dot{q}}(x, 0, z)) \tag{7}$$

The wall heat fluxes in the case of steady simulations as well as for the smooth-wall configuration are also shown. Several consecutive peaks of increased wall heat flux are found at the roughness patch between $x = 3.8$ m and $x = 3.9$ m. For the first few centimeters downstream of the roughness patch, the values of the wall heat flux in the unsteady case are equal to the values of the wall heat flux in the steady case. A first deviation of the unsteady-case heat flux from the steady-case values becomes evident for $x > 4.05$ m, corresponding to the onset of the higher modes (cf. Fig. 5). The kink in the heating pattern observed in the case of chemical equilibrium at $x > 4.5$ m corresponds to a jump in the spanwise direction of the local maximum of the wall heat flux due to the presence of a second turbulent streak occurring at $z = -0.06$ m.

The deviation of the heat-flux profiles in the unsteady simulations from the smooth-wall laminar case is caused by both a significant contribution of the steady distortion of the flow due to the presence of the rough wall and a further increase due to the growth of the unsteady disturbances. In particular, the heat-flux profiles of the unsteady simulations build upon the heat-flux profiles of the steady simulations, which in turn are greatly affected by the roughness geometry. Therefore, the values of the wall heat flux reached during the transition process strongly depend on the roughness properties and cannot be generalized for other roughness geometries. In this regard, the importance of DNS for a comprehensive description of the roughness-induced transition is further stressed by the possibility of representing intermediate steps of the analysis, such as the steady laminar flow in the presence of the roughness, which is usually not achievable in experiments.

The wall heat flux in the steady base flow in the case of equilibrium air is almost three times larger than in the cases of steady flow in nonequilibrium, mainly because of the energy-releasing full
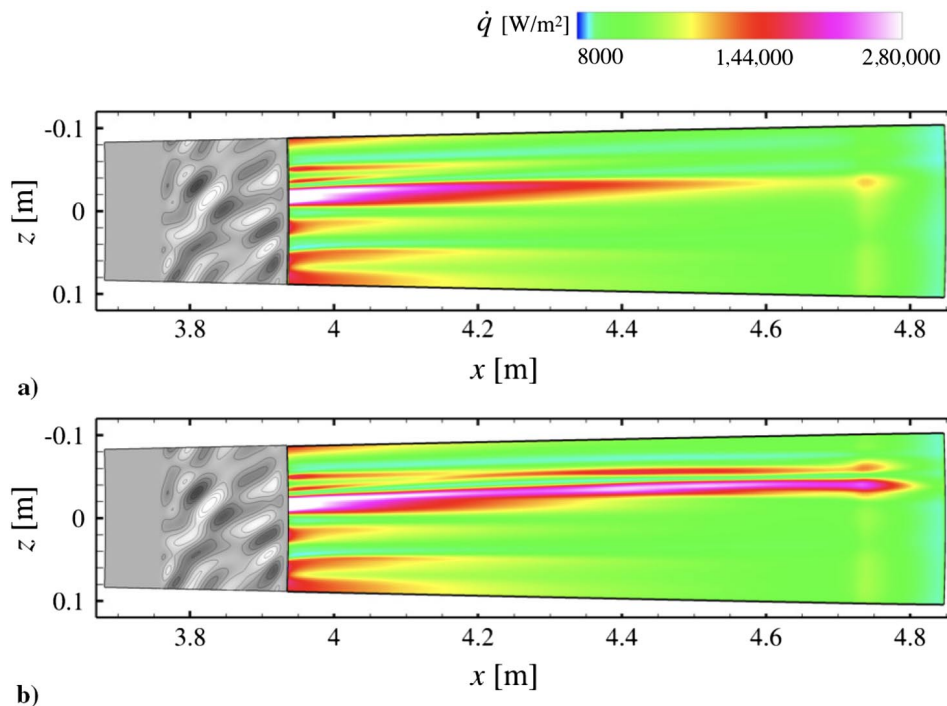
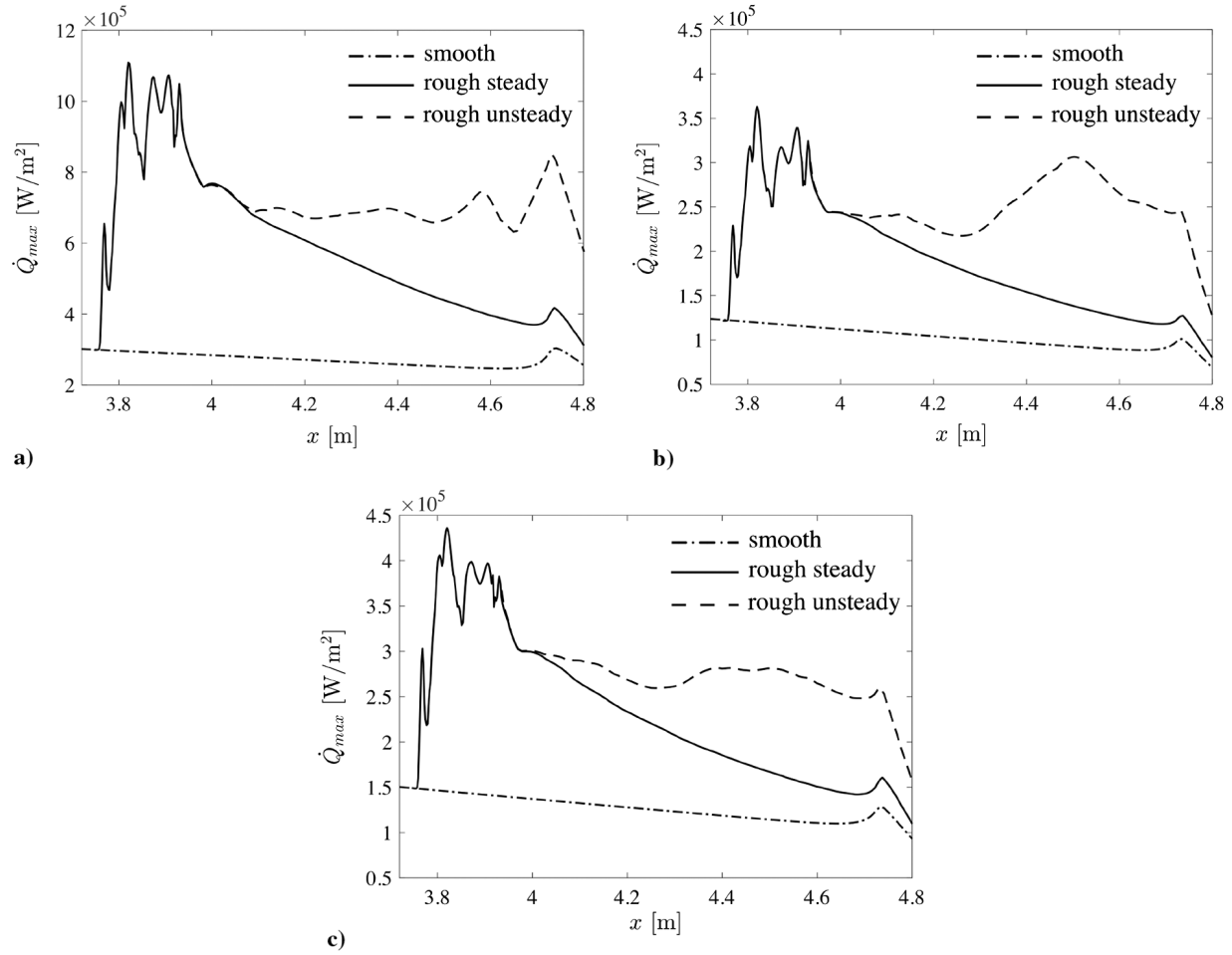**Fig. 12 Wall heat flux in the case of a) steady and b) unsteady flows.**

Fig. 13   Mean wall heat flux for a) equilibrium air, b) chemical nonequilibrium, and c) thermochemical nonequilibrium.

recombination of both oxygen and nitrogen at the isothermal wall ($T_w = 1800$ K) in the case of equilibrium. The case of equilibrium air is not appropriate for an accurate description of the wall heating in the present reentry scenario and should be regarded as reference only. The values of the wall heat flux for CEQ in the steady laminar case are even larger than the peak values reached in CNEQ and CTNEQ in the unsteady transitional flow. Furthermore, the wall heat flux in the steady case is slightly larger in CTNEQ than in CNEQ by about 20%. As observed in previous works (see, e.g., Ref. [42]), the difference between the vibrational and translational energies of the molecular species in the near-wall region for thermal nonequilibrium leads to a slight increase of the temperature gradients at the wall as compared to the pure chemical nonequilibrium case. However, at transition, the wall heat flux in the case of CNEQ undergoes a significantly higher increase than in the case of CTNEQ. Due to transition, the wall heat flux for CNEQ increases by a factor up to 2.2, reaching a peak value of $3.1 \cdot 10^5$ W/m²; whereas the wall heat flux for CTNEQ increases by a factor up to 1.6, with a peak value of $2.8 \cdot 10^5$ W/m². Hence, the gas in thermochemical nonequilibrium, which is the most complex gas model among the ones considered in the current analysis, exhibits the lowest peak values of wall heat flux in the region of laminar–turbulent transition.

To identify the location where transition occurs, different definitions can be used. In the case of high-enthalpy boundary layers, it is sometimes assumed that a sudden increase of the wall heat flux takes place at the transition location. However, setting a threshold for the rise in the wall heat flux is not unambiguous, and different definitions of the transition point can lead to different locations. With regard to the present geometry, the definition in absolute terms of a rise in the wall heat flux is difficult because the wall heat flux in the steady solution rapidly falls in the streamwise direction due both to a rapid cooling of the boundary layer and to the damping of the roughness-induced vortices. Because the steady laminar solutions on the rough wall are available through steady DNS, we can estimate the

increase of the wall heat flux relative to the steady laminar solution. We define the total augmentation of the wall heat flux at each position t due to the presence of unsteady disturbances as the difference between the mean heat flux in the unsteady flow $\bar{\dot{q}}_{un}$ and the heat flux in the steady flow $\dot{q}_{st}$, which is integrated in the spanwise extent of the domain $z \in [-\lambda_0/2, \lambda_0/2]$:

$$\Delta \dot{Q}(x) = \int_{-\lambda_0/2}^{\lambda_0/2} \bar{\dot{q}}_{un}(x, 0, z) - \dot{q}_{st}(x, 0, z) \, \mathrm{d}z \tag{8}$$

The argument of the integral in Eq. (8) tends to zero in the case of damped unsteady disturbances; therefore, only the regions of disturbance amplification are included in the definition.

The values of $\Delta \dot{Q}(x)$, normalized with the wall heat flux of the steady flow integrated in spanwise direction $\dot{Q}_{st}(x)$, are shown in Fig. 14 for the three gas models. Three main regions can be identified between the laminar and the fully turbulent flows. The first region extends from the inflow boundary until about $x = 4.07$ m, and it is characterized by a constant value of $\Delta \dot{Q}$ almost equal to zero. As already noticed in Sec. III.B, in this interval, the instability modes are found distant from the wall; and their amplitude is still too small to have a significant impact on the wall temperature gradients. Further downstream, the unsteady disturbances reach nonlinear amplitudes, leading to a nonnegligible contribution to the heat-flux augmentation (onset of the nonlinear region). In the present analysis, this point of increased wall heat flux $\tilde{x}_1$ is identified by the streamwise coordinate where the growth rate of the wall heat-flux augmentation relative to the local heat flux for the steady case becomes larger than 1%:

$$\tilde{x}_1 := \frac{1}{\dot{Q}_{st}(x)} \cdot \frac{\mathrm{d}}{\mathrm{d}x} \Delta \dot{Q}(x) = 0.01 \tag{9}$$
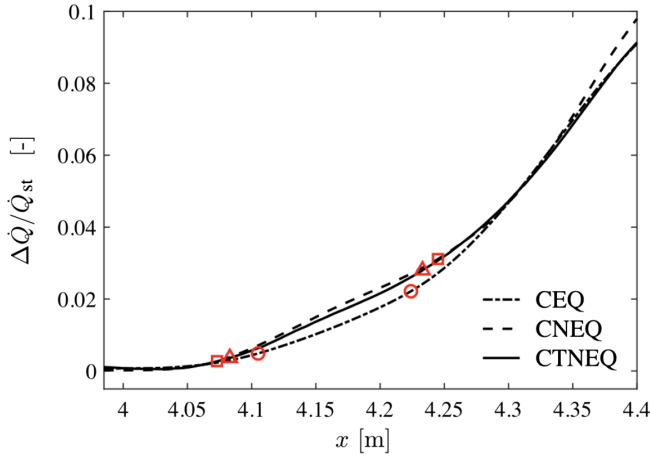
Fig. 14   Wall heat-flux augmentation in the unsteady boundary layer.

The growth rate of the heat-flux augmentation remains nearly constant until about $x = 4.25$ m, where a second abrupt increase of the slope of the curve can be observed, corresponding to the laminar–turbulent breakdown. Analogous to Eq. (9), the transition point $\tilde{x}_2$ is here defined as the point where the growth rate of the wall heat-flux augmentation relative to the local heat flux for the steady case becomes larger than 2%:

$$\tilde{x}_2 := \frac{1}{\dot{Q}_{st}(x)} \cdot \frac{d}{dx} \Delta \dot{Q}(x) = 0.02 \qquad (10)$$

The points $\tilde{x}_1$ and $\tilde{x}_2$ are marked in Fig. 14 with red symbols (circle for CEQ, square for CNEQ, and triangle for CTNEQ) and are listed in Table 6. At the position $\tilde{x}_1$, the amplitude of the total velocity disturbance, obtained as a sum of the amplitude of the different Fourier modes (cf. Fig. 5), is 8.0% for CEQ, 8.5% for CNEQ, and 8.5% for CTNEQ. These values are consistent with the assumption that $\tilde{x}_1$, defined through the growth rates of the heat-flux augmentation, correlates with the beginning of a region of strong nonlinear growth for the unsteady disturbances. By comparing the values of $\tilde{x}_1$ for the different gas models, we observe that a nonnegligible contribution of the unsteady disturbances to the wall heat flux is first reached by the gas in chemical nonequilibrium ($\tilde{x}_1 = 4.073$ m), followed by the gas in thermochemical non-equilibrium ($\tilde{x}_1 = 4.083$ m), and finally by the gas in chemical equilibrium ($\tilde{x}_1 = 4.105$ m). In particular, the distance between $\tilde{x}_1$ and the inflow boundary x_0^* in the case of chemical equilibrium is 15% larger than in the case of thermochemical nonequilibrium and 23% larger than in the case of chemical nonequilibrium. This result is not surprising because the case of gas in chemical nonequilibrium presents the largest roughness Reynolds number and, accordingly, was found to be the most linearly unstable. However, the onset of laminar–turbulent breakdown, as defined in the present work, is first reached by the gas in chemical equilibrium ($\tilde{x}_2 = 4.224$ m), followed by the gas in thermochemical nonequilibrium ($\tilde{x}_2 = 4.233$ m), and finally by the gas in chemical nonequilibrium ($\tilde{x}_2 = 4.245$ m). The distance $\tilde{x}_2 - x_0^*$ in the case of equilibrium air is 7.5% larger than in the case of gas in chemical nonequilibrium, suggesting a small, albeit nonnegligible, delay of the transition due to the influence of chemical nonequilibrium. At the position $\tilde{x}_2$, the amplitude of the total disturbance has reached values in the range of 14–16% for all gas models and remains almost constant until the shoulder of the capsule. The further development of the wall heat-flux

augmentation for larger values of x can be easily deduced by the curves of the steady and unsteady flows in Fig. 13. The maximum distance between the curves, and thus the maximum heat-flux augmentation, is reached at about $x = 4.5$ m. Eventually, as the turbulent vortical structures are rapidly damped due to the strong acceleration of the flow at the capsule shoulder, the curves of the steady and unsteady flows gradually converge for $x > 4.7$ m.

IV.   Conclusions

In this work, we investigated the influence of high-temperature gas effects on the laminar–turbulent transition on a capsule-like geometry with roughness. As expected, the heat flux at the wall in the transitional boundary layer was significantly larger than in the laminar case. At high-altitude reentry conditions, where high-temperature gas effects are dominant, the inclusion of both chemical and thermal nonequilibrium turns out to be of great importance in order to determine both location and peak values of the heat augmentation induced by the laminar–turbulent breakdown. These results have been obtained by numerically investigating the instability mechanisms in the wake of a patch of randomly distributed roughness in the reacting boundary layer of a capsule-like hemisphere at $M = 20$. Parallel Direct Numerical Simulations of the boundary layer have been performed on a restricted domain located close to the shoulder of the capsule in the transonic to supersonic region. Here, the local Reynolds number is large enough for the roughness wake to exhibit modal instabilities for roughness heights as small as one-fifth of the boundary-layer thickness. The development of unsteady disturbances forced in the roughness wake has been analyzed and quantified in both the linear and nonlinear ranges, including laminar–turbulent breakdown. Due to the high temperature of the flow in this reentry configuration ($T > 5000$ K), the air cannot be considered as calorically and thermally perfect any more. Different gas models have been used to highlight the effects of the high temperature on the instability mechanisms in the roughness wake. Starting with the model of reacting gas in equilibrium, we gradually included chemical nonequilibrium and, finally, thermal nonequilibrium.

The inclusion of nonequilibrium significantly affects the boundary-layer profiles. Hence, different values of the roughness variables are found for the different gas models. In particular, the largest roughness Reynolds number is presented by the case of gas in chemical nonequilibrium ($Re_{kk} = 244$), followed by the gas in chemical equilibrium ($Re_{kk} = 226$), and finally by the gas in thermochemical nonequilibrium ($Re_{kk} = 221$). Due to the skewed profile in the spanwise direction of the largest roughness protuberance, a crossflow-type vortex originates downstream of the roughness. This crossflow-type vortex exhibits unstable shear layers. All roughness Reynolds numbers are lower than effective Re_{kk} for immediate transition to turbulence. Modal growth of linear disturbances can be observed in the crossflow-type vortex in the wake of the roughness. The comparison between previous simulations conducted at wind-tunnel conditions with $M = 5.9$ and the current simulations conducted at atmospheric reentry conditions with $M = 20$ revealed that roughness-induced transition is qualitatively similar in both scenarios. Nevertheless, roughness elements with the same values of the ratio roughness height to boundary-layer thickness exhibit larger values of Re_{kk} in the case of reentry conditions than in the case of cold wind-tunnel conditions, leading to more persistent, and thus potentially more unstable, roughness wakes.

Six different disturbance modes with six different frequencies in the range of 8.3–50.0 kHz have been perturbed simultaneously in the roughness wake. The amplitude of the forced disturbances is such that linear growth is expected close to the inflow boundary of the unsteady simulations downstream of the roughness, whereas large nonlinear disturbances are found further downstream. In the region of growth saturation, a significant nonlinear interaction between the different modes takes place.

The shapes of the velocity modes are similar for both the equilibrium and nonequilibrium cases and, at the analyzed frequencies, feature the shape of y and z modes already known

Table 6   Location of onset of the nonlinear region and transition point

Onset location	CEQ	CNEQ	CTNEQ
$\tilde{x}_1$, m	4.105	4.073	4.083
$\tilde{x}_2$, m	4.224	4.245	4.233

from crossflow instabilities in three-dimensional subsonic boundary layers. The temperature modes, for which the shape is strongly correlated to the modes of the chemical species, are found on the top of the crossflow-type vortex; and their impact on the wall temperature gradient is negligible throughout the linear range of modal growth. Instead, a first nonnegligible contribution to the temperature gradient, and hence to the heat flux, is observed after the onset of the region of nonlinear growth of the perturbed modes. Finger-like vortical structures originate in the nonlinear range of the mode development and wrap around the main vortex core. These vortical structures grow in size as they move downstream and evolve to ring vortices, eventually leading to laminar–turbulent breakdown.

The instability and transition mechanisms in the roughness wake are qualitatively similar for all gas models considered here. However, the choice of the gas model has a nonnegligible impact both on the values of the wall heat flux and on the transition location. The wall heat flux in the case of steady flow in chemical equilibrium is almost three times larger than the wall heat flux observed in the cases of nonequilibrium in the steady flow, and it is even larger than the peak values reached in the nonequilibrium cases in the unsteady transitional flow. Equilibrium air is not an appropriate gas model for the chosen flight conditions and grossly overestimates the wall heating rates. Furthermore, at transition, the wall heat flux in the case of chemical nonequilibrium undergoes a significantly larger augmentation than in the case of thermochemical nonequilibrium. The gas in thermochemical nonequilibrium, which represents the most appropriate gas model for the chosen flight conditions, exhibits the lowest values of the wall heat flux in the region of the laminar–turbulent transition, with a peak value of $2.8 \cdot 10^5$ W/m^2 as compared to a peak value of $3.1 \cdot 10^5$ W/m^2 reached by the gas in chemical nonequilibrium and about $8 \cdot 10^5$ W/m^2 reached by the gas in equilibrium.

The onset of the nonlinear region, originating in the nonlinear interaction of the disturbed modes, is identified by a first significant increase of the heat flux at the wall in the unsteady flow as compared to the steady laminar flow. This point is first reached by the gas in chemical nonequilibrium, which produced the largest roughness Reynolds number. Analogously, the transition onset location has been identified by a second noticeable augmentation of the wall heat flux, where the growth rate of the wall heat-flux augmentation suddenly changes by a factor of two. The point of laminar–turbulent breakdown is first reached by the gas in chemical equilibrium, followed by the gas in thermochemical nonequilibrium, and finally by the gas in chemical nonequilibrium.

For the first time, the nonlinear instability mechanisms up to laminar–turbulent breakdown in a roughness-induced crossflow-type vortex have been numerically studied in the case of a high-enthalpy capsule boundary layer including nonequilibrium effects. This work suggests that, for the extrapolation of results from cold wind-tunnel conditions to atmospheric reentry conditions at large Mach numbers, nonequilibrium high-temperature effects must be taken into account because they could lead to an increased instability of the roughness wake given the similarity of certain roughness parameters, such as the ratio of the roughness height to boundary-layer thickness. The inclusion of nonequilibrium effects has a nonnegligible influence on the development of instabilities in both the linear and nonlinear ranges, slightly affecting the absolute location of laminar–turbulent transition. Even though transition is first reached by the gas in thermochemical nonequilibrium, and then by the gas in chemical nonequilibrium, the presence of thermal nonequilibrium seems to lower the level of wall heat flux of the transitional flow. In this regard, both chemical and thermal nonequilibrium turn out to be important in order to correctly predict the location and value of the peak of heat augmentation induced by the laminar–turbulent breakdown.

Acknowledgments

References

[1] Schneider, S. P., "Summary of Hypersonic Boundary-Layer Transition Experiments on Blunt Bodies with Roughness," *Journal of Spacecraft and Rockets*, Vol. 45, No. 6, 2008, pp. 1090–1105.
doi:10.2514/1.37431

[2] Malik, M. R., and Anderson, E. C., "Real Gas Effects on Hypersonic Boundary Layer Stability," *Physics of Fluids*, Vol. 3, No. 5, 1991, pp. 803–821.
doi:10.1063/1.858012

[3] Johnson, H. B., Seipp, T. G., and Candler, G. V., "Numerical Study of Hypersonic Reacting Boundary Layer Transition on Cones," *Physics of Fluids*, Vol. 10, No. 10, 1998, pp. 2676–2685.
doi:10.1063/1.869781

[4] Germain, P. D., and Hornung, H. G., "Transition on a Slender Cone in Hypervelocity Flow," *Experiments in Fluids*, Vol. 22, No. 3, 1997, pp. 183–190.
doi:10.1007/s003480050036

[5] Stuckert, G., and Reed, H. L., "Linear Disturbances in Hypersonic, Chemically Reacting Shock Layers," *AIAA Journal*, Vol. 32, No. 7, 1994, pp. 1384–1393.
doi:10.2514/3.12206

[6] Hudson, M. L., Chokani, N., and Candler, G., "Linear Stability of Hypersonic Flow in Thermochemical Nonequilibrium," AIAA Paper 1996-0671, 1996.
doi:10.2514/2.204

[7] Hudson, M. L., "Linear Stability of Hypersonic Flow in Thermal and Chemical Nonequilibrium," Ph.D. Thesis, North Carolina State Univ., Raleigh, NC, 1996.

[8] Chang, C.-L., Vinh, H., and Malik, M., "Hypersonic Boundary-Layer Stability with Chemical Reactions Using PSE," AIAA Paper 1997-2012, 1997.
doi:10.2514/6.1997-2012

[9] Johnson, H. B., and Candler, G. V., "PSE Analysis of Reacting Hypersonic Boundary Layer Transition," AIAA Paper 1999-3793, 1999.
doi:10.2514/6.1999-3793

[10] Stemmer, C., Birrer, M., and Adams, N. A., "Hypersonic Boundary-Layer Flow with an Obstacle in Thermochemical Equilibrium and Nonequilibrium," *Journal of Spacecraft and Rockets*, Vol. 54, No. 4, 2017, pp. 899–915.
doi:10.2514/1.A32984

[11] Stemmer, C., Birrer, M., and Adams, N. A., "Disturbance Development in an Obstacle Wake in a Reacting Hypersonic Boundary Layer," *Journal of Spacecraft and Rockets*, Vol. 54, No. 4, 2017, pp. 945–960.
doi:10.2514/1.A33708

[12] De Tullio, N., Paredes, P., Sandham, N., and Theofilis, V., "Laminar Turbulent Transition Induced by a Discrete Roughness Element in a Supersonic Boundary Layer," *Journal of Fluid Mechanics*, Vol. 735, Nov. 2013, pp. 613–646.
doi:10.1017/jfm.2013.520

[13] Marxen, O., Iaccarino, G., and Magin, T. E., "Direct Numerical Simulations of Hypersonic Boundary-Layer Transition with Finite-Rate Chemistry," *Journal of Fluid Mechanics*, Vol. 755, Sept. 2014, pp. 35–49.
doi:10.1017/jfm.2014.344

[14] Morkovin, M., "Bypass Transition to Turbulence and Research Desiderata," *Transition in Turbines*, NASA CP-2386, 1984, pp. 161–199.

[15] Theiss, A., Ali, S. R., Hein, S., Heitmann, D., and Radespiel, R., "Numerical and Experimental Investigation of Laminar-Turbulent Boundary Layer Transition on a Blunt Generic Re-Entry Capsule," AIAA Paper 2014-2353, 2014.
doi:10.2514/6.2014-2353

[16] Hein, S., Theiss, A., Di Giovanni, A., Stemmer, C., Schilden, T., Schröder, W., Paredes, P., Choudhari, M. M., Li, F., and Reshotko, E., "Numerical Investigation of Roughness Effects on Transition on Spherical Capsules," *Journal of Spacecraft and Rockets*, Vol. 56, No. 2, March 2019, pp. 388–404.
doi:10.2514/1.A34247

[17] Hollis, B. R., "Distributed Roughness Effects on Blunt-Body Transition and Turbulent Heating," AIAA Paper 2014-0238, 2014.
doi:10.2514/6.2014-0238

[18] Hollis, B. R., "Experimental Investigation of Roughness Effects on Transition Onset and Turbulent Heating Augmentation on a Hemisphere at Mach 6 and Mach 10," NASA TM-2017-219613, 2017.

[19] Reda, D. C., "Review and Synthesis of Roughness-Dominated Transition Correlations for Reentry Applications," *Journal of

Spacecraft and Rockets, Vol. 39, No. 2, 2002, pp. 161–167.
doi:10.2514/2.3803

[20] Reda, D. C., Wilder, M. C., Bogdanoff, D. W., and Prabhu, D. K., "Transition Experiments on Blunt Bodies with Distributed Roughness in Hypersonic Free Flight," *Journal of Spacecraft and Rockets*, Vol. 45, No. 2, 2008, pp. 210–215.
doi:10.2514/1.30288

[21] Theiss, A., Hein, S., Ali, S. R. C., and Radespiel, R., "Wake Flow Instability Studies Behind Discrete Roughness Elements on a Generic Re-Entry Capsule," AIAA Paper 2016-4382, 2016.
doi:10.2514/6.2016-4382

[22] Theiss, A., Leyh, S., and Hein, S., "Pressure Gradient Effects on Wake Flow Instabilities Behind Isolated Roughness Elements on Re-Entry Capsules," *7th European Conference for Aeronautics and Aerospace Sciences (EUCASS)*, Paper FP-594, 2017.
doi:10.13009/EUCASS2017-594

[23] Radespiel, R., Ali, S. R. C., Muñoz, F., Bowersox, R., Leidy, A., Tanno, H., Kirk, L. C., and Reshotko, E., "Experimental Investigation of Roughness Effects on Transition on Blunt Spherical Capsule Shapes," *Journal of Spacecraft and Rockets*, Vol. 56, No. 2, March 2019, pp. 405–420.
doi:10.2514/1.A34295

[24] Di Giovanni, A., and Stemmer, C., "Crossflow-Type Breakdown Induced by Distributed Roughness in the Boundary Layer of a Hypersonic Capsule Configuration," *Journal of Fluid Mechanics*, Vol. 856, Dec. 2018, pp. 470–503.
doi:10.1017/jfm.2018.706

[25] Chang, C.-L., Choudhari, M., Venkatachari, B. S., and Li, F., "Effects of Cavities and Protuberances on Transition over Hypersonic Vehicles," AIAA Paper 2011-3245, 2011.
doi:10.2514/6.2011-3245

[26] Marineau, E. C., Laurence, S. J., and Hornung, H. G., "Apollo-Shaped Capsule Boundary Layer Transition at High-Enthalpy in T5," AIAA Paper 2010-0446, 2010.
doi:10.2514/6.2010-446

[27] Tanno, H., Kodera, M., Komuro, T., Sato, K., Takahashi, M., and Itoh, K., "Aeroheating Measurements on a Reentry Capsule Model in Free-Piston Shock Tunnel HIEST," AIAA Paper 2010-1181, 2010.
doi:10.2514/6.2010-1181

[28] Tanno, H., Sato, K., Komuro, T., and Itoh, K., "Free-Flight Aerodynamic Test of Reentry Vehicles in High-Temperature Real-Gas Flow," AIAA Paper 2014-3109, 2014.
doi:10.2514/6.2014-3109

[29] Park, C., "A Review of Reaction Rates in High Temperature Air," AIAA Paper 1989-1740, 1989.
doi:10.2514/6.1989-1740

[30] Landau, L., and Teller, E., "On the Theory of Sound Dispersion," *Physikalische Zeitschrift der Sowjetunion*, Vol. 10, 1936, Paper 34.

[31] Millikan, R., and White, D., "Systematics of Vibrational Relaxation," *Journal of Chemical Physics*, Vol. 39, No. 12, 1963, pp. 3209–3213.
doi:10.1063/1.1734182

[32] Blottner, F. G., Johnson, M., and Ellis, M., "Chemically Reacting Viscous Flow Program for Multi-Component Gas Mixtures," Sandia National Labs. TR SC-RR-70-754, Albuquerque, NM, 1971.

[33] Hirschfelder, J. O., Curtiss, C. F., and Bird, R. A., *Molecular Theory of Gases and Liquids*, Wiley, New York, 1964.

[34] Wilke, C., "A Viscosity Equation for Gas Mixtures," *Journal of Chemical Physics*, Vol. 18, No. 4, 1950, pp. 517–519.
doi:10.1063/1.1747673

[35] Di Giovanni, A., and Stemmer, C., "Roughness-Induced Crossflow-Type Instabilities in a Hypersonic Capsule Boundary Layer Including Nonequilibrium," *Journal of Spacecraft and Rockets*, March 2019.
doi:10.2514/1.A34404

[36] Park, C., "Stagnation-Point Radiation for Apollo 4," *Journal of Thermophysics and Heat Transfer*, Vol. 18, No. 3, 2004, pp. 349–357.
doi:10.2514/1.6527

[37] Downs, R. S., White, E. B., and Denissen, N. A., "Transient Growth and Transition Induced by Random Distributed Roughness," *AIAA Journal*, Vol. 46, No. 2, 2008, pp. 451–462.
doi:10.2514/1.31696

[38] Vos, J., Duquesne, N., and Lee, H., "Shock Wave Boundary Layer Interaction Studies Using the NSMB Flow Solver," *Proceedings of the 3rd European Symposium on Aerothermodynamics for Space and Vehicles*, edited by R. A. Harris, Vol. 426, European Space Agency (ESA) Paper ESA SP-426, Paris, 1999, pp. 229–236.

[39] Hoarau, Y., Pena, D., Vos, J. B., Charbonier, D., Gehri, A., Braza, M., Deloze, T., and Laurendeau, E., "Recent Developments of the Navier Stokes Multi Block (NSMB) CFD Solver," AIAA Paper 2016-2056, 2016.
doi:10.2514/6.2016-2056

[40] Goebel, F., Vos, J., and Mundt, C., "CFD Simulation of the FIRE II Flight Experiment," AIAA Paper 2012-3350, 2012.
doi:10.2514/6.2012-3350

[41] Stemmer, C., and Fehn, J., "High-Temperature Gas Effects at a Capsule Under Re-Entry and Wind-Tunnel Conditions," AIAA Paper 2014-2645, 2014.
doi:10.2514/6.2014-2645

[42] Di Giovanni, A., and Stemmer, C., "Numerical Simulations of the High-Enthalpy Boundary Layer on a Generic Capsule Geometry with Roughness," *New Results in Numerical and Experimental Fluid Mechanics XI, STAB/DGLR Symposium*, Springer International Publishing, 2017, pp. 189–198.

[43] Malik, M. R., Li, F., and Chang, C.-L., "Crossflow Disturbances in Three-Dimensional Boundary Layers: Nonlinear Development, Wave Interaction and Secondary Instability," *Journal of Fluid Mechanics*, Vol. 268, June 1994, pp. 1–36.
doi:10.1017/S0022112094001242

[44] Malik, M. R., Li, F., Choudhari, M. M., and Chang, C.-L., "Secondary Instability of Crossflow Vortices and Swept-Wing Boundary-Layer Transition," *Journal of Fluid Mechanics*, Vol. 399, Nov. 1999, pp. 85–115.
doi:10.1017/S0022112099006291

[45] Wassermann, P., and Kloker, M., "Transition Mechanisms Induced by Travelling Crossflow Vortices in a Three-Dimensional Boundary Layer," *Journal of Fluid Mechanics*, Vol. 483, May 2003, pp. 67–89.
doi:10.1017/S0022112003003884

[46] White, E. B., and Saric, W. S., "Secondary Instability of Crossflow Vortices," *Journal of Fluid Mechanics*, Vol. 525, Feb. 2005, pp. 275–308.
doi:10.1017/S002211200400268X

[47] Chou, A., King, A., and Kegerise, M. A., "Transition Induced by Tandem Rectangular Roughness Elements on a Supersonic Flat Plate," AIAA Paper 2018-3531, 2018.
doi:10.2514/6.2018-3531

M. Borg
Associate Editor

B.4 Numerical Investigation of Roughness Effects on Transition on Spherical Capsules

License Number	4612420692185
License date	Jun 19, 2019
Licensed content publisher	American Inst of Aeronautics and Astronautics (AIAA)
Licensed content title	Journal of spacecraft and rockets
Licensed content date	Jan 1, 1964
Type of Use	Thesis/Dissertation
Requestor type	Academic institution
Format	Print, Electronic
Portion	chapter/article
Number of pages in chapter/article	17
The requesting person/organization is:	Antonio Di Giovanni (co-author)
Title or numeric reference of the portion(s)	Numerical Investigation of Roughness Effects on Transition on Spherical Capsules. Vol. 56, No. 2, pp. 388-404, March-April 2019 (full article)
Title of the article or chapter the portion is from	Numerical Investigation of Roughness Effects on Transition on Spherical Capsules
Editor of portion(s)	R. M. Cummings
Author of portion(s)	Hein, S., Theiss, A., Di Giovanni, A., Stemmer, C., Schilden, T., Schröder, W., Paredes, P., Choudhari, M. M., Li, F., and Reshotko, E.
Volume of serial or monograph.	56
Page range of the portion	388-404
Publication date of portion	March-April 2019
Rights for	Main product
Duration of use	Life of current and all future editions
Creation of copies for the disabled	yes
With minor editing privileges	no
For distribution to	Worldwide

122

3.1 All Works and all rights therein, including copyright rights, remain the sole and exclusive property of the Rightsholder. The license created by the exchange of an Order Confirmation (and/or any invoice) and payment by User of the full amount set forth on that document includes only those rights expressly set forth in the Order Confirmation and in these terms and conditions, and conveys no other rights in the Work(s) to User. All rights not expressly granted are hereby reserved.

3.2 General Payment Terms: You may pay by credit card or through an account with us payable at the end of the month. If you and we agree that you may establish a standing account with CCC, then the following terms apply: Remit Payment to: Copyright Clearance Center, 29118 Network Place, Chicago, IL 60673-1291. Payments Due: Invoices are payable upon their delivery to you (or upon our notice to you that they are available to you for downloading). After 30 days, outstanding amounts will be subject to a service charge of 1-1/2% per month or, if less, the maximum rate allowed by applicable law. Unless otherwise specifically set forth in the Order Confirmation or in a separate written agreement signed by CCC, invoices are due and payable on "net 30" terms. While User may exercise the rights licensed immediately upon issuance of the Order Confirmation, the license is automatically revoked and is null and void, as if it had never been issued, if complete payment for the license is not received on a timely basis either from User directly or through a payment agent, such as a credit card company.

3.3 Unless otherwise provided in the Order Confirmation, any grant of rights to User (i) is "one-time" (including the editions and product family specified in the license), (ii) is non-exclusive and non-transferable and (iii) is subject to any and all limitations and restrictions (such as, but not limited to, limitations on duration of use or circulation) included in the Order Confirmation or invoice and/or in these terms and conditions. Upon completion of the licensed use, User shall either secure a new permission for further use of the Work(s) or immediately cease any new use of the Work(s) and shall render inaccessible (such as by deleting or by removing or severing links or other locators) any further copies of the Work (except for copies printed on paper in accordance with this license and still in User's stock at the end of such period).

3.4 In the event that the material for which a republication license is sought includes third party materials (such as photographs, illustrations, graphs, inserts and similar materials) which are identified in such material as having been used by permission, User is responsible for identifying, and seeking separate licenses (under this Service or otherwise) for, any of such third party materials; without a separate license, such third party materials may not be used.

3.5 Use of proper copyright notice for a Work is required as a condition of any license granted under the Service. Unless otherwise provided in the Order Confirmation, a proper copyright notice will read substantially as follows: "Republished with permission of [Rightsholder's name], from [Work's title, author, volume, edition number and year of copyright]; permission conveyed through Copyright Clearance Center, Inc. " Such notice must be provided in a reasonably legible font size and must be placed either immediately adjacent to the Work as used (for example, as part of a by-line or footnote but not as a separate electronic link) or in the place where substantially all other credits or notices for the new work containing the republished Work are located. Failure to include the required notice results in loss to the Rightsholder and CCC, and the User shall be liable to pay liquidated damages for each such failure equal to twice the use fee specified in the Order Confirmation, in addition to the use fee itself and any other fees and charges specified.

3.6 User may only make alterations to the Work if and as expressly set forth in the Order Confirmation. No Work may be used in any way that is defamatory, violates the rights of third parties (including such third parties' rights of copyright, privacy, publicity, or other tangible or intangible property), or is otherwise illegal, sexually explicit or obscene. In addition, User may not conjoin a Work with any other material that may result in damage to the reputation of the Rightsholder. User agrees to inform CCC if it becomes aware of any

123

infringement of any rights in a Work and to cooperate with any reasonable request of CCC or the Rightsholder in connection therewith.

4. Indemnity. User hereby indemnifies and agrees to defend the Rightsholder and CCC, and their respective employees and directors, against all claims, liability, damages, costs and expenses, including legal fees and expenses, arising out of any use of a Work beyond the scope of the rights granted herein, or any use of a Work which has been altered in any unauthorized way by User, including claims of defamation or infringement of rights of copyright, publicity, privacy or other tangible or intangible property.

5. Limitation of Liability. UNDER NO CIRCUMSTANCES WILL CCC OR THE RIGHTSHOLDER BE LIABLE FOR ANY DIRECT, INDIRECT, CONSEQUENTIAL OR INCIDENTAL DAMAGES (INCLUDING WITHOUT LIMITATION DAMAGES FOR LOSS OF BUSINESS PROFITS OR INFORMATION, OR FOR BUSINESS INTERRUPTION) ARISING OUT OF THE USE OR INABILITY TO USE A WORK, EVEN IF ONE OF THEM HAS BEEN ADVISED OF THE POSSIBILITY OF SUCH DAMAGES. In any event, the total liability of the Rightsholder and CCC (including their respective employees and directors) shall not exceed the total amount actually paid by User for this license. User assumes full liability for the actions and omissions of its principals, employees, agents, affiliates, successors and assigns.

6. Limited Warranties. THE WORK(S) AND RIGHT(S) ARE PROVIDED "AS IS". CCC HAS THE RIGHT TO GRANT TO USER THE RIGHTS GRANTED IN THE ORDER CONFIRMATION DOCUMENT. CCC AND THE RIGHTSHOLDER DISCLAIM ALL OTHER WARRANTIES RELATING TO THE WORK(S) AND RIGHT(S), EITHER EXPRESS OR IMPLIED, INCLUDING WITHOUT LIMITATION IMPLIED WARRANTIES OF MERCHANTABILITY OR FITNESS FOR A PARTICULAR PURPOSE. ADDITIONAL RIGHTS MAY BE REQUIRED TO USE ILLUSTRATIONS, GRAPHS, PHOTOGRAPHS, ABSTRACTS, INSERTS OR OTHER PORTIONS OF THE WORK (AS OPPOSED TO THE ENTIRE WORK) IN A MANNER CONTEMPLATED BY USER; USER UNDERSTANDS AND AGREES THAT NEITHER CCC NOR THE RIGHTSHOLDER MAY HAVE SUCH ADDITIONAL RIGHTS TO GRANT.

7. Effect of Breach. Any failure by User to pay any amount when due, or any use by User of a Work beyond the scope of the license set forth in the Order Confirmation and/or these terms and conditions, shall be a material breach of the license created by the Order Confirmation and these terms and conditions. Any breach not cured within 30 days of written notice thereof shall result in immediate termination of such license without further notice. Any unauthorized (but licensable) use of a Work that is terminated immediately upon notice thereof may be liquidated by payment of the Rightsholder's ordinary license price therefor; any unauthorized (and unlicensable) use that is not terminated immediately for any reason (including, for example, because materials containing the Work cannot reasonably be recalled) will be subject to all remedies available at law or in equity, but in no event to a payment of less than three times the Rightsholder's ordinary license price for the most closely analogous licensable use plus Rightsholder's and/or CCC's costs and expenses incurred in collecting such payment.

8. **Miscellaneous.**

8.1 User acknowledges that CCC may, from time to time, make changes or additions to the Service or to these terms and conditions, and CCC reserves the right to send notice to the User by electronic mail or otherwise for the purposes of notifying User of such changes or additions; provided that any such changes or additions shall not apply to permissions already secured and paid for.

8.2 Use of User-related information collected through the Service is governed by CCC's privacy policy, available online here:
http://www.copyright.com/content/cc3/en/tools/footer/privacypolicy.html.

8.3 The licensing transaction described in the Order Confirmation is personal to User. Therefore, User may not assign or transfer to any other person (whether a natural person or an organization of any kind) the license created by the Order Confirmation and these terms

and conditions or any rights granted hereunder; provided, however, that User may assign such license in its entirety on written notice to CCC in the event of a transfer of all or substantially all of User's rights in the new material which includes the Work(s) licensed under this Service.

8.4 No amendment or waiver of any terms is binding unless set forth in writing and signed by the parties. The Rightsholder and CCC hereby object to any terms contained in any writing prepared by the User or its principals, employees, agents or affiliates and purporting to govern or otherwise relate to the licensing transaction described in the Order Confirmation, which terms are in any way inconsistent with any terms set forth in the Order Confirmation and/or in these terms and conditions or CCC's standard operating procedures, whether such writing is prepared prior to, simultaneously with or subsequent to the Order Confirmation, and whether such writing appears on a copy of the Order Confirmation or in a separate instrument.

8.5 The licensing transaction described in the Order Confirmation document shall be governed by and construed under the law of the State of New York, USA, without regard to the principles thereof of conflicts of law. Any case, controversy, suit, action, or proceeding arising out of, in connection with, or related to such licensing transaction shall be brought, at CCC's sole discretion, in any federal or state court located in the County of New York, State of New York, USA, or in any federal or state court whose geographical jurisdiction covers the location of the Rightsholder set forth in the Order Confirmation. The parties expressly submit to the personal jurisdiction and venue of each such federal or state court.If you have any comments or questions about the Service or Copyright Clearance Center, please contact us at 978-750-8400 or send an e-mail to info@copyright.com.

v 1.1

Questions? customercare@copyright.com or +1-855-239-3415 (toll free in the US) or +1-978-646-2777.

Numerical Investigation of Roughness Effects on Transition on Spherical Capsules

Stefan Hein[*] and Alexander Theiss[*]
DLR, German Aerospace Center, 37073 Göttingen, Germany
Antonio Di Giovanni[†] and Christian Stemmer[‡]
Technical University of Munich, 85748 Garching, Germany
Thomas Schilden[§] and Wolfgang Schröder[¶]
RWTH Aachen University, 52062 Aachen, Germany
Pedro Paredes[**]
National Institute of Aerospace, Hampton, Virginia 23666
Meelan M. Choudhari[††] and Fei Li[‡‡]
NASA Langley Research Center, Hampton, Virginia 23681
and
Eli Reshotko[§§]
Case Western Reserve University, Cleveland, Ohio 44106

To address the hitherto unknown mechanism of boundary-layer transition on blunt reentry capsules, the role of roughness-induced disturbance growth on a spherical-section forebody is assessed via optimal transient growth theory and direct numerical simulations (DNS). Optimal transient-growth studies have been performed for the blunt capsule experiments at Mach 5.9 in the Hypersonic Ludwieg tube at the Technische Universität Braunschweig (HLB), which included measurements behind a patch of controlled, distributed micron-sized surface roughness. Transient-growth results for the HLB capsule indicate similar trends as the corresponding numerical data for a Mach 6 experiment in the Actively Controlled Expansion (ACE) facility of the Texas A&M University (TAMU) at a lower Reynolds number. Both configurations indicate a similar dependence on surface temperature ratio and, more important, rather low values of maximum energy gain. DNS are performed for the conditions of the HLB experiment to understand the generation of stationary disturbances by the roughness patch and the accompanying evolution of unsteady perturbations. However, no evidence of either modal or nonmodal disturbance growth in the wake of the roughness patch is found in the DNS data; thus, the physical mechanism underlying the observed onset of transition still remains unknown.

Nomenclature

$A_{m,n}(\xi)$	=	amplitude of the spatiotemporal mode
$\boldsymbol{A}, \boldsymbol{B}, \boldsymbol{C}, \boldsymbol{D}, \boldsymbol{L}$	=	parabolized stability equation matrix operators
c	=	damping function
c_T	=	power-law exponent
D	=	face diameter, m
d	=	Cartesian cell length, μm
E	=	energy norm based on total energy, J/m^2
f_i	=	disturbance frequency for unsteady computations, 1/s
G	=	energy gain
$G_{m,n}(\xi, \eta)$	=	azimuthal wavenumber-frequency spectra
$g(\xi, \zeta, \eta, t)$	=	generic flow variable
h_t	=	total enthalpy, J/kg
h_ξ, h_ζ	=	streamwise (nondimensional) and azimuthal (in m) metric factors, respectively
J	=	objective function
K	=	energy norm based on kinetic energy, J/m^2
k	=	peak-to-valley roughness height, μm or m
L	=	twice the edge length of a roughness element, μm
$\boldsymbol{M}$	=	energy weight matrix
M, N	=	number of time and space samples, respectively
Ma	=	Mach number
m_ζ	=	nondimensional azimuthal wavenumber
m, n	=	time and space indices in the spatiotemporal analysis, respectively
N_E, N_K	=	N-factor, that is, integrated logarithmic amplification factor, based on E and K, respectively
p	=	pressure, N/m^2
$\bar{\boldsymbol{q}}$	=	basic flow vector
$\tilde{\boldsymbol{q}}$	=	unsteady perturbation vector
$\hat{\boldsymbol{q}}$	=	vector of amplitude functions
R	=	face radius, m
R_a	=	surface mean roughness, μm

*Research Scientist, Institute of Aerodynamics and Flow Technology, Bunsenstr. 10.

†Ph.D. Candidate, Chair of Aerodynamics and Fluid Mechanics, Boltzmannstr. 15.

‡Privatdozent, Adjunct Teaching Professor, Chair of Aerodynamics and Fluid Mechanics, Boltzmannstr. 15.

§Research Scientist, Institute of Aerodynamics, Wüllnerstr. 5a.

¶Head, Institute of Aerodynamics, Wüllnerstr. 5a. Member AIAA.

**Research Engineer, Computational AeroSciences Branch; also NASA Langley Research Center. Senior Member AIAA.

††Research Scientist, Computational AeroSciences Branch. Associate Fellow AIAA.

‡‡Research Scientist, Computational AeroSciences Branch.

§§Kent H. Smith Professor Emeritus of Engineering. Fellow AIAA.

R_s	=	spherical-segment radius, m
Re_{δ^*}	=	Reynolds number based on displacement thickness and flow conditions at the boundary-layer edge, $\bar{\rho}_e \bar{u}_e \delta^* / \bar{\mu}_e$
Re_θ	=	Reynolds number based on boundary-layer momentum thickness, $\bar{\rho}_e \bar{u}_e \theta / \bar{\mu}_e$
Re_{kk}	=	roughness Reynolds number based on roughness height and flow conditions at this height, $\bar{\rho}_k \bar{u}_k k / \bar{\mu}_k$
Re_k	=	roughness Reynolds number with dynamic viscosity evaluated at wall temperature, $\bar{\rho}_k \bar{u}_k k / \bar{\mu}_w$
Re_R	=	freestream Reynolds number based on capsule-face radius
Re/l	=	freestream unit Reynolds number, 1/m
r_b	=	local radius, m
$s, \hat{s}$	=	streamwise coordinate with reference to the stagnation point, mm or m
T	=	temperature, K
t	=	time, s
$\hat{U}_m(\xi, \zeta, \eta)$	=	time Fourier transform of the streamwise velocity
(u, v, w)	=	velocity components along streamwise, azimuthal, and wall-normal directions, m/s
β	=	dimensional azimuthal wavenumber, 1/m
γ	=	ratio of specific heats
δ	=	boundary-layer thickness, μm or m
δ^*	=	boundary-layer displacement thickness, μm or m
(ξ, ζ, η)	=	streamwise, azimuthal, and wall-normal coordinates, mm or m, (in Sec. IV: ζ in rad)
θ	=	boundary-layer momentum thickness, μm or m
κ_ξ	=	streamwise curvature, 1/m
λ	=	azimuthal wavelength, mm or m
μ	=	dynamic viscosity, kg/(m $\cdot$ s)
ρ	=	density, kg/m^3
ϕ	=	angular coordinate, deg
χ	=	inclination of the local tangent to the body surface, deg

Superscripts

$()^{\text{mean}}$	=	mean energy gain
$()^{\text{out}}$	=	outlet energy gain
$()^H$	=	conjugate transpose
$()^\dagger$	=	adjoint

Subscripts

$()_e$	=	value at the boundary-layer edge
$()_k$	=	value at the roughness height
$()_L$	=	left adjacent cell
$()_{\text{opt}}$	=	optimal value
$()_R$	=	right adjacent cell
$()_{\text{tr}}$	=	transition location
$()_w$	=	value at the wall
$()_0$	=	inlet disturbance location
$()_1$	=	outlet disturbance location
$()_\infty$	=	freestream value

I. Introduction

VEHICLES flying at hypersonic Mach numbers are exposed to a significant amount of heat load and thus often require a thermal protection system (TPS). Because heat transfer rates of a turbulent boundary layer are much higher compared with the laminar state, the location of laminar-turbulent transition is a crucial design parameter for the TPS. The mechanisms of laminar-turbulent transition on the windward side of blunt bodies like reentry capsules are not well understood so far. However, experiments have shown that surface roughness plays an important role during the transition process [1,2]. Based on systematic studies of the roughness effects on blunt-body

transition, different empirical correlations have been proposed in the literature [3,4].

Blunt reentry capsules with a sphere-cone-shaped forebody like the Mars Science Laboratory (MSL) support modal growth of boundary-layer instabilities on the conical part of the heat shield strong enough to trigger laminar-turbulent transition [5–7]. Configurations where the forebody consists of a spherical segment only, like the Apollo capsule or the Orion Crew Exploration Vehicle (CEV), require a much higher Reynolds number for the onset of modal disturbance growth [8]. Owing to the strong bow shock, the boundary-layer edge Mach number remains subsonic or slightly supersonic on the spherical heat shield, which excludes the possibility of second-mode amplification. Because of the spherical body shape, there is a sustained, strongly favorable pressure gradient that has a highly stabilizing effect on the first-mode instabilities. Moreover, although the flow is strongly accelerated, the crossflow velocity component inside the boundary layer remains small because of the weak curvature of the boundary-layer edge streamlines. Therefore, crossflow-mode amplification is not relevant either, and the Görtler-type instability is precluded due to the convex surface curvature. Nevertheless, laminar-turbulent transition is observed on such configurations, even at Reynolds numbers for which, according to the linear stability theory, no modal disturbance growth can be found. This phenomenon is denoted as "blunt-body paradox" in the literature [9].

In situations where the flow does not support modal disturbance amplification, transient growth is still a possible scenario for significant disturbance growth [10]. Basically, a linear superposition of modal disturbances may exhibit transient growth in amplitude despite the fact that each individual mode is decaying in the downstream direction. The transient amplification becomes possible only because the individual modes are nonorthogonal to each other, which is a consequence of the non-normality of the underlying governing equations. The overall nonmodal growth strongly depends on the initial shape of the disturbance. Therefore, an optimization procedure is typically used to identify the optimal initial condition that leads to the maximum transient growth, excluding the question of a physical realizability of the initial disturbance. Hence, such optimal transient-growth studies provide an upper limit on the nonmodal disturbance growth.

Transient disturbance growth has been proposed in literature as a possible cause for laminar-turbulent transition, in particular for those cases where modal disturbance amplification is too weak. Reshotko and Tumin [11] considered nosetip transition and used optimal transient-growth results to derive a correlation for roughness-induced transition in the near vicinity of the stagnation point of blunt geometries. Their correlation uses the same parameters as these purely empirical correlations [3,4], which relate the momentum thickness Reynolds number at the transition-onset location with the surface-roughness height and the ratio of surface to boundary-layer edge temperatures. However, the exponents describing the roughness and surface temperature effects are derived from physical considerations together with optimal transient-growth theory. The correlation of Reshotko and Tumin will be denoted as "RT-correlation" from here on. The RT-correlation was able to reproduce the trends of the various data sets used to derive the empirical correlations. However, the optimal transient-growth approach of Reshotko and Tumin included some simplifying assumptions. Therefore, Paredes et al. [12] used an improved framework of optimal transient-growth analysis that removed the shortcomings of the approach of Reshotko and Tumin and applied it to the scale model of the Orion CEV geometry studied in the Mach 6 ACE wind tunnel at Texas A&M University (TAMU) [13,14]. In these experiments, the effect of uniformly distributed surface roughness on transition onset was systematically studied. For the comparatively small Reynolds numbers considered in this experiment, the necessary roughness height to trigger transition in the stagnation flow region was in the order of 0.7 to 1.5 boundary-layer thicknesses [14]. Despite the significant effects of the nonsimilar boundary layer on the transient-growth characteristics, Paredes et al. found that the transient-growth scaling with respect to Reynolds number and the ratio of surface to edge temperature did not change significantly after the improved framework was applied. Because the RT-correlation depends only on

those two scalings, the modified correlation remained close to the original correlation of Reshotko and Tumin despite the improvements in the calculation of optimal growth factors. Thus, both correlations based on optimal transient-growth analysis reproduce equally well the trends observed for roughness-induced transition at the stagnation-flow region of spherical blunt forebodies. On the other hand, Paredes et al. [12] also pointed out that the magnitude of transient growth up to the measured transition locations at the experiments at TAMU was rather small, which raises questions regarding the relevance of the optimal growth paradigm.

Additional experimental studies [8,15,16] on laminar-turbulent transition in the boundary layer of a blunt Apollo-like capsule were performed at Mach 5.9 in the Hypersonic Ludwieg tube at the Technische Universität Braunschweig (HLB) in the unit Reynolds number range of $Re/l \approx 6 \times 10^6/\text{m}$ to $Re/l \approx 20 \times 10^6/\text{m}$. Infrared (IR) thermography was used to monitor laminar and transitional surface heating. IR measurements based on a standard IR coating with a mean roughness of $R_a \approx 10~\mu\text{m}$ revealed the appearance of transitional surface heating at $Re/l \approx 15 \times 10^6/\text{m}$. For a highly polished surface with $R_a \approx 0.5~\mu\text{m}$, no indication of transition was found within the unit Reynolds number range of the HLB. As expected, linear stability analyses for the nominally smooth surface showed that the laminar boundary layer is highly stable. Much larger unit Reynolds numbers would be required for the onset of modal boundary-layer instability growth [8]. Numerical studies on modal disturbance growth in the wake of discrete roughness elements at unit Reynolds number conditions of the experiment showed that roughness element heights well above the mean roughness of the IR coating are required for the onset of a noteworthy modal disturbance growth in the wake flow [17,18]. For further studies of the distributed surface-roughness effects, a specifically designed micron-sized surface-roughness patch of 20 mm × 20 mm was fabricated and placed at the center of the capsule forebody [16], that is, at some distance downstream of the stagnation point region. The patch consists of uniformly spaced rectangular micron-sized roughness elements. It features a similar R_a value as the surface with the standard IR coating but has a roughness structure that is well defined, reproducible, and also amenable to numerical studies. The roughness patch triggered laminar-turbulent transition in recent experiments in the HLB at unit Reynolds numbers that are similar to those required in the case of the standard IR coating, but the onset of transition depends on the position of the capsule model in the wind-tunnel test section [16]. If the capsule model with increased roughness height due to the patch is positioned such that its stagnation point region is located closer to the centerline of the test section, transition is observed for $Re/l \gtrsim 15 \times 10^6/\text{m}$. In the transitional region, several broadband peaks appear in the hot-wire spectra above 100 kHz. If the stagnation flow region is moved further away from the wind-tunnel centerline, then no transition is observed. Because of peculiar design characteristics of the HLB, the freestream disturbance level near the center is moderately higher than that outside the centerline zone. The roughness heights of the standard IR coating and of the roughness patch normalized with a characteristic boundary-layer length scale were significantly lower than those of the sandgrit coatings considered in the experiments of Leidy et al. [13,14].

One of the main objectives of the present paper is to assess the potential for nonmodal disturbance growth on the forebody of the HLB capsule by using optimal transient-growth theory. Specifically, the effects of surface temperature and unit Reynolds number on the optimal transient growth are investigated and compared with the results for the TAMU capsule at a similar Mach number but lower Reynolds numbers [12]. Furthermore, the steady disturbance flow field introduced by the roughness patch on the HLB capsule and its interaction with additional unsteady disturbances is studied by direct numerical simulations (DNS) in order to investigate possible modal or nonmodal disturbance growth mechanisms either in the vicinity of the roughness patch or in the wake region behind the patch. The different numerical approaches used are briefly introduced in Sec. II and the blunt body configurations considered are described in Sec. III. The optimal transient-growth results for the HLB capsule are presented in Sec. IV and compared with corresponding data for the

TAMU capsule. The additional data set for the HLB capsule is used to further substantiate the value of the power-law exponent of the wall to boundary-layer edge temperature ratio of the correlation for roughness-induced transition that was originally proposed by Reshotko and Tumin [11] and the slightly different value recently derived by Paredes et al. [12] based on optimal transient-growth data for the TAMU capsule. In Sec. V, the results of DNS are presented that attempt to replicate the conditions of the HLB capsule experiment with the specifically tailored roughness patch. The experimental results for the HLB and TAMU capsules among others are discussed in further detail in a companion paper by Radespiel et al. [16].

II. Methodologies

This section introduces the different methodologies used in this paper. First, a brief overview of the linear optimal transient-growth theory based on parabolized stability equations is given, where an initial disturbance is sought that maximizes an objective function. The following subsection highlights the methods used for the DNS.

A. Optimal Transient-Growth Theory

The optimal transient-growth analysis is performed using the framework of linear parabolized stability equations (PSE) as elucidated in the literature [19–22]. The method is outlined here for the sake of completeness.

1. Governing Equations

In the PSE concept, the stationary three-dimensional disturbance $\tilde{q}$ can be written as

$$\tilde{q}(\xi, \zeta, \eta) = \hat{q}(\xi, \eta) \exp(i\beta\zeta) + \text{c.c.} \qquad (1)$$

where c.c. denotes the complex conjugate and $\hat{q}(\xi, \eta) = [\hat{\rho}, \hat{u}, \hat{v}, \hat{w}, \hat{T}]^T$ represents the vector of amplitude functions, containing the density and temperature fluctuations ($\hat{\rho}, \hat{T}$), as well as the velocity disturbances ($\hat{u}, \hat{v}, \hat{w}$) in the streamwise ($\xi$), azimuthal ($\zeta$), and wall-normal direction (η), respectively. The wavenumber along the azimuthal (ζ) direction is β and the disturbance azimuthal wavelength is defined as $\lambda(\xi) = 2\pi/\beta$.

Introducing the perturbation form from Eq. (1) into the linearized Navier-Stokes equations and assuming a slow streamwise variation of the basic state and of the amplitude functions to neglect the viscous derivatives in the streamwise direction, the nonlocal linear stability equations are obtained and can be written in the form

$$L\hat{q}(\xi, \eta) = \left(A + B\frac{\partial}{\partial \eta} + C\frac{\partial^2}{\partial \eta^2} + D\frac{\partial}{\partial \xi} \right)\hat{q}(\xi, \eta) = 0 \qquad (2)$$

The linear operators A, B, C, and D are provided in Ref. [23] along with a more detailed explanation on the derivation of the PSE. The parabolized stability equations [Eq. (2)] are integrated in the downstream ξ direction using a marching procedure. Even though the system has been "parabolized", some ellipticity remains and information is allowed to propagate upstream, which in turn can cause numerical instabilities if the step size in ξ becomes too small. Chang et al. [24] identified the $\partial\hat{p}/\partial\xi$ term as the most relevant source of remaining ellipticity; however, this term is of higher order for transient-growth problems [25,26] and therefore will be omitted for the present work.

2. Optimality System

In the optimal transient-growth framework, a set of perturbation profiles at an initial location, $\tilde{q}_0 = \tilde{q}_{\xi_0}$, are sought that maximize a suitably defined objective function, $J(\tilde{q})$, which is a measure of disturbance energy gain within the optimization interval $[\xi_0, \xi_1]$. There are two definitions of the energy gain that are commonly used for optimal-perturbation problems [19,22,27], namely, the outlet energy gain,

$$J = G^{\text{out}} = \frac{E(\xi_1)}{E(\xi_0)} \qquad (3)$$

and the mean energy gain,

$$J = G^{\text{mean}} = \frac{1}{\xi_1 - \xi_0} \frac{\int_{\xi_0}^{\xi_1} E(\xi') \, d\xi'}{E(\xi_0)} \qquad (4)$$

where E denotes the energy norm of $\tilde{q}$. In this work, we use the positive-definite energy norm, proposed by Chu [28], Mack [29], and Hanifi et al. [30], defined as

$$E(\xi) = \frac{1}{\lambda} \int_\zeta \int_\eta \tilde{q}(\xi,\zeta,\eta)^H M_E \tilde{q}(\xi,\zeta,\eta) h_\xi h_\zeta \, d\eta \, d\zeta \qquad (5)$$

where the superscript H denotes conjugate transpose and h_ξ, h_ζ are metric factors associated with the streamwise and azimuthal curvature, respectively. The total energy weight matrix, M_E, includes all five state variables and is defined by

$$M_E = \text{diag}\left[\frac{\bar{T}(\xi,\eta)}{\bar{\rho}(\xi,\eta)\gamma Ma^2}, \bar{\rho}(\xi,\eta), \bar{\rho}(\xi,\eta), \bar{\rho}(\xi,\eta), \frac{\bar{\rho}(\xi,\eta)}{\gamma(\gamma-1)\bar{T}(\xi,\eta)Ma^2} \right] \qquad (6)$$

An overbar denotes mean flow quantities, γ is the ratio of specific heats, and Ma is the Mach number. Additionally, an energy norm, which is solely based on the kinetic energy of the disturbance, is also used in this paper. The energy weight matrix, in this case, reduces to

$$M_K = \text{diag}\left[0, \bar{\rho}(\xi,\eta), \bar{\rho}(\xi,\eta), \bar{\rho}(\xi,\eta), 0 \right] \qquad (7)$$

To distinguish when the objective function is maximized for the total energy E or the kinetic energy K of a disturbance, a corresponding subscript is added to the objective function, resulting in four different possible options: J_E^{out}, J_K^{out}, J_E^{mean}, and J_K^{mean}.

An adjoint-based optimization algorithm is applied to determine the maximum of the objective functional J, employing the intrinsic parabolic nature of the equations. Starting from an initial guess at ξ_0 the direct PSE, $L\tilde{q} = 0$, are used to march the solution $\tilde{q}$ from $\xi = \xi_0$ to $\xi = \xi_1$, where the final optimality condition is used to obtain the initial condition for the backward integration of the adjoint PSE, $L^\dagger \tilde{q}^\dagger = \text{RHS}$, where $\text{RHS} = 0$ in case of outlet energy gain optimization (J^{out}) and $\text{RHS} = 2M^H \tilde{q}$ for the mean energy optimization (J^{mean}). A new initial condition for the forward problem is obtained from the adjoint solution at ξ_0 employing the initial optimality condition. The optimization procedure is terminated when the value of J has converged to a prescribed tolerance, which was set to 10^{-4} in the present computations. In this work, we have used the continuous, as well as the discrete adjoint approach for integrating $\tilde{q}^\dagger$ from ξ_1 to ξ_0, revealing no impact of the adjoint method on the optimal disturbance growth. All results shown in this paper have been computed by applying the continuous adjoint approach.

3. Spatial Discretization and Boundary Conditions

The PSE are discretized with a stable high-order finite-difference scheme (FD-q) [31] of sixth order along the wall-normal direction. The perturbations are integrated along the streamwise coordinate by using second-order backward differentiation and a constant step size. The number of discretization points was varied in both spatial directions to ensure grid convergence of the optimal transient-growth results, whereas clustering of grid points toward the wall was performed. No-slip, isothermal boundary conditions are imposed at the wall, that is, $\hat{u} = \hat{v} = \hat{w} = \hat{T} = 0$. At the upper boundary, which is located just below the shock layer, homogeneous Dirichlet conditions, $\hat{\rho} = \hat{u} = \hat{v} = \hat{T} = 0$, and a Neumann boundary condition for the wall-normal velocity component, $\hat{w}_\eta = 0$, are prescribed.

4. Cross Comparison of the Optimal Transient-Growth Codes

The nonmodal disturbance growth results presented in this paper have been computed with two different codes. The optimal-growth framework developed by NASA is used for the computations for the TAMU ACE capsule configuration and has been extensively verified [21]. On the other hand, a newly developed optimal transient-growth code by DLR is employed for characterizing the nonmodal growth properties of the boundary layer on the HLB capsule. A more detailed overview of the two different capsule configurations is given in Sec. III.

The boundary-layer flow over a hemisphere at $Ma = 7.32$ is considered to cross-verify the two different transient-growth implementations used in this work. Details on the basic flow computations by NASA were reported by Li et al. [32], and the nonmodal disturbance growth characteristics of the boundary layer in downstream direction are given in Ref. [22]. Figure 1 depicts the streamwise evolution of basic flow variables at the edge of the boundary layer along the angular coordinate ϕ ($\phi = \xi/R_s$ with R_s being the radius of the hemisphere). The boundary-layer edge is defined as the wall-normal position where the total enthalpy reaches 99.5% of the freestream value ($h_t/h_{t,\infty} = 0.995$). The basic state computed by DLR uses the numerical framework described in Theiss et al. [8]. Figure 2 shows the optimal outlet energy gain based on the total energy of the disturbance, G_E, at a fixed output location, $\phi_1 = 32.2°$, and varying inflow positions, ϕ_0, as a function of the azimuthal wavenumber, m_ζ, for the basic state computed by DLR. An excellent agreement of the predicted gain from both codes is observed.
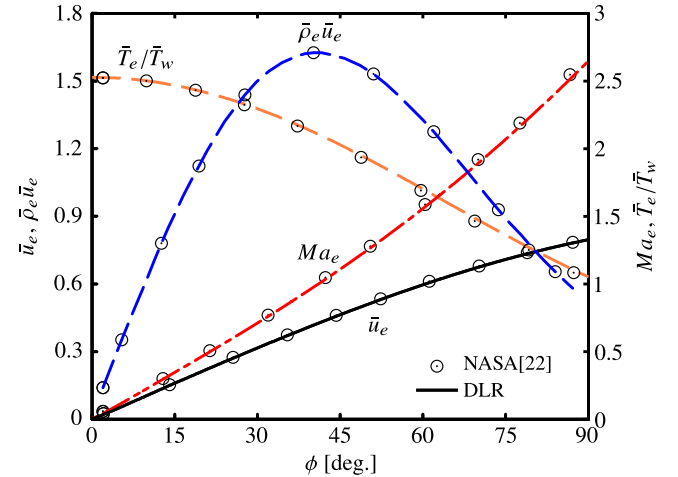

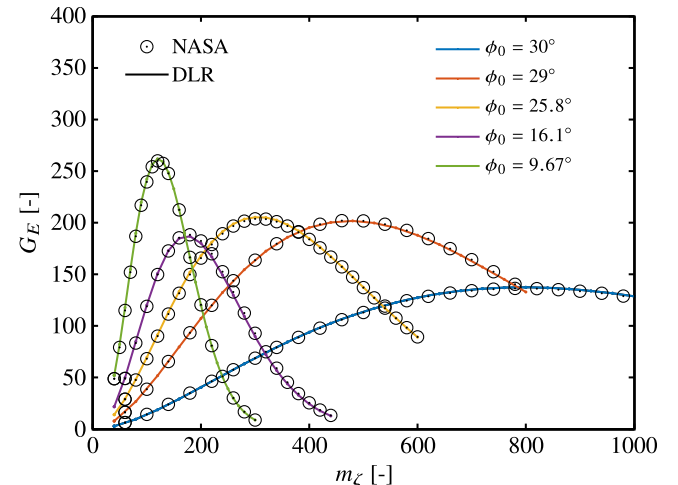**Fig. 1** Streamwise evolution of basic flow variables at the edge of the boundary layer for the hemisphere.

Fig. 2 Total energy gain G_E at $\phi_1 = 32.2°$ optimized for $J = G^{\text{out}}$.

B. Direct Numerical Simulations

The numerical method used by RWTH solves the compressible Navier–Stokes equations in space and time [33]. The computational domain is discretized by an unstructured hierarchical Cartesian mesh whose cells are arranged in an octree structure. The domain decomposition for parallel computations is based on the Hilbert space-filling curve and subtree workloads to distribute subtrees of the hierarchical octree of equal loads to processors [34]. The governing equations are integrated using a finite-volume method [35]. The boundaries of the computational domain are embedded in the Cartesian mesh and modeled employing cut cells [33]. Small cut cells are treated using an interpolation and flux-redistribution scheme [35].

For the spatial discretization, an advection upstream splitting method (AUSM) is used. The advection Mach number on the cell surface is the mean of the extrapolated Mach numbers from the adjacent cells $Ma_{1/2} = 0.5(Ma_L + Ma_R)$. The same formulation holds for the pressure on the cell surface. The cell-center gradients are computed using a second-order accurate least-squares reconstruction scheme [33]. Shock capturing is achieved by adding additional numerical dissipation at the shock position. The temporal integration is based on a five-stage second-order accurate Runge-Kutta scheme. For supersonic flows, the code has been employed and validated for the flow past a cone and around a blunt stagnation point probe [36,37].

The DNS by the Technical University of Munich (TUM) are performed using the Navier–Stokes Multi Block solver (NSMB). NSMB is an MPI-parallelized, finite-volume code for structured grids with a wide variety of numerical schemes, and it has been extensively tested in studies of hypersonic flows [38,39]. The spatial discretization is based on a fourth-order, central difference scheme, whereas a fourth-order Runge–Kutta method is used for time integration. Artificial numerical dissipation is added to capture the shock and to suppress spurious oscillations.

III.   Configurations

A. TAMU Capsule

The first configuration for which transient-growth results are presented corresponds to a blunt, spherical-section forebody at 28° angle of incidence with respect to the free stream. The forebody configuration models the Orion CEV capsule geometry [40]. The face diameter is $D = 2R = 0.0762$ m and the remaining dimensions are scaled according to Hollis et al. [40], resulting in a sphere of radius $R_s = 0.09144$ m. The flow conditions at Mach 6 match those of a wind-tunnel experiment in the Actively Controlled Expansion (ACE) tunnel at the National Aerothermochemistry Laboratory (NAL) of TAMU [13,14]. Paredes et al. [12] performed transient growth calculations for four freestream unit Reynolds numbers, namely, $Re/l = 3.4 \times 10^6$/m, 4.4×10^6/m, 5.4×10^6/m, and 6.4×10^6/m. The freestream temperature was set to $\bar{T}_\infty = 54.69$ K and the surface temperature was equal to $\bar{T}_w = 391.0$ K. To investigate the effects of surface temperature on the transient-growth characteristics, computations were also performed for additional, cooler surface temperatures corresponding to $\bar{T}_w = 300.0$, 195.5, and 130.33 K, respectively, with the unit Reynolds number held fixed at $Re/l = 4.4 \times 10^6$/m.

The basic state, laminar boundary-layer flow over the forebody was computed by using a second-order accurate algorithm as implemented in the finite-volume compressible Navier-Stokes flow solver VULCAN-CFD (see Ref. [41] and http://vulcan-cfd.larc.nasa.gov for further information about the solver). Further details about the laminar basic flow computations are given in Ref. [12].

B. HLB Capsule

The second capsule studied in this work corresponds to an Apollo-shaped capsule with a spherical-section forebody ($D = 0.17$ m and $R_s = 0.204$ m) at an angle of attack of AoA = 24°. Laminar basic flow computations are performed for Mach 5.9 freestream conditions that match the experiments of Ali et al. [15] in the HLB. Overall, four

different unit Reynolds numbers have been computed, namely, $Re/l = 10 \times 10^6$/m, 12.5×10^6/m, 16×10^6/m, and 18×10^6/m, with the freestream temperature set to $\bar{T}_\infty = 59.03$ K and prescribed surface temperature of $\bar{T}_w = 295$ K. To also assess the impact of surface temperature on the nonmodal disturbance growth characteristics, additional simulations have been performed at fixed freestream conditions for $Re/l = 10 \times 10^6$/m and modified surface temperatures with $\bar{T}_w = 170$, 245, and 395 K, respectively.

The laminar basic flow was computed with the second-order accurate, three-dimensional, finite-volume, compressible Navier–Stokes flow solver FLOWer [42] on a block-structured grid. More details about the numerical settings and the employed grid are given in Ref. [8].

C. Comparison of Boundary-Layer Edge Data for the Two Capsules

Figure 3 shows a three-dimensional view of the HLB capsule forebody. Mach number isocontours in the symmetry plane and the Reynolds number based on momentum thickness, Re_θ, with boundary-layer edge streamlines on the capsule forebody are plotted for $Re/l = 10 \times 10^6$/m and $\bar{T}_w = 295$ K. The thick dashed lines indicate the sonic lines. Only one half of the model was used in the basic flow computations, exploiting the azimuthal symmetry of the flow field. Because of the strong bow shock, the boundary-layer edge Mach number falls within the subsonic to transonic range and the flow continuously accelerates from the stagnation point at $\xi = 0$ toward the capsule shoulder. In this work, we focus on the leeward symmetry region above the stagnation point, where transition has been observed in experiments [8,14]. The HLB capsule has been investigated at higher unit Reynolds numbers, and its diameter is about twice the size of the Orion CEV model. The angle of attack differs also, but due to the spherical forebody, the boundary-layer edge values normalized with the respective freestream values are very similar for the two flow configurations as depicted in Fig. 4. Boundary-layer edge quantities along the symmetry plane for the HLB capsule at $Re/l = 10 \times 10^6$/m and $\bar{T}_w = 395$ K are compared with those for the TAMU capsule at $Re/l = 4.4 \times 10^6$/m and $\bar{T}_w = 391$ K. In accordance with Sec. II.A.4, the boundary-layer edge is determined from the total enthalpy criterion ($h_t/h_{t,\infty} = 0.995$). For both capsule geometries, the mass flux, $\bar{\rho}_e \bar{u}_e$, increases with growing distance from the stagnation point and reaches its maximum at the sonic point, $Ma_e = 1$, in agreement with the inviscid flow theory.
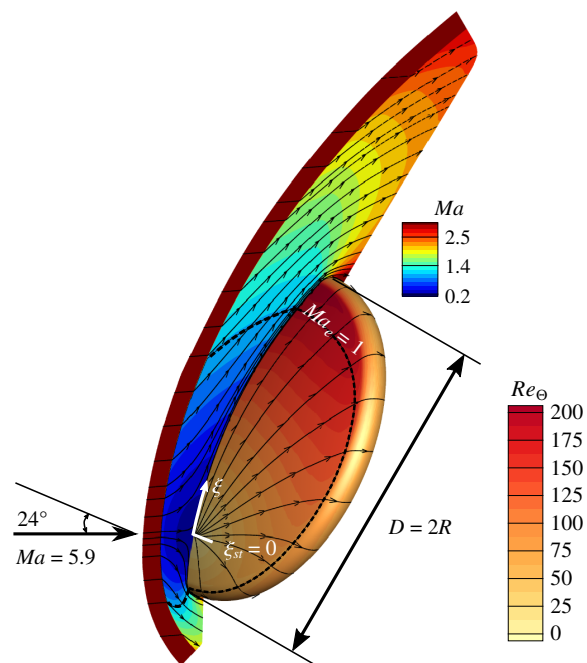

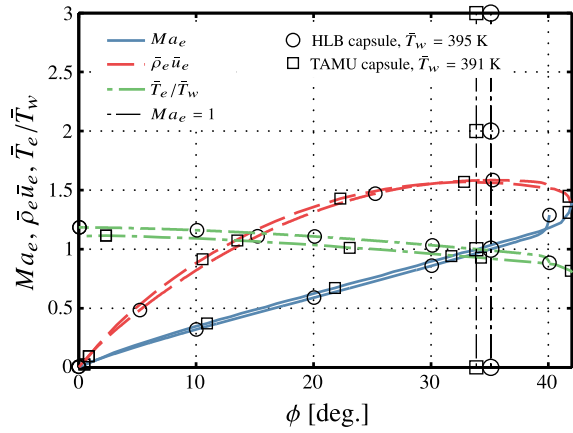**Fig. 3   Three-dimensional view of the HLB capsule forebody.**

Fig. 4 Streamwise evolution of boundary-layer edge quantities along the symmetry plane.

D. Hemisphere Approximation

To ease the computational effort in the case of unsteady DNS, a reduction of the domain size is performed in the simulations of TUM as shown in Fig. 5. First, the flow over a hemisphere is considered. The flow over the hemisphere well represents the flow over the HLB

capsule with angle of attack with minor restrictions outside of the area of interest. Second, results for the laminar steady flow on the whole hemispheric forebody (full domain) are used to generate inflow profiles for a restricted computational domain. The grid resolution of the restricted domain can be increased to match the resolution requirements imposed by the presence of the rough wall. Simulations for the smooth configuration are conducted on the entire hemisphere (full domain), whereas simulations for roughness investigations are conducted on a restricted domain. The box in Fig. 5a shows the position of the restricted domain. The roughness position is indicated by the red square in Fig. 5b.

The steady base flow for the entire hemisphere with smooth surface is computed on an axisymmetric two-dimensional grid. The grid consists of about 76,000 points clustered around the shock location and inside the boundary layer. To provide similar outflow boundaries as in the case of the reentry capsule, the hemisphere ends with a shoulder resembling the one of the HLB capsule.

For both the 3D capsule and the axisymmetric 2D hemisphere, boundary-layer streamwise velocity and temperature profiles at different positions are shown in Fig. 6 for a unit Reynolds number of $Re/l = 18 \times 10^6 /\text{m}$. The profiles on the 3D capsule geometry are extracted along the symmetry plane. The origin of the streamwise coordinates s and $\hat{s}$ is set on the stagnation point of the respective configuration. A clear match of the profiles is observed for the two configurations. In particular, the equivalence of the two flows is
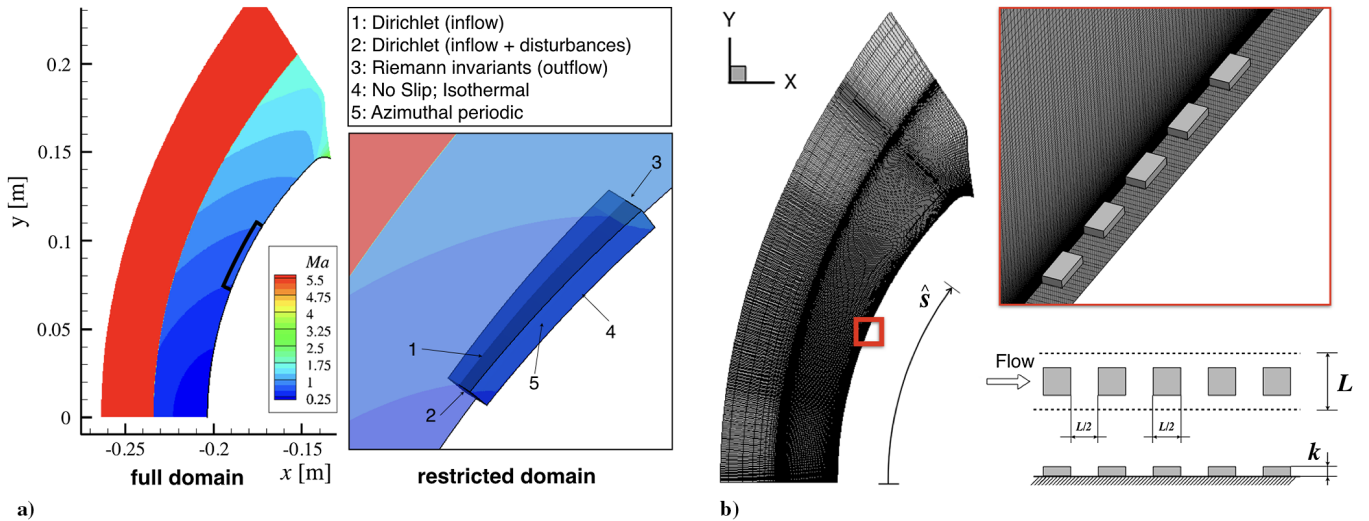

Fig. 5 Simulation domains with a) the specified boundary conditions and b) computational grid with close-up on the roughness position.
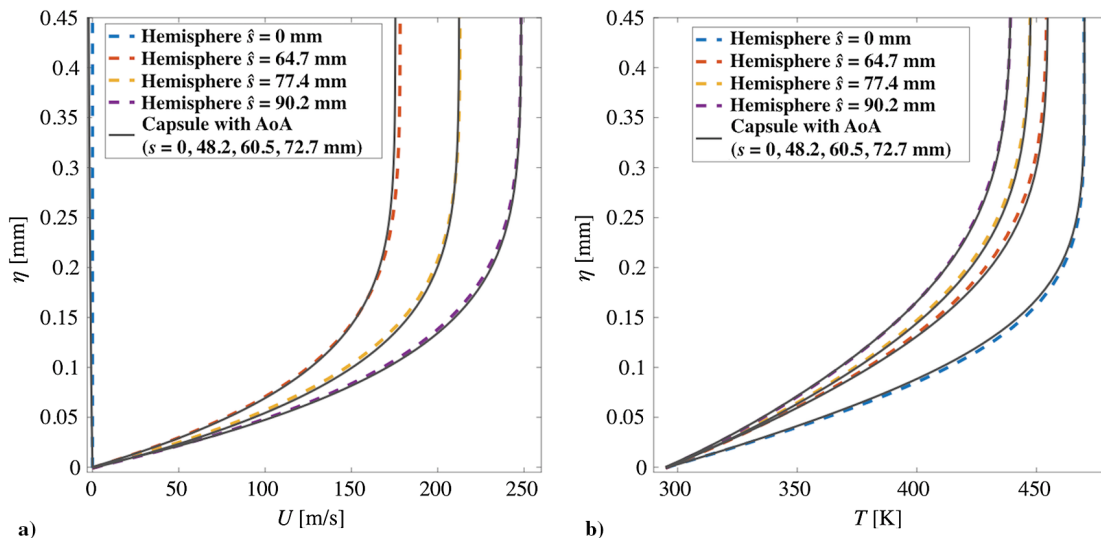

Fig. 6 Comparison of a) boundary-layer velocity and b) temperature profiles for the smooth hemisphere and the HLB capsule geometry with AoA = 24°.

obtained by comparing velocity and temperature profiles on the capsule at a given position s with the ones on the hemisphere at $\hat{s} = s + \Delta s$, with s and $\hat{s}$ being the streamwise coordinates on the two geometries with origin on the respective stagnation points. On the capsule, the distance between the stagnation point and the rotation axis is $s = 60.5$ mm. In the vicinity of this position, the flow corresponds to the one on the hemisphere at $\hat{s} = 77.4$ mm. Details on the restricted domains and further comparisons between the capsule and the hemisphere boundary layer in presence of roughness are discussed in Sec. V.B.1.

IV. Results on Optimal Transient Growth

Optimal transient-growth results are presented for the HLB capsule with an emphasis on the effects of unit Reynolds number and wall temperature on the nonmodal growth characteristics and optimal optimization parameters, namely, spanwise wavelength and optimization interval length. For each parametric study, the transient-growth characteristics will be compared with the findings for the TAMU capsule presented in Ref. [12]. Subsequently, the implications of optimal growth results on the transition correlation of Reshotko and Tumin [11] and Paredes et al. [12] are investigated.

In this work, we assume that the spanwise disturbance wavelength, $\lambda(\xi)$, increases in proportion to the distance from the stagnation point. This ensures a constant wavenumber in the azimuthal direction, m_ζ, at each streamwise position, as it was also used in the axisymmetric case for the hemisphere in Sec. II.A.4. Note that the dimensional spanwise wavenumber β of Eq. (1) turns into the nondimensional, azimuthal wavenumber m_ζ. However, this assumption may not hold for the fully three-dimensional flows investigated in this work. In general, a physically accurate specification of azimuthal-wavenumber variation along a prescribed trajectory in a fully three-dimensional flow remains an open question in the literature for both modal and nonmodal disturbance growth. For the TAMU capsule, Paredes et al. [12] have examined the effect of different strategies for specifying the streamwise variation in spanwise disturbance wavelength on the transient-growth characteristics for the boundary layer along the leeward line of symmetry. In their study, the authors tested a constant wavelength approach, a variation based on streamline divergence, and the assumption of axisymmetric flow. Their calculations revealed only a minor impact of the chosen wavelength variation on the optimal transient growth across the optimization interval that led to the highest gain. The assumption of axisymmetric flow for the azimuthal-wavelength variation resulted in the strongest growth of disturbance energy and hence can be considered as the strategy that provides the upper bound for nonmodal disturbance growth on the geometries regarded in this work. Under the assumption of axisymmetric flow, the metric factors yield in

$$h_\xi = 1 + \kappa_\xi \eta \tag{8}$$

$$h_\zeta = r_b + \eta \cos(\chi) \tag{9}$$

where κ_ξ denotes the streamwise curvature ($\kappa_\xi = 1/R_s$), r_b is the local radius ($r_b = R_s \sin(\phi)$), and χ specifies the inclination of the local tangent to the body surface ($\sin(\chi) = \mathrm{d}r_b/\mathrm{d}\xi$).

A. Effects of Unit Reynolds Number and Energy Norm

Paredes et al. [12] pointed out that, in order to apply the optimal transient-growth predictions toward transition correlations for nonsimilar boundary-layer flows such as the HLB and TAMU capsules, both the initial and final locations of the transient-growth interval must be varied in addition to the azimuthal wavenumber of the disturbance. First, we address the impact of energy norm (total energy vs kinetic energy only) on the gain based on outlet energy [Eq. (3)] at $Re/l = 10 \times 10^6$/m and $\bar{T}_w = 295$ K. The maximum gain within all possible optimization intervals $[\phi_0, \phi_1]$ ($\max_{[\phi_0, \phi_1]} G$) at the corresponding optimal azimuthal wavenumber, $m_{\zeta,\mathrm{opt}}$, is plotted for the total energy norm in Fig. 7a and for the kinetic energy norm in Fig. 7b with $J = G^{\mathrm{out}}$, respectively. The black dot indicates the location of the optimal interval where the highest gain occurs, $[\phi_0, \phi_1]_{\mathrm{opt}}$. The black line denotes the value of ϕ_1 corresponding to maximum G_E and G_K for a given ϕ_0. The region included in the figure is limited by the line of zero length optimization interval $\phi_1 = \phi_0$ with $G = 1$ on the diagonal, and a line on the left that delimits the region of the $[\phi_0, \phi_1]$ space that is omitted because the initial disturbance profiles at ϕ_0 peak above the boundary-layer edge and do not exhibit sufficient decay in wall-normal direction (especially the wall-normal velocity component), which in turn prevents the adjoint-based optimization algorithm to converge toward a satisfactory result. However, the excluded portion of the plot is not considered to be important for the present analysis because perturbations with an extended wall-normal support are unlikely to be excited by surface roughness. The maximum disturbance energy gain in the case of J_E^{out} occurs close to the stagnation point, which is in line with the observations for a hemisphere in hypersonic flow [22,27] and the TAMU capsule with $\bar{T}_w/\bar{T}_e < 1$ [12]. When the norm for the optimization is based on the kinetic energy alone (J_K^{out}), the location of the maximum gain shifts further downstream toward the vicinity of the sonic point as depicted in Fig. 7b ($\phi_{Ma_e=1} \approx 35°$; see also Fig. 4), which again is in close agreement with previous observations for blunt body configurations [12,22].

From here on, the overall nonmodal growth characteristics of the flow are presented in terms of optimal combination of azimuthal wavenumber, $m_{\zeta,\mathrm{opt}}$, and optimal optimization interval length, $[\phi_0, \phi_1]_{\mathrm{opt}}$, that lead to the maximum value of the energy gain for a specific initial location. In the following, the impact of unit Reynolds
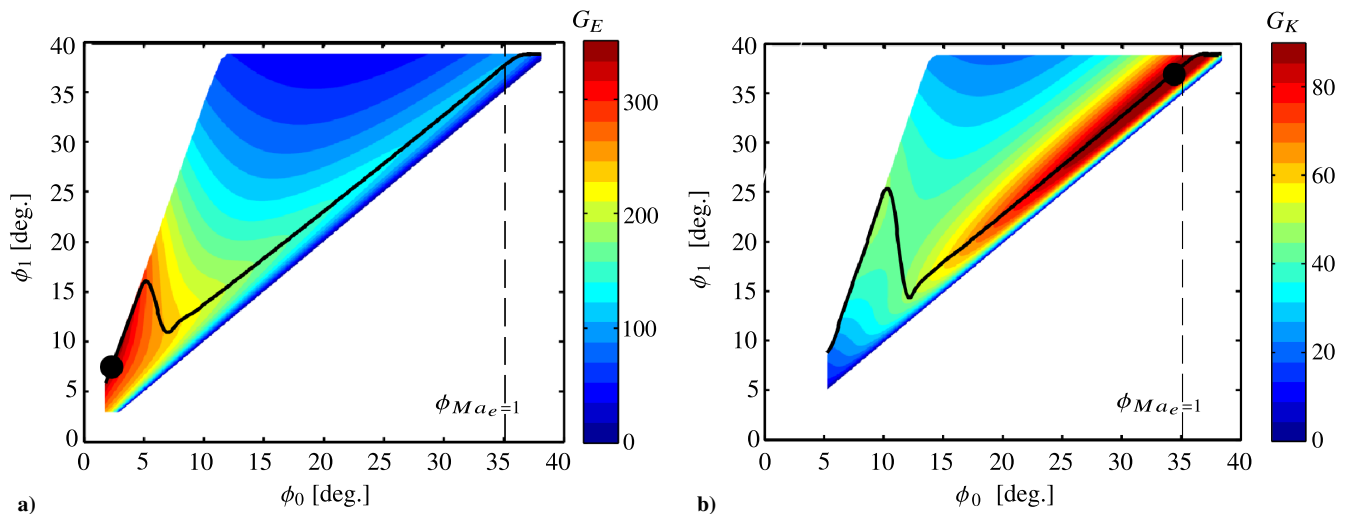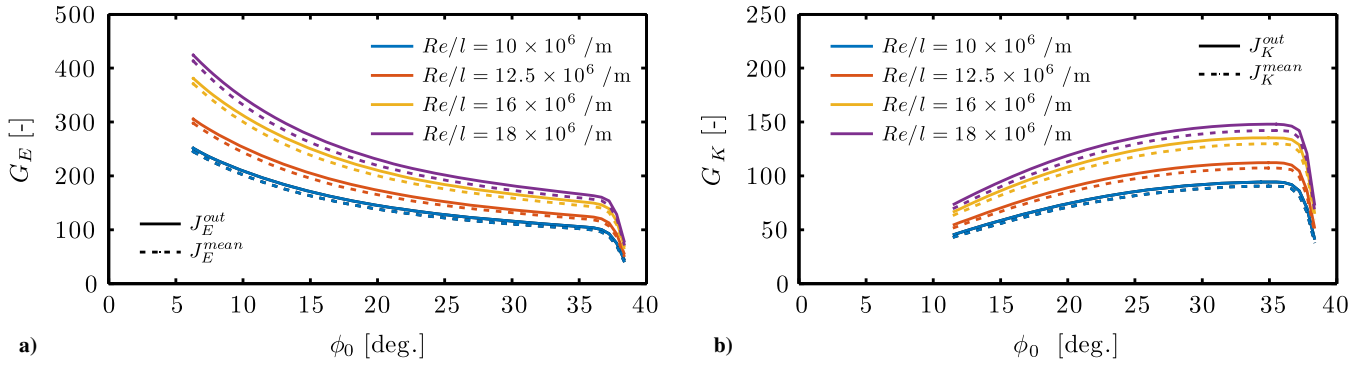

Fig. 7   Isocontours of maximum gain in interval $[\phi_0, \phi_1]$, $\max_{[\phi_0, \phi_1]} G$, for an optimization of a) total energy gain J_E^{out} and b) kinetic energy gain J_K^{out}.

Fig. 8   Streamwise evolution of the maximum optimal disturbance energy gain, $\max_{[\phi_0,\phi_1]} G$, based on a) total energy and b) kinetic energy.

number on the optimal transient-growth characteristics is discussed with respect to objective functions based on outlet energy and mean energy, respectively. The former objective function maximizes the disturbance energy at a prescribed outlet location ϕ_1 [see Eq. (3)], whereas $J = G^{\mathrm{mean}}$ maximizes the integral energy in the interval $[\phi_0, \phi_1]$ [see Eq. (4)], which can lead to a higher possible overshoot in the disturbance energy evolution in comparison to $J = G^{\mathrm{out}}$.

Figure 8 depicts the evolution of the maximum disturbance energy gain along the angular coordinate for the four possible optimization options (J_E^{out}, J_E^{mean}, J_K^{out}, and J_K^{mean}) at different unit Reynolds numbers and $\bar{T}_w = 295$ K. Note that the region below $\phi_0 < 6°$ for G_E and $\phi_0 < 11°$ for G_K is omitted, respectively. In those areas, the length of the optimization interval is limited by the boundaries of the parameter space depicted in Fig. 7. In the case of mean energy gain as the objective function for optimization, the length of the optimal optimization interval is much longer than when the objective function corresponds to the outlet energy gain. Therefore, a meaningful comparison of both objective functions with regard to the highest possible disturbance energy gain is not feasible below the mentioned regions. For all cases shown in Fig. 8, maximizing the outlet energy, J^{out}, leads to the highest possible disturbance energy gain within $[\phi_0, \phi_1]_{\mathrm{opt}}$ at $m_{\zeta,\mathrm{opt}}$. On that account, all of the results presented below to define the upper bound of optimal transient growth for the HLB capsule will pertain only to the objective function based on outlet energy gain ($J = G^{\mathrm{out}}$). For all unit Reynolds numbers considered here, the total energy gain of the perturbations reduces with increasing distance from the stagnation point, whereas the kinetic energy gain grows toward the shoulder of the capsule, which in turn implies an increasing share of the overall energy. The sudden decay in energy gain at $\phi_0 \approx 37°$ for both energy norms, G_E and G_K, is attributed to the shortened optimization interval length at the end of the simulation domain (see Fig. 7).

From the optimal transient-growth analysis for boundary-layer flows over flat plates, the disturbance energy gain at high Reynolds numbers is known to scale with the body-length Reynolds number Re_L [27,43]. Figure 9 indicates the nearly linear scaling of the optimal total disturbance energy gain (G_E) with the unit Reynolds number ($Re_R = R \cdot Re/l$). The results shown in Fig. 9 are for J_E^{out} and $\bar{T}_w = 295$ K. Because the dimension of the body is kept

constant when the unit Reynolds number is varied, the observed small deviations from the linear trend are attributed to the differences in the ratio of boundary-layer thickness to the radius of surface curvature. The linear-like unit Reynolds number dependency of the optimal disturbance energy gain is also reported for the TAMU capsule [12].

The transient-growth amplification with regard to the logarithmic amplification ratio, that is, N-factor, for $\bar{T}_w = 295$ K is shown in Fig. 10 in terms of N-factor envelope curves and $\max_{[\phi_0,\phi_1]_{\mathrm{opt}}}(N)$ optimized for J^{out} with optimal outlet energy norms based on total and kinetic energy, respectively. The N-factors based on the total energy norm N_E and kinetic energy norm N_K are defined as

$$N_E(\xi) = 1/2 \ln[E(\xi)/E(\xi_0)], \quad N_K(\xi) = 1/2 \ln[K(\xi)/K(\xi_0)] \tag{10}$$

The vertical dashed lines in Fig. 10 indicate the transition locations for the experiments of Ali et al. [15]. The N-factors at the observed transition location based on the norm for total disturbance energy and kinetic energy are $N_E = 2.54$ and $N_K = 2.45$ at $Re/l = 16 \times 10^6$/m and $N_E = 2.61$ and $N_K = 2.48$ at $Re/l = 18 \times 10^6$/m, respectively.

The optimal transient-growth results in Figs. 8–10 have been presented at the optimal parameters of spanwise wavelength and optimization interval. Figure 11a depicts the optimal spanwise wavelength for J_E^{out} in terms of boundary-layer thickness along the initial optimization locations for the HLB capsule with $\bar{T}_w = 295$ K and for four different Reynolds numbers. In addition, the optimal parameters for the TAMU capsule with $\bar{T}_w = 391$ K are also plotted at the unit Reynolds numbers from Ref. [12]. For both capsule geometries, the optimal disturbance wavelength displays a good scalability with the boundary-layer thickness. The optimal wavelength with respect to the boundary-layer thickness varies in the range of $(\lambda/\delta)_{\mathrm{opt}} \approx [1.6, 2.7]$ for the HLB capsule and $(\lambda/\delta)_{\mathrm{opt}} \approx [2.2, 3.0]$ for the TAMU capsule (in the region without domain boundary effects) and is not too different from the findings of Reshotko and Tumin [11] with $(\lambda/\delta)_{\mathrm{opt}} \approx [3, 3.5]$ for the flat plate and $(\lambda/\delta)_{\mathrm{opt}} \approx 3.2$ for stagnation point flows. Although the predicted optimal wavelengths are similar for both configurations, the small
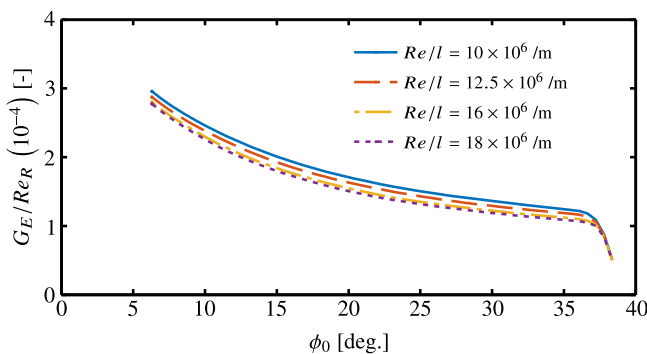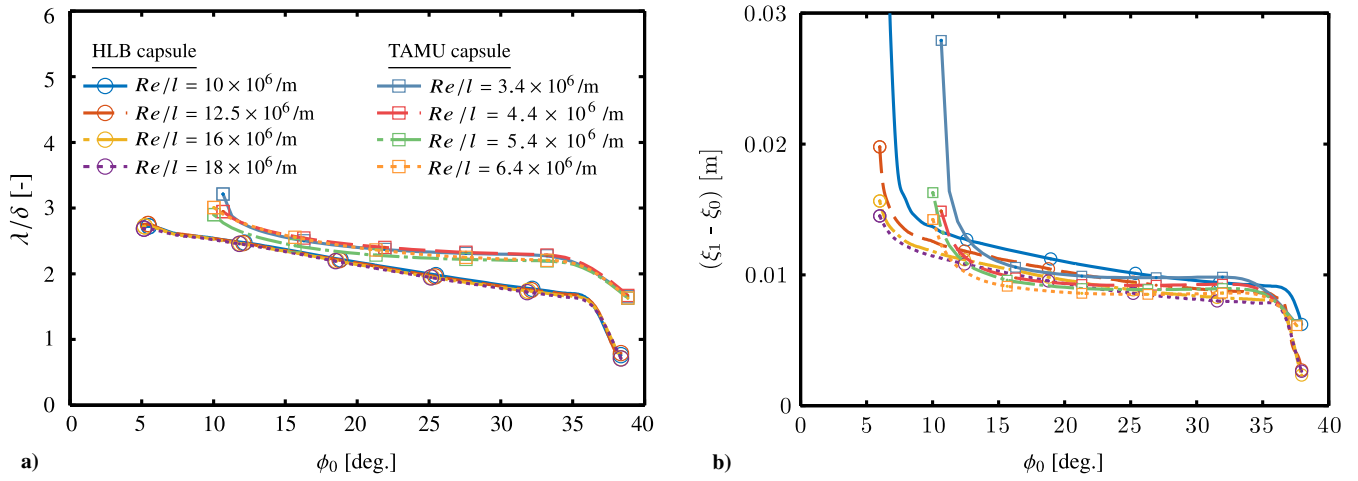

Fig. 9   Impact of unit Reynolds number on the maximum total energy gain, $\max_{[\phi_0,\phi_1]} G_E$. The energy gain is scaled with Re_R.
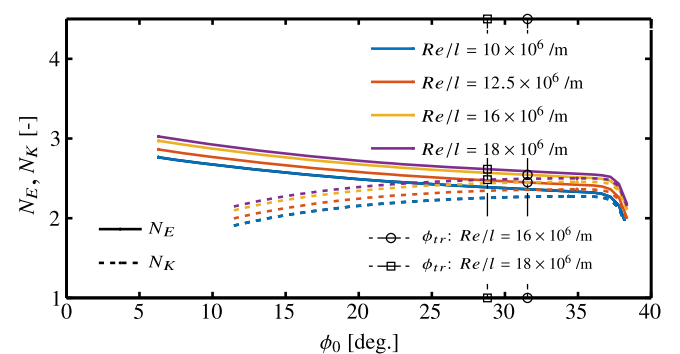
Fig. 10   Impact of unit Reynolds number on the maximum N-factor, $\max_{[\phi_0,\phi_1]} N$.

Fig. 11 Impact of unit Reynolds number on a) optimal spanwise disturbance wavelength and b) optimal optimization interval length.

difference may have been caused by the different wall temperatures used in the two studies ($\bar{T}_{w,\text{HLB}} = 295$ K, $\bar{T}_{w,\text{TAMU}} = 391$ K) and the resulting ratios of wall temperature to boundary-layer edge temperature ($(\bar{T}_w/\bar{T}_e)_{\text{HLB}} < 1$ and $(\bar{T}_w/\bar{T}_e)_{\text{TAMU}} \approx 1$). The impact of the $\bar{T}_w/\bar{T}_e$ ratio on the optimal parameters for nonmodal disturbance growth will be addressed in the next subsection. Figure 11b shows the length of the optimal transient-growth interval as a function of the initial location for the HLB and TAMU capsules at the respective unit Reynolds numbers. Even though the dimension of the TAMU capsule is only about one half the size of the HLB capsule, the optimal length of the transient-growth interval is nearly the same for both geometries ($(\xi_1 - \xi_0)_{\text{opt}} \approx 1.0$ cm) and decreases slightly with the unit Reynolds number. The relatively short optimal optimization length is consistent with the findings of Theiss et al. [17,18] for the laminar wake flow development behind an isolated roughness element on the forebody of the HLB capsule. The authors have shown that, due to the strongly favorable pressure gradient [44],

the laminar wake flow experiences growth and decay of the streak amplitude (and also modal disturbance growth) only within a few roughness diameters downstream of the element. Although not shown here, choosing J_E^{out} as the objective function, the boundary layer on both capsule forebodies undergoes optimal nonmodal disturbance growth within 30–40 boundary-layer thicknesses depending on the angular coordinate, which is about 15 times shorter in comparison to the findings of Reshotko and Tumin [11] for flat plate flows.

B. Effect of Wall Temperature

The effect of the wall temperature on the optimal disturbance growth based on the total and kinetic energy norm is shown in Fig. 12 for the TAMU capsule with $Re/l = 4.4 \times 10^6$/m optimized for the outlet energy gain. The corresponding results for the HLB capsule with $Re/l = 10 \times 10^6$/m are plotted in Fig. 13. In accordance with
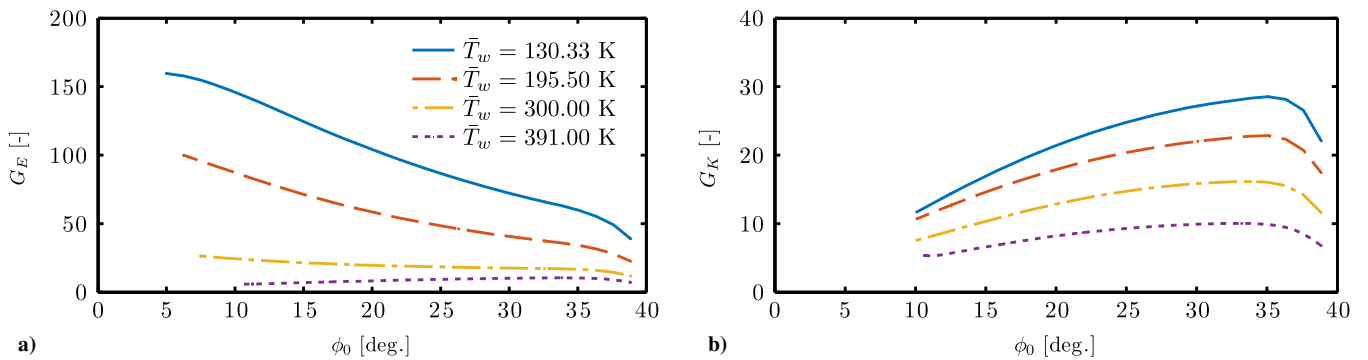
Fig. 12 Streamwise evolution of the maximum optimal disturbance energy gain, $\max_{[\phi_0,\phi_1]}G$, based on a) total energy and b) kinetic energy for the TAMU capsule.
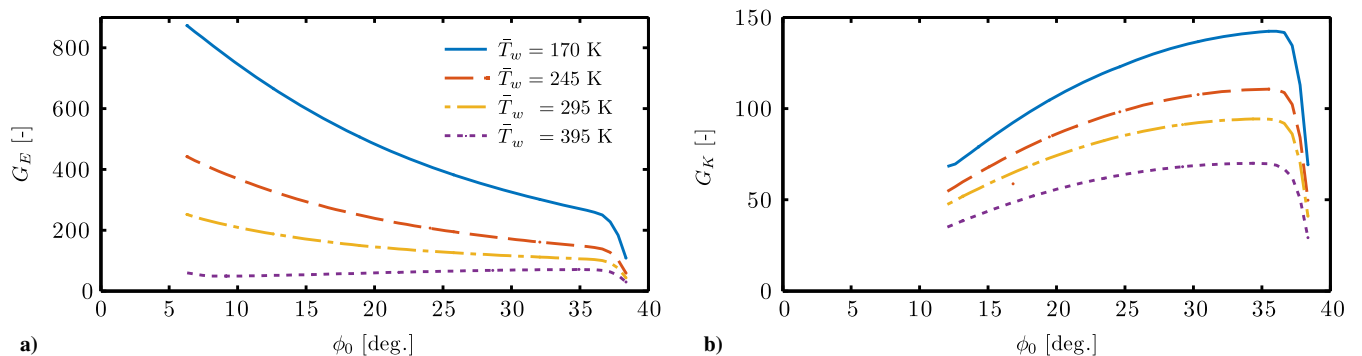
Fig. 13 As in Fig. 12, but for the HLB capsule.

Fig. 14   Impact of wall temperature on a) optimal spanwise disturbance wavelength and b) optimal optimization interval length.
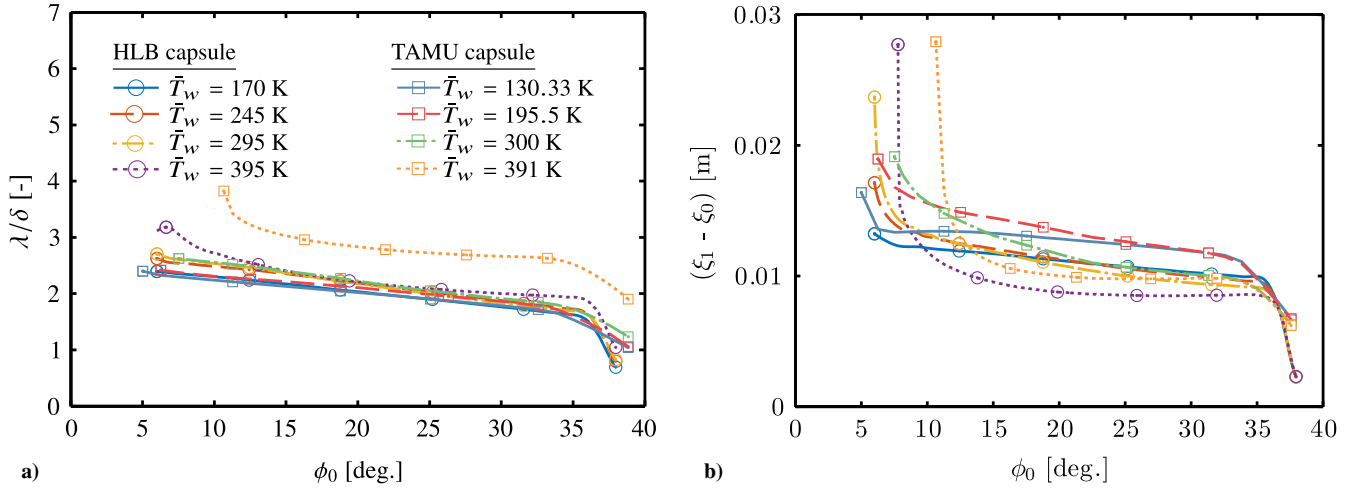
previous findings in the literature [9,11,20,27,45–47], the disturbance energy gain increases with wall cooling, whereas the effect is more pronounced in the case of the total energy norm, especially in the vicinity of the stagnation point. The disturbance energy gain based on total and kinetic energy norms is higher for the HLB capsule due to the larger body-length Reynolds number by a factor of about five. The share of the kinetic energy on the total energy of the disturbance increases with $\bar{T}_w/\bar{T}_e$ and for $\bar{T}_w/\bar{T}_e \approx 1$ (HLB capsule: $\bar{T}_w = 395$ K; TAMU capsule: $\bar{T}_w = 391$ K; see also Fig. 4) the total energy mainly consists of kinetic energy, that is, at $\phi_0 = 35.5°$, $G_E = 70.6$ and $G_K = 69.7$ for the HLB capsule, and $G_E = 10.3$ and $G_K = 9.9$ for the TAMU capsule, respectively.

The effect of wall temperature on the optimal spanwise wavelength and the optimal optimization interval for both capsules is shown in Figs. 14a and 14b, respectively. The objective function is J_E^{out}. The optimal azimuthal wavelength scaled by the boundary-layer thicknesses decreases slightly with wall cooling for both capsule configurations. The results for the TAMU capsule at $Re/l = 4.4 \times 10^6$/m fall within the range of the HLB capsule data for $Re/l = 10 \times 10^6$/m when $(\bar{T}_w/\bar{T}_e)_{\text{TAMU}} < 1$. On the other hand, the optimal optimization length increases slightly with wall cooling $((\xi_1 - \xi_0)_{\text{opt}} \approx 1.1$ cm) along with a higher deviation from the mean value.

C.   Revision of Transient-Growth-Based Transition Correlation

Recently, Paredes et al. [12] revisited the distributed roughness-induced transition correlation of Reshotko and Tumin [11], which is the only physics-based model that tackles the blunt-body paradox. The RT-correlation is defined as

$$Re_\theta \left(\frac{k}{\theta}\right)\left(\frac{\bar{T}_e}{\bar{T}_w}\right)^{1.27} = 434 \qquad (11)$$

where θ denotes the momentum thickness, Re_θ is the Reynolds number based on θ, and k is the roughness height. Reshotko and Tumin [11] assumed that an energy norm at the transition location is related to the roughness-induced energy through the transient-growth energy gain factor G with $E_{\text{tr}} = GE_{\text{in}}$. Further assumptions are that the input energy scales with $E_{\text{in}} = \bar{\rho}_k \bar{u}_k^2$, where the roughness-induced disturbance velocities are proportional to the roughness height, $\bar{u}_k/\bar{u}_e \propto k/\theta$, and the wall-cooling ratio $\bar{T}_e/\bar{T}_w$ is equivalent to $\bar{\rho}_k/\bar{\rho}_e$. As a result, the input energy can be approximated to $E_{\text{in}} = (\bar{T}_e/\bar{T}_w)(k/\theta)^2$. Furthermore, the gain is assumed to scale with the length Reynolds number (as shown in Fig. 9) or with the square of a thickness Reynolds number. Thus, the energy at the transition location results in

$$(E_{\text{tr}})^{1/2} = \left(\frac{G^{1/2}}{Re_\theta}\right) Re_\theta \left(\frac{k}{\theta}\right)\left(\frac{\bar{T}_e}{\bar{T}_w}\right)^{0.5} \qquad (12)$$

Assuming a power-law variation of the scaled optimum transient energy gain with respect to the surface-to-edge temperature ratio,

$$\left(\frac{G^{1/2}}{Re_\theta}\right) \propto \left(\frac{\bar{T}_w}{\bar{T}_e}\right)^{c_T} \qquad (13)$$

Reshotko and Tumin [9,11] in the vicinity of $\bar{T}_w/\bar{T}_e \approx 0.5$ obtained a value for the power-law exponent of $c_T = -0.77$, which finally yields Eq. (11). For their analysis they used optimal transient-growth computations based on local, parallel theory and self-similar boundary-layer flow without curvature effects. Furthermore, the initial optimization position and the spanwise wavenumber also remained unchanged. Paredes et al. [12] applied an advanced framework to improve the shortcomings of the optimal transient-growth computations by Reshotko and Tumin [9,11], namely, nonlocal transient growth computations including curvature effects for full Navier–Stokes basic state solutions of the TAMU capsule at varying wall temperatures $(\bar{T}_w/\bar{T}_e)_{\text{TAMU}} < 1$. The initial ($\xi_{\text{in}} = \xi_0$) and final locations ($\xi_{\text{tr}} = \xi_1$), as well as the spanwise wavenumber, were also optimized. Based on the improved framework, Paredes et al. [12] revised the original RT-correlation and also assumed a power-law variation for the optimum transient energy gain with respect to the surface-to-edge temperature ratio:

$$\left(\frac{G^{1/2}}{Re_{\theta_0}}\right)\left(\frac{\bar{\rho}_{e,0}\bar{u}_{e,0}^2}{\bar{\rho}_{e,\text{tr}}\bar{u}_{e,\text{tr}}^2}\right)^{1/2} \propto \left(\frac{\bar{T}_w}{\bar{T}_{e,0}}\right)^{c_T} \qquad (14)$$

In their analysis, they computed the c_T value for several possible transition onset locations, ϕ_{tr}, based on the optimal parameter combinations (λ_{opt}, $m_{\zeta,\text{opt}}$, $(\phi_{tr} - \phi_0)_{\text{opt}}$) for each of the different wall temperatures involved ($\bar{T}_w/\bar{T}_e < 1$) and for maximizing the total energy gain (J_E^{out}). Moreover, three assumed variations in spanwise disturbance wavelength were also considered. As a result, the set of exponents was nearly insensitive to the assumed λ variation and all c_T values were averaged, resulting in a mean value of $c_T \approx -0.81$, which is remarkably close to the value computed by Reshotko and Tumin [9,11] based on parallel flow transient-growth calculations. For that reason, the following revised RT-correlation of Paredes et al. [12] only slightly deviates from the originally proposed correlation [Eq. (11)]

$$Re_\theta \left(\frac{k}{\theta}\right)\left(\frac{\bar{T}_e}{\bar{T}_w}\right)^{1.31} = 455 \qquad (15)$$
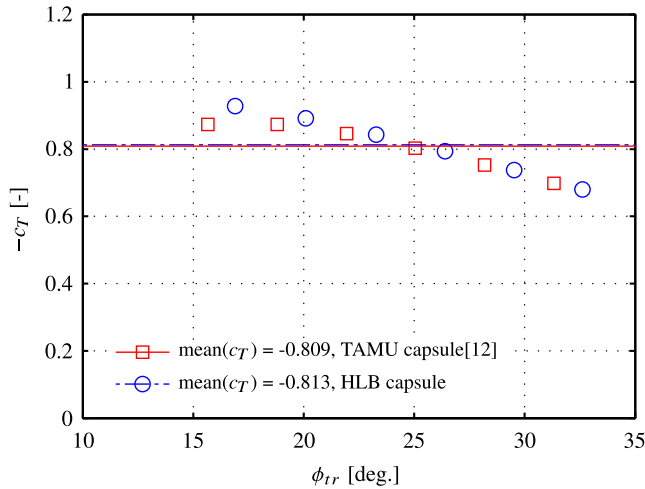
Fig. 15 Best-fit power-law exponent of wall-to-edge temperature ratio for HLB capsule (°) and TAMU capsule (□).

The purpose of this section is not to provide an additional transient-growth-based transition correlation, but rather to check if the presented nonmodal growth data for the HLB capsule will result in a similar power-law exponent, c_T, as derived based on the TAMU capsule data. The results shown in Fig. 13a are used to estimate the best-fit exponent through the relation given in Eq. (14). Note that results were considered only when $\bar{T}_w/\bar{T}_e < 1$, in particular, $\bar{T}_w = 170$ K, 245 K, and 295 K. Figure 15 depicts the variation of the c_T value at selected transition onset locations for the HLB capsule with $Re/l = 10 \times 10^6$/m. In addition, the results for the TAMU capsule at $Re/l = 4.4 \times 10^6$/m with the spanwise disturbance wavelength variation based on axisymmetric flow (the same assumption as used in this work) are also shown. The angular coordinate for the HLB capsule data is shifted by $\Delta\phi \approx 1.3°$ to match the boundary-layer edge Mach number conditions on the TAMU capsule (see Fig. 4). The averaged power-law exponent for the HLB capsule data is $c_{T,\text{HLB}} = -0.813$ and therefore in very good agreement with the equivalent TAMU capsule value of $c_{T,\text{TAMU}} = -0.809$.

V. DNS Results for Roughness Patches

To investigate the effect of micron-sized roughness on the capsule boundary layer, DNS of the supersonic flow around the HLB capsule and the corresponding hemisphere are performed considering finite patches of distributed roughness. The roughness patch geometry for these simulations is deduced from capsule experiments in the HLB [16] and will be quantified subsequently. The generic roughness mimics the Nextel Velvet Coating that allows for infrared surface temperature measurements and showed to have a distinct influence on transition [8]. The Reynolds number based on the height of the roughness is $Re_{kk} = \mathcal{O}(1)$, which is well below the critical value. Thus, immediate transition can be excluded [18,48]. The possible presence of modal as well as nonmodal growth mechanisms in the roughness wake is investigated in Sec. V.B. Three studies are presented and compared. Freestream conditions for the different simulations are listed in Table 1. First, the steady flow at $Re/l = 6.25 \times 10^6$/m over two different roughness patches located on the HLB capsule is analyzed by RWTH. The computational domain contains capsule, shock wave, and roughness patch. The flow disturbances in the vicinity

of the two roughness patches are analyzed and compared. Second, a roughness patch located on the hemisphere from Sec. III.D is investigated by TUM. The wake of the roughness is analyzed for modal instabilities at $Re/l = 18 \times 10^6$/m, and unsteady DNS imposing pressure disturbances are performed to investigate the interaction of roughness and forced disturbance modes.

A. HLB Capsule Roughness Simulations by RWTH

The roughness patches are located in the center of the spherical forebody of the generic Apollo-like "HLB capsule" in Fig. 3. The origin of the spherical coordinate system is set in the center of the roughness patch, with ξ, ζ, and η being the streamwise, spanwise, and wall-normal direction, respectively. At the given location, the Mach number at the edge of the boundary layer is $Ma_e = 0.5$. For the current Reynolds number $Re/l = 6.25 \times 10^6$/m, the boundary-layer thickness, displacement thickness, and momentum loss thickness are $\delta = 492$ μm, $\delta^* = 89.2$ μm, and $\theta = 74.3$ μm, respectively. In this section, the boundary-layer edge is defined as the wall-normal distance where the flow has 99% of the total enthalpy of the freestream. The Reynolds number based on the displacement thickness is $Re_{\delta^*} = 109.65$. The roughness patch elements protrude 20 μm into the boundary layer, which is 4% of the boundary-layer thickness and 22% of the displacement thickness. The corresponding roughness Reynolds numbers are $Re_{kk} = 5.82$ and $Re_k = 6.02$, respectively.

The geometry of the aforementioned finite roughness patches is illustrated in Fig. 16, where the flow direction at the boundary-layer edge is from left to right. Each of the patches consists of a certain number of identical single roughness elements having a square base of 100 μm × 100 μm and a height of 20 μm. Two patterns of elements are considered. In Fig. 16a, the "aligned" or "checkerboard" configuration with 5 × 5 elements is depicted. Based on the flow direction, neighboring elements in the spanwise direction form rows, whereas columns are found in the streamwise direction. This configuration possesses infinite channels between the columns of elements. The spacing between the elements in both streamwise and spanwise direction is $L = 200$ μm. The "staggered" configuration is shown in Fig. 16b. The second and fourth rows of elements are reduced by one element and misaligned in the spanwise direction by $L/2$. The projected area in the streamwise direction is gapless. The base area of both patches is 0.9 mm × 0.9 mm.

To resolve the micron-sized roughness patch, the unstructured Cartesian grid is massively refined in the vicinity of the roughness patch. The regions of constant grid resolution around the patch are evidenced in Fig. 17, where thin lines indicate a change of grid resolution of the Cartesian mesh. The streamwise and normal variation of the grid is shown in Fig. 17a, whereas the variation in the ζ direction is sketched in Fig. 17b. Note that instead of the single elements of the roughness patch, the thick line depicts the extent of the complete patch. Furthermore, the capsule surface is sketched flat. The gray dashed line in Fig. 17a indicates the surface of the spherical forebody. The Cartesian cell length in the innermost region with the highest resolution is $\Delta d = 1.945$ μm, and it is doubled from region to region. An example of the change in resolution (scaled by a factor of 2) is given in Fig. 17a at the outermost frame. In total, the mesh contains 300×10^6 cells and 30×10^6 cells are clustered in the refined vicinity of the roughness patch.

The streamwise velocity deficit with respect to the smooth configuration u' downstream of the second and third rows of the elements, that is, at $\xi = -L/2$ and $\xi = L/2$, is shown in Fig. 18. In each figure, the staggered and the aligned configurations are shown in the left and right half plane, respectively. Differences between the configurations are restricted to the region close to the wall, that is, for $\eta < 0.1$ mm. Downstream of the staggered second row in Fig. 18a, the highest velocity deficit occurs downstream of the elements slightly above the top of the element at $\eta \approx 30$ μm. Note that it is more intense in the aligned configuration. In the channel between the elements, higher velocities, that is, a lower velocity deficit, are evident in the aligned configuration. This statement also holds downstream of the identically aligned third row in Fig. 18b. Inside the

Table 1 Freestream conditions for the configurations with rough wall

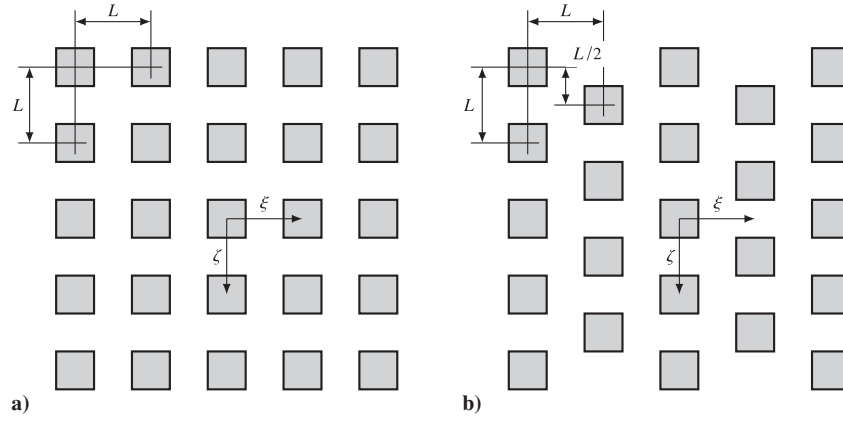| Case	Geometry	Ma	$\bar{p}_\infty$, Pa	$\bar{T}_\infty$, K	$\bar{T}_w$, K	Re/l, 1/m	AoA, °
1	HLB capsule	5.9	478	59	295	6.25×10^6	24
2	Hemisphere	5.9	478	59	295	6.25×10^6	0
3	Hemisphere	5.9	1377	59	295	18.0×10^6	0

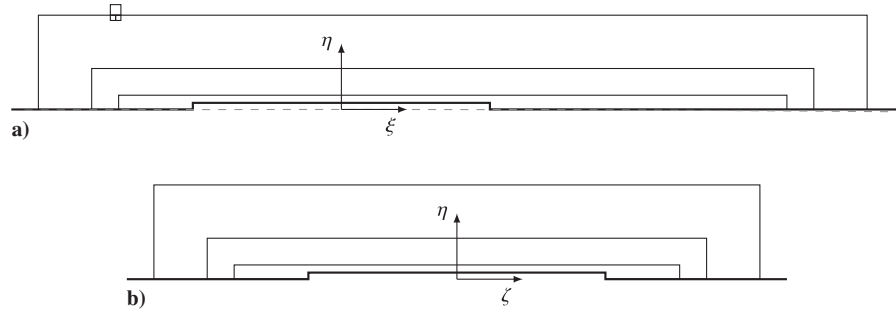**Fig. 16 Schematic of the distributed roughness: a) aligned; b) staggered.**

Fig. 17 Grid topology in the vicinity of the roughness patch: a) $\xi - \eta$ plane at $\zeta = 0$; b) $\zeta - \eta$ plane at $\xi = 0$.
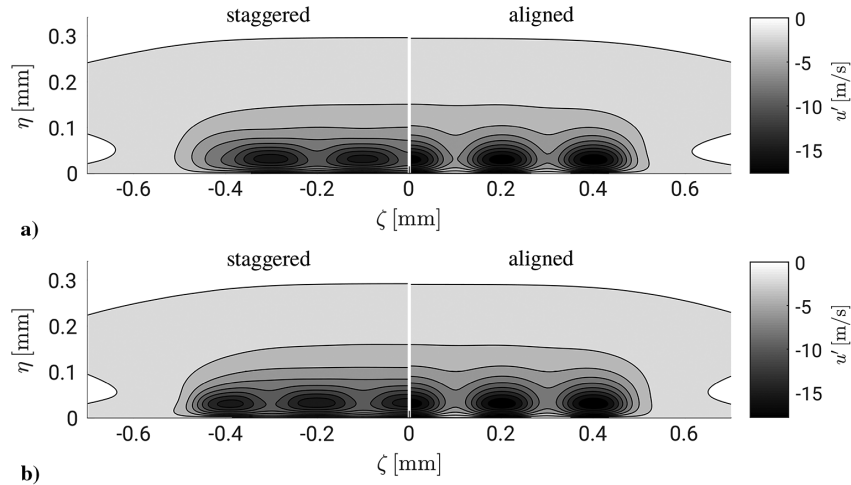
Fig. 18 Streamwise velocity deficit u': a) at $\xi = -L/2 = -100\ \mu$m; b) at $\xi = L/2 = 100\ \mu$m.

patch, the difference in the streamwise velocity between the flow-channel and the postelement location is higher for the aligned configuration.

The spanwise velocity component normal to the symmetry plane is evidenced in Fig. 19 downstream of the roughness patch. Again, the staggered and aligned roughness elements are compared. The velocity component of the aligned configuration in the positive half-plane is multiplied by −1 to yield a better comparison. The thick line indicates $\bar{v} = 0$. The overall pattern for both cases is identical, but the inward flow, that is, the bright peaks in Fig. 19, is stronger for the staggered configuration. This can be attributed to the inward flow generated by the sum of the elements acting as a finite patch.

Fig. 19 Velocity in spanwise direction downstream of the last row of elements at $\xi = 2.5L = 500\ \mu$m.

This discussion is resumed in the subsequent analysis in Sec. V.B on the infinite extent of the rows of roughness elements located on the hemisphere.

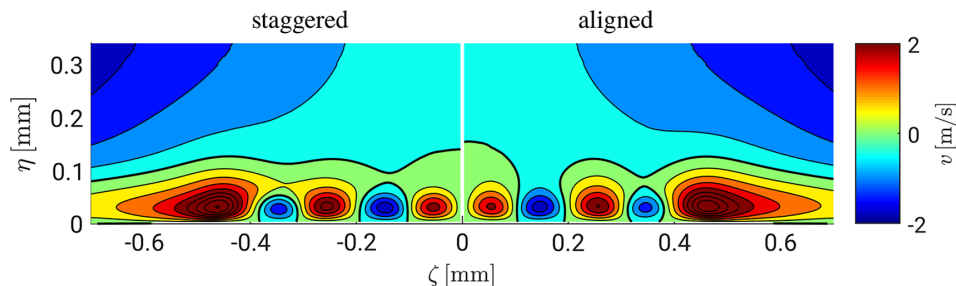## B.   Hemisphere Roughness Simulations by TUM

The TUM-DNS were carried out on a restricted 3D domain extracted on the hemisphere geometry for $\hat{s} \in [74, 116]$ mm. Details of the restricted domain and the roughness patch are shown in Fig. 5. The roughness patch of the hemisphere consists of five squared elements in the streamwise direction. The size of each element and the streamwise spacing are described in Sec. V.A. The patch is centered at $\hat{s} = 77.4$ mm. Dirichlet boundary conditions are applied at the inflow, Riemann invariants are used at the outflow, and azimuthal-periodic boundary conditions are used in the spanwise direction. By using periodic boundary conditions, the domain can be limited in spanwise direction to one single roughness periodicity (L). As a result, a considerable reduction of the domain size and, consequently, of computational cost is achieved. The grid of the restricted domain consists of about 29×10^6 points (1320 points in the streamwise and 220 in the wall-normal direction clustered at the roughness location and 100 points equally spaced in the spanwise direction).

1.   Steady Simulations

For the case of $Re/l = 6.25 \times 10^6$/m, we compare the results with the ones presented in Sec. V.A for the HLB capsule configuration. We found that the presence of the roughness on the hemisphere has a similar effect on the flow as in the case of the HLB capsule. In particular, because several roughness elements are present in the spanwise direction in the case of the HLB capsule, the flow in the vicinity of the symmetry plane presents the same periodicity features as in the case of the rough hemispherical geometry. The profiles of the streamwise velocity at three different positions are shown in Fig. 20. Profiles are extracted at spanwise coordinate $\zeta = 0$ mm. The roughness patch is centered on $\xi = 0$ mm, whereas $\xi = -0.5$ mm and $\xi = 0.5$ mm refer to positions at 0.5 mm before and after the roughness patch, respectively. A good match can be observed at all three positions. Moreover, Fig. 21 shows a contour map for the spanwise component of the velocity in the $\zeta - \eta$ plane at the position $\xi = 2.5L = 0.5$ mm downstream of the last roughness row. Contour lines are used for the capsule results and color shading for the hemisphere results. Contour level spacing is 0.3 m/s. For clarity, the dashed line shows the projection of the roughness elements. Also in this case, the spanwise velocity data for the hemisphere and the capsule are similar.

Results for the base flow at $Re/l = 18 \times 10^6$/m are also shown in Fig. 20. Compared with the case with lower unit Reynolds number, a less-stable boundary layer is expected, and a higher roughness height–to–boundary-layer thickness ratio is found, in particular, $k/\delta = 0.069$ and $Re_{kk} = 25$.

Further numerical studies on the hemispherical geometry (not shown here) have been undertaken to investigate the influence of the patch length in the streamwise direction. In fact, compared with the
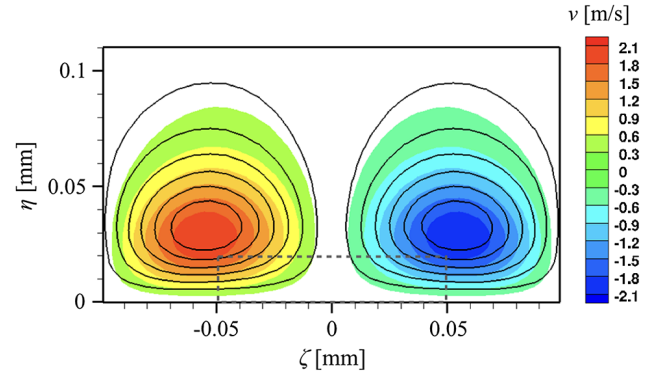

Fig. 21   Contour map for the spanwise velocity at the position $\xi = 2.5L = 0.5$ mm.

experiments in the HLB, the roughness in the present analysis has a smaller spatial extension. However, we found that further lengthening of the rough region in the streamwise direction, obtained by adding roughness elements upstream of the patch, has a negligible influence on the flow downstream of the patch. Therefore, no significant influence is expected on the stability properties of the wake developing downstream of the last roughness element.

2.   Unsteady Simulations

For the case of $Re/l = 18 \times 10^6$/m, the base flow downstream of the roughness patch has been analyzed with the help of spatial two-dimensional linear stability analysis (LST-2D). The code used to perform LST-2D has already been validated and tested in the case of wake flow instability behind isolated roughness elements [17,18]. No modal instability could be found in the boundary layer downstream of the roughness patch.

To investigate the presence of possible nonmodal instability mechanisms (i.e., transient growth), time-varying pressure disturbances are introduced at the inflow of the restricted domain (side 2 in Fig. 5a) and the development of unsteady disturbances is analyzed by means of unsteady DNS. The disturbance is defined as a superposition of five spatial modes with random amplitude A_n and phase ϕ_n,

$$p'(\zeta, \eta) = c(\eta) \cdot \sum_{n=1}^{5} A_n \cos\left(\frac{2\pi n}{\lambda_\zeta}\zeta + \phi_n\right) \qquad (16)$$

where λ_ζ equals the spanwise length of the domain at the inflow position. The function $c(\eta) = e^{-(\eta/\delta)^3}$, with δ being the boundary-layer thickness, guarantees that the perturbation vanishes outside the boundary layer. Experimental investigations at HLB have revealed that relevant frequencies over the rough-wall capsule for large Reynolds numbers lie in the range 100–300 kHz [16]. Based
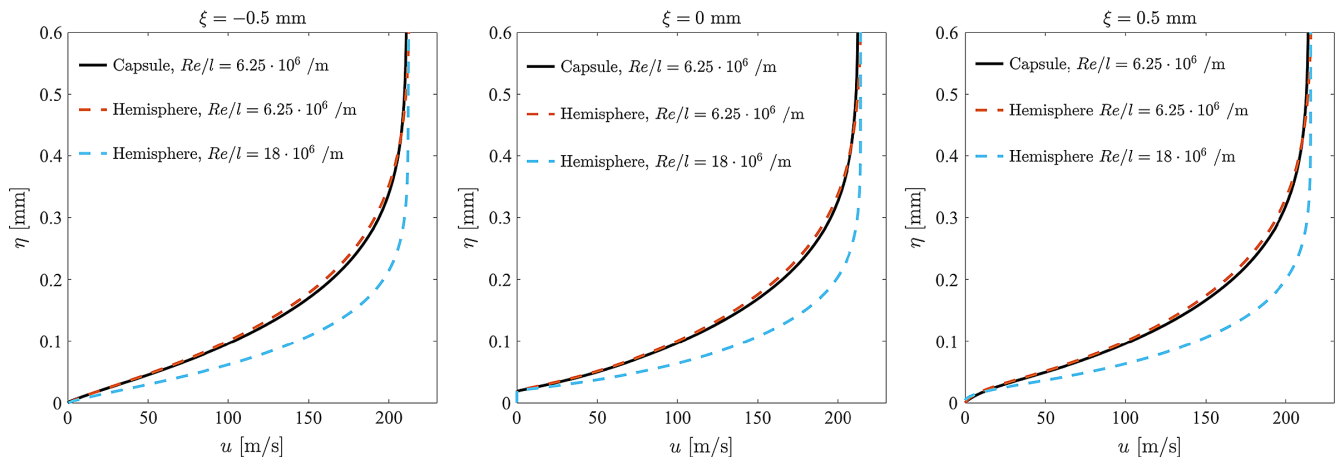

Fig. 20   Comparison of the streamwise velocity profiles of the boundary layer for the hemisphere and the HLB capsule geometry with AoA = 24°.

on this observation, three different frequencies are investigated in the present analysis: $f_1 = 167$ kHz, $f_2 = 250$ kHz, and $f_3 = 333$ kHz. The resulting inflow condition for the pressure at $\xi = -3.4$ mm is given by:

$$p(\xi_0, \zeta, \eta, t) = \bar{p}(\xi_0, \zeta, \eta) + p'(\zeta, \eta) \sum_{m=1}^{3} \cos(2\pi f_m t) \qquad (17)$$

where ξ_0 is the streamwise coordinate value of the inflow boundary and $\bar{p}(\xi_0, \zeta, \eta)$ is the pressure distribution of the steady base flow.
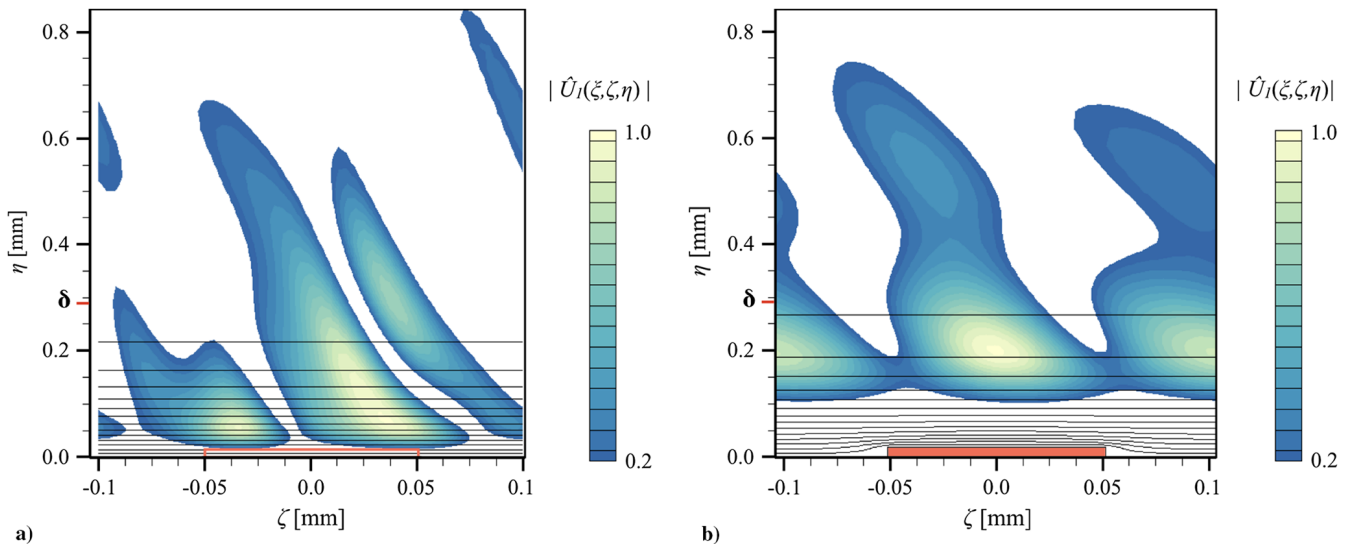
Simulations over a long enough time interval corresponding to multiple periods of the forcing field are needed for the transient effects to vanish and we verified the convergence of the spectrum across the entire simulation domain. The spatiotemporal analysis is conducted by performing a two-dimensional fast Fourier transform (FFT). Any flow variable $g(\xi, \zeta, \eta, t)$ is thus decomposed into spanwise wavenumber-frequency spectra, $G_{m,n}(\xi, \eta)$:

$$g(\xi, \zeta, \eta, t) = \sum_{m=0}^{M-1} \sum_{n=0}^{N-1} G_{m,n}(\xi, \eta) \exp[i2\pi(n\zeta/N + mt/M)] \quad (18)$$

where M and N are the number of time and space samples, respectively. The amplitude $A_{m,n}(\xi)$ of the modes (m, n) is defined as the maximum value of $|G_{m,n}(\xi, \eta)|$ at the position ξ.
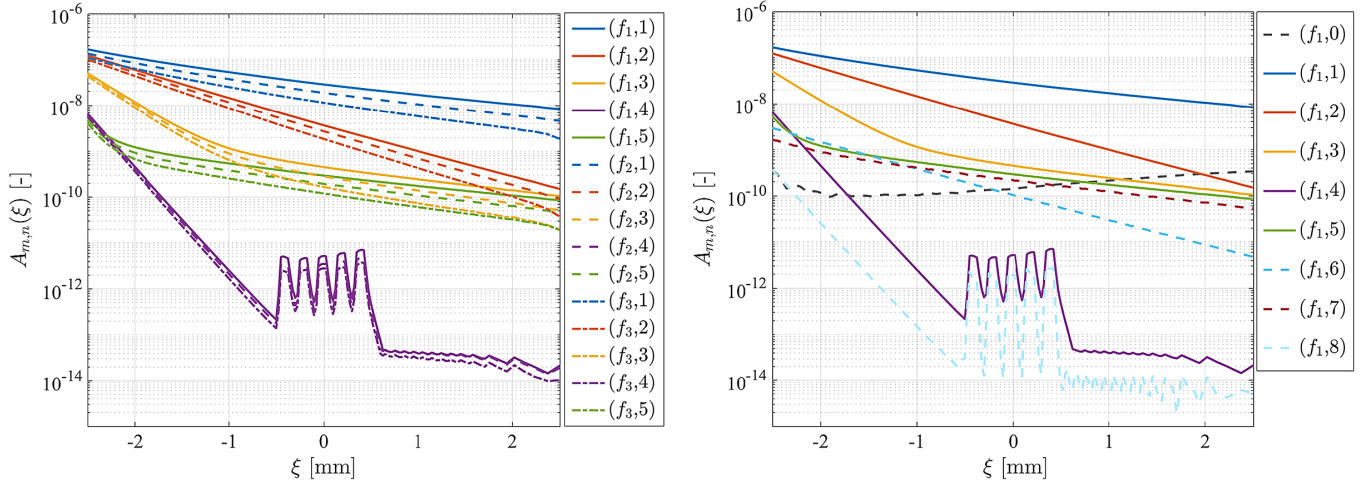
Figure 22 shows the amplitude of the perturbed modes with regard to the streamwise component of the velocity as well as the evolution of higher modes for the frequency f_1. Values are normalized with the edge velocity at the inflow. The origin of the streamwise coordinate, $\xi = 0$ mm, is set on the center of the roughness patch. Qualitatively similar results are found for the other frequencies and they are not shown here.

As predicted by LST-2D analysis, no amplified modes are found for the analyzed frequencies. In addition, no evidence of possible transient growth could be found for the considered disturbances. Even though a rapid disturbance growth at the roughness location is evident for the modes $(\cdot, 4)$ and $(\cdot, 8)$, their contribution to the total disturbance energy is small.

The absolute value of the time Fourier transform of the streamwise velocity $|\hat{U}_m(\xi, \zeta, \eta)|$ at different streamwise positions is shown in Fig. 23 for $f_1 = 167$ kHz. The absolute values are normalized on a scale of 0 to 1 and values below 0.2 are blanked out. The black isolines indicate the streamwise-velocity distribution, and the red line the projection of the roughness element. For clarity, the roughness height and the boundary-layer edge are marked in the figure. At the inflow, the maximum value of the disturbance is found at a height of about $\eta = 0.07$ mm, corresponding to about $0.14\,\delta$. Further downstream, viscous effects are responsible for a strong damping of the disturbance in the region close to the wall and the disturbance maximum moves to about $\eta = 0.2$ mm. As the roughness does not produce a significant perturbation at this height, no significant interaction can be observed with the incoming unsteady disturbance.

Fig. 22 **Evolution of the amplitude of different spatiotemporal Fourier modes along the streamwise coordinate for the streamwise component of the velocity.**

a)   **b)**

Fig. 23 **Time Fourier transform of the streamwise velocity for $f_1 = 167$ kHz: a) at the inflow ($\xi = -3.4$ mm); b) at the roughness position ($\xi = 0$ mm).**

VI.   Conclusions

Optimal transient-growth results for the capsule experiment in the Technische Universität Braunschweig (HLB) at Mach 5.9 were presented and compared with predictions by Paredes et al. [12] for a similar experiment at Mach 6 in the Actively Controlled Expansion tunnel at Texas A&M University (TAMU). The angle of attack in the two setups was different, but due to the spherical-segment forebody of both capsule models, the normalized boundary-layer edge data are still very much comparable. In each of the two sets of data, the unit Reynolds number varied only by a factor of about two. Both sets cover a Reynolds number range based on capsule diameter that extends over more than one order of magnitude, however. The maximum gain in energy is higher for the HLB capsule owing to the higher Reynolds numbers but still remains rather moderate in comparison with the amplification factors that correlate the onset of transition in other flows with modal instabilities. Similar trends were observed for the two setups, for example, concerning the spanwise wavelength normalized by the boundary-layer thickness of the optimal disturbances and the relatively short optimal optimization interval length. In particular, the surface-temperature dependence of the optimal transient-energy gain is very much comparable. Therefore, the value of the power-law exponent of the wall to boundary-layer edge temperature ratio of the correlation for roughness-induced transition that was originally proposed by Reshotko and Tumin [11] and the slightly different value recently derived by Paredes et al. [12] based on optimal transient-growth data for the TAMU capsule are further substantiated by the HLB capsule data at higher Reynolds numbers.

In some of the HLB experiments, a patch of well-defined micronsized surface roughness had been applied to the capsule model. The effect of this roughness patch on the boundary-layer flow field was replicated by direct numerical simulations (DNS). A hemisphere geometry has been introduced to reduce the size of the simulation domain and thus the computational costs of some of these DNS. We compared the flow on the capsule at angle of attack in the vicinity of the symmetry plane with the one on the hemisphere for both the smooth and the rough-wall geometry and showed that the flow over the hemisphere is similar to the flow over the capsule. In particular, a good match of velocity and temperature profiles is observed.

The stationary disturbance flow field introduced by the well-defined roughness patch was simulated, and its instability characteristics were analyzed. In the case of $Re/l = 18 \times 10^6/\text{m}$ where transitional surface heating in the HLB experiment was observed, 2D linear eigenvalue analysis (LST-2D) based on partial differential equations did not reveal any modal instability. Unsteady DNS have been undertaken to investigate possible nonmodal instability mechanisms. Unsteady pressure disturbances are introduced in the domain at three different frequencies ($f_1 = 167$, 200, and 333 kHz) and a spatiotemporal Fourier analysis has been performed on the entire domain. Neither modal amplification nor transient growth of disturbances could be found. In particular, the height of the roughness elements has been shown to be too small for the roughness wake to amplify the incoming unsteady disturbances.

In summary, several potential mechanisms have been considered to explain laminar-turbulent transition on the spherical forebody of blunt reentry capsules. At the conditions of the wind-tunnel experiments, modal disturbances are strongly damped in the boundary layer of the nominally smooth configuration, as shown in Ref. [8]. The complementary studies on the upper limit of nonmodal disturbance growth by using optimal transient-growth theory revealed that the maximum transient gain in energy for stationary disturbances is rather moderate. The maximum transient growth in total energy is found in a relatively short distance downstream of the stagnation point. Roughness-induced transient growth of stationary disturbances is unlikely to serve as the primary cause for the observed onset of transition for the rather low surface-roughness values of the HLB experiment. The DNS supplemented by the LST-2D studies on the effects of the roughness patch showed that the modifications of the steady flow field due to the patch are too weak to trigger modal disturbance growth in its wake. Present DNS did not reveal any noteworthy nonmodal disturbance growth in the wake flow.

Therefore, a plausible explanation for the observed transition onset in experiment for low surface-roughness values under conditions investigated in the HLB experiment remains to be found and further studies on the interaction of freestream disturbances with small surface roughness are required.

Very recent HLB experiments have yielded transition data for sandgrit-type coatings with significantly increased roughness heights. These data are in good agreement with the correlations derived from transient-growth scalings [49]. However, single discrete roughness elements of comparable height have already been found to produce a large enough deformation of the mean flow to support a significant modal growth within the wake of the roughness elements [17,18]. Hence, future numerical studies for distributed surface roughness at increased roughness heights should take into account the effects of the distributed surface roughness on the mean flow and its modal and nonmodal (transient) disturbance growth characteristics.

References

[1] Schneider, S. P., "Effects of Roughness on Hypersonic Boundary-Layer Transition," *Journal of Spacecraft and Rockets*, Vol. 45, No. 2, 2008, pp. 193–209.
doi:10.2514/1.29713

[2] Schneider, S. P., "Summary of Hypersonic Boundary-Layer Transition Experiments on Blunt Bodies with Roughness," *Journal of Spacecraft and Rockets*, Vol. 45, No. 6, 2008, pp. 1090–1105.
doi:10.2514/1.37431

[3] Reda, D. C., "Review and Synthesis of Roughness-Dominated Transition Correlations for Reentry Applications," *Journal of Spacecraft and Rockets*, Vol. 39, No. 2, 2002, pp. 161–167.
doi:10.2514/2.3803

[4] Hollis, B. R., "Correlation of Recent and Historical Rough-Wall Transition Data on Hemispherical Nosetips," *33rd AIAA Aerodynamic Measurement Technology and Ground Testing Conference, AIAA AVIATION Forum*, AIAA Paper 2017-3986, 2017.
doi:10.2514/6.2017-3986

[5] Johnson, H. B., Candler, G. V., and Wright, M. J., "Boundary Layer Stability Analysis of Mars Science Laboratory Aeroshell," *44th AIAA Aerospace Sciences Meeting and Exhibit, Aerospace Sciences Meetings*, AIAA Paper 2006-0920, 2006.
doi:10.2514/6.2006-920

[6] Chang, C.-L., Choudhari, M. M., Hollis, B. R., and Li, F., "Transition Analysis for the Mars Science Laboratory Entry Vehicle," *41st AIAA Thermophysics Conference*, AIAA Paper 2009-4076, 2009.
doi:10.2514/6.2009-4076

[7] Theiss, A., Lichtmess, M., and Hein, S., "Local Stability Analysis of Laminar-Turbulent Transition on Blunt Generic Re-Entry Capsules," *New Results in Numerical and Experimental Fluid Mechanics X, Notes on Numerical Fluid Mechanics and Multidisciplinary Design*, Vol. 132, Springer International Publishing, Switzerland, 2016, pp. 279–288.
doi:10.1007/978-3-319-27279-5_25

[8] Theiss, A., Hein, S., Heitmann, D., Ali, S. R. C., and Radespiel, R., "Numerical and Experimental Investigation of Laminar-Turbulent Boundary Layer Transition on a Blunt Generic Re-Entry Capsule," *44th AIAA Fluid Dynamics Conference, AIAA AVIATION Forum*, AIAA Paper 2014-2353, 2014.
doi:10.2514/6.2014-2353

[9] Reshotko, E., and Tumin, A., "The Blunt Body Paradox — A Case for Transient Growth," *Laminar-Turbulent Transition*, Springer, Berlin, 2000, pp. 403–408.
doi:10.1007/978-3-662-03997-7_60

[10] Schmid, P. J., and Henningson, D. S., "Stability and Transition in Shear Flows," *Applied Mathematical Sciences*, Vol. 142, Springer, New York, 2001.
doi:10.1007/978-1-4613-0185-1

[11] Reshotko, E., and Tumin, A., "Role of Transient Growth in Roughness-Induced Transition," *AIAA Journal*, Vol. 42, No. 4, 2004, pp. 766–770.
doi:10.2514/1.9558

[12] Paredes, P., Choudhari, M. M., and Li, F., "Blunt-Body Paradox and Improved Application of Transient-Growth Framework," *AIAA Journal*, Vol. 56, No. 7, 2018, pp. 2604–2614.
doi:10.2514/1.J056678

[13] Leidy, A. N., Reshotko, E., Siddiqui, F., and Bowersox, R. D. W., "Characterizing the Transient Growth Mechanism on a Hypersonic Blunt Body at a High Angle of Attack," *46th AIAA Fluid Dynamics Conference*, AIAA Paper 2016-3951, 2016.
doi:10.2514/6.2016-3951

[14] Leidy, A. N., Reshotko, E., Siddiqui, F., and Bowersox, R. D. W., "Transition Due to Roughness on Blunt Capsule: Comparison with Transient Growth Correlation," *Journal of Spacecraft and Rockets*, Vol. 55, No. 1, 2018, pp. 167–180.
doi:10.2514/1.A33625

[15] Ali, S. R. C., Radespiel, R., and Theiss, A., "Transition Experiment with a Blunt Apollo Shape Like Capsule in Hypersonic Ludwieg Tube," *63. Deutscher Luft- und Raumfahrtkongress 2014*, DGLR Paper 2014–340270, Bonn, 2014.

[16] Radespiel, R., Ali, S. R. C., Bowersox, R. D. W., Leidy, A. N., Tanno, H., Kirk, L. C., and Reshotko, E., "Experimental Investigation of Roughness Effects on Transition on Blunt Spherical Capsule Shapes," *2018 AIAA Aerospace Sciences Meeting, AIAA SciTech Forum*, AIAA Paper 2018-0059, 2018.
doi:10.2514/6.2018-0059

[17] Theiss, A., Hein, S., Ali, S. R. C., and Radespiel, R., "Wake Flow Instability Studies Behind Discrete Roughness Elements on a Generic Re-Entry Capsule," *46th AIAA Fluid Dynamics Conference, AIAA AVIATION Forum*, AIAA Paper 2016-4382, 2016.
doi:10.2514/6.2016-4382

[18] Theiss, A., and Hein, S., "Investigation on the Wake Flow Instability Behind Isolated Roughness Elements on the Forebody of a Blunt Generic Reentry Capsule," *Progress in Flight Physics*, edited by D. Knight, Y. Bondar, I. Lipatov, and P. Reijasse, EDP Sciences, Torus Press, Moscow, 2017, pp. 451–488.
doi:10.1051/eucass/201709451

[19] Pralits, J., Airiau, C., Hanifi, A., and Henningson, D., "Sensitivity Analysis Using Adjoint Parabolized Stability Equations for Compressible Flows," *Flow, Turbulence and Combustion*, Vol. 65, Nos. 3–4, 2000, pp. 321–346.
doi:10.1023/A:1011434805046

[20] Tempelmann, D., Hanifi, A., and Henningson, D. S., "Spatial Optimal Growth in Three-Dimensional Compressible Boundary Layers," *Journal of Fluid Mechanics*, Vol. 704, Aug. 2012, pp. 251–279.
doi:10.1017/jfm.2012.235

[21] Paredes, P., Choudhari, M. M., Li, F., and Chang, C.-L., "Optimal Growth in Hypersonic Boundary Layers," *AIAA Journal*, Vol. 54, No. 10, 2016, pp. 3050–3061.
doi:10.2514/1.J054912

[22] Paredes, P., Choudhari, M. M., and Li, F., "Blunt-Body Paradox and Transient Growth on a Hypersonic Spherical Forebody," *Physical Review Fluids*, Vol. 2, No. 5, 2017, Paper 053903.
doi:10.1103/PhysRevFluids.2.053903

[23] Hein, S., Bertolotti, F., Simen, M., Hanifi, A., and Henningson, D., "Linear Nonlocal Instability Analysis- The Linear NOLOT Code," Tech. Rept. DLR-IB 223-94 A56, Deutsches Zentrum für Luft- und Raumfahrt e. V. (DLR), Germany, 1994.

[24] Chang, C.-L., Malik, M., Erlebacher, G., and Hussaini, M., "Compressible Stability of Growing Boundary Layers Using Parabolized Stability Equations," *22nd Fluid Dynamics, Plasma Dynamics and Lasers Conference*, AIAA Paper 1991-1636, 1991.
doi:10.2514/6.1991-1636

[25] Tempelmann, D., Hanifi, A., and Henningson, D. S., "Spatial Optimal Growth in Three-Dimensional Boundary Layers," *Journal of Fluid Mechanics*, Vol. 646, Dec. 2010, pp. 5–37.
doi:10.1017/S0022112009993260

[26] Levin, O., and Henningson, D. S., "Exponential vs Algebraic Growth and Transition Prediction in Boundary Layer Flow," *Flow, Turbulence and Combustion*, Vol. 70, Nos. 1–4, 2003, pp. 183–210.
doi:10.1023/B:APPL.0000004918.05683.46

[27] Zuccher, S., Tumin, A., and Reshotko, E., "Parabolic Approach to Optimal Perturbations in Compressible Boundary Layers," *Journal of Fluid Mechanics*, Vol. 556, June 2006, pp. 189–216.
doi:10.1017/S0022112006009451

[28] Chu, B.-T., "On the Energy Transfer to Small Disturbances in Fluid Flow (Part I)," *Acta Mechanica I*, Vol. 1, No. 3, 1965, pp. 215–234.
doi:10.1007/BF01387235

[29] Mack, L. M., "Boundary Layer Stability Theory," Tech. Rept. TR-900-277, Jet Propulsion Lab., California Institute of Technology, Pasadena, CA, Nov. 1969.

[30] Hanifi, A., Schmid, P. J., and Henningson, D. S., "Transient Growth in Compressible Boundary Layer Flow," *Physics of Fluids*, Vol. 8, No. 3, 1996, pp. 826–837.
doi:10.1063/1.868864

[31] Hermanns, M., and Hernández, J. A., "Stable High-Order Finite-Difference Methods Based on Non-Uniform Grid Point Distributions," *International Journal for Numerical Methods in Fluids*, Vol. 56, No. 3, 2008, pp. 233–255.
doi:10.1002/(ISSN)1097-0363

[32] Li, F., Choudhari, M. M., Chang, C.-L., and White, J., "Effects of Injection on the Instability of Boundary Layers over Hypersonic Configurations," *Physics of Fluids*, Vol. 25, No. 10, Oct. 2013, Paper 104107.
doi:10.1063/1.4825038

[33] Hartmann, D., Meinke, M., and Schröder, W., "An Adaptive Multilevel Multigrid Formulation for Cartesian Hierarchical Grid Methods," *Computers & Fluids*, Vol. 37, No. 9, 2008, pp. 1103–1125.
doi:10.1016/j.compfluid.2007.06.007

[34] Lintermann, A., Schlimpert, S., Grimmen, J. H., Günther, C., Meinke, M., and Schröder, W., "Massively Parallel Grid Generation on HPC Systems," *Computer Methods in Applied Mechanics and Engineering*, Vol. 277, Aug. 2014, pp. 131–153.
doi:10.1016/j.cma.2014.04.009

[35] Schneiders, L., Hartmann, D., Meinke, M., and Schröder, W., "An Accurate Moving Boundary Formulation in Cut-Cell Methods," *Journal of Computational Physics*, Vol. 235, Feb. 2013, pp. 786–809.
doi:10.1016/j.jcp.2012.09.038

[36] Schilden, T., Schröder, W., Ali, S. R. C., Wu, J., Schreyer, A.-M., and Radespiel, R., "Analysis of Acoustic and Entropy Disturbances in a Hypersonic Wind Tunnel," *Physics of Fluids*, Vol. 28, No. 5, 2016, Paper 056104.
doi:10.1063/1.4948435

[37] Schilden, T., and Schröder, W., "Numerical Analysis of High Speed Wind Tunnel Flow Disturbance Measurements Using Stagnation Point Probes," *Journal of Fluid Mechanics*, Vol. 833, Dec. 2017, pp. 247–273.
doi:10.1017/jfm.2017.674

[38] Hoarau, Y., Pena, D., Vos, J. B., Charbonnier, D., Gehri, A., Brazak, M., Deloze, T., and Laurendeau, E., "Recent Developments of the Navier Stokes Multi Block (NSMB) CFD Solver," *54th AIAA Aerospace Sciences Meeting, AIAA SciTech Forum*, AIAA Paper 2016-2056, 2016.
doi:10.2514/6.2016-2056

[39] Stemmer, C., Birrer, M., and Adams, N. A., "Disturbance Development in an Obstacle Wake in a Reacting Hypersonic Boundary Layer," *Journal of Spacecraft and Rockets*, Vol. 54, No. 4, 2017, pp. 945–960.
doi:10.2514/1.A33708

[40] Hollis, B. R., Berger, K. T., Horvath, T. J., Coblish, J. J., Norris, J. D., Lillard, R. P., and Kirk, B. S., "Aeroheating Testing and Predictions for Project Orion Crew Exploration Vehicle," *Journal of Spacecraft and Rockets*, Vol. 46, No. 4, 2009, pp. 766–780.
doi:10.2514/1.38579

[41] Litton, D., Edwards, J., and White, J., "Algorithmic Enhancements to the VULCAN Navier-Stokes Solver," *16th AIAA Computational Fluid Dynamics Conference*, AIAA Paper 2003-3979, 2003.
doi:10.2514/6.2003-3979

[42] Raddatz, J., and Fassbender, J. K., "Block Structured Navier-Stokes Solver Flower," *MEGAFLOW- Numerical Flow Simulation for Aircraft Design*, Springer, Berlin, 2005, pp. 27–44.
doi:10.1007/3-540-32382-1_2

[43] Andersson, P., Berggren, M., and Henningson, D. S., "Optimal Disturbances and Bypass Transition in Boundary Layers," *Physics of Fluids*, Vol. 11, No. 1, 1999, pp. 134–150.
doi:10.1063/1.869908

[44] Theiss, A., Leyh, S., and Hein, S., "Pressure Gradient Effects on Wake Flow Instabilities Behind Isolated Roughness Elements on Re-Entry Capsules," *7th European Conference for Aeronautics and Space Sciences (EUCASS)*, EUCASS Association, Paper FP-594, 2017, https://www.eucass.eu/doi/EUCASS2017-594.pdf.

[45] Tumin, A., and Reshotko, E., "Spatial Theory of Optimal Disturbances in Boundary Layers," *Physics of Fluids*, Vol. 13, No. 7, 2001, pp. 2097–2104.
doi:10.1063/1.1378070

[46] Tumin, A., and Reshotko, E., "Optimal Disturbances in Compressible Boundary Layers," *AIAA Journal*, Vol. 41, No. 12, 2003, pp. 2357–2363.
doi:10.2514/2.6860

[47] Zuccher, S., Shalaev, I., Tumin, A., and Reshotko, E., "Optimal Disturbances in the Supersonic Boundary Layer Past a Sharp Cone," *AIAA Journal*, Vol. 45, No. 2, 2007, pp. 366–373.
doi:10.2514/1.22541

[48] Klebanoff, P. S., Cleveland, W. G., and Tidstrom, K. D., "On the Evolution of a Turbulent Boundary Layer Induced by a Three-Dimensional Roughness Element," *Journal of Fluid Mechanics*, Vol. 237, April 1992, pp. 101–187.
doi:10.1017/S0022112092003379

[49] Radespiel, R., Ali, S. R. C., Bowersox, R. D. W., Leidy, A. N., Tanno, H., Kirk, L. C., and Reshotko, E., "Experimental Investigation of Roughness Effects on Transition on Blunt Spherical Capsule Shapes," *Journal of Spacecraft and Rockets* (in press).

R. M. Cummings
Associate Editor

Bibliography

Ali, S. R., Radespiel, R., and Theiss, A. (2014). Transition Experiment with a Blunt Apollo Shape Like Capsule in Hypersonic Ludwieg Tube. *Paper 2014-340270,* 63. Deutscher Luft- und Raumfahrtkongress 2014, Augsburg, Germany.

Anderson Jr., J. D. (2006). *Hypersonic and High-Temperature Gas Dynamics.* AIAA Education Series.

Berry, S. A. and Horvath, T. J. (2008). Discrete-Roughness Transition for Hypersonic Flight Vehicles. *Journal of Spacecraft and Rockets,* 45(2):216–227.

Bertin, J. J. and Cummings, R. M. (2006). Critical hypersonic aerothermodynamic phenomena. *Annual Review of Fluid Mechanics,* 38:129–157.

Blottner, F. G., Johnson, M., and Ellis, M. (1971). *Chemically Reacting Viscous Flow Program for Multi-Component Gas Mixtures.* Technical Report SC-RR-70-754, Sandia Natl. Laboratories.

Chang, C.-L., Choudhari, M., Venkatachari, B. S., and Li, F. (2011). Effects of Cavities and Protuberances on Transition over Hypersonic Vehicles. *AIAA Paper 2011-3245,* 41st AIAA Fluid Dynamics Conference and Exhibit, Honolulu, Hawaii, USA.

Chang, C.-L., Vinh, H., and Malik, M. (1997). Hypersonic boundary-layer stability with chemical reactions using PSE. *AIAA Paper 1997-2012,* 28th AIAA Fluid Dynamics Conference, Snowmass Village, Colorado, USA.

Choudhari, M., Li, F., Minwei, W., Chang, C., Edwards, J., Kegerise, M., and King, R. (2010). Laminar-turbulent transition behind discrete roughness elements in a high-speed boundary layer. *AIAA Paper 2010-1575,* 48th AIAA Aerospace Sciences Meeting Including the New Horizons Forum and Aerospace Exposition, Orlando, Florida, USA.

De Tullio, N., Paredes, P., Sandham, N., and Theofilis, V. (2013). Laminar turbulent transition induced by a discrete roughness element in a supersonic boundary layer. *Journal of Fluid Mechanics,* 735:613–646.

Di Giovanni, A. and Stemmer, C. (2017). Numerical Simulations of the High-Enthalpy Boundary Layer on a Generic Capsule Geometry with Roughness. In *New Results in Numerical and Experimental Fluid Mechanics XI, Contributions to the 20th STAB/DGLR Symposium*, pages 189–198. Dillmann, A. et al. (eds). Springer, Cham.

Di Giovanni, A. and Stemmer, C. (2018). Crossflow-type breakdown induced by distributed roughness in the boundary layer of a hypersonic capsule configuration. *Journal of Fluid Mechanics*, 856:470–503.

Di Giovanni, A. and Stemmer, C. (2019a). Roughness-Induced Boundary-Layer Transition on a Hypersonic Capsule-Like Forebody Including Nonequilibrium. *Journal of Spacecraft and Rockets*, 56(6):1795–1808.

Di Giovanni, A. and Stemmer, C. (2019b). Roughness-Induced Crossflow-Type Instabilities in a Hypersonic Capsule Boundary Layer including Non-Equilibrium. *Journal of Spacecraft and Rockets*, 56(5):1409–1423.

Drews, S., Downs, R., Doolittle, C., Goldstein, D., and White, E. (2011). Direct Numerical Simulations of Flow Past Random Distributed Roughness. *AIAA Paper 2011-0564*, 49th AIAA Aerospace Sciences Meeting including the New Horizons Forum and Aerospace Exposition, Orlando, Florida, USA.

Germain, P. D. and Hornung, H. G. (1997). Transition on a slender cone in hyper-velocity flow. *Experiments in Fluids*, 22:183–190.

Goebel, F., Vos, J., and Mundt, C. (2012). CFD Simulation of the FIRE II Flight Experiment. *AIAA Paper 2012-3350*, 42nd AIAA Fluid Dynamics Conference and Exhibit, New Orleans, Louisiana, USA.

Grabow, R. and White, C. (1975). Surface roughness effects on nosetip ablation characteristics. *AIAA Journal*, 13(5):605–609.

Graves, R. A. and Witte, W. G. (1996). *Flight-test analysis of Apollo heat-shield material using the pacemaker vehicle system*. Technical Report TN D-4713, NASA.

Groskopf, G. and Kloker, M. J. (2016). Instability and transition mechanisms induced by skewed roughness elements in a high-speed laminar boundary layer. *Journal of Fluid Mechanics*, 805:262–302.

Hein, S., Theiss, A., Di Giovanni, A., Stemmer, C., Schilden, T., Schröder, W., Paredes, P., Choudhari, M. M., Li, F., and Reshotko, E. (2019). Numerical Investigation of Roughness Effects on Transition on Spherical Capsules. *Journal of Spacecraft and Rockets*, 56(2):388–404.

Hirschfelder, J. O., Curtiss, C. F., and Bird, R. A. (1964). *Molecular Theory of Gases and Liquids.* Wiley and Sons, New York.

Hoarau, Y., Pena, D., Vos, J. B., Charbonier, D., Gehri, A., Braza, M., Deloze, T., and Laurendeau, E. (2016). Recent Developments of the Navier Stokes Multi Block (NSMB) CFD solver. *AIAA Paper 2016-2056,* 54th AIAA Aerospace Sciences Meeting, San Diego, California, USA.

Hollis, B. R. (2014). Distributed Roughness Effects on Blunt-Body Transition and Turbulent Heating. *AIAA Paper 2014-0238,* 52nd AIAA Aerospace Sciences Meeting, National Harbor, Maryland, USA.

Hudson, M. L., Chokani, N., and Candler, G. (1996). Linear stability of hypersonic flow in thermochemical nonequilibrium. *AIAA Journal*, 35(6):958–964.

Johnson, H. B. and Candler, G. V. (1999). PSE Analysis of Reacting Hypersonic Boundary Layer Transition. *AIAA Paper 1999-3793,* 30th Fluid Dynamics Conference, Norfolk,Virginia, USA.

Johnson, H. B. and Candler, G. V. (2005). Hypersonic Boundary Layer Stability Analysis Using PSE-Chem. *AIAA Paper 2005-5023,* 35th AIAA Fluid Dynamics Conference and Exhibit, Toronto, Ontario, Canada.

Johnson, H. B., Seipp, T. G., and Candler, G. V. (1998). Numerical study of hypersonic reacting boundary layer transition on cones. *Physics of Fluids*, 10(10):2676–2685.

Kurz, H. B. E. and Kloker, M. J. (2016). Mechanisms of flow tripping by discrete roughness elements in a swept-wing boundary layer. *Journal of Fluid Mechanics*, 796:158–194.

Leidy, A. N., Reshotko, E., Siddiqui, F., and Bowersox, R. D. W. (2018). Transition due to Roughness on Blunt Capsule: Comparison with Transient Growth Correlation. *Journal of Spacecraft and Rockets*, 55(1):167–180.

Mack, L. M. (1987). Review of Linear Compressible Stability Theory. In *Stability of Time Dependent and Spatially Varying Flows*, pages 164–187. Dwoyer, D.L. and Hussaini, M.Y. (eds). Springer-Verlag, New York.

Malik, M. R. (2003). Disturbance Development in an Obstacle Wake in a Reacting Hypersonic Boundary Layer. *Journal of Spacecraft and Rockets*, 40(3):332–344.

Malik, M. R. and Anderson, E. C. (1991). Real gas effects on hypersonic boundary layer stability. *Physics of Fluids*, 3(5):803–821.

145

Malik, M. R., Li, F., Choudhari, M. M., and Chang, C.-L. (1999). Secondary instability of crossflow vortices and swept-wing boundary-layer transition. *Journal of Fluid Mechanics*, 399:85–115.

Marineau, E. C., Laurence, S. J., and Hornung, H. G. (2010). Apollo-Shaped Capsule Boundary Layer Transition at High-Enthalpy in T5. *AIAA Paper 2010-0446,* 48th AIAA Aerospace Sciences Meeting Including the New Horizons Forum and Aerospace Exposition, Orlando, Florida, USA.

Marxen, O., Iaccarino, G., and Magin, T. E. (2014). Direct numerical simulations of hypersonic boundary-layer transition with finite-rate chemistry. *Journal of Fluid Mechanics*, 755:35–49.

Morkovin, M. (1984). Bypass transition to turbulence and research desiderata. *Transition in Turbines,* NASA CP-2386, pages 161–199.

Mortensen, C. H. and Zhong, X. (2016). Real-Gas and Surface-Ablation Effects on Hypersonic Boundary-Layer Instability over a Blunt Cone. *AIAA Journal*, 54(3):980–998.

Muppidi, S. and Mahesh, K. (2012). Direct Numerical Simulations of roughness-induced transition in supersonic boundary layers. *Journal of Fluid Mechanics*, 693:28–56.

Olejniczak, J., Wright, M. J., Laurence, S., and Hornung, H. G. (2005). Computational Modeling of T5 Laminar and Turbulent Heating Data on Blunt Cones, Part 1: Titan Application. *AIAA Paper 2005-0176,* 43rd AIAA Aerospace Sciences Meeting and Exhibit, Reno, Nevada, USA.

Paredes, P., Choudhari, M. M., and Li, F. (2017). Blunt-body paradox and transient growth on a hypersonic spherical forebody. *Physical Review Fluids*, 2:053903.

Paredes, P., Choudhari, M. M., and Li, F. (2018). Blunt-Body Paradox and Improved Application of Transient-Growth Framework. *AIAA Journal*, 56(7):2604–2614.

Park, C. (1989). A Review of Reaction Rates in High Temperature Air. *AIAA Paper 1989-1740,* 24th Thermophysics Conference, Buffalo, New York, USA.

Park, C. (2004). Stagnation-Point Radiation for Apollo 4. *Journal of Thermophysics and Heat Transfer*, 18(3):349–357.

Radespiel, R., Ali, S. R. C., Muñoz, F., Bowersox, R., Leidy, A., Tanno, H., Kirk, L. C., and Reshotko, E. (2019). Experimental Investigation of Roughness Effects on Transition on Blunt Spherical Capsule Shapes. *Journal of Spacecraft and Rockets*, 56(2):405–420.

Reda, D. C. (2002). Review and Synthesis of Roughness-Dominated Transition Correlations for Reentry Applications. *Journal of Spacecraft and Rockets*, 39(2):161–167.

Reda, D. C., Wilder, M. C., Bogdanoff, D. W., and Prabhu, D. K. (2008). Transition Experiments on Blunt Bodies with Distributed Roughness in Hypersonic Free Flight. *Journal of Spacecraft and Rockets*, 45(2):210–215.

Reshotko, E. and Tumin, A. (2000). The Blunt Body Paradox - A Case for Transient Growth. In *IUTAM Symposium: Laminar-Turbulent Transition*, pages 403–408. Fasel, H.F. and Saric, W.S. (eds). Springer, Berlin, Heidelberg.

Reshotko, E. and Tumin, A. (2004). Role of Transient Growth in Roughness-Induced Transition. *AIAA Journal*, 42(4):766–770.

Schneider, S. P. (2006). Laminar-Turbulent Transition on Reentry Capsules and Planetary Probes. *Journal of Spacecraft and Rockets*, 43(6):1153–1173.

Schneider, S. P. (2008a). Effects of Roughness on Hypersonic Boundary-Layer Transition. *Journal of Spacecraft and Rockets*, 45(2):193–209.

Schneider, S. P. (2008b). Summary of Hypersonic Boundary-Layer Transition Experiments on Blunt Bodies with Roughness. *Journal of Spacecraft and Rockets*, 45(6):1090–1105.

Stemmer, C., Birrer, M., and Adams, N. A. (2017a). Disturbance Development in an Obstacle Wake in a Reacting Hypersonic Boundary Layer. *Journal of Spacecraft and Rockets*, 54(4):945–960.

Stemmer, C., Birrer, M., and Adams, N. A. (2017b). Hypersonic Boundary-Layer Flow with an Obstacle in Thermochemical Equilibrium and Nonequilibrium. *Journal of Spacecraft and Rockets*, 54(4):899–915.

Stemmer, C. and Fehn, J. (2014). High-temperature gas effects at a capsule under re-entry and wind-tunnel conditions. *AIAA Paper 2014-2645,* 44th AIAA Fluid Dynamics Conference, Atlanta, Georgia, USA.

Stuckert, G. and Reed, H. L. (1994). Linear Disturbances in Hypersonic, Chemically Reacting Shock Layers. *AIAA Journal*, 32(7):1384–1393.

Tanno, H., Kodera, M., Komuro, T., Sato, K., Takahashi, M., and Itoh, K. (2010). Aeroheating measurements on a reentry capsule model in free-piston shock tunnel HIEST. *AIAA Paper 2010-1181,* 48th AIAA Aerospace Sciences Meeting Including the New Horizons Forum and Aerospace Exposition, Orlando, Florida, USA.

Tanno, H., Sato, K., Komuro, T., and Itoh, K. (2014). Free-flight aerodynamic test of reentry vehicles in high-temperature real-gas flow. *AIAA Paper 2014-3109,* 19th AIAA International Space Planes and Hypersonic Systems and Technologies Conference, Atlanta, Georgia, USA.

Theiss, A., Ali, S. R., Hein, S., Heitmann, D., and Radespiel, R. (2014). Numerical and experimental investigation of laminar-turbulent boundary layer transition on a blunt generic re-entry capsule. *AIAA Paper 2014-2353,* 44th AIAA Fluid Dynamics Conference, Atlanta, Georgia, USA.

Theiss, A., Hein, S., Ali, S. R. C., and Radespiel, R. (2016). Wake flow instability studies behind discrete roughness elements on a generic re-entry capsule. *AIAA Paper 2016-4382,* 46th AIAA Fluid Dynamics Conference, Washington, D.C., USA.

Theiss, A., Leyh, S., and Hein, S. (2017). Pressure gradient effects on wake flow instabilities behind isolated roughness elements on re-entry capsules. *Paper FP-594,* 7th EUCASS (European Conference for Aeronautics and Aerospace Sciences), Milan, Italy.

Van den Eynde, J. P. J. P. and Sandham, N. D. (2016). Numerical Simulations of Transition due to Isolated Roughness Elements at Mach 6. *AIAA Journal,* 54(1):53–65.

Vos, J., Duquesne, N., and Lee, H. (1999). Shock Wave Boundary Layer Interaction Studies Using the NSMB Flow Solver. In *Proceedings of the 3rd European Symposium on Aerothermodynamics for Space and Vehicles,* ESA SP-426, ESTEC, pages 229–236. Harris, R. A. (eds). European Space Agency (ESA).

Wilder, M. C., Reda, D., and Prabhu, D. K. (2015). Transition Experiments on Blunt Bodies with Distributed Roughness in Hypersonic Free Flight in Carbon Dioxide. *AIAA Paper 2015-1738,* 53rd AIAA Aerospace Sciences Meeting, Kissimmee, Florida, USA.

Wilke, C. (1950). A Viscosity Equation for Gas Mixtures. *Journal of Chemical Physics,* 18(4):517–519.